



**1 A search for flavour changing neutral currents
2 involving a top quark and a Z boson, using the
3 data collected by the CMS collaboration at a
4 centre-of-mass energy of 13 TeV**

5 Isis Van Parijs

**6 Proefschrift ingediend met het oog op het behalen van de academische graad
7 Doctor in de Wetenschappen.**

Published in Faculteit Wetenschappen & Bio-ingenieurswetenschappen
 Vrije Universiteit Brussel
At 10 November 2017.

8

Responsible Contact: Isis Van Parijs
 Institute for High Energy Physics
Promotor: Prof. Jorgen D'Hondt

9 First Referee: Prof. Dr. J. D'Hondt
 Date of Hand-in: 10 November 2017
 Date of Defense: 10 December 2017

Contents

11	1 Theoretical basis	1
12	1.1 Elementary particles and forces	1
13	1.2 Standard Model Lagrangian, connecting fields with particles	3
14	1.3 Flavours in the SM	5
15	1.4 The top quark in the SM	6
16	1.5 Effective field theories	11
17	1.6 Motivation for new physics	14
18	1.7 An effective approach beyond the SM: FCNC involving a top quark	15
19	1.8 Experimental constraints on top-FCNC	18
20	2 Experimental set-up	23
21	2.1 The Large Hadron Collider	23
22	2.2 The Compact Muon Solenoid	27
23	2.2.1 CMS coordinate system	27
24	2.2.2 Towards the heart of CMS	28
25	2.2.3 Data acquisition	37
26	2.2.4 Phase 1 upgrades	37
27	2.2.5 CMS computing model	39
28	3 Analysis techniques	41
29	3.1 Hadron collisions at high energies	41
30	3.2 Event generation	44
31	3.2.1 Fundamentals of simulating a proton collision	44
32	3.2.2 Programs for event generation	44
33	3.2.3 Generating FCNC top-Z interactions	46
34	3.2.4 Generating SM background events	48
35	3.3 Multivariate analysis techniques: Boosted Decision Trees	50
36	3.4 Statistical methodology	52
37	4 Event reconstruction and identification	55
38	4.1 Object Reconstruction	55
39	4.1.1 Charged particle tracks	57
40	4.1.2 Following the Muon's Footsteps	57
41	4.1.3 The path of the Electron	57

42	4.1.4 Primary Vertex Reconstruction	58
43	4.1.5 Calorimeter clusters	58
44	4.2 Particle flow identification	59
45	4.3 Pileup mitigation and luminosity measurement	59
46	4.4 Physics object reconstruction and identification	60
47	4.4.1 Muons	60
48	4.4.2 Electrons	62
49	4.4.3 Jets	63
50	4.4.4 Jets from b fragmentation	66
51	4.4.5 Missing transverse energy	69
52	4.5 Summary of corrections	69
53	5 Event selection and categorisation	71
54	5.1 Baseline event selection and filters	71
55	5.1.1 Event cleaning	74
56	5.1.2 Estimation of the trigger efficiency	76
57	5.1.3 Corrections	77
58	5.1.4 Reconstruction of kinematic variables	81
59	5.2 Analysis Strategy	82
60	5.3 Data driven NPL background simulation	83
61	5.4 Statistical independent regions	85
62	5.4.1 WZCR	86
63	5.4.2 TTCR and STCR	87
64	5.4.3 TTSR and STSR	87
65	6 The search for FCNC involving a top quark and a Z boson	89
66	6.1 Construction of template distributions	89
67	6.1.1 Distributions of the BDT variables	89
68	6.1.2 BDTs	94
69	6.1.3 Transverse mass in WZCR	96
70	6.2 Systematic uncertainties	96
71	6.2.1 Effect of systematic uncertainties on the transverse mass distribution	99
72	6.2.2 Effect of the systematic uncertainties on the multivariate discriminator distributions	99
73	6.3 Limit setting procedure validation	108■
74	6.4 Results and discussion	109■
75	6.4.1 One dimensional limits	121■
76	6.4.2 Two-dimensional limits	124■
78	7 Denouement of the top-Z FCNC hunt at 13 TeV	127■
79	Appendices	127■
80	A Trigger scale factors	129■
81	B Dilepton controlplots	131■

82	C Statistical independent regions	133■
83	D Details about the BDTs	135■
84	E Prefit distributions	153■
85	E.1 BDT distributions	153■
86	E.2 Transverse W boson mass distributions	158■
87	E.3 Input variables of the BDT	160■
88	F Limit setting validations	163■
89	F.1 Blinded initial fit, postfit distributions	163■
90	F.2 Post fit distributions of the BDT input vars	164■
91	Bibliography	165■

Theoretical basis

1

93 The Standard Model (SM) [1] is a name given in the 1970s to a theory describing the fun-
 94 damental particles and their interactions. This quantum field theory describes the particles
 95 and their interactions as fields and has successfully incorporated three of the four fundamental
 96 forces in the universe. In [Section 1.1](#), the particle content of the SM is summarised, while
 97 [Section 1.2](#) describes the SM Lagrangian and its symmetries. In [Section 1.3](#), the flavour content
 98 of the SM is highlighted, and [Section 1.4](#) focusses on the top quark in the SM.

99 The successful theory of the SM has some shortcomings which are discussed in [Section 1.6](#)
 100 and lead to searches for a more general theory. One of such is using an effective field theory
 101 (EFT) approach [2] to search for new physics in a model independent way. In [Section 1.7](#) an
 102 EFT model focussing on flavour changing neutral currents (FCNC) involving a top quark is
 103 presented. Its current experimental constraints are given in [Section 1.8](#).

104 **1.1 Elementary particles and forces**

105 The interactions in nature can be described by four forces, the strong force, the electromagnetic
 106 (EM) force, the weak force and the gravitational force. These interactions happen via particles
 107 with an integer spin known as bosons. The strong interaction is mediated by eight gluons g ,
 108 while the electromagnetic force is mediated by photons γ , and the weak force by Z and W^\pm
 109 bosons. In [Table 1.1](#), the forces and their characteristics are shown. The gravitational force is
 110 the only force not included in the SM and can be neglected for energies lower than the Planck
 scale (1.22×10^{19} GeV).

Table 1.1: The four forces of nature and their characteristics.

	Range	Mediator
Strong force	10^{-15} m	8 gluons
Electromagnetic force	∞	photon
Weak force	10^{-18} m	W^\pm , Zbosons
Gravitational force	∞	unknown

The fermions are the particles that make up the visible matter in the universe. They carry half integer spin and can be subdivided into leptons and quarks, where leptons do not interact strongly. Each fermion has a corresponding anti-fermion which has the same mass and is oppositely charged. The electron e is the first elementary particle discovered [3] and belongs to the first generation of leptons together with the electron neutrino ν_e . The second generation comprises the muon μ and muon neutrino ν_μ , whereas the third generation consists of the tau τ and tau neutrino ν_τ . The neutrinos are neutral particles, while the other leptons have charge $\pm q_e$ with q_e representing the elementary charge of 1.602×10^{-19} C. The masses of charged leptons differ by four orders of magnitude between the first and third generations. In the SM the neutrinos are assumed to be massless, nonetheless it is experimentally established that neutrinos do have a tiny non-zero mass [4, 5]. In Table 1.2, the leptons and their properties in the SM are summarised.

Table 1.2: The properties of the leptons in the three generations of the SM [6], where q_e represents the elementary charge.

Generation	Particle	Mass	Charge
First	e^-	0.511 MeV	$-q_e$
	ν_e	≈ 0	0
Second	μ^-	106 MeV	$-q_e$
	ν_μ	≈ 0	0
Third	τ^-	1 777 MeV	$-q_e$
	ν_τ	≈ 0	0

123

The quarks can also be divided into three generations. Unlike the leptons, they carry colour charge and can interact via the strong interaction. The top quark, discovered in 1995 at the Tevatron [7, 8], is the heaviest SM particle with a mass¹ measured to be $173.34 \pm 0.27(\text{stat}) \pm 0.71(\text{syst})$ GeV [9]. The quarks and their properties are summarised in Table 1.3. In nature, only colour neutral objects can exist. This has as consequence that quarks are bound through gluons into mesons (quark+anti-quark) and baryons (three quarks). These mesons and baryons are mostly short-lived and unstable particles that rapidly decay through W^\pm and Z bosons. The only known stable baryon is the proton, made up of two up quarks and one down quark.

The scalar boson, commonly known as the Higgs boson, is the last piece of the SM discovered in 2012 [10, 11]. It is responsible for the masses of the W^\pm and Z boson, and that of the fermions.

¹In this thesis all masses and energies are expressed in natural units, where the speed of light and \hbar are taken to be equal to one.

Table 1.3: The properties of the quarks in the three generations of the SM [6], where q_e represents the elementary charge.

	Generation	Particle	Mass	Charge
First	up u	$2.2^{+0.6}_{-0.4}$ MeV	$\frac{2}{3} q_e$	
	down d	$4.7^{+0.5}_{-0.4}$ MeV	$\frac{-1}{3} q_e$	
Second	charm c	1.28 ± 0.03 GeV	$\frac{2}{3} q_e$	
	strange s	96^{+8}_{-4} MeV	$\frac{-1}{3} q_e$	
Third	top t	173.1 ± 0.6 GeV	$\frac{2}{3} q_e$	
	bottom b	$4.18^{+0.04}_{-0.03}$ GeV	$\frac{-1}{3} q_e$	

135 1.2 Standard Model Lagrangian, connecting fields with particles

136 The SM is a quantum field theory and thus describes the dynamics and kinematics of particles
 137 and forces by a Lagrangian \mathcal{L} . The theory is based on the $SU(3)_C \times SU(2)_L \times U(1)_Y$ gauge
 138 symmetry, where $SU(2)_L \times U(1)_Y$ describes the electroweak interaction and $SU(3)_C$ the strong
 139 interaction. The indices refer to colour C, the left chiral nature of the $SU(2)_L$ coupling L, and the
 140 weak hypercharge Y. Its Lagrangian is constructed such that symmetries representing physics
 141 conservation laws such as conservation of energy, momentum and angular momentum are
 142 contained. The symmetries under local gauge transformations are sustained by demanding
 143 gauge invariance².

The $U(1)_Y$ group has one generator Y with an associated gauge field B_μ . The three gauge fields W_μ^1 , W_μ^2 , and W_μ^3 , are associated to $SU(2)_L$ with three generators that can be written as half of the Pauli matrices:

$$T_1 = \frac{1}{2} \begin{pmatrix} 0 & 1 \\ 1 & 0 \end{pmatrix}, \quad T_2 = \frac{1}{2} \begin{pmatrix} 0 & -i \\ i & 0 \end{pmatrix}, \quad \text{and} \quad T_3 = \frac{1}{2} \begin{pmatrix} 1 & 0 \\ 0 & -1 \end{pmatrix}. \quad (1.1)$$

The generators T^a satisfy the Lie algebra:

$$[T_a, T_b] = i\epsilon_{abc} T^c \text{ and } [T_a, Y] = 0, \quad (1.2)$$

144 where ϵ_{abc} is an antisymmetric tensor. The gauge fields of $SU(2)_L$ only couple to left-handed
 145 fermions as required by the observed parity violating nature of the weak force. The $SU(3)_C$
 146 group represents quantum chromodynamics (QCD). It has eight generators corresponding to
 147 eight gluon fields $G_\mu^{1\dots 8}$. Unlike $SU(2)_L \times U(1)_Y$, $SU(3)_C$ is not chiral.

Under $SU(3)_C$ quarks are colour triplets while leptons are colour singlets. This implies that the quarks carry a colour index ranging between one and three, whereas leptons do not take part in strong interactions. Based on the chirality, the quarks and leptons are organized in doublets or singlets. Each generation i of fermions consists of left-handed doublets and right-handed

²Different field configurations of unobservable fields can result in identical quantities. Transformations between such configurations are called gauge transformation and the absence of change in the measurable quantities is a characteristic called gauge invariance.

singlets:

$$l_{L,i} = \begin{pmatrix} e_{L,i} \\ v_{L,i} \end{pmatrix}, e_{R,i}, q_{L,i} = \begin{pmatrix} u_{L,i} \\ d_{L,i} \end{pmatrix}, u_{R,i}, \text{ and } d_{R,i} \quad (1.3)$$

The SM Lagrangian can be decomposed as a sum of four terms

$$\mathcal{L}_{SM} = \mathcal{L}_{gauge} + \mathcal{L}_f + \mathcal{L}_{Yuk} + \mathcal{L}_\phi, \quad (1.4)$$

148 that are related to the gauge, fermion, Yukawa and scalar sectors. The gauge Lagrangian
 149 regroups the gauge fields of all three symmetry groups, and the fermionic part consists of kinetic
 150 energy terms for quarks and leptons. The interaction between fermions and the scalar doublet
 151 ϕ gives rise to fermion masses and is described by the Yukawa Lagrangian. The scalar part of
 152 the Lagrangian is composed of a kinematic and potential component related to the scalar boson.

For the electroweak theory, two coupling constants are introduced, namely g' for $U(1)_Y$ and g for $SU(2)_L$. The physically observable gauge bosons of this theory are the photon field A_μ , the Z boson field Z_μ^0 , and the W boson fields W_μ^\pm . These are a superposition of the four gauge fields of $SU(2)_L \times U(1)_Y$:

$$\begin{aligned} A_\mu &= \sin \theta_W W_\mu^3 + \cos \theta_W B_\mu, \\ Z_\mu^0 &= \cos \theta_W W_\mu^3 - \sin \theta_W B_\mu, \text{ and} \\ W_\mu^\pm &= \sqrt{\frac{1}{2}} (W_\mu^1 \mp i W_\mu^2), \end{aligned} \quad (1.5)$$

153 where θ_W represents the weak mixing angle defined as $\tan \theta_W = \frac{g'}{g}$.

154 The coupling constant representing the strength of the QCD interactions is denoted as g_s . In
 155 QCD there is asymptotic freedom whereby the strong coupling constant becomes weaker as the
 156 energy with which the interaction between strongly interacting particles is probed increases,
 157 and stronger as the distance between the particles increases. A consequence of this is known as
 158 colour confinement, the quarks and gluons can not exist on their own and are not observed
 159 individually. They are bound in colour neutral states called hadrons, this process is known as
 160 hadronisation.

161 Electroweak symmetry breaking

162 In \mathcal{L}_{gauge} and \mathcal{L}_f are no mass terms for fermions present because only singlets under $SU(3)_C \times$
 163 $SU(2)_L \times U(1)_Y$ can acquire a mass with an interaction of the type $m^2 \phi^\dagger \phi$ without breaking
 164 the gauge invariance. In order to accommodate mass terms for fermions and gauge fields,
 165 electroweak symmetry breaking, leading to \mathcal{L}_ϕ is introduced.

The scalar doublet is introduced in the SM as

$$\phi = \frac{1}{\sqrt{2}} \begin{pmatrix} \varphi_1 + i\varphi_2 \\ \varphi_3 + i\varphi_4 \end{pmatrix}. \quad (1.6)$$

Its field potential is of the form

$$V(\phi) = \mu^2 \phi^\dagger \phi + \lambda (\phi^\dagger \phi)^2, \quad (1.7)$$

with $\mu^2 < 0$ and λ a positive integer. This choice of parameters gives the potential a "Mexican hat" shape. It has an infinite set of minima (ground states) and by expanding the field around an arbitrary choice of ground state, the electroweak symmetry is broken (EW):

$$\phi = \begin{pmatrix} 0 \\ \frac{v}{\sqrt{2}} \end{pmatrix} + \hat{\phi}, \quad (1.8)$$

where v is the vacuum expectation value (vev), measured to be around 245 GeV and corresponds to $\sqrt{\frac{-\mu}{\lambda}}$. The scalar doublet's four degrees of freedom are reduced to three degrees of freedom that couple to the gauge fields and fix the W^+ , W^- and Zbosons. The remaining fourth degree of freedom has given rise to a physically observable particle, called the Brout-Englert-Higgs (BEH) boson. This spontaneous symmetry breaking leaves the gauge invariance intact and gives masses to the W^\pm and Zbosons as:

$$m_W = \frac{1}{2} v |g| \quad \text{and} \quad m_Z = \frac{1}{2} v \sqrt{g'^2 + g^2}. \quad (1.9)$$

¹⁶⁶ The Brout-Englert-Higgs field couples universally to fermions with a strength proportional to their masses, and to gauge bosons with a strength proportional to the square of their masses.

1.3 Flavours in the SM

Flavour changing charged currents are introduced in 1963 by Nicola Cabibbo [12]. Via interactions with a W boson the flavour of the quarks is changed. At the time of the postulation only up, down, and strange quarks were known and the charged weak current was described as a coupling between the up quark and d_{weak} , where d_{weak} is a linear combination of the down and strange quarks, $d_{\text{weak}} = \cos\theta_c d + \sin\theta_c s$. This linear combination is a direct consequence of the chosen rotation

$$\begin{pmatrix} d_{\text{weak}} \\ s_{\text{weak}} \end{pmatrix} = \begin{pmatrix} \cos\theta_c & \sin\theta_c \\ -\sin\theta_c & \cos\theta_c \end{pmatrix} \begin{pmatrix} d \\ s \end{pmatrix} = \mathcal{R} \begin{pmatrix} d \\ s \end{pmatrix}, \quad (1.10)$$

where the rotation angle θ_c is known as the Cabibbo angle. This provides a definition for the charged weak current between u and d quarks,

$$J_\mu = \bar{u} \gamma_\mu (1 + \gamma_5) d_{\text{weak}}. \quad (1.11)$$

A consequence of Cabibbo's approach is that the s_{weak} is left uncoupled, leading to Glashow, Iliopoulos and Maiani (GIM) [13–15] to require the existence of a fourth quark with charge $\frac{2}{3}q_e$. This quark, known as the charm quark, couples to s_{weak} and a new definition of the charged weak current is modified to

$$J_\mu = (\bar{u} \quad \bar{c}) \gamma_\mu (1 + \gamma_5) \mathcal{R} \begin{pmatrix} d \\ s \end{pmatrix} = \bar{U} \gamma_\mu (1 + \gamma_5) \mathcal{R} D. \quad (1.12)$$

The neutral weak current is defined as

$$J_3 = \bar{U} \gamma_\mu (1 + \gamma_5) [\mathcal{R}, \mathcal{R}^\dagger] D, \quad (1.13)$$

and is diagonal in flavour space. This has as consequence that no flavour changing neutral currents occur at tree-level interactions [1].

Kobayashi and Maskawa generalised the Cabibbo rotation matrix to accommodate a third generation of quarks. The result is a 3×3 unitary matrix known as the CKM matrix, responsible for the mixing of weak interaction states of down-type quarks:

$$\begin{pmatrix} d_{\text{weak}} \\ s_{\text{weak}} \\ b_{\text{weak}} \end{pmatrix} = \begin{pmatrix} V_{ud} & V_{us} & V_{ub} \\ V_{cd} & V_{cs} & V_{cb} \\ V_{td} & V_{ts} & V_{tb} \end{pmatrix} \begin{pmatrix} d \\ s \\ b \end{pmatrix} = \mathcal{V}_{\text{CKM}} \begin{pmatrix} d \\ s \\ b \end{pmatrix}, \quad (1.14)$$

where \mathcal{V}_{CKM} is unitary ($\mathcal{V}_{\text{CKM}}^\dagger \mathcal{V}_{\text{CKM}} = \mathbb{1}$). A general 3×3 unitary matrix depends on three real angles and six phases. For the CKM matrix, the freedom to redefine the phases of the quark eigenstates can remove five of the phases, leaving a single physical phase known as the Kobayashi-Maskawa phase. This phase is responsible for the charge parity violation in the SM [16]. Each element V_{ij} of \mathcal{V}_{CKM} represents the transition probability of a quark i going to a quark j , and is experimentally determined to be [6]

$$\mathcal{V}_{\text{CKM}} = \begin{pmatrix} 0.97425 \pm 0.00022 & 0.2253 \pm 0.0008 & (4.13 \pm 0.49) \times 10^{-3} \\ 0.225 \pm 0.008 & 0.986 \pm 0.016 & (41.1 \pm 1.3) \times 10^{-3} \\ (8.4 \pm 0.6) \times 10^{-3} & (40.0 \pm 2.7) 10^{-3} & 1.021 \pm 0.032 \end{pmatrix}. \quad (1.15)$$

From Equation 1.15 follows that top quarks predominantly decay via charged weak currents to bottom quarks, with a probability consistent with unity. In the SM, FCNC can only occur via higher loop interactions which are highly suppressed. The expected transition probabilities for a top quark decaying via a FCNC interaction in the SM are given in Table 1.4, where it is clear that the FCNC top quark interactions of the SM is still beyond the reach of the sensitivity of current experiments.

Table 1.4: The predicted branching fractions \mathcal{B} for FCNC decays involving the top quark in the SM [17].

Process	\mathcal{B} in the SM	Process	\mathcal{B} in the SM
$t \rightarrow uZ$	8×10^{-17}	$t \rightarrow cZ$	1×10^{-14}
$t \rightarrow u\gamma$	4×10^{-16}	$t \rightarrow c\gamma$	5×10^{-14}
$t \rightarrow ug$	4×10^{-14}	$t \rightarrow cg$	5×10^{-12}
$t \rightarrow uH$	2×10^{-17}	$t \rightarrow cH$	3×10^{-15}

176

1.4 The top quark in the SM

Discovered in 1995 by the CDF and D0 collaborations at the Tevatron with proton-antiproton data [18, 19], the top quark plays an important role in studying high energy physics. Its Yukawa

interaction is given by

$$\mathcal{L}_{\text{top-Yukawa}} = -\frac{\lambda_t \nu}{\sqrt{2}} \bar{t}_L t_R - \frac{\lambda_t}{\sqrt{2}} H \bar{t}_L t_R + \text{h.c.}, \quad (1.16)$$

yielding a Yukawa coupling of [6]

$$\lambda_t = \frac{\sqrt{2} m_t}{\nu} = 0.991 \pm 0.003. \quad (1.17)$$

178 This Yukawa coupling is very large compared to the other Yukawa couplings in the SM ($\mathcal{O}(10^{-2})$),
 179 leading to the belief that the top quark may have an important role in understanding the
 180 mechanism of electroweak symmetry breaking. On top of this, the very short lifetime of the top
 181 quark makes it an excellent candidate to study the properties of a bare quark. Its high mass,
 182 almost 40 times higher than the mass of the closest fermion in mass, leads to a large coupling
 183 with the Higgs boson and makes the top quark an interesting candidate to investigate how
 184 particles acquire mass.

185 The CKM matrix element V_{tb} , given in [Equation 1.15](#), is experimentally found to be much
 186 larger than V_{ts} , V_{td} , and close to unity. The top quark decays through electroweak interactions
 187 since the W boson mass is smaller than the top quark mass and the W boson can be on shell. A
 188 consequence of this is that the top quark has a very short lifetime of only $1/\Gamma_t \approx 5 \cdot 10^{-25}$ s [6]
 189 leading to the fact that the formation of bound states involving top quarks are not allowed.
 190 This lifetime is even shorter than the typical hadronisation timescale of $1/\Lambda_{\text{QCD}} \approx 10^{-23}$ s,
 191 prohibiting gluons to radiate from the top quark and keeping its spin coherent. Since the
 192 electroweak interactions have a vector-axial vector (V-A) coupling structure³, the top quark
 193 spin orientation can be derived from the angular distributions of its decay products. This makes
 194 it possible to study the polarisation of top quarks from the angular distributions in various
 195 processes.

196 The massiveness of the top quark leads to the fact that a large amount of energy is needed to
 197 create one. This is only the case for high energy collisions such as those happening in the Earth's
 198 upper atmosphere when cosmic rays collide with particles in air, or by particle accelerators.
 199 The production of top quarks happens in two ways: single via the electroweak interaction or in
 200 pairs via the strong interaction. At hadron colliders, the dominant production mechanism is top
 201 quark production via gluon ($gg \rightarrow t\bar{t}$) or quark fusion ($q\bar{q} \rightarrow t\bar{t}$). In [Figure 1.1](#), the different top
 202 quark pair production mechanisms are shown. The production channel of gluon fusion is the
 203 main contributor to the top quark pair cross section at the LHC compared to quark fusion at the
 204 Tevatron. The $gg \rightarrow t\bar{t}$ process contributes 80-90% to the total top quark pair cross section in
 205 the LHC centre-of-mass energy regime of 7-14 TeV [6]. In [Table 1.5](#) the predicted top quark
 206 pair production cross sections are given for the LHC and the Tevatron, while in [Figure 1.2](#), a
 207 summary plot of the LHC and Tevatron top quark pair cross section measurements as a function
 208 of the centre-of-mass energy can be found.

209 The singly produced top quarks are produced via the electroweak interaction. These production
 210 mechanisms are subdivided at leading order into three main channels based on the virtuality

³In the SM a vector - axial vector coupling structure $(\gamma^\mu - \gamma^\mu \gamma^5)$ is predicted that only permits left-handed fermions or right-handed anti fermions to interact with a spin-1 particle.

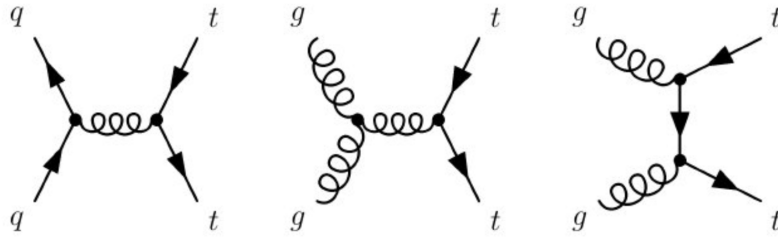


Figure 1.1: Leading order diagrams of the top quark pair production. Gluon fusion (right and middle) are the dominant processes at the LHC, while quark fusion (left) is the dominant one at the Tevatron.

Table 1.5: Predictions on the top quark pair production cross sections at next-to-next-to-leading order with next-to-next-to-leading log soft gluon resummation per centre-of-mass energy [6]. The first uncertainty is from scale dependence, while the second uncertainty originates from parton density functions.

Experiment	Top quark mass	Centre-of-mass energy	Cross section (pb)
Tevatron	$m_t = 173.3$ GeV	$\sqrt{s} = 1.96$ TeV	$\sigma_{\bar{t}t} = 7.16^{+0.11+0.17}_{-0.20-0.12}$
LHC	$m_t = 173.2$ GeV	$\sqrt{s} = 7$ TeV	$\sigma_{\bar{t}t} = 173.6^{+4.5+8.9}_{-5.9-8.9}$
LHC	$m_t = 173.2$ GeV	$\sqrt{s} = 8$ TeV	$\sigma_{\bar{t}t} = 247.7^{+6.3+11.5}_{-8.5-11.5}$
LHC	$m_t = 173.2$ GeV	$\sqrt{s} = 13$ TeV	$\sigma_{\bar{t}t} = 816.0^{+19.4+34.4}_{-28.6-34.4}$

211 ($Q^2 = -p_\mu p^\mu$) of the exchanged W boson. In Figure 1.3, the corresponding Feynman diagrams
 212 are shown. The single top quark production cross sections, given in Table 1.6, are smaller than
 213 the top quark pair production cross sections since the electroweak coupling strength is smaller
 214 than the strong coupling strength. In addition, for the single top quark production, there is the
 215 need of sea quarks (b, \bar{q}) in the initial states for which the parton density functions increase
 216 less steeply at low momentum fractions compared to the gluon parton density functions.

217 The production via the t -channel has a virtuality of the W boson $Q^2 > 0$, making it space-like.
 218 It is produced via the scattering of the W boson of a bottom quark coming from a proton
 219 or from gluon splitting ($g \rightarrow b\bar{b}$). It has the highest single top quark cross section in proton
 220 collisions and the top quark production is roughly twice as large than the antitop quark. This is
 221 a consequence of the up-down valence quark composition of the proton. This feature makes the
 222 t -channel sensitive to the parton density functions of the proton. The s -channel is the production
 223 mechanism with the smallest cross section. Here the W boson is time-like ($Q^2 < 0$) which
 224 requires the W boson to have a large virtuality to produce the heavier top quark. It is produced
 225 from two quarks belonging to the same isodoublet (e.g. $u\bar{d}$) and subsequently decays to $t\bar{b}$.
 226 This process gets enhanced by many beyond the Standard Model scenarios via the addition of
 227 new heavy particles such as W' . The tW -channel has a top quark produced in association with a
 228 W boson produced on shell $Q^2 = -m_W^2$. This mode is negligible at the Tevatron, but of relevant
 229 size at the LHC. The tW -channel is sensitive to new physics affecting the Wtb vertex. The single
 230 top quark production cross section measurements by the CMS collaboration can be found in
 231 Figure 1.4.

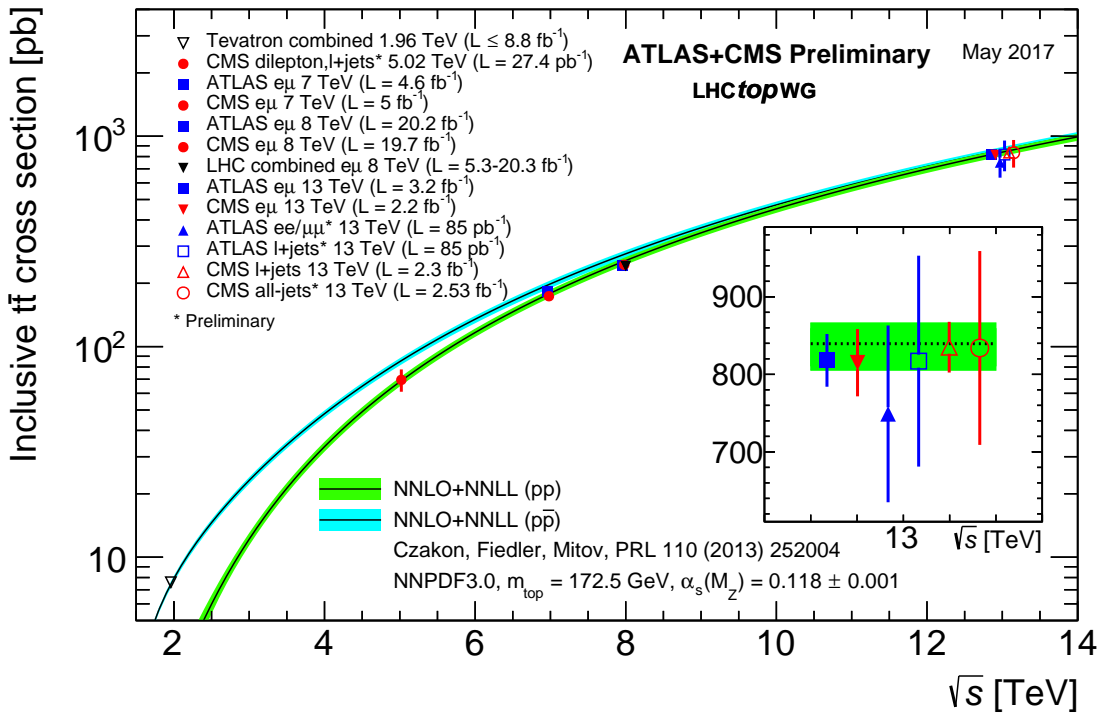


Figure 1.2: Summary of the LHC and the Tevatron measurements of the top quark pair production cross section as function of the centre-of-mass energy compared with the next-to-next-to-leading order QCD calculation. The theory bands are the uncertainties due to renormalization and factorisation scales, parton density functions and the strong coupling. The mass of the top quark is assumed to be 172.5 GeV. Measurements for the same centre-of-mass energy are slightly off-set for clarity. Figure taken from [20].

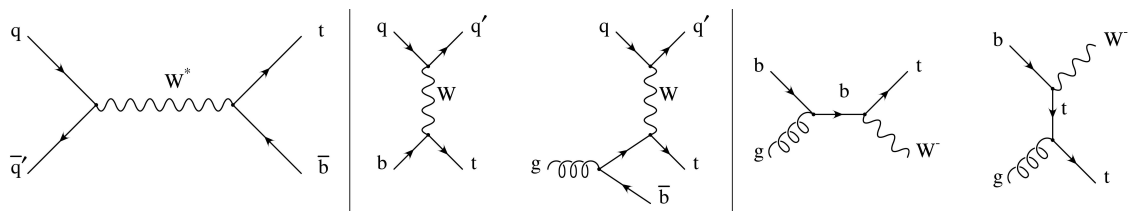


Figure 1.3: Leading order Feynman diagrams of the electroweak production of single top quarks in the s -channel (left), t -channel (middle), and for the tW associated production. Figure taken from [21].

Table 1.6: Predictions on the single top quark production cross sections at next-to-leading order per centre-of-mass energy [6]. The uncertainties from scale dependence and from parton density functions are combined in quadrature or given separately (scale + PDF). For the t -channel the relative proportions to t and \bar{t} are 65% and 35%. For the s -channel this is respectively 69% and 31%. The tW -channel has an equal proportion of top and antitop quarks. For Tevatron, the top quark mass is assumed to be 173.3 GeV, while the LHC predictions use $m_t = 172.5$ GeV [6, 22].

Collider	Centre-of-mass energy	Cross section $\sigma_{t+\bar{t}}$ (pb)		
		t -channel	s -channel	tW -channel
Tevatron	$\sqrt{s} = 1.96$ TeV	$2.06^{+0.13}_{-0.13}$	$1.03^{+0.05}_{-0.05}$	-
LHC	$\sqrt{s} = 7$ TeV	$63.89^{+2.91}_{-2.52}$	$4.29^{+0.19}_{-0.17}$	$15.74^{+0.40+1.10}_{-0.40-1.14}$
LHC	$\sqrt{s} = 8$ TeV	$84.69^{+3.76}_{-3.23}$	$5.24^{+0.22}_{-0.20}$	$22.37^{+0.60+1.40}_{-0.60-1.40}$
LHC	$\sqrt{s} = 13$ TeV	$216.99^{+9.04}_{-7.71}$	$10.32^{+0.40}_{-0.36}$	$71.7^{+1.80+3.40}_{-1.80-3.40}$

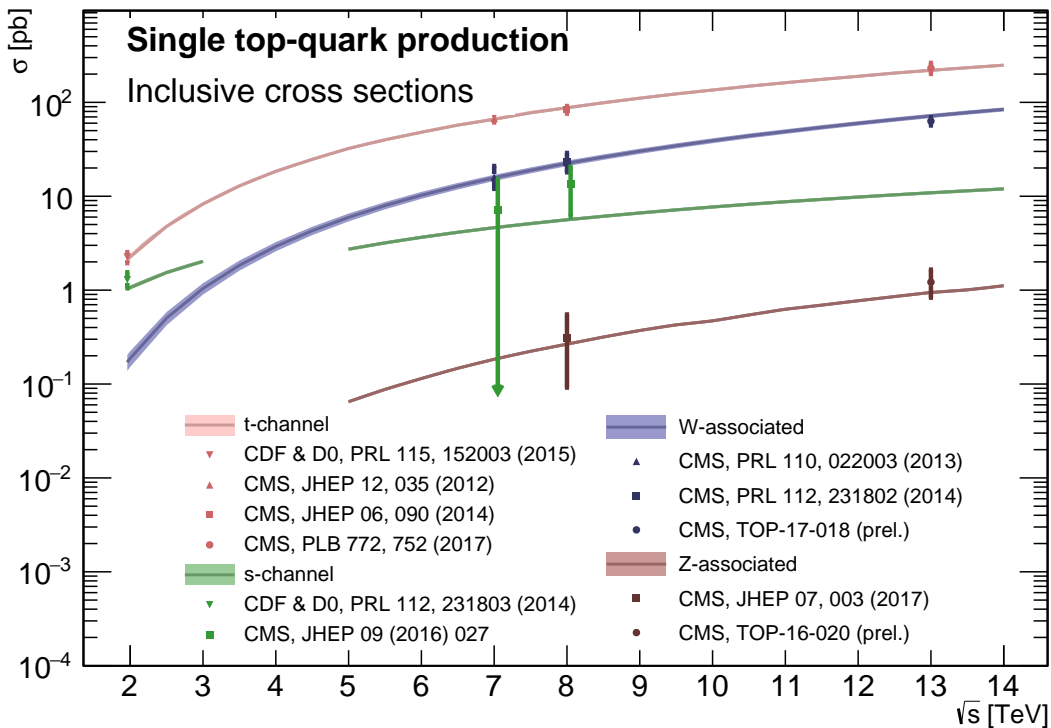


Figure 1.4: Summary of the measurements of the single top quark production cross section as function of the centre-of-mass energy. Figure taken from [23].

232 1.5 Effective field theories

233 Problems can be simplified if one looks at the relevant scale of the process that one want to
 234 investigate, for example the chemical properties of an hydrogen atom can be described without
 235 any knowledge of quark interactions inside the proton. In this case, the proton can be considered
 236 the elementary object (indivisible) due to the fact that the binding energy of the constituents is
 237 much bigger than the energy of the electron in orbit around the proton. Effective field theories
 238 are based on this kind of separation of different energy scales in a system [24]. Effective field
 239 theories can be used for theories where the perturbative expansion cannot be trusted, e.g. QCD
 240 at low energy, or as bottom up approach to look for new physics in a model independent way.
 241 The latter is the way effective field theory will be used throughout this thesis.

The main idea behind effective field theory is easily explained via the example of the Fermi theory. Fermi explained in 1933 [25] the β -decay as a product of currents:

$$\mathcal{L}_{\text{EFT}}^{\text{Fermi}} = -\frac{G_F}{\sqrt{2}} J^\mu J_\mu^\dagger, \quad (1.18)$$

where G_F is the Fermi coupling constant, measured to be $G_F \approx 1.17 \times 10^{-5} \text{ GeV}^{-2}$. The current J_μ can written as the sum of an hadronic J_μ^h and leptonic J_μ^l current, where for simplicity only the leptonic current discussed.

$$J_\mu^l = \sum_i \bar{\nu}_i \gamma_\mu (1 - \gamma_5) l. \quad (1.19)$$

242 Historically, charged currents were flavour universal and the later discovered parity violation of
 243 the weak interaction led to the V-A structure. After this, the $SU(2)_L$ symmetry was postulated
 244 and the existence of neutral currents was predicted. The effective Lagrangian used then (given
 245 in Equation 1.18), could nowadays be build starting from $SU(2)_L$ symmetries only.

The muon decay can be computed from two different starting points. The effective Fermi Lagrangian provides the decay width of the muon into an electron and two neutrinos

$$\Gamma(\mu \rightarrow e \bar{\nu}_e \nu_\mu) \approx \frac{1}{96\pi^3} \frac{m_\mu^2}{\Lambda_F^4}, \quad (1.20)$$

where Λ_F is the energy scale defined as

$$\frac{G_F}{\sqrt{2}} = \frac{1}{\Lambda_F^2}. \quad (1.21)$$

From muon decay measurements, the value of Λ_F is determined to be $\Lambda_F \approx 348 \text{ GeV}$ [24]. From the SM Lagrangian, one could also calculate the muon decay. Considering that the momenta involved are small compared to the W boson mass, the propagator's denominator can be expanded as [1]

$$\frac{1}{p^2 - m_W^2} = -\frac{1}{m_W^2} - \frac{p^2}{m_W^4} + \dots \quad (1.22)$$

Looking at the first term, and identifying

$$\frac{g^2}{8m_W} = \frac{1^2}{\Lambda_F}, \quad (1.23)$$

one sees that this corresponds with [Equation 1.20](#), thus the effective Lagrangian in [Equation 1.18](#) is the first term of the expansion in $\frac{1}{m_W^2}$ applied on the full Lagrangian.

An effective theory is thus a Taylor expansion in the ratio of two scales and the only remnants of the full theory at low energies are the symmetries and the values of the coupling constants. If the expansion parameter is small, one can truncate the series leading to the Lagrangian containing a finite number of free coefficients, making predictions possible. The error on these predictions is then of the order as the truncated piece.

The SM can be seen as an effective theory applicable up to energies not exceeding a scale Λ . Therefore, remnants should still be valid and the theory above that scale should have a gauge group containing $SU(3)_C \times SU(2)_L \times U(1)_Y$ and all the SM degrees of freedom, as well as reduce to the SM at lower energies. The general SM Lagrangian becomes then

$$\mathcal{L}_{SM+EFT} = \mathcal{L}_{SM}^{(4)} + \frac{1}{\Lambda} \sum_k C_k^{(5)} Q_k^{(5)} + \frac{1}{\Lambda^2} \sum_k C_k^{(6)} Q_k^{(6)} + \mathcal{O}\left(\frac{1}{\Lambda^3}\right), \quad (1.24)$$

where $Q_k^{(n)}$ are dimension- n operators (currents) and $C_k^{(n)}$ the corresponding dimensionless coupling constants, so-called Wilson coefficients. The Wilson coefficients are determined by the underlying high energy theory.

In the Warsaw basis [\[26\]](#), a set of independent operators of dimension 5 and 6 are built out of the SM fields and are consistent with the SM gauge symmetries and is fully derived in Ref. [\[26\]](#). In general the various measurements show a good agreement with the SM predictions and by lack of deviations from the SM, limits on the anomalous couplings can be derived. The estimated coupling strengths per operator contributing to single top quark production obtained from various measurements at the LHC and Tevatron are shown in [Figure 1.5](#) for which the conventions are discussed in Ref. [\[27\]](#). These results are consistent with the SM expectation for which those operators vanish.

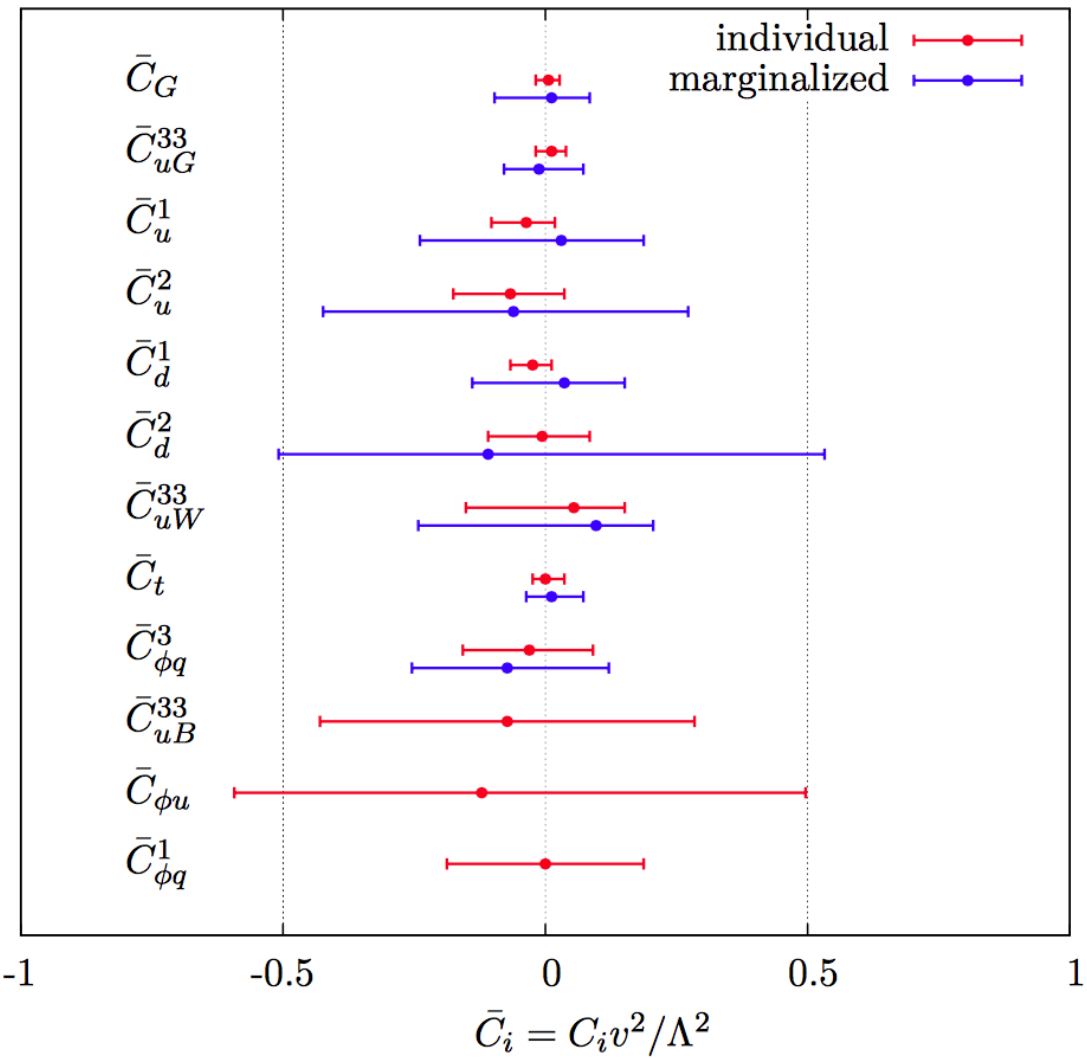


Figure 1.5: Global fit results of top quark effective field theory to experimental data including all constrained operators at dimension six. For the operators, the Warsaw basis of [26] is used. The bounds are set on the Wilson coefficients of various operators contributing to top quark production and decay in two cases (red) all other coefficients set to zero, or (blue) all other coefficients marginalized over. Figure taken from [28].

264 1.6 Motivation for new physics

265 Many high energy experiments confirm the success of the SM. In particular the scalar boson,
 266 the cornerstone of the SM, has consecrated the theory. Unfortunately there are also strong
 267 indications that the SM ought to be a lower energy expression of a more global theory. The
 268 existence of physics beyond the SM (BSM) [29] is strongly motivated. These motivations are
 269 based on direct evidence from observation such as the existence of neutrino masses, the existence
 270 of dark matter and dark energy, or the matter-antimatter asymmetry, and also from theoretical
 271 problems such as the hierarchy problem, the coupling unification or the large numbers of free
 272 parameters in the SM.

273 In the SM, the neutrinos are assumed to be massless, while experiments with solar, atmospheric,
 274 reactor and accelerator neutrinos have established that neutrinos can oscillate and change flavour
 275 during flight [4, 5]. These oscillations are only possible when neutrinos have masses. The
 276 flavour neutrinos (ν_e , ν_μ , ν_τ) are then linear expressions of the fields of at least three mass
 277 eigenstate neutrinos ν_1 , ν_2 , and ν_3 .

278 The ordinary or baryonic matter described by the SM describes only 5% of the mass (energy)
 279 content of the universe. Astrophysical evidence indicated that dark matter is contributing
 280 to approximately 27% and dark energy to 68% of the content of the universe. From the
 281 measurements of the temperature and polarizations anisotropies of the cosmic microwave
 282 background by the Planck experiment [30], the density of cold non baryonic matter is determined.
 283 Cold dark matter is assumed to be only sensitive to the weak and gravitational force, leading
 284 to only one possible SM candidate: the neutrino. However, these are too light to account for
 285 the vast amount of dark matter and other models are needed. Dark energy is assumed to be
 286 responsible for the acceleration in the expansion of the universe [31].

287 At the Big Bang, matter and antimatter are assumed to be produced in equal quantities.
 288 However, it is clear that we are surrounded by matter. So where did all the antimatter go?
 289 In 1967, Sakharov identified three mechanisms that are necessary to obtain a global matter
 290 antimatter asymmetry [32]. These mechanisms are those of baryon and lepton number violation,
 291 that at a given moment in time there was a thermal imbalance for the interactions in the universe,
 292 and there is charge C and charge parity CP violation⁴.

293 The large number of free parameters in the SM comes from the nine fermion masses, three
 294 CKM mixing angles and one CP violating phase, one EM coupling constant g' , one weak coupling
 295 constant g , one strong coupling constant g_s , one QCD vacuum angle, one vacuum expectation
 296 value, and one mass of the scalar boson. This large number of free parameters leads to the
 297 expectation of a more elegant and profound theory beyond the SM.

298 The hierarchy problem [33] is related to the huge difference in energy between the weak
 299 scale and the Planck scale. The vev of the Brout-Englert-Higgs field determines the weak scale
 300 that is approximately 246 GeV. The radiative corrections to the scalar boson squared mass m_H^2 ,
 301 coming from its self couplings and couplings to fermions and gauge bosons, are quadratically

⁴The rate of a process $i \rightarrow f$ can be different from the CP-conjugate process: $\tilde{i} \rightarrow \tilde{f}$. The SM includes sources of CP-violation through the residual phase of the CKM matrix. However, these could not account for the magnitude of the asymmetry observed.

302 proportional to the ultraviolet momentum cut-off Λ_{UV} . This cut-off is at least equal to the energy
 303 to which the SM is valid without the need of new physics. For the SM to be valid up to the
 304 Planck mass, the correction to m_H^2 becomes thirty orders of magnitude larger than m_H^2 . This
 305 implies that an extraordinary cancellation of terms should happen. This is also known as the
 306 naturalness problem of the H boson mass.

The correction to the squared mass of the scalar boson coming from a fermion f , coupling to the scalar field ϕ with a coupling λ_f is given by

$$\Delta m_H^2 = -\frac{|\lambda_f|^2}{8\pi^2} \Lambda_{\text{UV}}^2, \quad (1.25)$$

while the correction to the mass from a scalar particle S with a mass m_S , coupling to the scalar field with a Lagrangian term $-\lambda_S |\phi|^2 |S|^2$ is

$$\Delta m_H^2 = \frac{|\lambda_S|^2}{16\pi^2} \left(\Lambda_{\text{UV}}^2 - 2m_S^2 \ln \left(\frac{\Lambda_{\text{UV}}}{m_S} \right) + \dots \right). \quad (1.26)$$

307 As one can see the correction term to m_H^2 is much larger than m_H^2 itself. By introducing BSM
 308 physics models that introduce new scalar particles at the TeV scale that couple to the scalar
 309 boson one can cancel the Λ_{UV}^2 divergence and avoid this fine-tuning.

310 The choice of the $SU(3)_C \times SU(2)_L \times U(1)_Y$ symmetry group itself as well as the separate
 311 treatment of the three forces included in the SM raises concern. The intensity of the forces
 312 show a large disparity around the electroweak scale, but have comparable strengths at higher
 313 energies. The electromagnetic and weak forces are unified in a electroweak interaction, but the
 314 strong coupling constant does not encounter the other coupling constants at high energies. In
 315 order to reach a grand unification, the running of couplings can be modified by the addition of
 316 new particles in BSM models.

317 1.7 An effective approach beyond the SM: FCNC involving a top 318 quark

319 The closeness of the top quark mass to the electroweak scale led physicists to believe that it is a
 320 sensitive probe for new physics. Studying its properties is therefore an important topic of the
 321 experimental program at the LHC. Several extensions of the SM enhance the FCNC branching
 322 fractions and can be probed at the LHC [17], from which some of them are shown in Table
 323 1.7. Previous searches have been performed at the Tevatron by the CDF [34] and D0 [35]
 324 collaborations, and at the LHC by the ATLAS [36–40] and CMS [41–45] collaborations.

325 The impact of BSM models can be written in a model independent way by means of an
 326 effective field theory valid up to an energy scale Λ . The leading effects are parametrized by a
 327 set of fully gauge symmetric operators that are added to the SM Lagrangian and can be reduced
 328 to a minimal set of operators as seen in Equation 1.24. For simplicity, the assumption is made
 329 that new physics effects are exclusively described by dimension-6 operators, thus neglecting

Table 1.7: The predicted branching fractions \mathcal{B} for FCNC interactions involving the top quark in some BSM models [17]: quark singlet (QS), generic two Higgs doublet model (2HDM) and the minimal supersymmetric extensions to the SM (MSSM);

Process	QS	2HDM	MSSM	Process	QS	2HDM	MSSM
$t \rightarrow uZ$	$\leq 1.1 \times 10^{-4}$	—	$\leq 2 \times 10^{-6}$	$t \rightarrow cZ$	$\leq 1.1 \times 10^{-4}$	$\leq 10^{-7}$	$\leq 2 \times 10^{-6}$
$t \rightarrow u\gamma$	$\leq 7.5 \times 10^{-9}$	—	$\leq 2 \times 10^{-6}$	$t \rightarrow c\gamma$	$\leq 7.5 \times 10^{-9}$	$\leq 10^{-6}$	$\leq 2 \times 10^{-6}$
$t \rightarrow ug$	$\leq 1.5 \times 10^{-7}$	—	$\leq 8 \times 10^{-5}$	$t \rightarrow cg$	$\leq 1.5 \times 10^{-7}$	$\leq 10^{-4}$	$\leq 8 \times 10^{-5}$
$t \rightarrow uH$	$\leq 4.1 \times 10^{-5}$	$\leq 5.5 \times 10^{-6}$	$\leq 10^{-5}$	$t \rightarrow cH$	$\leq 4.1 \times 10^{-5}$	$\leq 10^{-3}$	$\leq 10^{-5}$

330 neutrino physics. In the fully gauge symmetric case, the EFT Lagrangian is then given by

$$\mathcal{L}_{\text{SM+EFT}} = \mathcal{L}_{\text{SM}} + \sum_i \frac{\bar{c}_i}{\Lambda^2} O_i + \mathcal{O}\left(\frac{1}{\Lambda^3}\right), \quad (1.27)$$

where the Wilson coefficients \bar{c}_i depend on the considered theory and on the way that new physics couples to the SM particles. Taking into account that Λ is large, contributions suppressed by powers of Λ greater than two are neglected. Additionally, all four fermion operators are omitted for the rest of this thesis. The Warsaw basis is adopted for the independent effective operators [26], parametrising the new physics effects relevant for the flavour changing neutral current interactions of the top quark as, all flavour indices understood,

$$\begin{aligned} \mathcal{L}_{\text{EFT}}^t = & \frac{\bar{c}_{uG}}{\Lambda^2} \Phi^\dagger \cdot [\bar{Q}_L \sigma^{\mu\nu} \mathcal{T}_a u_R] G_{\mu\nu}^a + \frac{\bar{c}_{uB}}{\Lambda^2} \Phi^\dagger \cdot [\bar{Q}_L \sigma^{\mu\nu} u_R] B_{\mu\nu} + \frac{2\bar{c}_{uW}}{\Lambda^2} \Phi^\dagger T_i \cdot [\bar{Q}_L \sigma^{\mu\nu} u_R] W_{\mu\nu}^i \\ & + i \frac{\bar{c}_{hu}}{\Lambda^2} \left[\Phi^\dagger \overleftrightarrow{D}_\mu \Phi \right] [\bar{u}_R \gamma^\mu u_R] + i \frac{\bar{c}_{hq}^{(1)}}{\Lambda^2} \left[\Phi^\dagger \overleftrightarrow{D}_\mu \Phi \right] [\bar{Q}_L \gamma^\mu Q_L] \\ & + i \frac{4\bar{c}_{HQ}^{(3)}}{\Lambda^2} \left[\Phi^\dagger T_i \overleftrightarrow{D}_\mu \Phi \right] [\bar{Q}_L \gamma^\mu T^i Q_L] + \frac{\bar{c}_{uh}}{\Lambda^2} \Phi^\dagger \Phi \Phi^\dagger \cdot [\bar{Q}_L u_R] + \text{h.c.}, \end{aligned} \quad (1.28)$$

where the left handed $SU(2)_L$ doublet of the quark fields is denoted by Q_L , the up-type right handed fields by u_R , the down-type right handed fields by d_R , the $SU(2)_L$ doublet of the Higgs field by Φ , the field strength tensors as

$$\begin{aligned} B_{\mu\nu} &= \partial_\mu B_\nu - \partial_\nu B_\mu, \\ W_{\mu\nu}^k &= \partial_\mu W_\nu^k - \partial_\nu W_\mu^k - g \epsilon_{ij}^k W_\mu^i W_\nu^j, \\ G_{\mu\nu} &= \partial_\mu G_\nu^a - \partial_\nu G_\mu^a + g_s f_{bc}^a G_\mu^b G_\nu^c, \end{aligned} \quad (1.29)$$

denoting the structure constant of the $SU(3)_C$ group as f_{bc}^a and the structure constant of the $SU(2)_L$ group as ϵ_{ij}^k . The gauge covariant derivatives are also standard defined as

$$D_\mu \Phi = \partial_\mu \Phi - \frac{1}{2} i g' B_\mu \Phi - i g T_k W_\mu^k \Phi \quad (1.30)$$

with the conventions of Section 1.2. The representation matrices T of $SU(2)_L$ are defined in Equation 1.1, while the representation matrices \mathcal{T} of $SU(3)_C$ are the Gell-Mann matrices [1].

The hermitian derivative operator is defined as

$$\Phi^\dagger \overleftrightarrow{D} \Phi = \Phi^\dagger D^\mu \Phi - D_\mu \Phi^\dagger \Phi. \quad (1.31)$$

After electroweak symmetry breaking, the operators induce [17, 46] both corrections to the SM couplings and new interactions at tree level such as FCNC interactions. The FCNC interactions of the top quark that are not present in the SM are given by

$$\mathcal{L}_{\text{EFT}}^t = \frac{\sqrt{2}}{2} \sum_{q=u,c} \left[g' \frac{\kappa_{t\gamma q}}{\Lambda} A_{\mu\nu} \bar{t} \sigma^{\mu\nu} (f_{\gamma q}^L P_L + f_{\gamma q}^R P_R) q \right. \quad (1.32)$$

$$+ \frac{g}{2\cos\theta_W} \frac{\kappa_{tZq}}{\Lambda} Z_{\mu\nu} \bar{t} \sigma^{\mu\nu} (f_{Zq}^L P_L + f_{Zq}^R P_R) q \quad (1.33)$$

$$+ \frac{\sqrt{2}g}{4\cos\theta_W} \zeta_{tZq} \bar{t} \gamma^\mu (\tilde{f}_q^L P_L + \tilde{f}_q^R P_R) q Z_\mu \quad (1.34)$$

$$+ g_s \frac{\kappa_{tgq}}{\Lambda} Z_{\mu\nu} \bar{t} \sigma^{\mu\nu} (f_{gq}^L P_L + f_{gq}^R P_R) q G_\mu^a \quad (1.35)$$

$$+ \eta_{Hqt} \bar{t} (\hat{f}_q^L P_L + \hat{f}_q^R P_R) q H + \text{h.c.} \Big], \quad (1.36)$$

where the value of the FCNC couplings at scale Λ are represented by $\kappa_{tZq}, \kappa_{tgq}, \kappa_{t\gamma q}, \zeta_{tZq}$, and η_{Hqt} . These are assumed to be real and positive, with the unit of GeV^{-1} for κ_{txq}/Λ and no unit for ζ_{xqt} and η_{xqt} . In the equation $\sigma^{\mu\nu}$ equals to $\frac{i}{2} [\gamma^\mu, \gamma^\nu]$, and the left- and right-handed chirality projector operators are denoted by P_L and P_R . The electromagnetic coupling constant is denoted by g' , the strong interaction coupling is denoted as g_s , while the electroweak interaction is parametrised by the coupling constant g and the electroweak mixing angle θ_W . The complex chiral parameters are normalized according to $|f_{xq}^L|^2 + |f_{xq}^R|^2 = 1$, $|\tilde{f}_q^L|^2 + |\tilde{f}_q^R|^2 = 1$, and $|\hat{f}_q^L|^2 + |\hat{f}_q^R|^2 = 1$. In the expression for $\mathcal{L}_{\text{EFT}}^t$, the unitary gauge is adopted and the scalar field is expanded around its vacuum expectation value v with H being the SM scalar boson. The field strength tensors of the photon A_μ , the gluon field $G_\mu^{a..8}$, and the Z boson Z_μ^0 are defined as

$$\begin{aligned} A_{\mu\nu} &= \partial_\mu A_\nu - \partial_\nu A_\mu, \\ Z_{\mu\nu} &= \partial_\mu Z_\nu - \partial_\nu Z_\mu, \text{ and} \\ G_{\mu\nu} &= \partial_\mu G_\nu^a - \partial_\nu G_\mu^a + g_s f_{bc}^a G_\mu^b G_\nu^c. \end{aligned} \quad (1.37)$$

331 Note that there are two coupling constants arising in $\mathcal{L}_{\text{EFT}}^t$, which is a residue of electroweak
 332 symmetry breaking. The massive Z boson will appear in both the Z_μ^0 field as well as the covariant
 333 derivative, leading to an extra Z-vertex.

334 The relations between the Wilson coefficients in (1.28) and the coupling strengths of the
 335 interactions in Equation 1.36 can be derived. The 14 effective operators are mapped onto 10
 336 free parameters providing a more minimal parametrisation of the anomalous interactions of the
 337 top quark.

$$\begin{aligned}
 \kappa_{tgq} f_{gq}^L &= \frac{\nu}{g_s \Lambda} [\bar{c}_{uG}]_{i3}^*, & \kappa_{tgq} f_{gq}^R &= \frac{\nu}{g_s \Lambda} [\bar{c}_{uG}]_{3i}, \\
 \kappa_{t\gamma q} f_{\gamma q}^L &= \frac{\nu}{g' \Lambda} [\cos \theta_W \bar{c}_{uB} - \sin \theta_W \bar{c}_{uW}]_{i3}^*, & \kappa_{t\gamma q} f_{\gamma q}^R &= \frac{\nu}{g' \Lambda} [\sin \theta_W \bar{c}_{uB} - \cos \theta_W \bar{c}_{uW}]_{3i}, \\
 \kappa_{tZq} f_{Zq}^L &= -\frac{2\cos \theta_W \nu}{g \Lambda} [\sin \theta_W \bar{c}_{uB} + \cos \theta_W \bar{c}_{uW}]_{i3}^*, & \kappa_{tZq} f_{Zq}^R &= -\frac{2\cos \theta_W \nu}{g \Lambda} [\cos \theta_W \bar{c}_{uB} + \sin \theta_W \bar{c}_{uW}]_{3i}, \\
 \zeta_{tZq} \tilde{f}_{Zq}^L &= -\frac{2\nu^2}{\Lambda^2} [(\bar{c}_{hq}^{(1)} - \bar{c}_{hq}^{(3)})_{i3} + (\bar{c}_{hq}^{(1)} - \bar{c}_{hq}^{(3)})_{3i}^*], & \zeta_{tZq} \tilde{f}_{Zq}^R &= -\frac{2\nu^2}{\Lambda^2} [(\bar{c}_{hu})_{i3} + (\bar{c}_{hu})_{3i}^*], \\
 \eta_{tHq} \hat{f}_{Hq}^L &= \frac{3\nu^2}{2\Lambda^2} [\bar{c}_{uh}]_{i3}^*, & \eta_{tHq} \hat{f}_{Hq}^R &= \frac{3\nu^2}{2\Lambda^2} [\bar{c}_{uh}]_{3i}.
 \end{aligned} \tag{1.38}$$

338 1.8 Experimental constraints on top-FCNC

Experiments commonly put limits on the branching fractions which allow an easier interpretation across different EFT models by use of the branching fraction

$$\mathcal{B}(t \rightarrow qX) = \frac{\delta_{txq}^2 \Gamma_{t \rightarrow qX}}{\Gamma_t}, \tag{1.39}$$

339 where $\Gamma_{t \rightarrow qX}$ represents the FCNC decay width⁵ for a coupling strength $\delta_{txq}^2 = 1$, and Γ_t the full
 340 decay width of the top quark. In the SM, supposing a top quark mass of 172.5 GeV, the full
 341 width becomes $\Gamma_t^{\text{SM}} = 1.32$ GeV [47].

342 Searches for top-FCNC usually adopt a search strategy depending on the experimental set-up
 343 and the FCNC interaction of interest, looking either for FCNC interactions in the production of a
 344 single top quark or in its decay for top quark pair interactions. In Figure 1.6, these two cases
 345 are shown for the tZq vertex.

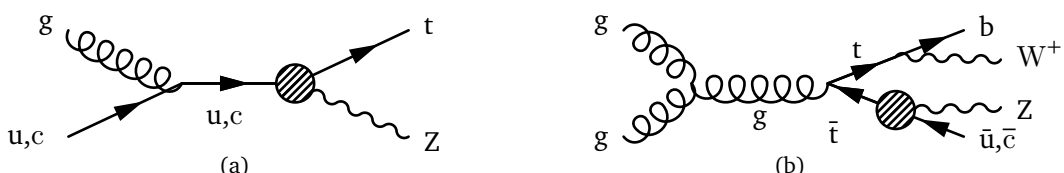


Figure 1.6: Feynman diagrams for the processes with a tZq FCNC interaction, where the FCNC interaction is indicated with the shaded dot. (a) Single top quark production through an FCNC interaction. (b) Top quark pair production with an FCNC induced decay.

⁵The decay width of a certain process represents the probability per unit time that a particle will decay. The total decay width, defined as the sum of all possible decay widths of a particle, is inversely proportional to its lifetime.

347 The observation of top-FCNC interactions has yet to come and experiments have so far only
 348 been able to put upper bounds on the branching fractions. An overview of the best current limits
 349 is given in [Table 1.8](#). In [Figure 1.7](#) a comparison is shown between the current best limits set by
 350 ATLAS and CMS with respect to several BSM model benchmark predictions. From there one can
 351 see that FCNC searches involving a Z or H boson are close to excluding or confirming several
 352 BSM theories. In [Figure 1.9](#), the searches performed by CMS are summarised. For the tZq
 353 vertex, the best limit from CMS comes from Ref. [41] where both single top quark and top quark
 354 pair are studied. The observed (expected) limits 95% CL at 8 TeV for the FCNC tZq interaction
 355 by CMS are $\mathcal{B}(t \rightarrow uZ) < 2.2 \times 10^{-4}$ (2.7×10^{-4}) and $\mathcal{B}(t \rightarrow cZ) < 4.9 \times 10^{-4}$ (12×10^{-4}). In
 356 [Figure 1.8](#), the summary of the 95% confidence level observed limits on the branching fractions
 357 of the top quark decays to a charm or up quark and a neutral boson is given, considering the
 results from the HERA, the LEP, the Tevatron, and the LHC.

Table 1.8: Overview of the most stringent observed and expected experimental limits on top-FCNC branching fractions \mathcal{B} at 95% confidence level.

Process	Search mode	Observed \mathcal{B}	Expected \mathcal{B}	Experiment	
$t \rightarrow uZ$	top quark pair decay	1.7×10^{-4}	2.4×10^{-4}	ATLAS	[40]
$t \rightarrow u\gamma$	single top quark production	1.3×10^{-4}	1.9×10^{-4}	CMS	[43]
$t \rightarrow ug$	single top quark production	4.0×10^{-5}	3.5×10^{-5}	ATLAS	[37]
$t \rightarrow uH$	top quark pair decay	2.4×10^{-3}	1.7×10^{-3}	ATLAS	[39]
$t \rightarrow cZ$	top quark pair decay	2.3×10^{-4}	3.2×10^{-4}	ATLAS	[40]
$t \rightarrow c\gamma$	single top quark production	2.0×10^{-3}	1.7×10^{-3}	CMS	[43]
$t \rightarrow cg$	single top quark production	2.0×10^{-4}	1.8×10^{-4}	ATLAS	[37]
$t \rightarrow cH$	top quark pair decay	2.2×10^{-3}	1.6×10^{-3}	CMS	[39]

358

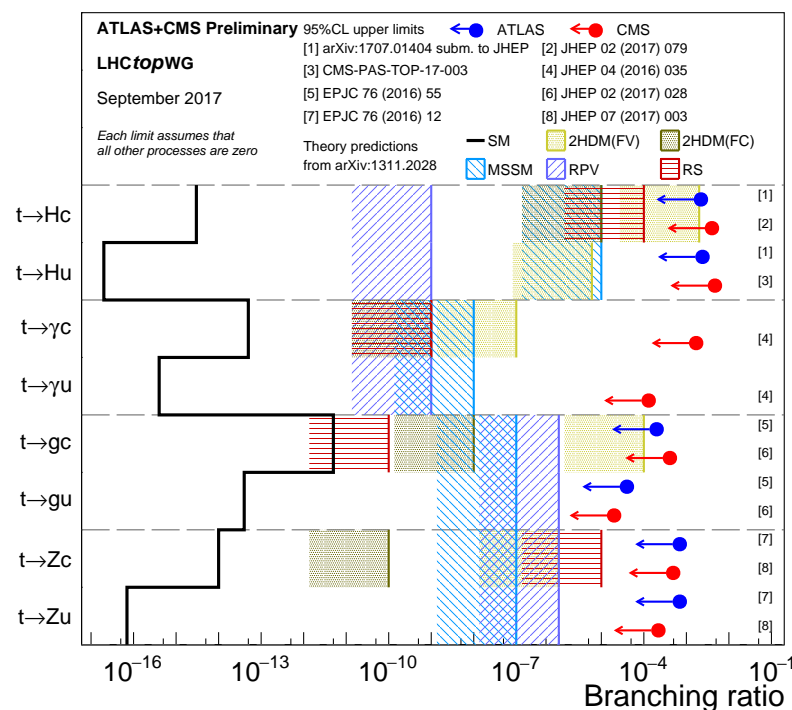


Figure 1.7: Current best limits set by CMS and ATLAS for top-FCNC interactions. Figure taken from [23]. (TO DO Remake with new atlas results)

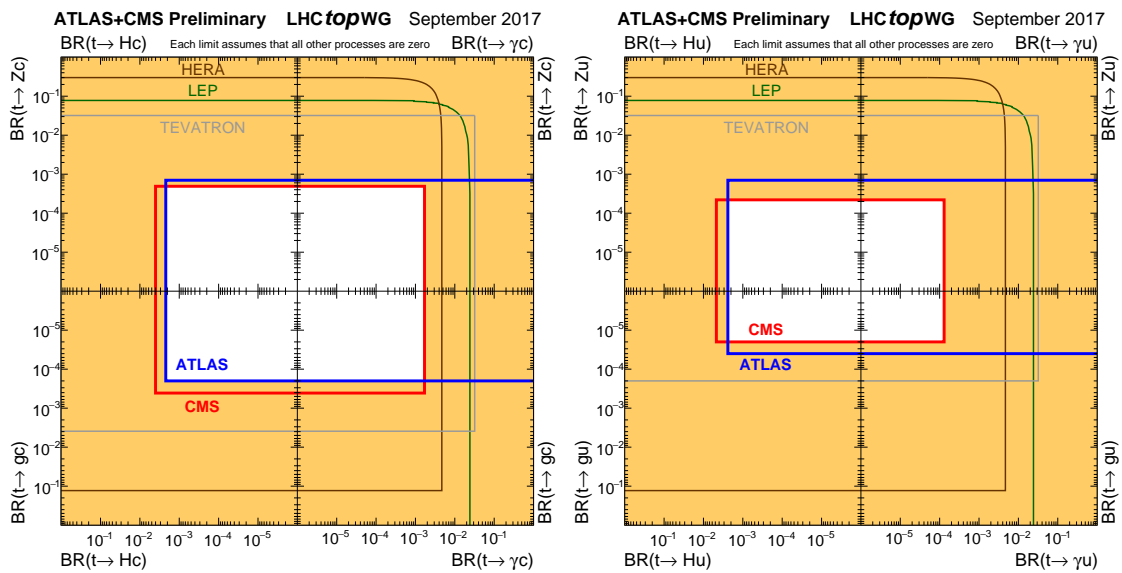


Figure 1.8: Summary of the current 95% confidence level observed limits on the branching fractions of the top quark decays via flavour changing neutral currents to a charm (left) or up (right) quark and a neutral boson. The coloured lines represent the results from HERA (the most stringent limits between the ones obtained by the H1 and ZEUS collaborations, in brown), LEP (combined ALEPH, DELPHI, L3 and OPAL collaborations result, in green), TEVATRON (the most stringent limits between the ones obtained by the CDF and D0 collaborations, in grey). The yellow area represents the region excluded by the ATLAS and the CMS Collaborations. Figure taken from [20].

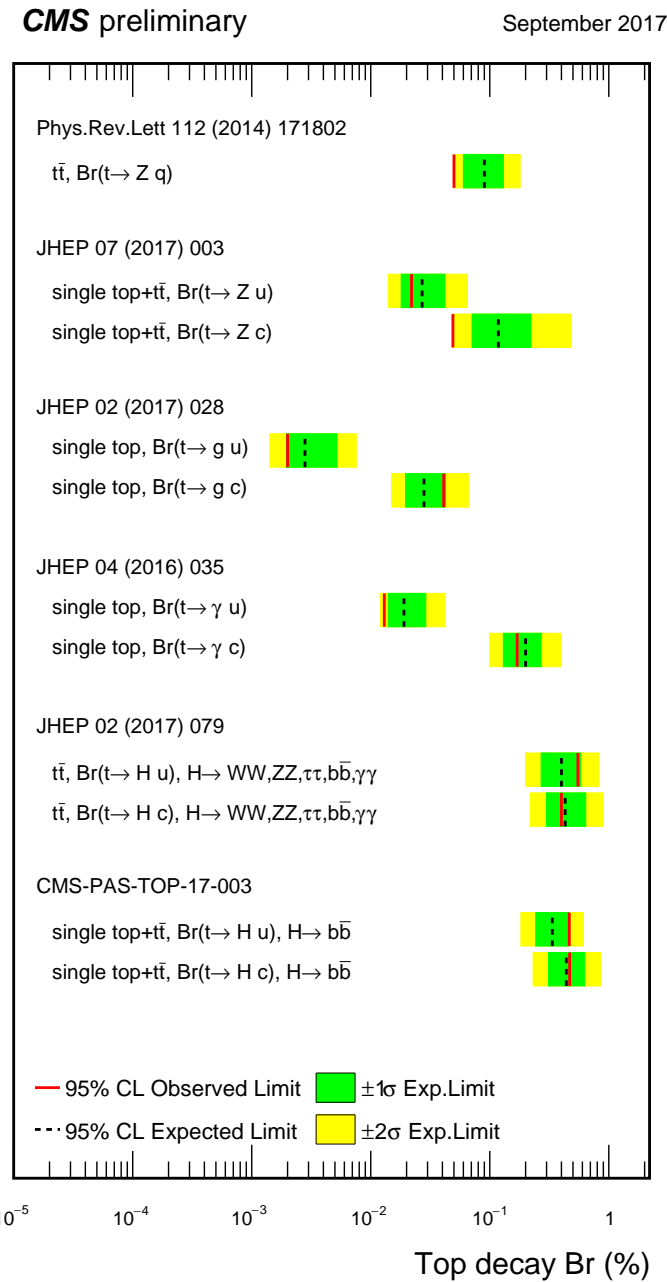


Figure 1.9: Summary of the FCNC branching fractions from CMS searches at 8 TeV. Figure taken from [23].

Experimental set-up

2

360 A key objective of the Large Hadron Collider (LHC) was the search for the Brout-Englert-Higgs
 361 boson. The Large Electron Positron (LEP) [48] and Tevatron [49] experiments established
 362 that the mass of the scalar boson has to be larger than 114 GeV [50, 51], and smaller than
 363 approximate 1 TeV due to unitarity and perturbativity constraints [52]. On top of this, the
 364 search for new physics such as supersymmetry or the understanding of dark matter were part
 365 of the motivation for building the LHC. Since the start of its operation, the LHC is pushing the
 366 boundaries of the Standard Model, putting the most stringent limits on physics beyond the
 367 Standard Model as well as precision measurements of the parameters of the Standard Model. A
 368 milestone of the LHC is the discovery of the scalar boson in 2012 by the two largest experiments
 369 at the LHC [10, 11].

370 This chapter is dedicated to the experimental set-up of the LHC and the Compact Muon
 371 Solenoid (CMS) experiment. Section 2.1 describes the LHC and its acceleration process for
 372 protons to reach their design energies. The CMS experiment and its components are presented
 373 in Section 2.2. The upgrades performed during the long shutdown in 2013 are discussed
 374 in Section 2.2.4. The data acquisition of CMS is presented in Section 2.2.3, while the CMS
 375 computing model is shown in Section 2.2.5.

376 2.1 The Large Hadron Collider

377 The LHC has started its era of cutting edge science on 10 September 2008 [53] after approval by
 378 the European Organisation of Nuclear Research (CERN) in 1995 [54]. Installed in the previous
 379 LEP tunnel, the LHC consists of a 26.7 km quasi ring, that is installed between 45 and 170 m
 380 under the French-Swiss border amidst Cessy (France) and Meyrin (Switzerland). Built to study
 381 rare physics phenomena at high energies, the LHC can accelerate mainly two types of particles,
 382 protons and lead ions Pb^{45+} , and provides collisions at four interaction points, where the particle
 383 bunches are crossing. Experiments for studying the collisions are installed at each interaction
 384 point.

385 As can be seen in Figure 2.1, the LHC is the last element in a chain that creates, injects and
 386 accelerates protons. The starting point is the ionisation of hydrogen, creating protons that are
 387 injected in a linear accelerator (LINAC 2). Here, the protons obtain an energy of 50 MeV. They

388 continue to the Proton Synchrotron Booster (PSB or Booster), where the packs of protons are
 389 accelerated to 1.4 GeV and each pack is split up in twelve bunches with 25 or 50 ns spacing.
 390 The Proton Synchrotron (PS) then increases their energy to 25 GeV before the Super Proton
 391 Synchrotron (SPS) increases the proton energy up to 450 GeV. Each accelerator ring expands in
 392 radius in order to reduce the energy loss of the protons by synchrotron radiation¹. Furthermore,
 393 the magnets responsible for the bending of the proton trajectories have to be strong enough
 394 to sustain the higher proton energy. Ultimately, the proton bunches are injected into opposite
 395 directions into the LHC, where they are accelerated to 3.5 TeV (in 2010 and 2011), 4 TeV (in
 2012 and 2013) or 6.5 TeV (in 2015 and 2016) [55].

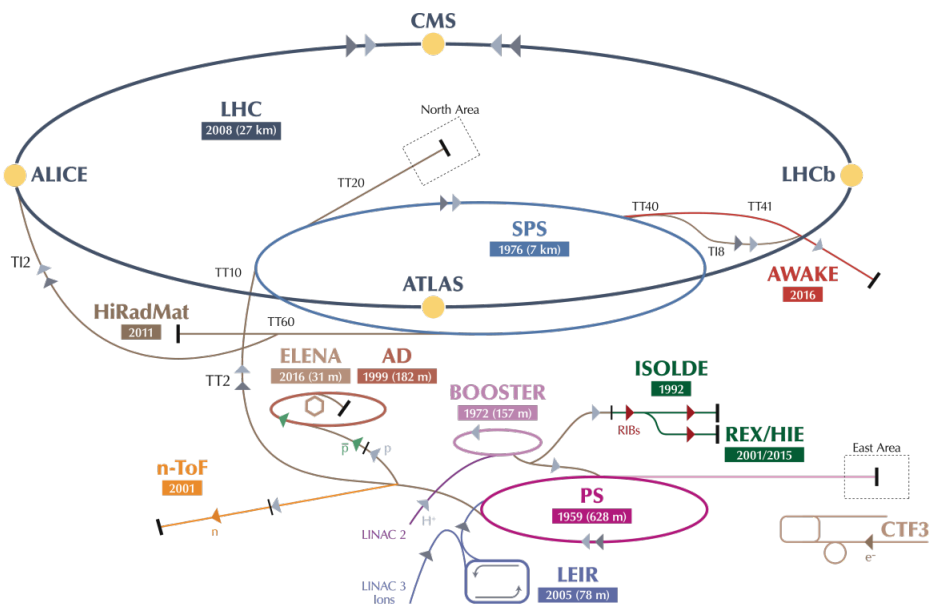


Figure 2.1: Schematic representation of the accelerator complex at CERN [56]. The LHC (dark blue) is the last element in chain of accelerators. Protons are successively accelerated by LINAC 2, the Booster, the Proton Synchrotron (PS) and the Super Proton Synchrotron (SPS) before entering the LHC.

396

397 In Figure 2.2 the LHC programme is shown. the first data collisions, so-called Run 1 period,
 398 lasted from 2008 until 16 February 2013 after which the CERN accelerator complex shut down
 399 for two years of planned maintenance and consolidation during so-called long shutdown 1
 400 (LS1). On 23 March 2015, the new data taking period known as Run 2 started. With a brief end
 401 of the year extended technical stop (EYETS). The main activities carried out during the EYETS
 402 were the maintenance of systems such as the cryogenics, the cooling, electrical systems, etc.; the
 403 replacement of the magnet, as well as a de-cabling and cabling campaign on the SPS[57]. Run 2
 404 will last until July 2018 when the long shutdown 2 (LS2) will begin for 2 years. The main goal
 405 of this shutdown is the LHC injectors upgrade (LUI), but also maintenance and consolidation
 406 will be performed. Furthermore, preparations for the High Luminosity LHC, which will start in

¹This energy loss is proportional to the fourth power of the proton energy and inversely proportional to the bending radius.

407 2024, will be done. More information about phase 1 upgrades during LS1 and EYETS is given
 408 in [Section 2.2.4](#).

409 Before the start of the LHC in 2010, the previous energy record was held by the Tevatron collider
 410 at Fermilab, colliding protons with antiprotons at $\sqrt{s} = 1.96$ TeV. When completely filled, the
 LHC nominally contains 2220 bunches in Run 2, compared to 1380 in Run 1 (design: 2200).

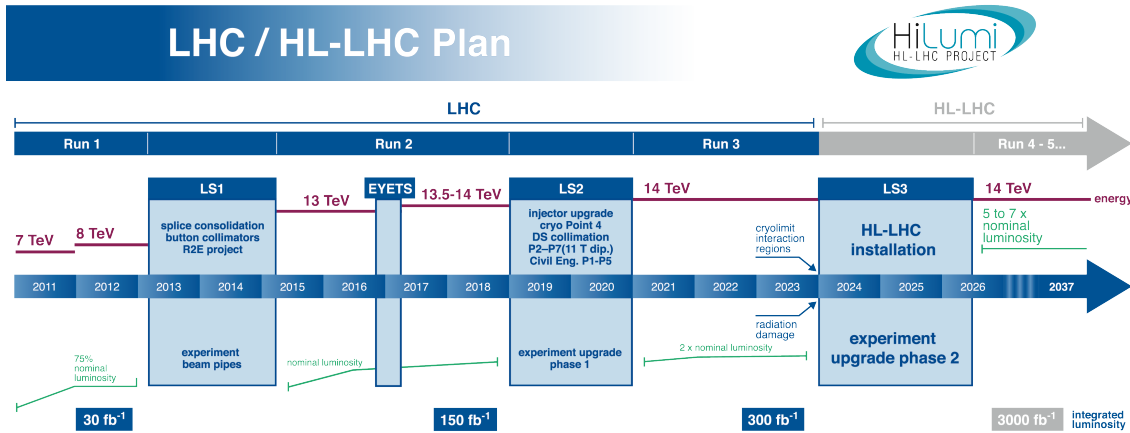


Figure 2.2: The HL-LHC timeline. Figure taken from [58].

411

412 Inside the LHC ring [59], the protons are accelerated by the means of radio frequency cavities,
 413 while 1232 dipole magnets of approximately 15 m long, each weighing 35 t ensure the deflection
 414 of the beams. The two proton beams circulate in opposite direction in separate pipes inside of
 415 the magnet. Through the use of a strong electric current in the coils of the magnet, magnetic
 416 fields are generated and cause the protons to bend in the required orbits. In order for the coil
 417 to become superconducting and able to produce a strong magnetic field of 8.3 T, the magnet
 418 structure is surrounded by a vessel. This vessel is filled with liquid Helium making it possible
 419 to cool down the magnet to 1.9 K. In order to get more focussed and stabilised proton beams,
 420 additional higher-order multipole and corrector magnets are placed along the LHC beam line.

421 The LHC is home to seven experiments, each located at an interaction point:

- 422 • A Toroidal LHC ApparatuS (ATLAS) [60] and the Compact Muon Solenoid (CMS) [61]
 423 experiments are the two general purpose detectors at the LHC. They both have a hermetic,
 424 cylindrical structure and were designed to search for new physics phenomena along with
 425 precision measurements of the Standard Model. The existence of two distinct experiments
 426 allows cross-confirmation of any discovery.
- 427 • A Large Ion Collider Experiment (ALICE) [62] and the LHC Beauty (LHCb) [63] experi-
 428 ments are focusing on specific phenomena. ALICE studies strongly interacting matter
 429 at extreme energy densities where a quark-gluon plasma forms in heavy ion collisions
 (Pb-Pb or p-Pb). LHCb searches for differences between matter and antimatter with the
 430 focus on b physics.

- The forward LHC (LHCf) [64] and the TOTal cross section, Elastic scattering and diffraction dissociation Measurement (TOTEM) [65] experiments are two smaller experiments that focus on head-on collisions. LHCf consists of two parts placed before and after ATLAS and studies particles created at very small angles. TOTEM is placed in the same cavern as CMS and measures the total proton-proton cross section and studies elastic and diffractive scattering.
- The Monopoles and Exotics Detector At the LHC (MoEDAL) [66] experiment is situated near LHCb and tries to find magnetic monopoles.

For the enhancement of the exploration of rare events and thus enhancing the number of collisions, high beam energies as well as high beam intensities are required. The luminosity [67] is a measurement of the number of collisions that can be produced in a detector per square meter and per second and is the key role player in this enhancement. The LHC collisions create a number of events per second given by

$$N_{\text{event}} = L\sigma_{\text{event}}, \quad (2.1)$$

where σ_{event} is the cross section of the process of interest and L the machine instantaneous luminosity. This luminosity depends only on the beam parameters and is for a Gaussian beam expressed as

$$L = \frac{1}{4\pi} N_b n_b f_{\text{rev}} \frac{N_b}{\epsilon_n} \left(1 + \left(\frac{\theta_c \sigma_z}{2\sigma^*} \right)^2 \right)^{-\frac{1}{2}} \frac{\gamma_r}{\beta^*}. \quad (2.2)$$

The number of particles per bunch is expressed by N_b , while n_b is the number of bunches per beam, f_{rev} the revolution frequency, γ_r the relativistic gamma factor, ϵ_n the normalized transverse beam emittance - a quality for the confinement of the beam, β^* the beta function at the collision point - a measurement for the width of the beam, θ_c the angle between two beams at the interaction point, σ_z the mean length of one bunch, and σ^* the mean height of one bunch. In Equation 2.2, the blue part represents the stream of particles, the red part the brilliance, and the green part the geometric reduction factor due to the crossing angle at the interaction point.

The peak design luminosity for the LHC is $10^{34} \text{ cm}^{-2}\text{s}^{-1}$, which leads to about 1 billion proton interactions per second. In 2016, the LHC was around 10% above this design luminosity [68]. The luminosity is not a constant in time since it diminishes due to collisions between the beams, and the interaction of the protons and the particle gas that is trapped in the centre of the vacuum tubes due to the magnetic field. The diffusion of the beam degrades the emittance and therefore also the luminosity. For this reason, the mean lifetime of a beam inside the LHC is around 15 h. The integrated luminosity - the luminosity provided in a certain time range - recorded by CMS and ATLAS over the year 2016 is given in Figure 2.3. In Run 2, the peak luminosity is $13\text{-}17 \times 10^{33} \text{ cm}^{-2}\text{s}^{-1}$ compared to $7.7 \times 10^{33} \text{ cm}^{-2}\text{s}^{-1}$ in Run 1. The recorded luminosity is validated for physics analysis keeping 35.9 fb^{-1} during 2016 data taking.

Multiple proton-proton interactions can occur during one bunch crossing, referred to as pileup. On average, the number of pileup events is proportional to the luminosity times the total inelastic proton-proton cross section. In 2016, an average of about 27 of pileup interactions has been observed in 13 TeV proton collisions at the interaction point of CMS. For 2012, this number was about 21 pileup interactions for 8 TeV collisions.

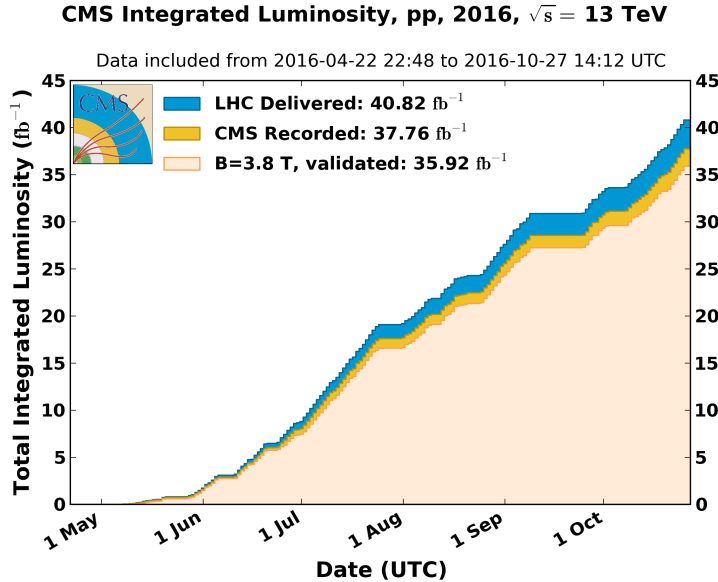


Figure 2.3: Cumulative off-line luminosity measured versus day delivered by the LHC (blue), and recorded by CMS (orange), and certified as good physics analysis during stable beams (light orange) during stable beams and for proton collisions at 13 TeV centre-of-mass energy in 2016. [69].

462 2.2 The Compact Muon Solenoid

463 At one of the collision points of the LHC, the CMS detector [70–72] is placed. Weighing 14 000 t,
464 this cylindrical detector is about 28.7 m long and 15 m in diameter. It has an onion like structure
465 of several specialised detectors and contains a superconducting solenoid with a magnetic field of
466 3.8 T. Living in a hadronic environment, multi-jet processes produced by the strong interaction
467 are the main source of background for rare physics processes. Therefore, good identification,
468 momentum resolution, and charge determination of muons, electrons and photons are one of
469 the main goals of the CMS detector. Additionally, a good charged particle momentum resolution
470 and reconstruction efficiency in the inner tracker provides identification for jets coming from b
471 quarks or tau particles. Also the electromagnetic resolution for an efficient photon and lepton
472 isolation as well as a good hadronic calorimeter for the missing transverse energy² were kept
473 into account while designing CMS. In Figure 2.4, an overview of the CMS detector is shown.

474 2.2.1 CMS coordinate system

The coordinate system used by CMS can be found in Figure 2.5. The origin of the right handed orthogonal coordinate system is chosen to be the point of collisions. The x-axis points towards the centre of the LHC ring such that the y-axis points towards the sky, and the z-axis lies tangent to the beam axis. Since the experiment has a cylindrical shape, customary coordinates are used to describe the momentum \vec{p} : the distance $p = |\vec{p}|$, the azimuthal angle³ $\phi \in [-\pi, \pi]$, the

²The missing transverse energy comes from an imbalance in the transverse plane. This will be discussed in Chapter 4.

³The azimuthal angle is the angle between the x-axis and the projection in the transverse plane of the momentum \vec{p} , denoted as \vec{p}_T .

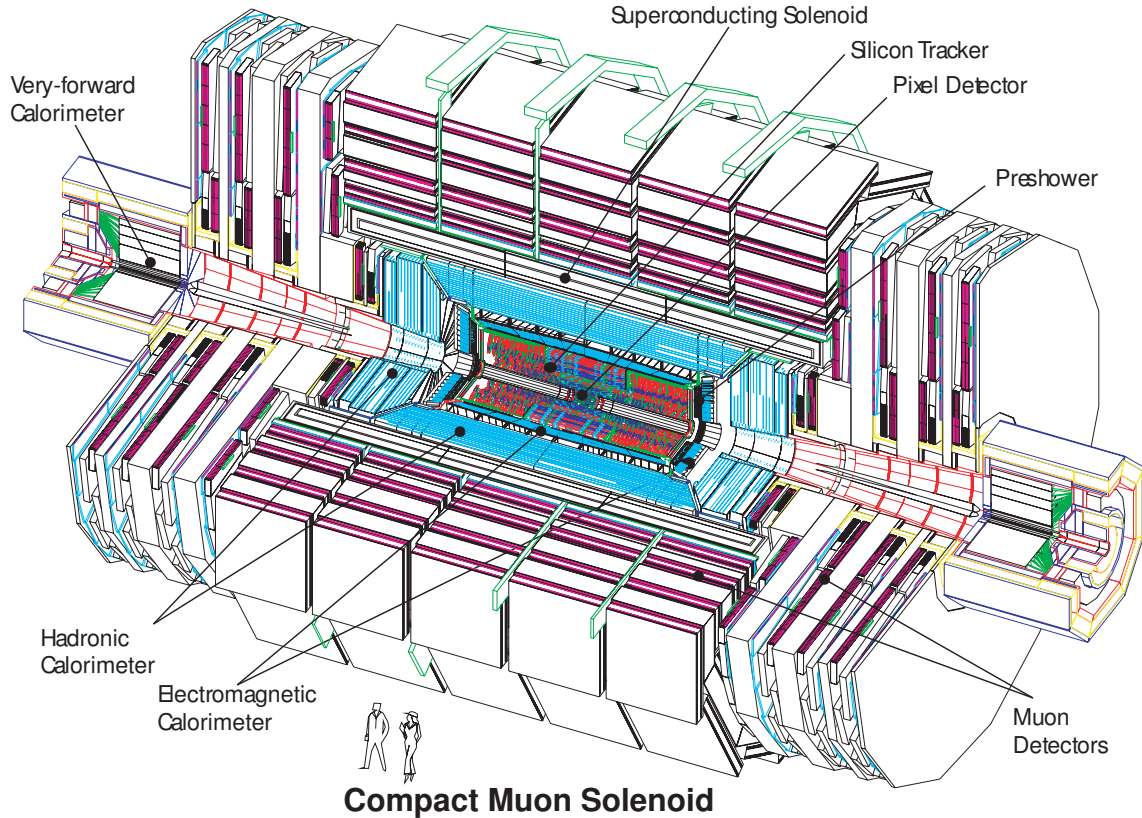


Figure 2.4: Mechanical layout of the CMS detector. Figure taken from [73].

pseudo-rapidity⁴ η :

$$\eta = -\ln \left(\tan \left(\frac{\theta}{2} \right) \right). \quad (2.3)$$

For the energies considered at the LHC, where $E \gg m$, the pseudo-rapidity is a good approximation of the rapidity y

$$y = \frac{1}{2} \ln \left(\frac{E + p_z}{E - p_z} \right), \quad (2.4)$$

475 where the difference of rapidities of two particles is invariant under a Lorentz boost in the
476 z-direction.

477 2.2.2 Towards the heart of CMS

478 The CMS detector can be divided into two parts. A central barrel is placed around the beam
479 pipe ($|\eta| < 1.4$), and two plugs (endcaps) ensure the hermeticity of the detector. In [Figure 2.4](#)
480 and [Figure 2.6](#) the onion like structure of the CMS detector is visible. The choice of a solenoid
481 of 12.9 m long and 5.9 m diameter gives the advantage of bending the particle trajectories in the

⁴The pseudo rapidity is expressed by the polar angle θ between the direction of \vec{p} and the beam.

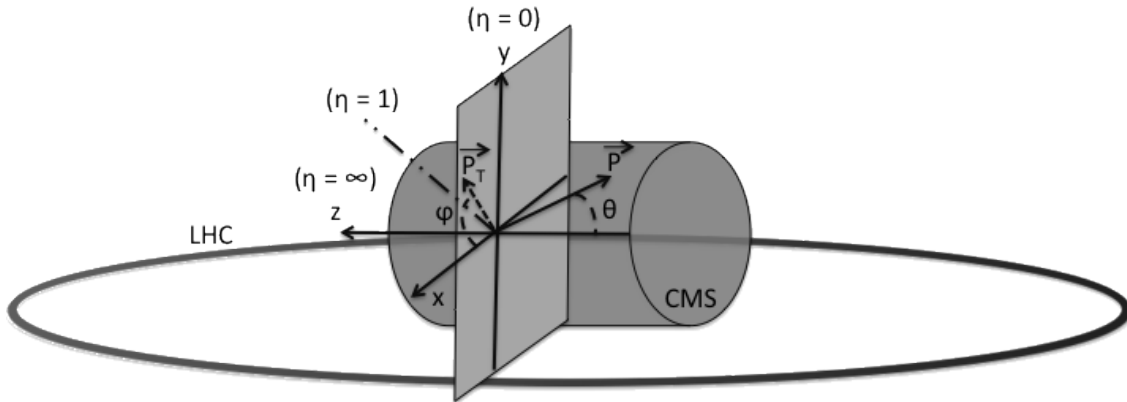


Figure 2.5: Representation of the coordinate system used by CMS. The point of origin is put at the collision point. The x-axis points towards the centre of the LHC ring such that the z-axis lies tangent to the beam axis.

482 transverse plane. The hadronic calorimeter (Section 2.2.2.3), the electromagnetic calorimeter
 483 (Section 2.2.2.4) and the tracker (Section 2.2.2.5) are within the solenoid (Section 2.2.2.2),
 484 while the muon chambers (Section 2.2.2.1) are placed outside the solenoid. The data used for
 485 the search presented in this thesis is collected after the long shutdown 1. After discussing each
 486 part of CMS in their Run 1 configuration, Section 2.2.4 elaborates on their different upgrades
 487 for the data collected in Run 2.

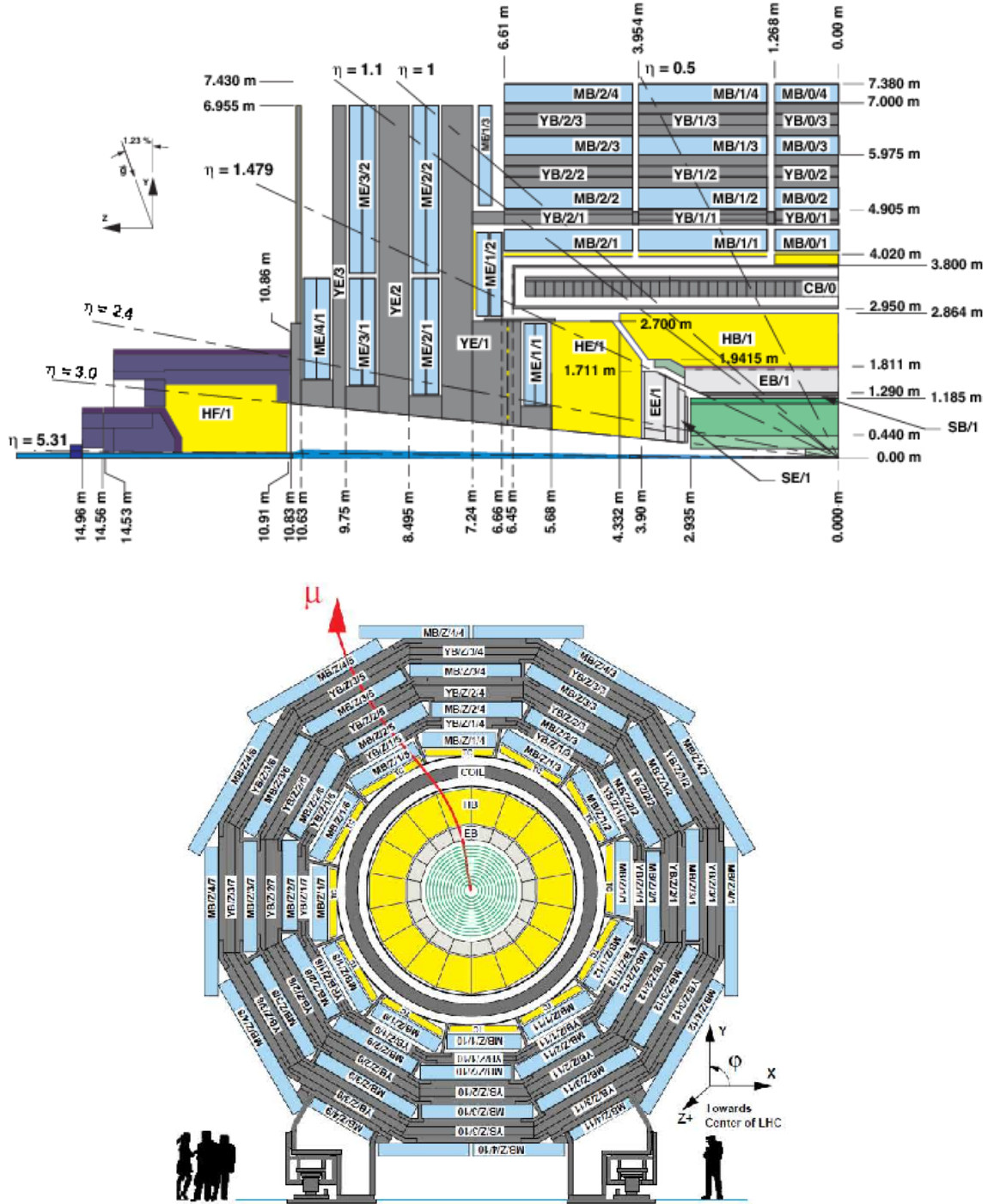


Figure 2.6: Schematic view of the CMS detector in the Run 1 configuration. The longitudinal view of one quarter of the detector is given at the top, while the transversal view is shown at the bottom. The muon system barrel elements are denoted as MBZ/N/S, where Z= -2... +2 is the barrel wheel number, N= 1...4 the station number and S= 1...12 the sector number. Similarly, the steel return yokes are denoted as YBZ/N/S. The solenoid is denoted as CB0, while the hadronic calorimeter is denoted as HE (endcap)/ HB (barrel)/HF (forward) and the electromagnetic calorimeter as EE (endcap)/EB (barrel). The green part represents the tracking system (tracker + pixel). Figure taken from [74].

488 **2.2.2.1 Muon system**

489 The outermost part of CMS consists of the muon system. The magnet return yoke is interleaved
 490 with gaseous detector chambers for muon identification and momentum measurement. The
 491 barrel contains muon stations arranged in five separate iron wheels, while in the endcap four
 492 muon stations are mounted onto three independent iron discs on each side. Each barrel wheel
 493 has 12 sectors in the azimuthal angle.

494 The muon system is divided into three parts, shown in [Figure 2.7](#). The muon rate and neutron
 495 induced backgrounds are small and the magnetic field is very low for the barrel, thus CMS can
 496 use drift tube (DT) chambers. For the endcaps however, the muon and background flux is much
 497 higher and there is a need to use cathode strip chambers (CSC) which are able to provide a
 498 faster response, higher granularity and have a better resistance against radiation. In order to
 499 form a redundant trigger system, resistive plate chambers (RPC) are added. This makes a total
 of 250 DT, 540 CSC and 610 RPC chambers. In [Figure 2.6](#) the arrangement is shown.

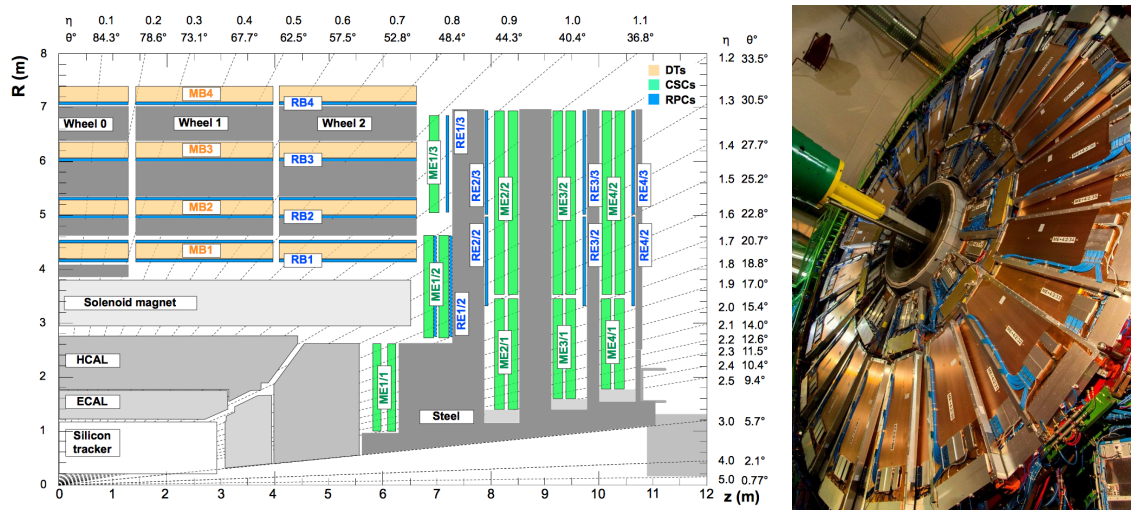


Figure 2.7: (Left) Schematic view of one quarter of the CMS muon system in the Run 1 configuration. The cathode strip chambers (CSC) are shown in green, the drift tubes (DT) are shown in yellow, while the resistive plate chambers (RPC) are shown in blue. Figure taken from [74]. (Right) Cathode strip chambers (ME+4/2 chambers on YE+3). Photo taken from [75].

500

501 Providing a measurement for $|\eta| < 1.2$, the DT chambers in the barrel are on average $2 \times 2.5\text{m}^2$
 502 in size and consist of 12 layers of DT cells⁵ arranged in three groups of four. The $r\phi$ coordinate is
 503 provided by the two outside groups, while the middle group measures the z coordinate. For the
 504 outer muon station, the DT chambers contain only 8 layers of DT cells, providing a muon position
 505 in the $r\phi$ plane. There are four CSC stations in each endcap, providing muon measurements for
 506 $0.9 < |\eta| < 2.4$ (Run 1 configuration). These CSCs are multi-wired proportional chambers that
 507 consist of 6 anode wire planes crossed by 7 copper strips cathode panels in a gas volume. The
 508 r coordinate is provided by the copper strips, while the ϕ coordinate comes from the anode
 509 wires, giving a two dimensional position measurement. There are six layers of RPCs in the

⁵The DT cells are 4 cm wide gas tubes with positively charged stretched wires inside.

510 barrel muon system and one layer into each of the first three stations of the endcap. They are
 511 made from two high resistive plastic plates with an applied voltage and separated by a gas
 512 volume. Read-out strips mounted on top of the plastic plates detect the signal generated by a
 513 muon passing through the gas volume. The RPCs provide a fast response with a time resolution
 514 of 1 ns and cover a range of $|\eta| < 1.8$ for the Run 1 configuration.

515 The muon system provides triggering on muons, identifying muons and improves the momen-
 516 tum measurement and charge determination of high p_T muons. On top of the muon system,
 517 a fraction of the muon energy is deposited in the electromagnetic calorimeter, the hadronic
 518 calorimeter, and outer calorimeter. The high magnetic field enables an efficient first level trigger
 519 and allows a good momentum resolution of $\Delta p/p \approx 1\%$ for a p_T of 100 GeV and $\approx 10\%$ for a
 520 p_T of 1 TeV. There is an efficient muon measurement up to $|\eta| < 2.4$.

521 2.2.2.2 Solenoid

522 Making use of the knowledge of previous experiments like ALEPH and DELPHI at LEP and H1
 523 at HERA, CMS chose for a large super conducting solenoid with a length of 12.9 m and a
 524 inner bore of 5.9 m [72]. With 2168 turns, a current of 18.5 kA resulting in a magnetic field of
 525 3.8 T, and a total energy of 2.7 GJ, a large bending power can be obtained for a modestly-sized
 526 solenoid. In order to ensure a good momentum resolution in the forward regions, a favourable
 527 length/radius was necessary. In [Figure 2.8](#), a photo of the CMS solenoid is shown.

528 The solenoid uses a high-purity aluminium stabilised conductor with indirect cooling from
 529 liquid helium, together with full epoxy impregnation. A four-layer winding is implemented that
 530 can withstand an outward pressure of 64 atm. The NbTi cable is co-extruded by pure aluminium
 531 that acts as a thermal stabilizer and has an aluminium alloy for mechanical reinforcement. The
 532 return of the magnetic field is done by five wheels, noted by YB in [Figure 2.6](#).

533 2.2.2.3 Hadronic calorimeter

534 The hadronic calorimeter (HCAL) is dedicated to precisely measure the energy of charged and
 535 neutral hadrons via a succession of absorbers and scintillators. This makes it crucial for physics
 536 analyses with hadronic jets or missing transverse energy. The HCAL barrel extends between
 537 $1.77 < r < 2.95$ m, where r is the radius in the transverse plane with respect to the beam. Due
 538 to space limitations, the HCAL needs to be as small as possible and is made from materials
 539 with short interaction lengths⁶. On top of this, the HCAL should be as hermetic as possible and
 540 extend to large absolute pseudo rapidities such that it can provide a good measurement of the
 541 missing transverse energy.

542 The quality of the energy measurements is dependent on the fraction of the hadronic shower
 543 that can be detected. Therefore, the HCAL barrel (HB) inside the solenoid is reinforced by an
 544 outer hadronic calorimeter between the solenoid and muon detectors (HO, see [Figure 2.9](#)), using
 545 the solenoid as extra absorber. This increases the thickness to 12 interaction lengths. The HB

⁶Here the interaction length is the nuclear interaction length and this is the length needed for absorbing 36.7% of the relativistic charged particles. For the electromagnetic calorimeter this is defined in radiation length X_0 . The radiation length is the mean distance over which a high energy electron loses all but $1/e$ of its energy by bremsstrahlung.

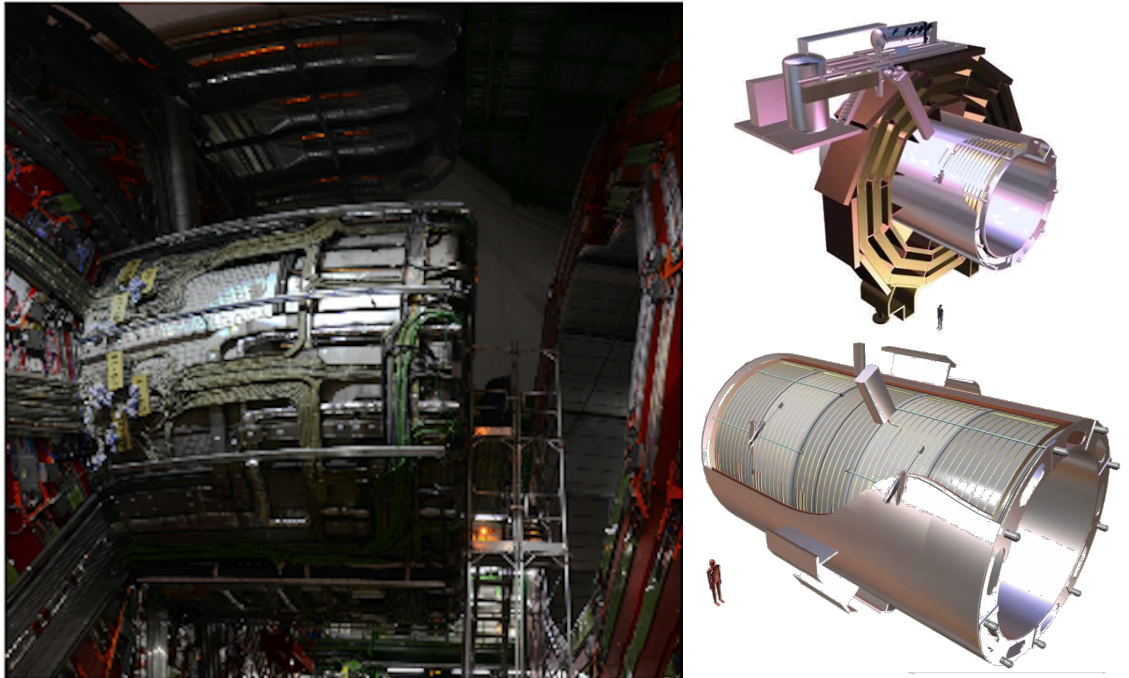


Figure 2.8: (Left) CMS solenoid during the long shutdown in 2013. (Right) An impression of the solenoid magnet taken from [76].

546 and HO provide measurements for $|\eta| < 1.3$, while an endcap on each side (HE, $1.3 < |\eta| < 3$)
 547 and a forward calorimeter (HF, $3.0 < |\eta| < 5.2$) extend the pseudo rapidity range.

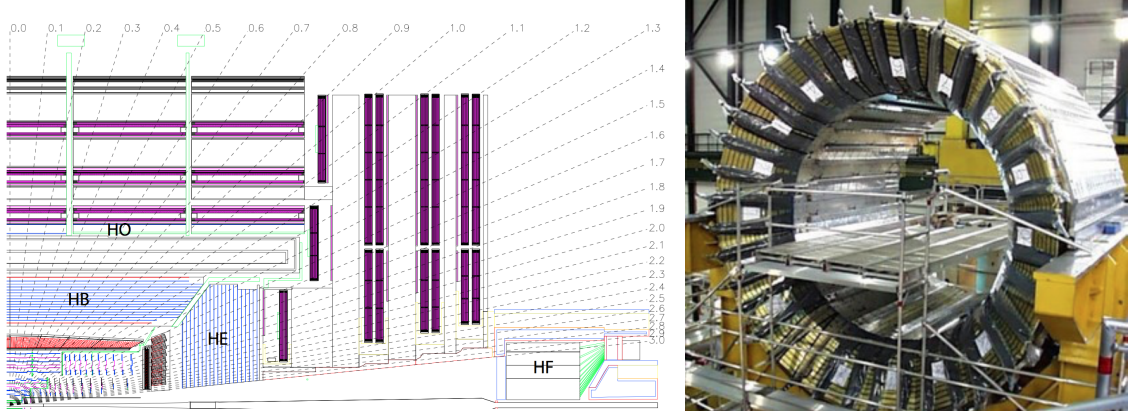


Figure 2.9: (Left) Longitudinal view of the CMS detector showing the locations of the HB, HE, HO, and HF calorimeters. Figure taken from [61]. (Right) CMS barrel calorimeter. Photo taken from [77].

548 The HB is made of 16 absorber plates where most of them are built from brass and others are
 549 made from stainless steel and is about five to ten interaction lengths thick. It is divided in $\eta \times \phi$
 550 towers and contains 2592 read-out channels. The HO complements the HB and extends the
 551 reach up to twelve interaction lengths. This subsystem contains 2160 read-out channels. The
 552 HE is also composed of brass absorber plates and has a thickness corresponding to approximately

ten interaction lengths, with 2592 read-out channels. The HF experiences intense particle fluxes with an expected energy of 760 GeV deposited on average in a proton interaction at a centre-of-mass of 14 TeV, compared to 100 GeV in the rest of the detector. Therefore, these are Cherenkov light detectors made of radiation hard quartz fibres. The main causes of such large energy events are high energy muons and charged particles from late showering hadrons. During Run 1, it became clear that the glass windows of the photon multiplier tubes (PMTs) had to be replaced, which was done during LS1 [78]. The HF represents 1728 read-out channels.

The HCAL and electromagnetic calorimeter combined, can measure the hadron energy with a resolution $\Delta E/E \approx 100\% \sqrt{E[\text{GeV}]} + 5\%$.

2.2.2.4 Electromagnetic calorimeter

The electromagnetic calorimeter (ECAL) is designed to measure the energy of photons and electrons and covers $|\eta| < 3$. It is an hermetic, homogeneous detector and consists of 75 848 lead tungstate (PbWO_4) crystals. These crystals have a fast response time - 80% of the light is emitted within 25 ns- and are radiation hard. The electromagnetic showers produced by passing electrons or photons, ionize the crystal atoms which emit a blue-green scintillation light, that is collected by silicon avalanche photodiodes (APDs) in the barrel and vacuum phototriodes (VPTs) in the endcaps. The crystals and the APD response are sensitive to temperature changes and require a stable temperature.

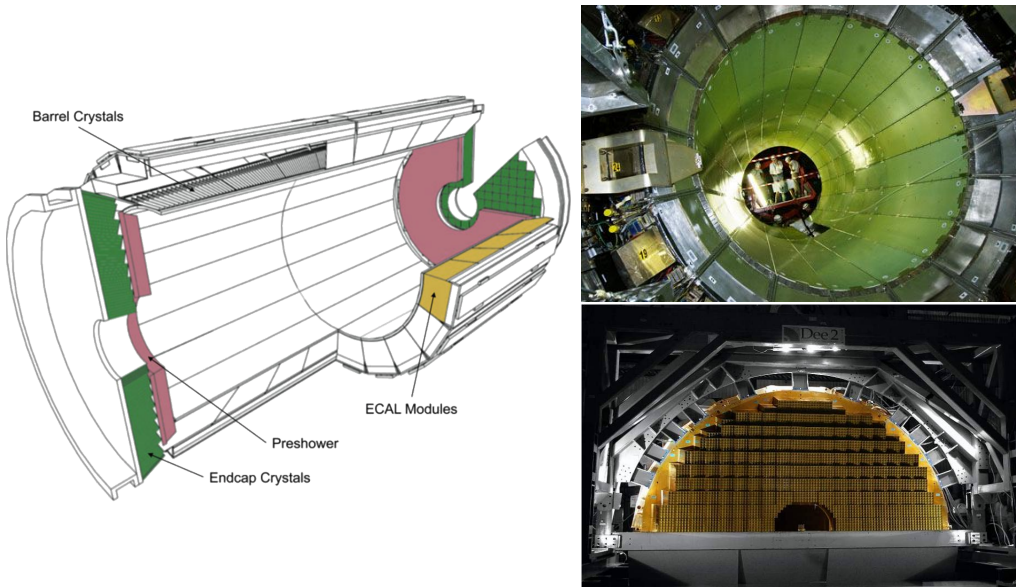


Figure 2.10: (Left) Schematic cross section of the electromagnetic calorimeter taken from [61]. (Right top) The ECAL barrel during construction [79]. (Right bottom) One half of an EE [80].

There are three parts: a central barrel (EB), an endcap region (EE) and a preshower (ES) (Figure 2.10). The EB has an inner radius of 129 cm and corresponds to a pseudo rapidity of $0 < |\eta| < 1.479$. At a distance of 314 cm from the vertex and covering a pseudo rapidity of $1.479 < |\eta| < 3.0$, are the EE. They consist of semi-circular aluminium plates from which structural units of 5×5 crystals (super crystals) are supported. The ES is placed in front of

576 the crystal calorimeter over the endcap pseudo rapidity range with two planes of silicon strip
 577 detectors as active elements.

The electromagnetic shower will typically involve more than one channel. More than 90% of the energy of a 35 GeV electron or photon is contained in a 5×5 matrix of crystals. Therefore, a clustering algorithm is performed in order to associate the energy deposits to the particles impinging the calorimeter. The achieved precision [81] for the barrel is 2×10^{-3} rad in ϕ and 10^{-3} in η . For the endcaps this is 5×10^{-3} rad in ϕ and 2×10^{-3} in η . The energy is reconstructed by a supercluster algorithm, taking into account energy radiated via bremsstrahlung or conversion [61]. The energy resolution is given by

$$\frac{\sigma(E)}{E} = \frac{2.8\%}{\sqrt{E}} \oplus \frac{0.128}{E(\text{GeV})} \oplus 0.3\%, \quad (2.5)$$

578 in the absence of a magnetic field, where the contributions come from the stochastic, noise and
 579 constant terms respectively. The dominating term is the constant term ($E_{\text{shower}} \approx 100$ GeV)
 580 and thus the performance is highly dependent on the quality of calibration and monitoring.

581 2.2.2.5 Inner tracking system and operations

582 The tracking system (tracker) [82] is the detecting unit closest to the point of interaction.
 583 Responsible for the reconstruction of trajectories from charged particles with $|\eta| < 2.5$ that
 584 are bent by the magnetic field, it provides a measurement of the momentum. The tracker is
 585 also responsible for the determination of the interaction point or vertex. It should be able to
 586 provide high granularity as well as fast read-out, and be able to endure high radiation. For
 587 these reasons, the CMS collaboration chose silicon detector technology.

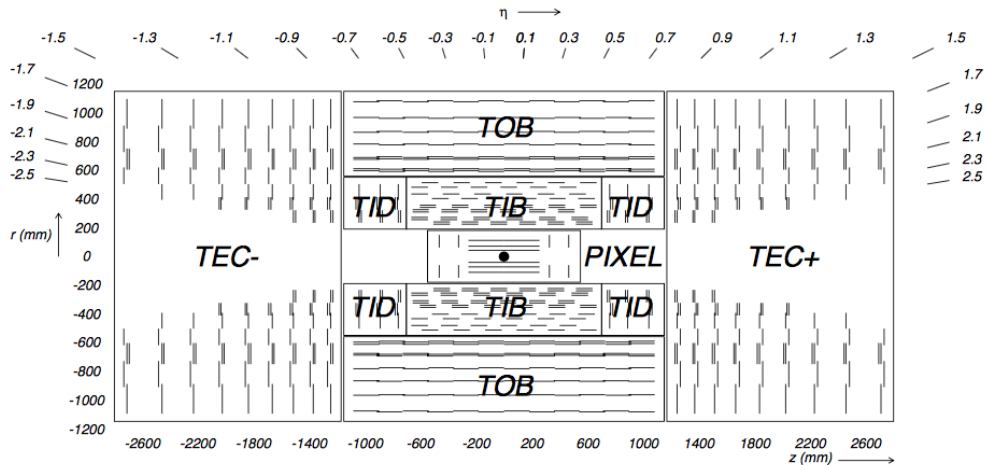


Figure 2.11: Schematic cross section through the CMS tracker. Each line represents a detector module. Double lines indicate back-to-back modules that deliver stereo hits. Figure taken from [61].

588 The tracking system consists of a cylinder of 5.8 m long and 2.5 m in diameter. It is immersed
 589 in a co-axial magnetic field of 3.8 T provided by the solenoid. As shown in Figure 2.11, the
 590 tracker is built up from a large silicon strip tracker with a small silicon pixel tracker inside. The

591 inner pixel region ($4.4 < r < 10.2$ cm), gets the highest flux of particles. Therefore, pixel silicon
 592 sensors of $100 \times 150 \mu\text{m}^2$ are used. It consists of three cylindrical barrels that are complemented
 593 by two discs of pixel modules at each side. The silicon strip tracker ($20 < r < 116$ cm) has three
 594 subdivisions. The Tracker Inner Barrel and Discs (TIB, TID, see [Figure 2.13](#)) are composed
 595 of four barrel layers accompanied by three discs at each end. The outer part of the tracker -
 596 Tracker Outer Barrel (TOB) - consists of 6 barrel layers. In the outer discs, there are nine discs
 597 of silicon sensors, referred to as Tracker End Caps (TEC).



Figure 2.12: The pixel barrel being re-installed after the Long Shutdown in 2015, around the beam pipe at CMS [83].



Figure 2.13: First half of the inner tracker barrel, consisting of three layers of silicon modules [84].

598 The pixel detector, shown in [Figure 2.12](#), has 1440 modules that cover an area of about 1 m^2
 599 and have 66 million pixels. It provides a three-dimensional position measurement of the hits
 600 arising from the interaction from charged particles with the sensors. In transverse coordinate
 601 ($r\phi$), the hit position resolution is about $10 \mu\text{m}$, while $20\text{-}40 \mu\text{m}$ is obtained in the longitudinal
 602 coordinate (z). The sensor plane position provides the third coordinate. The TIB/TID, shown in
 603 [Figure 2.13](#), delivers up to four $r\phi$ -measurements using $320 \mu\text{m}$ thick silicon micro-strip sensors.
 604 These sensors are placed with their strips parallel to the beam axis in the barrel and radial
 605 in the discs. In the TIB, the first two layers have a strip pitch of $80 \mu\text{m}$, while the remaining
 606 two have a strip pitch of $120 \mu\text{m}$. This leads to a respective single point resolution of $23 \mu\text{m}$
 607 and $35 \mu\text{m}$. For the TID, the pitch varies between $100 \mu\text{m}$ and $141 \mu\text{m}$. The TOB provides six
 608 $r\phi$ -measurements with a single point resolution of $53 \mu\text{m}$ in the first four layers, and $35 \mu\text{m}$ in
 609 the last two layers. It consists of $500 \mu\text{m}$ thick microstrip sensors with strip pitches of $183 \mu\text{m}$
 610 (first 4 layers) or $122 \mu\text{m}$ (last two layers). The TEC provides up to 9 ϕ -measurements via 9
 611 discs consisting of up to 7 rings of silicon microstrip sensors of $97 \mu\text{m}$ to $184 \mu\text{m}$ average pitch.

612 A second co-ordinate measurement (z in the barrel, r on the discs) is provided through the
 613 use of a second micro strip detector module mounted back-to-back with a stereo angle of 100
 614 mrad. This is done on the modules in the first two layers and rings of the TIB, TID, and TOB, as
 615 well as rings 1,2, and 5 of the TECs (blue line in [Figure 2.11](#)). The resolution in the z direction
 616 is approximately $230 \mu\text{m}$ in the TIB and $530 \mu\text{m}$ in the TOB, and is varying with pitch in the
 617 TID and TEC. To allow overlay and avoid gaps in acceptance, each module is shifted slightly
 618 in r or z with respect to its neighbouring modules within a layer. With this detector lay-out,
 619 at least nine points per charged particle trajectory can be measured in an $|\eta|$ range up to 2.4,
 620 where at least four of them being two dimensional. The CMS silicon tracker provides 9.3 million
 621 read-out channels and covers an active area of about 198 m^2 .

622 **2.2.3 Data acquisition**

623 At a design luminosity of $10^{34} \text{ cm}^{-2}\text{s}^{-1}$, the proton interaction rate exceeds 1 GHz. Given the
 624 large size of an event (about 1 MB), the high crossing rate, and that typically tens of collisions
 625 happen at the same time, it is impossible for the CMS experiment to store all the data generated.
 626 In order to deal with the large amount of data, a two level trigger system has been put in place.
 627 The first level (Level-1) is a custom hardware system, while a second high level trigger (HLT) is
 628 software based, running on a large farm of computers.

629 **CMS Level-1 Trigger**

630 The Level-1 Trigger has to be a flexible, maintainable system, capable of adapting to the
 631 evolving physics programme of CMS [85]. Its output rate is restricted to 100 kHz imposed
 632 by the CMS read-out electronics. It is implemented by custom hardware and selects events
 633 containing candidate objects - e.g. ionization deposits consistent with a muon, or energy clusters
 634 corresponding to an electron / photon / tau lepton / missing transverse energy / jet. Collisions
 635 with large momenta can be selected with the use of the scalar sum of the transverse momenta
 636 of the jets.

637 By buffering the raw data from the CMS subdetectors in front-end drivers, the Level-1 Trigger
 638 has a pipeline memory of 3.2 μs to decide whether to keep an event or reject it. The trigger
 639 primitives (TP) from the calorimeters and muon detectors are processed in several steps and
 640 combined into a global trigger. This information is then combined with the input from the other
 641 subsystems for the HLT. The separate inputs are synchronized to each other and the LHC orbit
 642 clock and sent to the global trigger module. Here, Level-1 Trigger algorithms are performed
 643 within 1 μs to decide whether to keep the event.

644 **CMS HLT Trigger**

645 The HLT is an array of commercially available computers with a programmable menu that has
 646 an output rate of on average 400 Hz for off-line event storage. The data processing is based on
 647 an HLT path. This is a set of algorithmic steps to reconstruct objects to define selection criteria.
 648 Here, the information of all subdetectors can be used to perform algorithms on higher level
 649 reconstructed objects.

650 **2.2.4 Phase 1 upgrades**

651 Before the start of taking collision data for 13 TeV operations on 3 June 2015, CMS had a
 652 long shutdown (LS1) [86]. During this shutdown, the section of the beryllium beam pipe
 653 within CMS was replaced by a narrower one. This operation required the pixel detector to be
 654 removed and reinserted into CMS. During Run 2, higher particle fluxes with respect to Run
 655 1 are expected. To avoid longterm damage caused by the intense particle flux at the heart of
 656 CMS, the tracker has been made ready to operate at much lower temperature than during Run
 657 1. The electromagnetic calorimeter preshower system was damaged during Run 1, therefore the
 658 preshower discs were removed, repaired and reinstalled successfully inside CMS in 2014. To
 659 help the discrimination between interesting low momentum muons coming from collisions and
 660 muons caused by backgrounds, a fourth triggering and measurement station for muons was

661 added in each of the endcaps. Several new detectors were installed into CMS for measuring the
 662 collision rate within the detector and to monitor beam related backgrounds.

663 During the LS1, the muon system underwent major upgrades [87, 88]. In the fourth station
 664 of each endcap, the outermost rings of CSC and RPC chambers were completed, providing an
 665 angular coverage of $1.2 < |\eta| < 1.8$ for Run 2, increasing the system redundancy, and allowing
 666 tighter cuts on the trigger quality. In order to reduce the environmental noise, outer yoke discs
 667 have been placed on both sides for the endcaps. At the innermost rings of the first station,
 668 the CSCs have been upgraded by refurbishing the read-out electronics to make use of the full
 669 detector granularity instead of groups of three as was the case for Run 1. In Figure 2.7 (right),
 670 the refurbishing of the CSCs is shown.

671 Since the HF experiences intense particle fluxes, it became clear during Run 1 that the glass
 672 windows of the PMTs need replacing. For the ECAL in Run 1, the energy reconstruction happened
 673 via a weighted sum of the digitized samples [89]. For Run 2 however, the reconstruction had to
 674 be made more resistant for out-of-time pileup and a multi-fit approach has been set into place.
 675 In this approach, the pulse shape is modelled as a sum of one in-time pulse plus the out-of-time
 676 pulses [81]. The energy resolution is better than 2% in the central barrel region and 2-5 %
 677 elsewhere.

During the first data taking period of the LHC (2010 to 2013), the tracker operated at +4°C. With the higher LHC beam intensities from 2015 onwards, the tracker needs to be operated at much lower temperatures. The reason for this is that with intense irradiation, the doping concentration changes, the leakage current increases proportional to the fluence and the charge collection efficiency decreases due to charge trapping. Mostly the leakage current (I) is affected by the temperature change:

$$I \propto T^2 e^{-\frac{E_g}{2kT}}, \quad (2.6)$$

678 where T is the operating temperature, E_g the band gap and k the Boltzmann constant. There is
 679 approximately a factor 15 between the leakage currents at room temperatures and at -10 °C.

680 During the LS1, the CMS cooling plant was refurbished [90] and the fluorocarbon cooling
 681 system overhauled. To help suppressing the humidity inside the tracker, new methods for vapour
 682 sealing and insulation were applied. Furthermore, several hundred high-precision sensors are
 683 used to monitor the humidity and temperature. In order to get as dry air as possible, a new
 684 dry-gas plant provides eight times more dry gas (air or nitrogen) than during the first run, and
 685 allows regulation of the flow. As a final addition, the cooling bundles outside the tracker are
 686 equipped with heater wires and temperature sensors in order to maintain safe operations above
 687 the cavern dew point. For the data taking in 2015-2016, the tracker operated at -15 °C.

688 In Run 2, with the increase in centre-of-mass energy and a higher luminosity, a larger number
 689 of simultaneous inelastic collisions per crossing is expected with respect to Run 1. For this, the
 690 CMS Level-1 has been upgraded [91]. All hardware, software, databases and the timing control
 691 system have been replaced for Run 2, where the main changes are that the muon system now
 692 uses the redundancy of the muon detector system earlier to make a high resolution muon trigger.

693 Other upgrades are also performed, including providing the global trigger with more Level-1
694 Trigger algorithms.

695 After the first half of Run 2, the innermost part of detection in CMS (pixel detector) was
696 replaced, enhancing the particle tracking capabilities of CMS. The data used in the framework
697 of this thesis however is from before this upgrade. More information on the Pixel upgrade can
698 be found in Refs. [92, 93].

699 2.2.5 CMS computing model

700 The selected data is stored, processed and dispersed via the Worldwide Large Hadron Collider
701 Computing Grid (WLCG) [94, 95]. This has a tiered structure that functions as a single, coherent
702 system.

703 At CERN and the Wigner Research Centre for physics, a single Tier-0 is located. The raw data
704 collected by the experiments is archived here, and a first reconstruction of the data is done.
705 This data is then already in a file format usable for physics analysis. Furthermore, it is able to
706 reprocess data when new calibrations become available. The Tier-0 site distributes this data
707 to a total of 14 Tier-1 centres. They carry out data reprocessing and store real data as well as
708 simulated data. The Tier-1 further distributes the data to over 150 Tier-2 centres. These make
709 the data accessible for physics analysis and are also being used for the production of simulated
710 data. The data is made accessible for physicists around the world. For CMS, the Tier-0 site at
711 CERN reconstructs the full collision events and the backup of the data is sent to seven Tier-1
712 computer centres in France, Germany, Italy, Spain, Taiwan, UK, and the US. At the Tier-1 sites
713 the events are again reconstructed using refined calibration constants. The patterns are created
714 and the more complex events are sent to forty Tier-2 centres for specific analysis tasks.

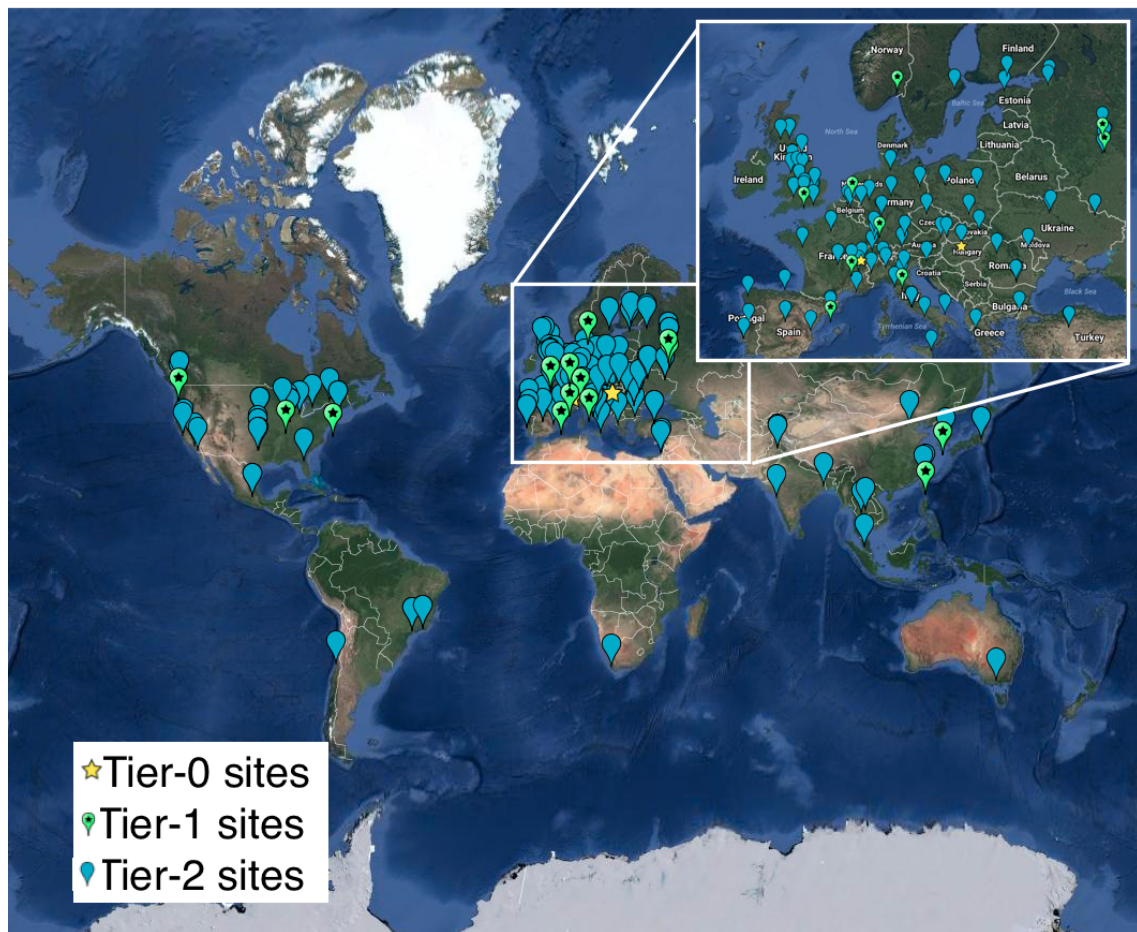


Figure 2.14: Worldwide LHC Computing Grid in 2017 [96].

Analysis techniques

3

716 In order to study the collisions coming from high energy experiments, many tools have been
 717 developed. In [Section 3.1](#), the physics of hadron collision at high energies are presented. These
 718 insights are used to generate events via Monte Carlo event generators, explained in [Section](#)
 719 [3.2](#). Machine learning helps to differentiate between signal- and background like events. In
 720 [Section 3.3](#), the multivariate technique of boosted decision trees is explained. This yields
 721 powerful discriminants for separating signal and background events and provides distributions
 722 for template-based maximum likelihood fits. The fitting method used in the search presented
 723 in this thesis is discussed in [Section 3.4](#).

724 3.1 Hadron collisions at high energies

All partons can be approximated as free when there is sufficiently high momentum transfer in hadron collisions. This makes it possible to treat a hadron-hadron scattering as a single parton-parton interaction. The momentum of the parton can then be expressed as a fraction of the hadron momentum

$$\vec{p}_{\text{parton}} = x \vec{p}_{\text{hadron}}, \quad (3.1)$$

where x is referred to as the Björken scaling variable. The interaction $p_A p_B \rightarrow X$ can then be factorised in terms of partonic cross sections $\hat{\sigma}_{ij \rightarrow X}$ [97]

$$\sigma_{p_A p_B \rightarrow X} = \sum_{ij} \iint dx_1 dx_2 f_i^A(x_1, Q^2) f_j^B(x_2, Q^2) d\hat{\sigma}_{ij \rightarrow X}, \quad (3.2)$$

725 where i and j are the partons resolved from protons A and B. The parton density functions
 726 (PDF) are denoted as $f_i(x_j, Q^2)$, and Q^2 is the factorisation scale more commonly denoted as
 727 μ_F . This factorisation scale represents the energy at which the hadronic interaction can be
 728 expressed as a product of the partonic cross section and the process independent PDF. In [Figure](#)
 729 [3.1](#), the kinematic regions in x and μ_F are shown for fixed target and collider experiments.

730 The parton density functions (PDF) [98–100] represent the momentum distribution of the
 731 proton amongst its partons at an energy scale μ_F . These functions are obtained from global fits
 732 to data since they can not be determined from first principles. From measurements on deep

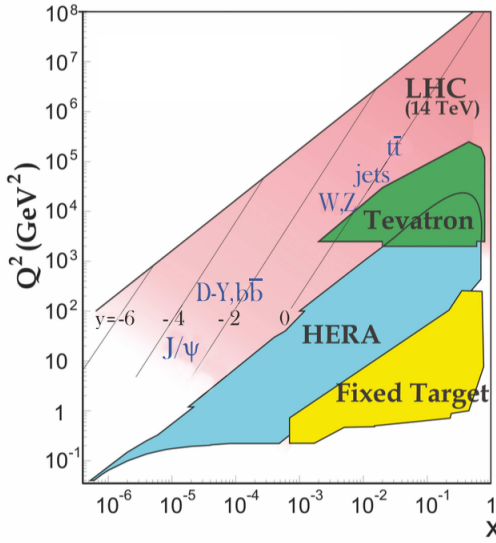


Figure 3.1: Kinematic regions in momentum fraction x and factorisation scale Q^2 probed by fixed-target and collider experiments. Some of the final states accessible at the LHC are indicated in the appropriate regions, where y is the rapidity. In this figure, the incoming partons have $x_{1,2} = (M/14 \text{ TeV})e^{\pm y}$ with $Q = M$ where M is the mass of the state shown in blue in the figure. For example, exclusive J/ψ and Υ production at high $|y|$ at the LHC may probe the gluon PDF down to $x \sim 10^{-5}$. Figure taken from [6].

733 inelastic scattering using lepton-proton collision by the HERA collider [101], supplemented
 734 with proton-antiproton collisions from the Tevatron [102], and proton collision data from the
 735 ATLAS, CMS and LHCb collaborations at the LHC (Run 1) [103] the PDFs are determined and
 736 included in global PDF sets known as the PDF4LHC recommendation [100]. Their measurement
 737 at scale μ_F is extrapolated to higher energies by use of the DGLAP equations [104]. Once
 738 these PDFs are known, the cross section of a certain process can be calculated and used as
 739 input for the Monte Carlo generators used to make the simulated data samples at the LHC. In
 740 the framework of this thesis, the NLO PDF4LHC15_100 set is used. This set is an envelope of
 741 three sets: CT14, MMHT2014 and NNPDF3.0 [100]. As illustration, the dependency of the PDFs
 742 on the momentum fraction x is shown for the NNPDF3.0 set on hadronic scale $\mu_F^2 = 10 \text{ GeV}^2$
 743 and LHC scale $\mu_F^2 = 10^4 \text{ GeV}^2$ in Figure 3.2. The gluon density dominated for most values of
 744 the momentum fraction, implying that it is easier to probe gluons than the quarks. When the
 745 Björken scale is to one, the parton densities of the valence quarks of the proton, up and down
 746 quarks, dominate over the gluon density. The sea quarks originating from gluon splitting, the
 747 charm, anti-up, and anti-down quarks, have lower densities in general for the proton. The
 748 resolution scale Q^2 is typically taken to be the energy scale of the collision. For the top quark pair
 749 production a scale of $Q^2 = (350 \text{ GeV})^2$ is chosen, meaning that the centre-of-mass energy of the
 750 hard interaction is about twice the top quark mass. The uncertainty on the parton distributions
 751 is evaluated using the Hessian technique [105], where a matrix with a dimension identical to
 752 the number of free parameters needs to be diagonalised. In the case of PDF4LHC15_100 set, this
 753 translates into 100 orthonormal eigenvectors and 200 variations of the PDF parameters in the
 754 plus and minus direction.

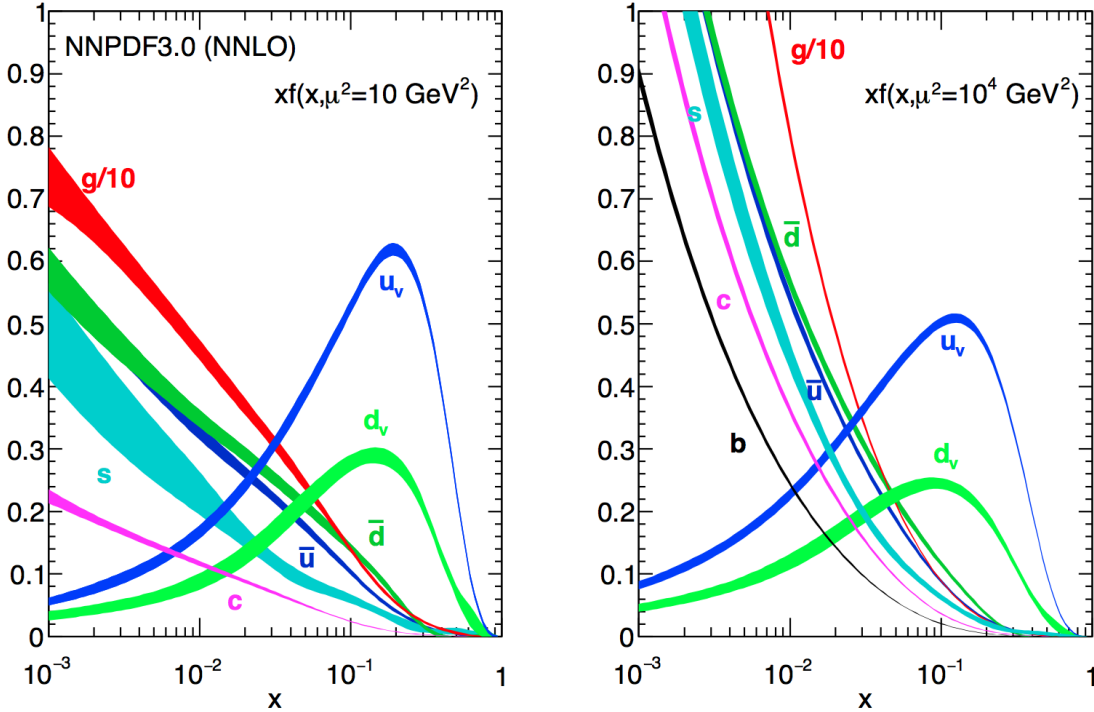


Figure 3.2: The momentum fraction x times the parton distribution functions $f(x)$, where $f = u_v, d_v, \bar{u}, \bar{d}, s, c$, or g as a function of the momentum fraction obtained in the NNLO NNPDF3.0 global analysis at factorisation scales $\mu^2 = 10 \text{ GeV}^2$ (left) and $\mu^2 = 10^4 \text{ GeV}^2$ (right), with $\alpha_s(M_Z^2) = 0.118$. The gluon PDF has been scaled down by a factor of 0.1. Figure taken from [6].

Quantum fluctuations can cause divergences at high energies. This is solved by introducing a renormalization scale μ_R to redefine physical quantities, making the theory still able to describe the experimental regime. A consequence of this method is that the coupling constants will run as a function of μ_R . Beyond the renormalization scale, the high energy effects such as the loop corrections to propagators (self energy) are absorbed in the physical quantities through a renormalization of the fields. In particular, the running behaviour of the strong coupling constant¹ α_S is found to be

$$\alpha_S = \frac{\alpha_S(\mu_0^2)}{1 + \alpha_S(\mu_0^2) \frac{33-2n_f}{12\pi} \ln\left(\frac{|\mu_R^2|}{\mu_0^2}\right)}, \quad (3.3)$$

with n_f the number of quarks and μ_0 the reference scale at which the coupling is known. The current world average of the strong coupling constant at the Z boson mass is $\alpha_S(\mu_R = m_Z) = 0.1181 \pm 0.0011$ [6]. From Equation 3.3 one can see easily that the coupling strength decreases with increasing renormalization scale, this is known as asymptotic freedom. Additionally, following the behaviour of $\alpha_S(\mu_R^2)$, a limit $\Lambda_{\text{QCD}} \approx 200 \text{ MeV}$ is found for which α_S becomes larger than one. Under this limit, the perturbative calculations of observables can no longer be done.

¹The strong coupling constant is defined as $\alpha_S = \frac{g_S^2}{4\pi}$.

Cross sections can be written in terms of interacting vertices contributing to the matrix element (ME) originating from elements of a perturbative series [106], allowing them to be expanded as a power series of the coupling constant α

$$\sigma = \sigma_{\text{LO}} \left(1 + \left(\frac{\alpha}{2\pi} \right) \sigma_1 + \left(\frac{\alpha}{2\pi} \right)^2 \sigma_2 + \dots \right). \quad (3.4)$$

Leading order (LO) accuracy contains the minimal amount of vertices in the process, then depending on where the series is cut-off one speaks of next-to-leading order (NLO), or next-to-next-to-leading order (NNLO) accuracy in α . Predictions including higher order corrections tend to be less affected by theoretical uncertainties originating from a variation of the chosen renormalization and factorisation scales.

3.2 Event generation

In order to compare reconstructed data with theoretical predictions, collision events are generated and passed through a simulation of the CMS detector and an emulation of its read-out. For the detector simulation, a so-called Full Simulation package [107, 108] based on the Geant4 toolkit [109] is employed. This allows detailed simulations of the interactions of the particles with the detector material.

3.2.1 Fundamentals of simulating a proton collision

The generation of $\text{pp} \rightarrow \text{X}$ events is subdivided into sequential steps [110–112], as shown in Figure 3.3.

The interaction of two incoming protons is often soft and elastic leading to events that are not interesting in the framework of this thesis. More intriguing are the hard interactions between two partons from the incoming protons. The event generation starts from the matrix elements of a hard scattering process of interest. The corresponding cross section integral is sampled using Monte Carlo techniques and the resulting sample of events reflects the probability distribution of a process over its final state phase space. A parton shower (PS) program is then used to simulate the hadronisation of final state partons, coming from the sample of events of the hard interaction, into hadrons which then decay further. On top of this, radiation of soft gluons or quarks from initial or final state partons is simulated. These are respectively referred to as initial state radiation (ISR) or final state radiation (FSR). The contributions from soft secondary interactions, the so-called underlying event (UE), and colour reconnection effects are also taken into account. A brief overview of the programs used for the event generation of the signal and main background processes used in the search presented in this thesis, is given in Section 3.2.2.

3.2.2 Programs for event generation

The FEYNRULES package [113] allows for the calculation of the Feynman rules in momentum space for any quantum field theory model. By use of a Lagrangian, the set of Feynman rules associated with this Lagrangian is calculated. Via the Universal FeynRules Output (UFO) [114] the results are then passed to matrix element generators.

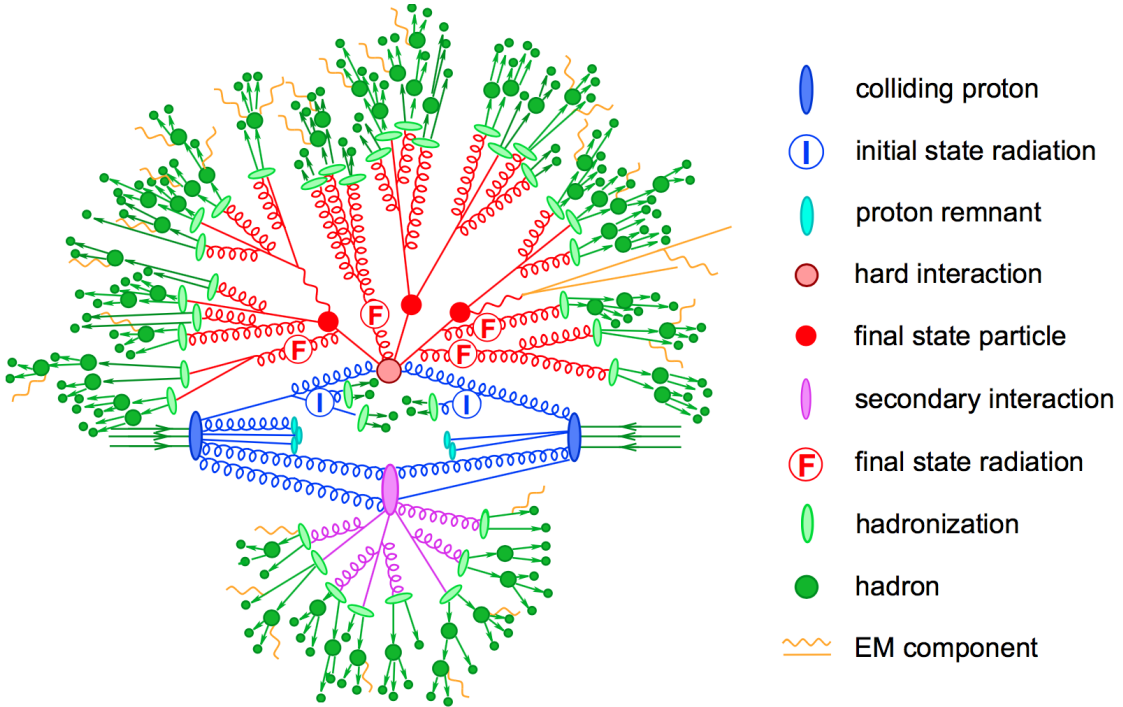


Figure 3.3: Sketch of a hadron collision as simulated by a Monte-Carlo event generator. The red blob in the centre represents the hard collision, surrounded by a tree-like structure representing Bremsstrahlung as simulated by parton showers. The purple blob indicates a secondary hard scattering event. Parton-to-hadron transitions are represented by light green blobs, dark green blobs indicate hadron decays, while yellow lines signal soft photon radiation. Figure taken from [112].

794 The MadGraph program [115] is used to interpret the physics model and calculate the cor-
 795 responding Feynman diagrams and matrix elements. After this, MadEvent [116] is used to
 796 calculate the corresponding partons. These generated parton configurations are then merged
 797 with Pythia [117–119] parton showers using the MLM merging scheme [120].

798 The MadGraph5_aMC@NLO program [121] combines the LO MadGraph [115] and the aMC@NLO
 799 program into a common framework. This combination supports the generation of samples at
 800 LO or NLO together with a dedicated matching to parton showers using the MC@NLO [122]
 801 or FxFx [123] schemes respectively. The FxFx scheme produces a certain fraction of events
 802 with negative weights originating from the subtraction of amplitudes that contain additional
 803 emissions from the NLO matrix element to prevent double-counting.

804 The POWHEG box (versions 1 and 2) [124–129] contains predefined implementations of various
 805 processes at NLO. It applies the POWHEG method for ME- to PS- matching, where the hardest
 806 radiation generated from the ME has priority over subsequent PS emission to remove the overlap
 807 with the PS simulation.

808 The JHU generator (version 7.02) [130–133] is used to generate the parton level information
 809 including full spin and polarization correlations. It is commonly used for studying the spin and
 810 parity properties of new resonances such as $ab \rightarrow X \rightarrow VV$, where $V = Z, W, \gamma$.

811 The generation of events from processes involving the production and decay of resonances
 812 creates a computational heavy load, especially at NLO. The narrow width approximation assumes
 813 that the resonant particle is on-shell. This factorizes the production and decay amplitude,
 814 allowing to perform the simulation of the production and decay of heavy resonances like top
 815 quarks or Higgs bosons to be performed in separate steps. The MadSpin program [134] extends
 816 this approach and accounts for off-shell effects through a partial reweighting of the events.
 817 Additionally, spin correlation effects between production and decay products are taken into
 818 account.

819 The Pythia program (versions 6 and 8) [117–119] generates events of various processes
 820 at LO. However, more commonly it is only used for its PS simulation and is then used after
 821 other LO and NLO event generators to perform subsequent parton showering, hadronisation,
 822 and simulation of the underlying event. In this thesis the underlying event tunes [135] are the
 823 CUETP8M2T4, CUETP8M1 and CUETP8M2.

824 The detector response is simulated via the Geant4 [109] program. This program tracks the
 825 particles through the detector material via a detailed description of the detector and generates
 826 several hits throughout several sensitive layers. In addition, the response of the detector
 827 electronics to these hits are simulated.

828 3.2.3 Generating FCNC top-Z interactions

829 The FCNC processes are generated by interfacing the Lagrangian in Equation 1.36 with
 830 MadGraph5_aMC@NLO by means of the FeynRules package and its Universal FeynRules
 NOTE: RH₈₃₁
 and LH₈₃₂
 gave the₈₃₃
 same re-₈₃₄
 sulting vari-₈₃₅
 ables and₈₃₆
 RH is easier₈₃₇
 to simulate₈₃₈
 since those₈₃₉
 are singlets₈₄₀
 under SU(3)
 (no doublet
 with b)

831 Output format. The complex chiral parameters are arbitrary chosen to be $f_{Xq}^L = 0$ and $f_{Xq}^R = 1$.
 The processes are generated with the MadGraph5_aMC@NLO (version 2.2.2) and showered with
 Pythia (version 8.22). The signal consists of two components: events describing the top quark
 pair production followed by an FCNC decay of one top quark ($t \rightarrow Zq$), and events with the FCNC
 single top quark production ($Zq \rightarrow t$) for which the top quark decays according to theSM. The
 leading order generation of the single top quark FCNC process $tZ + 0,1$ jet including a merging
 technique can not be done since $tZ + 1$ jet also contains contributions from top quark pair FCNC
 where one quark is decaying in tZ . Therefore, single top quark and top quark pair processes
 are generated independently, where the single top quark process is generated without the extra
 hard jet, and the top quark pair FCNC process is generated with up to two extra jets.

841 The signal rates are estimated by use of the MadGraph5_aMC@NLO program for estimating the
 842 partial widths. The anomalous couplings are left free to float for this estimation, and only one
 843 coupling is allowed to be non-vanishing at a time. The results are presented in Table 3.1.

844 The anomalous single top quark cross sections are calculated by convolution of the hard
 845 scattering matrix elements with the LO order set of NN23L01 [136] partons densities. The NLO
 846 effects are modelled by multiplying each LO cross section by a global k -factor. The LO single top
 847 quark production cross section and the global k -factors for the top-Z production are shown in
 848 Table 3.2. The hard scattering events are then matched to parton showers to Pythia to account
 849 for the simulation of the QCD environment relevant for hadronic collisions.

Table 3.1: Leading order partial widths related to the anomalous decay modes of the top quark, where the new physics scale Λ is given in GeV.

Anomalous coupling	vertex	Partial decay width (GeV)
κ_{tZq}/Λ	tZu	$1.64 \times 10^4 \times (\kappa_{tZu}/\Lambda)^2$
	tZc	$1.64 \times 10^4 \times (\kappa_{tZc}/\Lambda)^2$
ζ_{tZq}	tZu	$1.69 \times 10^{-1} \times (\zeta_{tZu})^2$
	tZc	$1.68 \times 10^{-1} \times (\zeta_{tZc})^2$

Table 3.2: Leading order single top quark production cross section at a centre-of-mass of 13 TeV for $pp \rightarrow tZ$ or $t\bar{Z}$, where the new physics scale is given in GeV. The NLO k -factors [137] are given in the last column.

Anomalous coupling	vertex	Cross section (pb) $pp \rightarrow t + pp \rightarrow \bar{t}$	$\sigma_{pp \rightarrow \bar{t}}/\sigma_{pp \rightarrow t}$	NLO k -factor
κ_{tZq}/Λ	tZu	$1.92 \times 10^7 \times (\kappa_{tZu}/\Lambda)^2$	0.12	1.40
	tZc	$2.65 \times 10^6 \times (\kappa_{tZc}/\Lambda)^2$	0.50	1.40
ζ_{tZq}	tZu	$8.24 \times 10 \times (\zeta_{tZu})^2$	0.14	1.40
	tZc	$1.29 \times 10 \times (\zeta_{tZc})^2$	0.50	1.40

The top quark pair cross sections are derived from the SM $t\bar{t}$ cross section, calculated with MadGraph5_aMC@NLO at NLO at a centre-of-mass of 13 TeV ($\sigma_{t\bar{t}}^{\text{SM,NLO}} = 6.741 \times 10^2 \text{ pb}$), and considering the decay $t\bar{t} \rightarrow (bW^\pm)(X_{qt})$. The branching fraction $\mathcal{B}(t \rightarrow bW^\pm)$ is assumed to be equal to one and the FCNC branching fraction is calculated as

$$\mathcal{B}(t \rightarrow qX) = \frac{\Gamma_{t \rightarrow qX}}{\Gamma_t^{\text{SM}} + \Gamma_t^{\text{FCNC}}} \approx \frac{\Gamma_{t \rightarrow qX}}{\Gamma_t^{\text{SM}}}, \quad (3.5)$$

where $\Gamma_{t \rightarrow qX}$ is given in Table 3.1, $\Gamma_t^{\text{SM}} = 1.32 \text{ GeV}$ [47], and the assumption $\Gamma_t^{\text{FCNC}} \ll \Gamma_t^{\text{SM}}$ is made. In Table 3.3 the resulting NLO cross sections for the top-Z FCNC interactions are given.

Table 3.3: Next to leading order top quark pair cross section for the top-Z FCNC interactions $t\bar{t} \rightarrow (bW^\pm)(X_{qt})$ with a full leptonic decay at a centre-of-mass of 13 TeV, where $\sigma_{pp \rightarrow t\bar{t}}^{\text{SM,NLO}} = 6.741 \times 10^2 \text{ pb}$, $\mathcal{B}(Z \rightarrow \ell\bar{\ell}) = 3.36 \times 3 \times 10^{-2}$, and $\mathcal{B}(W \rightarrow \ell\nu) = 10.80 \times 3 \times 10^{-2}$.

Anomalous coupling	vertex	Process	Cross section (pb)
κ_{tZq}/Λ	tZu	$t\bar{t} \rightarrow (b\ell^+\nu)(\bar{u}\ell^+\ell^-)$	$2.727 \times 10^5 \times (\kappa_{tZu}/\Lambda)^2$
		$t\bar{t} \rightarrow (\bar{b}\ell^-\bar{\nu})(u\ell^+\ell^-)$	$2.727 \times 10^5 \times (\kappa_{tZu}/\Lambda)^2$
	tZc	$t\bar{t} \rightarrow (b\ell^+\nu)(\bar{c}\ell^+\ell^-)$	$2.726 \times 10^5 \times (\kappa_{tZc}/\Lambda)^2$
		$t\bar{t} \rightarrow (\bar{b}\ell^-\bar{\nu})(c\ell^+\ell^-)$	$2.726 \times 10^5 \times (\kappa_{tZc}/\Lambda)^2$
ζ_{tZq}	tZu	$t\bar{t} \rightarrow (b\ell^+\nu)(\bar{u}\ell^+\ell^-)$	$2.807 \times (\zeta_{tZu})^2$
		$t\bar{t} \rightarrow (\bar{b}\ell^-\bar{\nu})(u\ell^+\ell^-)$	$2.807 \times (\zeta_{tZu})^2$
	tZc	$t\bar{t} \rightarrow (b\ell^+\nu)(\bar{c}\ell^+\ell^-)$	$2.807 \times (\zeta_{tZc})^2$
		$t\bar{t} \rightarrow (\bar{b}\ell^-\bar{\nu})(c\ell^+\ell^-)$	$2.807 \times (\zeta_{tZc})^2$

3.2.4 Generating SM background events

The SM tZq sample is generated using the MadGraph5_aMC@NLO generator (version 2.2.2) [138] at leading order accuracy. The t $\bar{t}Z$ and triboson samples were generated using the MadGraph5_aMC@NLO generator (version 2.2.2), interfaced through the dedicated MC@NLO matching scheme [122]. The WZ+jets and t $\bar{t}W$ samples are produced with up to one additional parton at next-to-leading order accuracy using MadGraph5_aMC@NLO (version 2.2.2) and using FxFx approach [139] for matching and merging. The samples of t $\bar{t}H$, WW, ZZ, and single top quark production channels are generated with the POWHEG box (versions 1 and 2) [124–129]. The JHU generator [130–133] is used for the tqH sample, while the tWZ sample is generated using MadGraph5_aMC@NLO at leading order [115]. All events are interfaced to Pythia version 8.22 [119] to simulate parton shower, hadronisation, and underlying event. Additionally, MadSpin is used for the tZq, WZ+jets, t $\bar{t}Z$, t $\bar{t}W$, tWZ, and triboson samples.

The complete list of SM samples is given in Table 3.4, along with their cross sections at a centre-of-mass of 13 TeV. The cross sections without a reference are coming from the generator with which the sample has been made, for some of them the uncertainties are provided by the Generator Group [140]. For each MC sample, the integrated luminosity that the sample represents is estimated as the number of simulated events divided by the cross section of the generated process. This luminosity is then matched to integrated luminosity of 35.9 fb^{-1} represented by the data used for analysis. For processes generated with MadGraph5_aMC@NLO, the effective number of simulated events is used, taking into account positive and negative event weights. In Figure 3.4, a summary is given of the SM cross section measurements performed by the CMS collaboration. These cross sections are all in agreement with their SM predictions.

Table 3.4: SM MC samples used in this analysis with their corresponding cross section at a centre-of-mass of 13 TeV and MadGraph5_aMC@NLO correction C when applicable. The generators used for each sample are indicated and the simulation of the parton shower, hadronisation, and underlying event is done by Pythia version 8.22 [119] for all samples.

Process	Generator	Cross section (pb)	C	Ref.
$WZ \rightarrow 3\ell\nu$	MadGraph5_aMC@NLO+MadSpin	5.26	1.61	[140]
tZq with $Z \rightarrow \ell^+\ell^-$	MadGraph5_aMC@NLO+MadSpin	0.0758	3.77	[140]
tqH with $H \rightarrow ZZ \rightarrow \ell^+\ell^-\ell^+\ell^-$	JHU	$8.80 \cdot 10^{-6}$	-	[140]
$t\bar{t}W + \text{jets}$ with $W \rightarrow \ell\nu$	MadGraph5_aMC@NLO+MadSpin	0.2043 ± 0.0020	1.94	[140]
$t\bar{t}Z \rightarrow 2\ell + 2\nu + \text{other}$, with $m_{\ell\ell} > 10$ GeV	MadGraph5_aMC@NLO+MadSpin	0.2529 ± 0.0004	2.15	[140]
$t\bar{t}H, \text{no } b\bar{b} \text{ decays}$	POWHEG	0.2151	-	[140]
$t\bar{t}H, b\bar{b} \text{ decays}$	POWHEG	0.2934	-	[140]
$WW \rightarrow 2\ell 2\nu$	POWHEG	12.178	-	[141]
$ZZ \rightarrow 4\ell$	POWHEG	0.3366	-	[140]
WZZ	MadGraph5_aMC@NLO+ MadSpin	0.05565	1.14	[140]
ZZZ	MadGraph5_aMC@NLO	0.01398	1.17	[140]
single top quark tWZ , with $Z_\mu \rightarrow \ell^+\ell^-$	MadGraph5_aMC@NLO(LO)+MadSpin	0.001123	-	[140]
single top quark t-channel \bar{t}	POWHEG+MadSpin	$44.33^{+1.76}_{-1.49}$	-	[140]
single top quark t-channel t	POWHEG+MadSpin	$26.38^{+1.32}_{-1.18}$	-	[140]
single top quark $t\bar{W}$	POWHEG	$35.85 \pm 0.90 \text{ (scale)} \pm 1.70 \text{ (PDF)}$	-	[140]
single top quark tW	POWHEG	$35.85 \pm 0.90 \text{ (scale)} \pm 1.70 \text{ (PDF)}$	-	[140]
$t\bar{t}$	POWHEG	$831.76^{+19.77+35.06}_{-29.20-35.06}$	-	[140]
$Z/\gamma^* + \text{jets}$, with $m_{\ell\ell} > 50$ GeV	MadGraph5_aMC@NLO	$3 \times (1921.8 \pm 0.6 \pm 33.2)$	1.49	[140]
$Z/\gamma^* + \text{jets}$, with $10 \text{ GeV} < m_{\ell\ell} < 50 \text{ GeV}$	MadGraph	18610	-	[140]

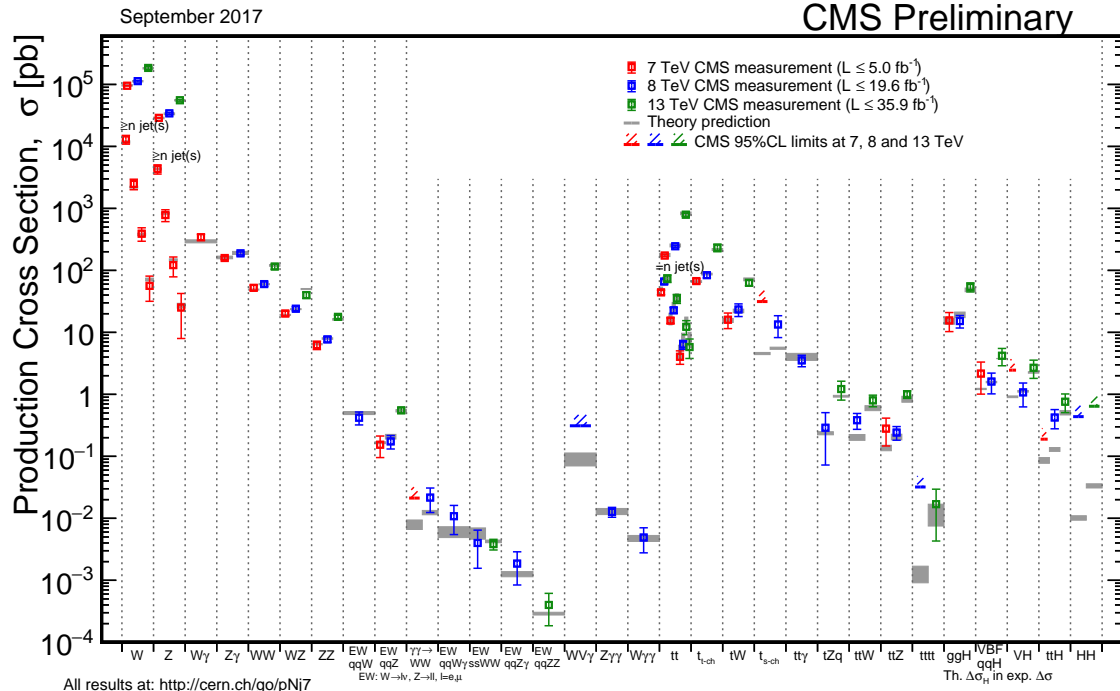


Figure 3.4: Summary of the SM cross section measurements performed by the CMS collaboration. Figure taken from [23].

874 3.3 Multivariate analysis techniques: Boosted Decision Trees

875 The need for processing large quantities of data and discriminating between events with largely
 876 similar experimental signatures makes multivariate analysis (MVA) a largely used method in the
 877 physics community. Multivariate classification methods based on machine learning techniques
 878 are a fundamental ingredient to most analyses. The advantage of using a MVA classifier is
 879 that it can achieve a better discrimination power with respect to a simpler analysis based on
 880 individual selection criteria or poorly discriminating variables. A risk of using MVA classifiers
 881 is overtraining. This happens when there are too many model parameters of an algorithm
 882 adjusted to too few data points. This leads to an increase in the classification performance over
 883 the objectively achievable one.

884 There are many software tools that exist for MVA. In this thesis, the Tool for Multivariate
 885 Analysis (TMVA) [142] is used. This software is an open source project included into
 886 ROOT [143]. By training on events for which the classification is known, a mapping function
 887 is determined that describes a classification or an approximation of the underlying behaviour
 888 defining the target value (regression). Boosted decision trees (BDT) are employed for the clas-
 889 sification of events as implemented in the TMVA framework [142]. This multivariate technique
 890 is based on a set of decision trees where each tree yields a binary output depending on the fact
 891 that an event is signal- or background-like. This has as advantage that several discriminating
 892 variables can be combined into a powerful one-dimensional discriminant D.

893 The decision tree is constructed by training on a dataset for which the outcome is already

provided, such as simulation datasets with signal and background processes (supervised learning). Different trees can be combined into a forest where the final output is determined by the majority vote of all trees, so-called boosting. This stabilises the decision trees against statistical fluctuations and makes it possible to keep the decision trees very shallow, making the method more robust against overtraining. Examples of such boosting algorithms are Adaptive Boosting (AdaBoost) and Gradient Boosting [144]. For the search presented in the following chapters, Gradient boost is used with a learning rate of 0.2-0.3 and the depth of the tree is set to three. Additionally, the Gradient boost is used in combination with bagging, so-called stochastic gradient boosting. Bagging smears the statistical fluctuations in the training data and therefore stabilises the response of the classifier and increases the performance by eliminating overtraining. More information about stochastic gradient boosting can be found in Ref. [145].

The discriminating power of a BDT is assessed by analysing the receiver operating characteristic (ROC) curve. This curve represents the background rejection over the signal efficiency of the remaining sample. The area under the curve (AUC) is compared to random guessing in order to identify the best classifier. When the multivariate discriminator has no discriminating power, the resulting AUC will be 0%, while 50% means fully separated event classes. In Figure 3.5 examples of ROC curves are shown.

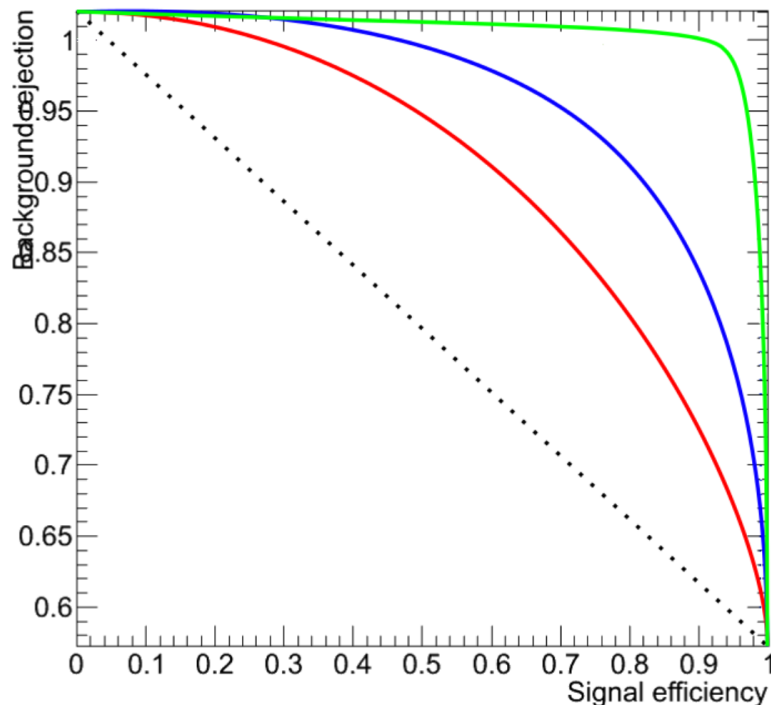


Figure 3.5: Example of ROC curves. In this example, the green method is better than the blue one, which is better than the red one. The dashed line represents a case where there is no separation. Figure taken from [146].

911 3.4 Statistical methodology

912 The search performed in the framework of this thesis requires the simultaneous analysis of data
 913 from different decay channels. The statistical methodology used for this search is developed by
 914 the ATLAS and CMS collaborations in the context of the LHC Higgs Combination group [147–
 915 150]. The Higgs Combined Tool [151] is a RooStats [152] framework which runs different
 916 statistical methods. In this section, only the statistical tools necessary for the performed search
 917 are described [153].

918 The event yields of signal and background processes are denoted as s and b respectively.
 919 These represent event counts in multiple bins or unbinned probability density functions. By
 920 use of simulation, predictions on both signal and background yields are made. The multiple
 921 uncertainties on these predictions are accounted for by introducing nuisance parameters θ such
 922 that $s = s(\theta)$ and $b = b(\theta)$.

923 The Bayesian and modified classical frequentist statistical approaches are used in high energy
 924 physics to characterise the absence of a signal. The level of incompatibility of data with a signal
 925 hypothesis is quantified in terms of confidence levels (CL). The convention is to require a 95%
 926 CL for excluding a signal. In general, limits are not set on the signal cross section directly, but
 927 are set on the signal strength modifier μ . The signal strength modifier is defined such that it
 928 equally changes all the cross sections of all production mechanisms of the signal by the same
 929 scale.

In this thesis, the modified frequentist approach [154, 155] for confidence levels that adopts the classical frequentist method to allow nuisance parameters, is used. It constructs a likelihood $\mathcal{L}(\text{data}|\mu, \theta)$ is as

$$\mathcal{L}(\text{data}|\mu, \theta) = \text{Poisson}(\text{data}|\mu s(\theta) + b(\theta)) \text{pdf}(\tilde{\theta}|\theta). \quad (3.6)$$

930 The probability density function $\text{pdf}(\tilde{\theta}|\theta)$ describes all sources of uncertainty. In this thesis, all
 931 sources of uncertainties are assumed to be either 100% correlated or uncorrelated. Partially
 932 correlated uncertainties are broken down to subcomponents that fit those requirements, allowing
 933 to include all constraints in the likelihoods in a clean factorised form.

A systematic uncertainty pdf $\rho(\theta|\tilde{\theta})$ for the nuisance θ with nominal value $\tilde{\theta}$ is used. It reflects the degree of belief of what the true value of the θ is. In this thesis, the approach from the Higgs Combined Tool is used where the pdfs $\rho(\theta|\tilde{\theta})$ are re-interpreted as posteriors of real or imaginary measurements $\tilde{\theta}$

$$\rho(\theta|\tilde{\theta}) \sim \text{pdf}(\tilde{\theta}|\theta) \pi_\theta(\theta), \quad (3.7)$$

934 where $\pi_\theta(\theta)$ is the hyper prior for the (imaginary) measurements. The pdfs used by the Higgs
 935 Combine Tool are described in Ref. [150].

The data in Equation 3.6 represents either the actual observation or pseudo-data to construct sampling distributions. For a binned likelihood, the Poisson probabilities to observe n_i events in bin i is given as

$$\text{Poisson}(\text{data}|\mu s(\theta) + b(\theta)) = \prod_i \frac{(\mu s_i(\theta) + b_i(\theta))^{n_i}}{n_i!} e^{-\mu s_i(\theta) - b_i(\theta)}. \quad (3.8)$$

At the LHC, the test statistic is defined as

$$q_\mu = -2 \ln \frac{\mathcal{L}(\text{data} | \mu, \hat{\theta}_\mu)}{\mathcal{L}(\text{data} | \hat{\mu}, \hat{\theta}_\mu)}, \quad (3.9)$$

where the likelihood is maximised in the numerator (maximum likelihood estimator, MLE) for a given μ and (pseudo) data at $\hat{\theta}_\mu$, while $\hat{\mu}$ combined with $\hat{\theta}$ defines the point for which the likelihood reaches its global maximum. The estimated signal strength modifier $\hat{\mu}$ can not become negative since a signal rate is positive defined by physics. Furthermore, an upper constraint on the MLE $\hat{\mu} \leq \mu$ is imposed.

The signal is excluded at $1 - \alpha$ confidence level when

$$\text{CLs} = \frac{P(q_\mu \geq q_\mu^{\text{obs}} | \mu s + b)}{P(q_\mu \geq q_\mu^{\text{obs}} | b)} \leq \alpha, \quad (3.10)$$

with $P(q_\mu \geq q_\mu^{\text{obs}} | \mu s + b)$ the probability to observe a value of the test statistic at least as large as the one observed in data q_μ^{obs} , under the signal plus background ($s + b$) hypothesis, and $P(q_\mu \geq q_\mu^{\text{obs}} | b)$ for the background only (b) hypothesis. These probabilities are defined as

$$p_\mu = P(q_\mu \geq q_\mu^{\text{obs}} | \mu s + b) = \int_{q_\mu^{\text{obs}}}^{\infty} f(q_\mu | \mu, \hat{\theta}_\mu^{\text{obs}}) dq_\mu, \\ 1 - p_b = P(q_\mu \geq q_\mu^{\text{obs}} | b) = \int_{q_{\mu=0}^{\text{obs}}}^{\infty} f(q_\mu | \mu = 0, \hat{\theta}_{\mu=0}^{\text{obs}}) dq_\mu, \quad (3.11)$$

where p_μ and p_b are the p-values associated to the two hypothesis, and $f(q_\mu | \mu, \hat{\theta}_\mu^{\text{obs}})$ and $f(q_\mu | \mu = 0, \hat{\theta}_{\mu=0}^{\text{obs}})$ are the probability density functions of the signal plus background and background only hypothesis constructed from toy Monte Carlo pseudo data. These are generated with nuisance parameters fixed to $\hat{\theta}_{\mu=0}^{\text{obs}}$ (background only) and $\hat{\theta}_\mu^{\text{obs}}$ (signal plus background). The 95% CL level upper limit on μ is achieved by adjusting μ until $\text{CL} = 0.05$, this is the so-called observe limit. The expected median upper limit and the $\pm 1\sigma$ and $\pm 2\sigma$ bands for a hypothesis is generated by a large set of pseudo data and calculate the CLs and the value of μ at 95% CL for each of them. A cumulative probability distribution can be build by starting the integration from the side corresponding to low event yields. The median expected value, so-called expected limit at 95% CL, is where the cumulative distribution function crosses the 50% quantile. The $\pm 1\sigma$ (68%) and $\pm 2\sigma$ (95%) bands on the expected limit are defined by the crossings of the 16% and 84%, and 2.5% and 97.5% quantiles.

In order to significantly reduce computing time, the Asymptotic CL method is used. This method avoids an ensemble of toy Monte Carlo samples and instead replaces it by one representative dataset, called Asimov dataset. This dataset is constructed such that all observed quantities are set equal to their MLE values ($\hat{\theta}_{\text{Asimov}} = \theta_0$). More information about this procedure can be found in Refs. [148].

Event reconstruction and identification

4

959 The simulated data after the detector simulation described in [Section 3.2](#), has the exact same
960 format as the real collision data recorded at the CMS experiment. Therefore the same software
961 can be used for the reconstruction of both simulation and real data. In [Section 4.1](#), the object
962 reconstruction is explained. After reconstructing the objects, they are connected to physics
963 objects, which need to be identified ([Section 4.2](#)) and corrected for pileup ([Section 4.3](#)). The
964 objects used for physics analysis have extra requirements as shown in [Section 4.4](#). A summary
965 of all the corrections applied to data and simulation is given in [Section 4.5](#).

966 4.1 Object Reconstruction

967 In [Figure 4.1](#), the particle interaction in a transverse slice of the CMS detector is shown. When
968 a particle enters the detector, it first enters the tracker where charged particle trajectories,
969 so-called tracks, and origins, so-called vertices, are reconstructed from signals or hits in the
970 sensitive layers. The magnetic field bends the charged particles making it able to measure the
971 electric charges and momenta of charged particles. The electrons and photons are absorbed in
972 the ECAL and the corresponding electromagnetic showers are detected as clusters of energy
973 in adjacent cells. From this, the energy and the direction of the particles can be determined.
974 The charged and neutral hadrons can also initiate a hadronic shower in the ECAL that is fully
975 absorbed in the HCAL. The clusters from these showers are also used to estimate the energy
976 and direction. Muons and neutrinos pass through the calorimeters without little to no energy
977 loss and the neutrinos even escape the CMS detector undetected while muons produce hits in
978 the muon detectors.

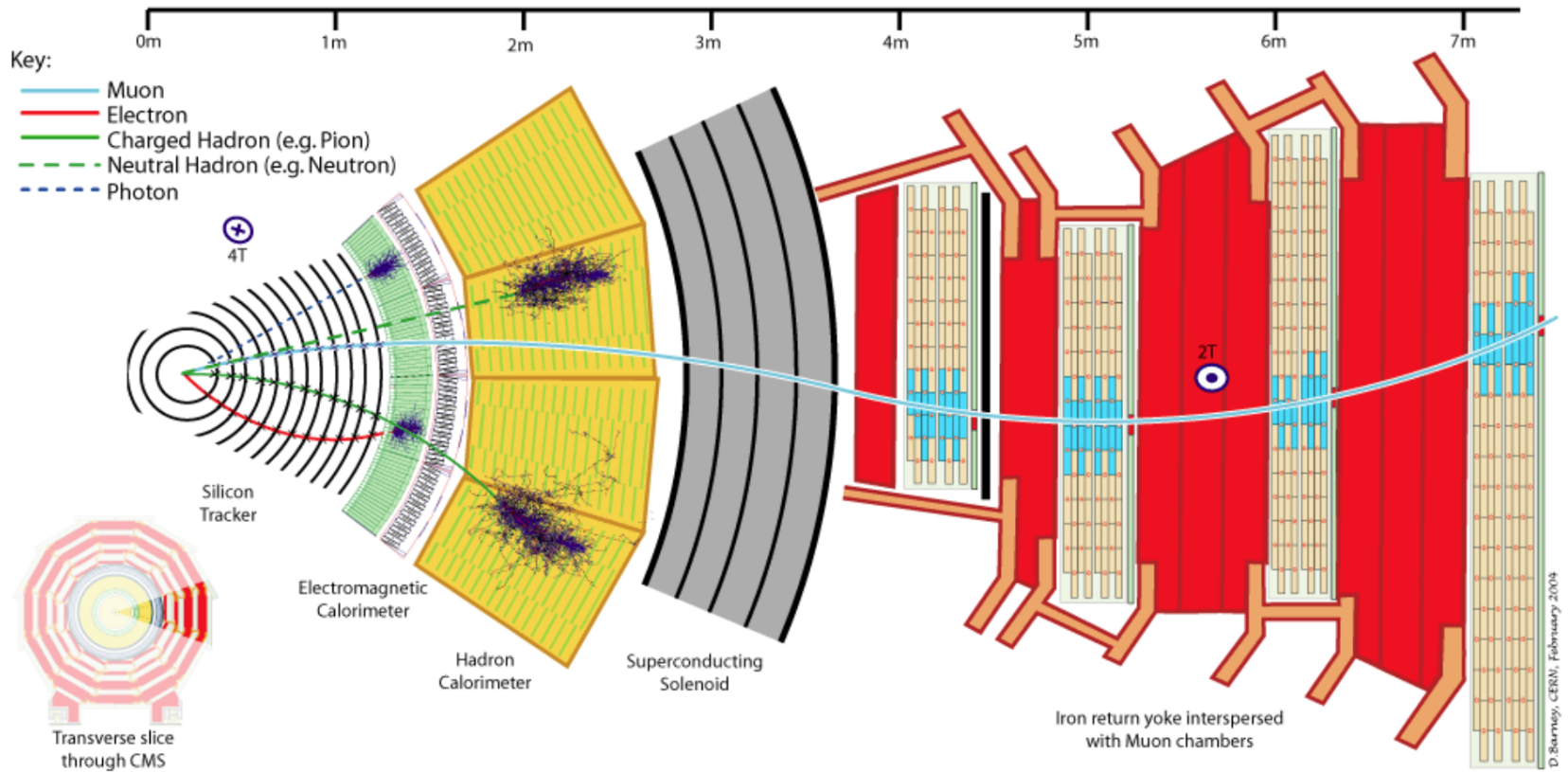


Figure 4.1: Cross-section of the CMS detector with all parts of the detector labelled. This sketch shows the specific particle interactions from a beam interaction region to the muon detector. The muon and charged pion are positively charged, the electron is negatively charged. Figure taken from [156].

979 The particle flow (PF) [156] reconstruction algorithm correlates the tracks and clusters
 980 from all detector layers with the identification of each final state particle, and combines the
 981 corresponding measurements to reconstruct the properties. The muon is identified by a track
 982 in the inner tracker, connected to a track in the muon detector as described in Section 4.1.2.
 983 The electrons are identified by a track and an ECAL cluster, not connected to an HCAL cluster
 984 as described in Section 4.1.3. The ECAL and HCAL clusters without a track link identify the
 985 photons and neutral hadrons, while the addition of the tracker determines the energy and
 986 direction of a charged hadron.

987 4.1.1 Charged particle tracks

988 An iterative tracking algorithm is responsible for the reconstruction of the tracks made by
 989 charged particles in the inner tracking system. Each iteration consists of four steps [72]: the
 990 track-seed generation, the pattern recognition algorithm, removal of track-hit ambiguities and
 991 a final track fit. The pattern recognitions done by use the Kalman filter method [157, 158]
 992 which takes into account the magnetic field and multiple scattering effects. All hits that are
 993 unambiguously associated to the final track are removed from the list of available hits. In order to
 994 associate the remaining hits, the procedure is repeated with looser track reconstruction criteria.
 995 The use of the iterative track reconstruction procedure has a high track finding efficiency, where
 996 the fake track reconstruction rate is negligible.

NOTE: Ik kan hier stoppen en 4.1.1, 4.1.2, 4.1.3.4.1.4 volledig schrappen (dus enkel primary vertex houden)

997 4.1.2 Following the Muon's Footsteps

998 The muon reconstruction [159] has three subdivisions: local reconstruction, regional reconstruc-
 999 tion and global reconstruction. The local reconstruction is performed on individual detector
 1000 elements such as strip and pixel hits in the inner tracking system, and muon hits and/or segments
 1001 in the muon chambers. Independent tracks are reconstructed in the inner tracker - called tracker
 1002 tracks - and in the muon system, called standalone muon tracks. Based on these tracks, two
 1003 reconstructions are considered: Global Muon reconstruction and Tracker Muon reconstruction.
 1004 The first is an outside-in approach starting from a standalone muon track while the second uses
 1005 an inside-out approach starting from tracker tracks. For low transverse momenta ($p_T \lesssim 5$ GeV),
 1006 the tracker muon reconstruction is more efficient than the global muon approach. This is due
 1007 to the fact that tracker muons only require a single muon segment in muon system, while the
 1008 global muon approach requires typically segments in at least two muon stations. These tracker
 1009 muons are used for identifying muons from the hadronisation of b or c quarks. The global muon
 1010 approach typically improves the tracker reconstruction for $p_T \gtrsim 200$ GeV.

1011 4.1.3 The path of the Electron

1012 Standard tracking algorithms are based on Kalman filtering which assume that the energy loss
 1013 is Gaussian distributed. Since the electron tracks are increasingly curved in the magnetic field
 1014 as a function of its flight distance, these standard tracking algorithms are not suitable to fit the
 1015 electron tracks and different filtering algorithm. The Gaussian sum filter (GSF) [160] is used
 1016 instead.

1017 In CMS, the electrons are reconstructed in two ways. The older ECAL based tracking is
 1018 developed to identify high energetic isolated electrons. This tracking algorithm starts from

1019 ECAL clusters with a transverse energy above 4 GeV and extrapolates from these cluster the
 1020 position of the hits in the tracker. Another, tracker based algorithm uses all the tracks with
 1021 a p_T higher than 2 GeV found with iterative tracking as seeds. The electron seeds from the
 1022 ECAL- and tracker-based procedures are merged into a unique collection and are then refitted
 1023 by using the summed Gaussian distributions as uncertainty per hit in the track fit. The electron
 1024 efficiency is measured in 8 TeV proton collision data to be better than 93% for electrons with an
 1025 ECAL supercluster energy of $E_T > 20$ GeV [161]. For electrons with an $E_T > 25$ GeV in 13 TeV
 1026 proton collision data, the efficiency is about 96%[162].

1027 4.1.4 Primary Vertex Reconstruction

1028 The primary vertex (PV) reconstruction is able to measure the location of all proton interaction
 1029 vertices in each event consisting of the signal vertex and all vertices from pileup events. First,
 1030 tracks are selected to be consistent with being produced promptly in the primary interaction [82].
 1031 Then the tracks are grouped according to the z coordinate of their closest approach to the beam
 1032 line [163] and a vertex fitting algorithm [164] is performed. The primary vertex is found as the
 1033 vertex corresponding to the highest sum of squared track transverse momenta and is taken to
 1034 be the main interaction point. The resolution on the primary vertex is about 14 μm in $r\phi$ and
 1035 about 19 μm in the z direction for primary vertices with the sum of the track $p_T > 100$ GeV
 1036 for 2016 data taking.

1037 4.1.5 Calorimeter clusters

1038 The energy and direction of stable neutral particles such as photons and neutral hadron are recon-
 1039 structed using a cluster algorithm. This algorithm also separates neutral particles from charged
 1040 hadron energy deposits, and reconstructs and identifies electrons and their bremsstrahlung
 1041 photons. Furthermore, the cluster algorithm is contributing to the energy measurements of
 1042 charged hadrons that don't have accurate tracks parameters, e.g. for low quality and high
 1043 transverse momentum tracks. The clustering is performed separately in each subdetector:
 1044 ECAL barrel and endcaps, HCAL barrel and endcaps, and the two preshower layers. The HF has
 1045 no clustering algorithm since the electromagnetic or hadronic components give rise to an HF
 1046 EM or HF HAD cluster.

1047 The clustering algorithm consist of different steps. First seeds are identified when cells have
 1048 an energy larger than the seeding threshold and larger than their neighbouring cells. Then
 1049 topological clusters are made by accumulating cells that share at least a corner with a cell
 1050 already in the cluster and an energy above a cell threshold set to twice the noise level. The
 1051 third step is an expectation maximization algorithm that reconstructs the cluster [156] and
 1052 assumes that the energy deposits are Gaussian distributed. The calorimeter clusters are used
 1053 for reconstructing photons and neutral hadrons. The clusters that are not in the vicinity of the
 1054 extrapolated charged tracks are identified as neutral hadrons or photons. If the energy deposits
 1055 are in vicinity of charged tracks, such is the case for charged hadrons, the neutral particle energy
 1056 deposit is measured as an excess over the charged particle deposit.

1057 4.2 Particle flow identification

1058 The several PF elements from the various CMS subdetectors are connected through a link
 1059 algorithm. This algorithm tests any pair of elements in an event, only considering nearest
 1060 neighbours in the $\eta\phi$ -plane. The quality of the link is determined via the distance between the
 1061 two elements and PF blocks of elements are formed from elements with a direct link or indirect
 1062 link through common elements. The identification and reconstruction follows a particular order
 1063 in each PF block. After each identification and reconstruction the corresponding PF elements
 1064 (tracks and clusters) are removed from the PF block.

1065 The muons are the first to be identified and reconstructed. These are reconstructed if their
 1066 momenta are compatible with corresponding track only momenta. Then the electron and its
 1067 corresponding brehmstrahung photons, are identified and reconstructed by using of the GSF
 1068 tracking. At the same time, the energetic and isolated photons are identified as well. The
 1069 remaining elements in the PF block are subjected to a cross identification of charged hadrons,
 1070 neutral hadrons, and photons that arise from parton fragmentation, hadronisation, and decays
 1071 in jets. The charged hadron candidate is made from the remaining candidates that have a
 1072 charged particle track associated with them. Then the charged particle energy fraction is
 1073 subtracted from the calibrated energy of the linked calorimeter clusters and the remaining
 1074 energy is assigned to the neutral energy. Depending on the excess of neutral energy in the ECAL
 1075 and HCAL clusters, a photon or a neutral hadron is assigned respectively. The pseudorapidity
 1076 range of the inner tracker limits the information on the particles charge to $|\eta| < 2.4$. Outside
 1077 this range a simplified identification is done for hadronic and electromagnetic candidates only.

1078 4.3 Pileup mitigation and luminosity measurement

For the 8 TeV dataset, an average of about 21 pileup interactions happen per bunch cross section. For the dataset taken at 13 TeV, the number of pileup interactions increases to about 27 interactions per bunch crossing. These interactions are spread around the beam axis around the centre of the CMS coordinate system and follow a normal distribution with a standard deviation of about 5 cm [156]. The number of pileup interactions is estimated from the number of interaction vertices reconstructed from charged particle tracks, or from the instantaneous luminosity of the given bunch crossing with dedicated detectors and the inelastic proton-proton crossing. The luminosity of the CMS interaction point is estimated from measuring certain process rates with luminometers such as the pixel detector, HF calorimeter, and the pixel luminosity telescope [165]. The instantaneous luminosity from recorded process rate R is then determined as

$$1079 \quad Ldt = \frac{Rdt}{\sigma_{fid}}, \quad (4.1)$$

1079 where $\sigma_{fid} = \sigma \times A$ corresponds to the fiducial cross section recorded in the luminometer
 1080 acceptance A which is determined using van der Meer scans [166]. The overall uncertainty on
 1081 the luminosity measurement is estimated to be 2.5%.

1082 The luminosity is used to infer the number of pileup interactions in data, which can be used
 1083 to correct the predefined pileup interactions in simulation. Then an event weight can be derived

1084 from the ratio of the distributions of pileup interactions in data and simulation. For 13 TeV
 1085 collisions, the inelastic cross section is measured to be 71.3 ± 3.5 mb [167]. However a better
 1086 agreement in data and simulation for the pileup sensitive variables, such as the number of
 1087 primary vertices, is found with a lower cross section of 69.2 mb with an uncertainty of 4.6%.

1088 4.4 Physics object reconstruction and identification

1089 The particle flow objects are used for building physics objects that are used for analysis. Analyses
 1090 use jets, muons, electrons, photons, taus and missing transverse momentum \vec{p}_T with extra,
 1091 analysis dependent requirements. In the following section, only the physics objects used
 1092 throughout this thesis are discussed.

1093 4.4.1 Muons

1094 The muon candidates used for analysis in this thesis correspond to the tight and loose working
 1095 point. Detailed reports on the performance can be found in [168].

1096 The tight working point rejects objects wrongly reconstructed as muons from hadron showers
 1097 that reach the muon system (punch-throughs), by requiring that the global muon fit includes
 1098 at least one valid hit in the muon chambers for which at least two muon segments in two
 1099 muon stations are present. Furthermore, the muon tracks should have a global fit yielding a
 1100 goodness-of-fit of $\chi^2/\text{ndof} < 10$. Requiring at least one pixel hit in the muon track suppresses
 1101 the decay of muons in flight. Also a minimum of five hits in the tracker is required. Cosmic
 1102 muons and muons originating from pileup interactions are rejected by constricting the distance
 1103 of the muon with respect to the primary vertex by putting limits on $d_{x,y} < 2$ mm and $d_z < 5$
 1104 mm. Also muons according to the loose muon working point will be used in the thesis. These
 1105 are either global muons or tracker muons reconstructed from the particle flow muon object. In
 1106 Table 4.1, the muon requirements for the muons used throughout this thesis are summarised.
 1107 In Figure 4.2, the muon efficiencies for data and simulation are presented. These efficiencies
 1108 are estimated from tag-and-probe methods [168]. Overall, the efficiency is about 95-100%,
 1109 with two drops due to the crack between the wheels of the DT system. The differences between
 1110 data and simulation are corrected by applying p_T - and η -dependent scale factors ($\epsilon_{\text{data}}/\epsilon_{\text{MC}}$)
 1111 to simulated events.

In addition to the identification criteria, the muons are required to be spatially isolated from electromagnetic and hadronic activity. The relative lepton isolation is defined as estimating the total transverse energy of the particles emitted around the direction of the lepton by defining a cone of radius ΔR in $\eta\phi$ plane around the lepton direction. Then a summed energy is calculated from the charged hadrons (CH), neutral hadrons (NH), and photons (γ), excluding the lepton itself. This sum is then corrected to remove the energy coming from pileup interactions. The relative isolation for muons \mathcal{I}_{μ} is defined as [156]:

$$\mathcal{I}_{\mu} = \frac{\sum p_T(\text{CH}) + \max(0., \sum E_T(\text{NH}), \sum E_T(\gamma) - 0.5 \times \sum E_T(\text{CH}))}{p_T(\mu)}, \quad (4.2)$$

1112 where a cone of $\Delta R = 0.4$ is adopted and the pileup mitigation is based on the $\Delta\beta$ correction.
 1113 The $\Delta\beta$ correction estimates the pileup energy as half of the contribution coming from charged

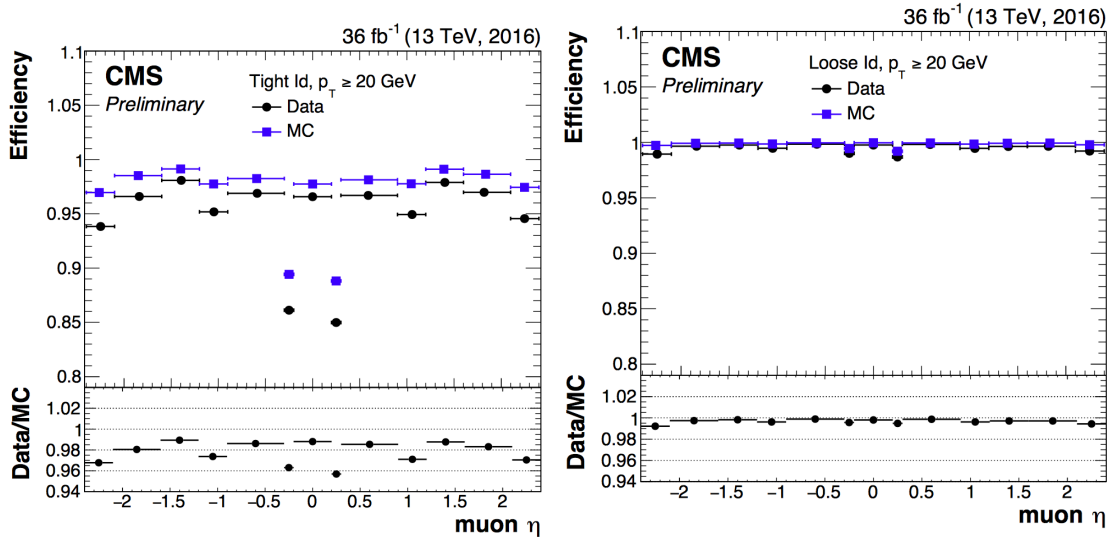


Figure 4.2: Comparison of the muon tight ID (left) and loose ID (right) efficiencies in data and simulation as a function of the pseudorapidity of the muon using the full 2016 dataset. Figure taken from [168].

hadrons. For tight ID muons, this relative isolation should $\mathcal{I}_\mu < 0.15$, while for loose muons this should be $\mathcal{I}_\mu < 0.25$. In Figure 4.3, the isolation efficiencies as a function of the pseudo rapidities using the tag and probe method are shown for the tight muon working point. The efficiencies are 85-100% and have a decline for low- p_T muons. The differences between data and simulation are accounted for by applying η - and p_T -dependent scale factors on the simulation.

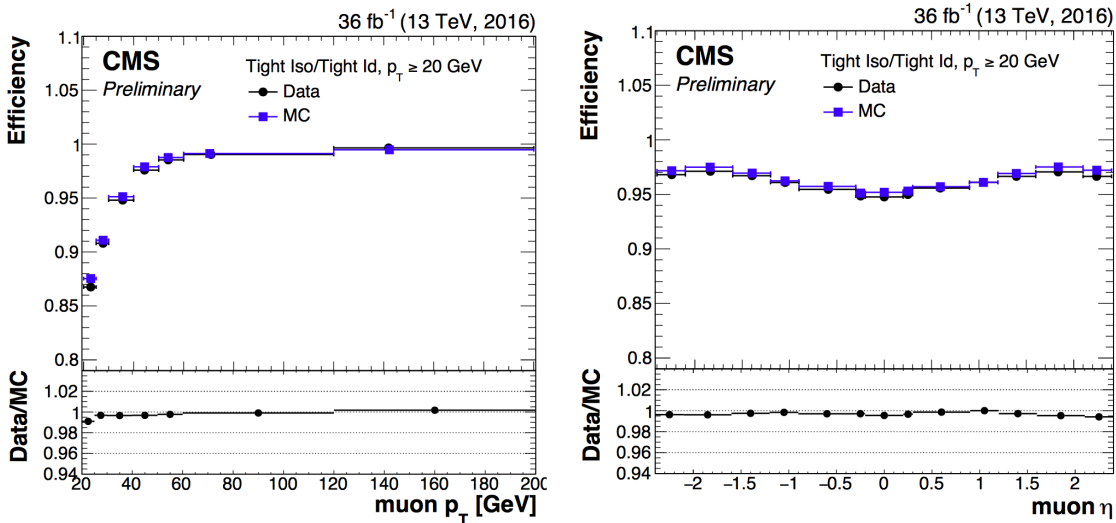


Figure 4.3: Comparison of the muon tight isolation requirement with the muon tight ID efficiencies in data and simulation as a function of the transverse momentum (left) or pseudorapidity (right) of the muon using the full 2016 dataset. Figure taken from [168].

Table 4.1: Muon requirements for the tight and loose working points, used throughout this thesis.

Properties	Loose Muons	Tight Muons
Global muon or Tracker Muon	One or the other	Both
Particle Flow muon	Y	Y
χ^2/ndof of global muon track fit	N/A	< 10
Nb. of hit muon chambers	N/A	> 0
Nb. of muon stations contained in the segment	N/A	> 1
Size of the transverse impact parameter of the track wrt. the PV	N/A	$d_{xy} < 2 \text{ mm}$
Longitudinal distance wrt. the PV	N/A	$d_z < 5 \text{ mm}$
Nb. of pixel hits	N/A	> 0
Nb. of tracker layers with hits	N/A	> 5
Relative Isolation	<0.25	<0.15

1120 4.4.2 Electrons

1121 The electron candidates used, correspond to the tight and veto working points. The study of
 1122 the electron reconstruction and identification performance can be found in [162].

1123 Starting from an electron PF candidate with a GSF track that is outside the barrel-endcap
 1124 transition region ($1.4443 < |\eta| < 1.5660$), several requirements are set. The electron track
 1125 should not have more than one (two or three) missing hit(s) in the innermost layer for the tight
 1126 (veto) working point. This dismisses electrons from photon conversions. Additionally, a photon
 1127 conversion veto is applied by testing if a pair of electron tracks is originating from a common
 1128 displaced vertex. Furthermore, refined cuts are applied on the shower shape variables such as
 1129 the difference in η or ϕ between the energy weighted supercluster position in the ECAL and
 1130 the track direction at the innermost tracker position ($\Delta\eta_{\text{in}}$, $\Delta\phi_{\text{in}}$), and the ECAL crystal based
 1131 shower covariance in the η direction ($\sigma_{\eta\eta}$). These cuts also include energy related variables
 1132 such as the absolute difference between the inverse electron energy measured in the ECAL
 1133 and the inverse momentum measured in the tracker ($|1/E - 1/p|$), and the ratio of the energy
 1134 measured in the HCAL and ECAL (H/E). Unlike the muon case, the identification criteria also
 1135 contain requirements on the isolation of the electrons.

Similar to the muons, the electron relative isolation is determined from the sum of the particles in a cone around the electron itself. The cone radius used for electrons is $\Delta R = 0.3$ and a ρ correction for pileup mitigation is applied. For this correction, the expected pileup energy inside the isolation cone is estimated from the median density energy per area of pileup contamination (ρ), computed event by event, and the effective area ($A_{\text{eff.}}$) [156]. This effective area is estimated from simulation and denotes the expected amount of neutral energy from

pileup interactions per ρ within the isolation cone as a function of the pseudo rapidity of the associated ECAL superclusters. Table 4.2 shows the values used for 13 TeV data. The relative electron isolation \mathcal{I}_e is calculated as

$$\mathcal{I}_e = \frac{\sum p_T(\text{CH}) + \max(0., \sum E_T(\text{NH}), \sum E_T(\gamma) - \rho \times A_{\text{eff}})}{p_T(e)}. \quad (4.3)$$

Table 4.2: The effective areas A_{eff} used for the electron relative isolation [169].

η region	A_{eff}
$0 < \eta < 0.1752$	0.1703
$1.0 < \eta < 0.1479$	0.1715
$1.479 < \eta < 2.0$	0.1213
$2.0 < \eta < 2.2$	0.1230
$2.2 < \eta < 2.3$	0.1635
$2.3 < \eta < 2.4$	0.1937
$2.4 < \eta < 2.5$	0.2393

1136

1137 The efficiency of electron identification is estimated from $Z \rightarrow e^- e^+$ events via the tag-and-
 1138 probe method and is shown in Figure 4.4 for the tight working point. The efficiencies reach
 1139 95 – 100%. The difference between data and simulation is corrected for by dedicated p_T - and
 1140 η dependent scale factors as well.

1141 **4.4.3 Jets**

1142 Jets are reconstructed from all reconstructed particles without the charged hadrons associated to
 1143 pileup vertices. The clustering is done via the anti – k_T algorithm [170] with a radius parameter
 1144 for the cone size of the resulting jet of $R = 0.4$. More information about the jet algorithm
 1145 performance can be found in Ref. [171].

1146 The jets used for the analysis in this thesis, use the loose identification working point sum-
 1147 marised in Table 4.4. The requirements on the jet constituents are based on the assumption
 1148 that a proper jet originating from the hadronisation of a quark or gluon consists of multiple PF
 1149 particles and types. Therefore, the jet should consist of more than one constituent, and the
 1150 neutral hadron fraction and neutral EM energy fractions should be less than 99%. For the jets
 1151 within the tracker acceptance ($|\eta| < 2.4$), at least one constituent has to be a charged hadron
 1152 resulting in a charged hadron energy fraction above 0%. Additionally the charged EM energy
 1153 fraction should be less than 99%. On top of these requirements, objects that are labelled as jets
 1154 and found in vicinity of any isolated lepton, $\Delta R < 0.3$, are removed from the jet collection in
 1155 that event to avoid duplications of objects.

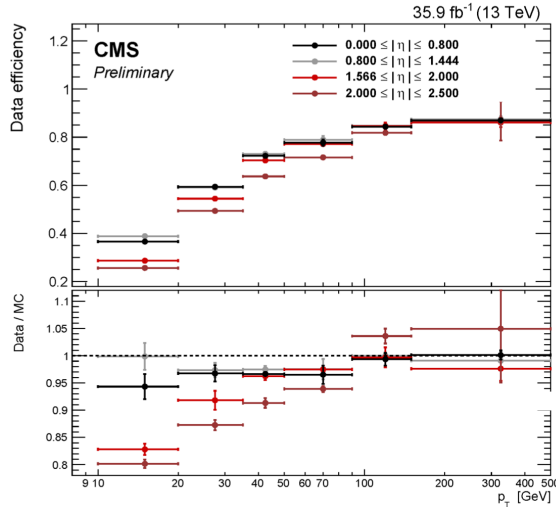


Figure 4.4: Electron identification efficiency as function of the electron transverse momentum from the full 2016 dataset. Figure taken from [162].

Table 4.3: Electron requirements used in this analysis. The requirements are set in the barrel ($|\eta_{supercluster}| \leq 1.479$) and the endcaps ($|\eta_{supercluster}| > 1.479$).

Properties	$ \eta_{supercluster} \leq 1.479$		$ \eta_{supercluster} > 1.479$	
	Veto electron	Tight electron	Veto electron	Tight electron
$\sigma_{\eta\eta}$	< 0.0115	< 0.00998	< 0.037	< 0.0292
$ \Delta\eta_{in} $	< 0.00749	< 0.00308	< 0.00895	< 0.00605
$ \Delta\phi_{in} $	< 0.228	< 0.0816	< 0.213	< 0.0394
H/E	< 0.356	< 0.0414	< 0.211	< 0.0641
relative isolation	< 0.175	< 0.0588	< 0.159	< 0.0571
$ 1/E - 1/p $	$< 0.299 \text{ GeV}^{-1}$	$< 0.0129 \text{ GeV}^{-1}$	$< 0.15 \text{ GeV}^{-1}$	$< 0.0129 \text{ GeV}^{-1}$
expected missing inner hits	≤ 2	≤ 1	≤ 3	≤ 1
pass conversion veto	Y	Y	Y	Y

Table 4.4: Jet criteria used throughout the thesis. The last three requirements are only for jets within the tracker acceptance.

Properties	Loose Jet ID
Neutral hadron fraction	< 0.99
Neutral EM fraction	< 0.99
Number of constituents	> 1
Charged hadron fraction	> 0
Charged multiplicity	> 0
Charged EM fraction	< 0.99

1156 The energy of the reconstructed jets deviates from the energies of the corresponding jets
 1157 clustered from the hadronisation products of true partons from simulations due to non-linear
 1158 subdetector response and efficiencies. The jet energy corrections (JEC) calibrate the jets
 1159 in order to have the correct energy scale and resolution. Jet energy scale corrections (JES)
 1160 are determined as a function of pseudorapidity and the transverse momentum from data and
 1161 simulated events by combining several channels and methods. This is extensively described
 1162 in [172]. These corrections account for the effects of pileup, the uniformity of the detector
 1163 response, and residual data-simulation jet energy scale differences. Furthermore, the jet energy
 1164 resolution (JER) is measured in data and simulation as function of pileup, jet size and jet flavour.
 1165 The performance of the jet energy corrections for the 13 TeV dataset can be found in [173].

1166 The JEC are factorised and subsequently correct for the off-set energy due to pileup, the
 1167 detector response to hadrons, and residual differences between data and simulation as a function
 1168 of the jet pseudorapidity and transverse momentum. The consecutive steps of JEC are shown
 in Figure 4.5. The off-set corrections remove the dependency of the jet energy response of

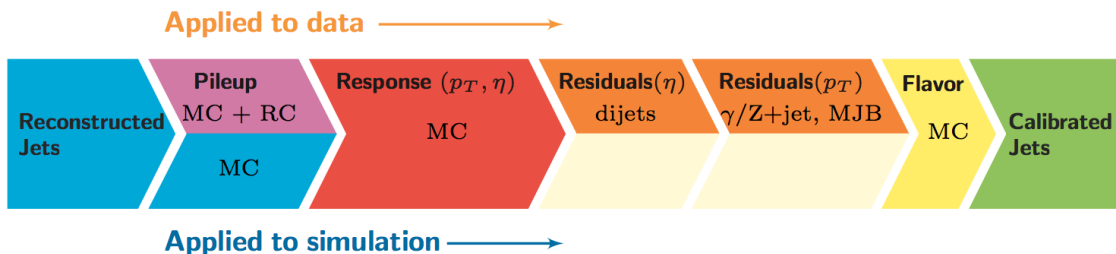


Figure 4.5: The sequence of the JEC for data and simulations. The corrections marked with MC are derived from simulation studies, while RC stands for random cone, and MJB for the analysis of multi-jet events. Figure taken from [172].

1169 additional pileup activity. It is based on the jet area method, which uses the effective area
 1170 of the jets multiplied by the average density in the event, to calculate the off-set energy to
 1171 be subtracted of the jets. The correction factors are derived by comparing the jet response

with and without pileup events overlaid. The residual differences between data and detector simulation are determined using the random cone method (RC). For this method, many jets are reconstructed in each event by clustering particles through placing random cones. This provides a mapping of the $\eta\phi$ -space and the average p_T of those jets gives the average energy off-set due to pileup [172]. The next level of corrections have as goal to have a uniform energy response independent of the transverse momentum or pseudorapidity of the jet. These corrections are determined from simulated events by matching the reconstructed to true particle jets and comparing there momenta. The residual corrections between data and simulation are determined by comparing the transverse momentum balance in various types of events (multi-jet, Z + jets, and γ + jets), using a reference jet in the barrel region. The jet flavour corrections are optional and not used for this thesis. More information on the jet flavour corrections can be found in [172]. For jets with a transverse momentum above 30 GeV, the uncertainties from the various corrections are 3-5% for the 13 TeV dataset [173].

After applying JEC, the transverse momentum resolution of the jet is extracted from data and simulated events. There are two methods used to rescale the reconstructed four momentum based on whether or not the simulated jet can be matched to a true jet in simulation. The factors are defined as

$$c_{\text{matched}} = 1 + \frac{p_T^{\text{reco.}} - p_T^{\text{true}}}{p_T^{\text{reco.}}} (s_{\text{JER}} - 1),$$

$$c_{\text{unmatched}} = 1 + N(0, \sigma_{\text{JER}}) \sqrt{\max(s_{\text{JER}}^2 - 1, 0)},$$
(4.4)

where $N(0, \sigma_{\text{JER}})$ denotes a sample value from a normal distribution centred at zero with standard deviation σ_{JER} , and s_{JER} the η -dependent resolution scale factors. These scale factors are derived from data from di-jet or γ + jets events and analysing the p_T balance. The resolution scale factors (data/simulation) are found to be 1.1-1.2, except for the transition regions around $|\eta| = 3$ and $|\eta| = 1.4$ [173] and given in Table 4.5.

4.4.4 Jets from b fragmentation

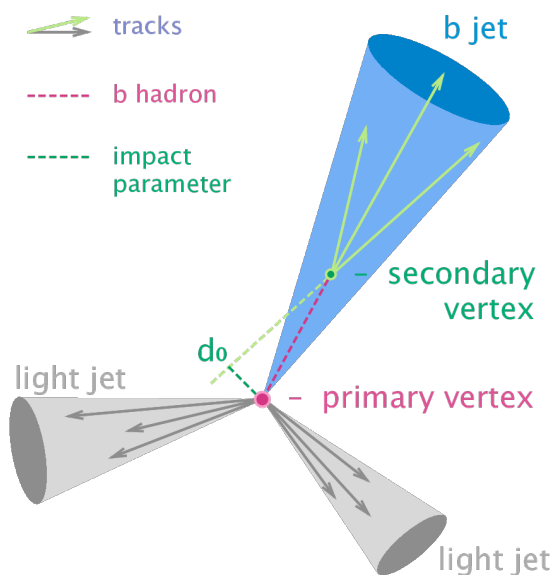
Jets originating from the hadronisation of bottom quarks can be discriminated from jets from gluons and light-flavour quarks as well as charm quark fragmentation through the use of b-tagging. There are several algorithms developed within CMS to perform b-tagging [174, 175] on jets that fall within the pseudorapidity acceptance of the trackers. These algorithms exploit the properties of the b quark to identify the jets formed by its fragmentation. These hadrons have relative large masses, long lifetimes and daughter particles with hard momentum spectra. Additionally, their semi-leptonic decays can be exploited as well. To use b-jet identification in an analysis, one needs to know its efficiency and misidentification probability. In general, these are function of the pseudorapidity and transverse momentum of the considered jet. Their performances are directly measured from data by use of b-jet enriched jet samples (multi-jet or top-quark decays).

This thesis uses b-jets identified by the Combined Secondary Vertex version 2 (CSVv2) algorithm [174]. This algorithm combines secondary vertices together with track based lifetime

Table 4.5: Jet energy scale factors in bins of η with uncertainty

$ \eta $	SF	Uncertainty (\pm)
0-0.5	1.109	0.008
0.5-0.8	1.138	0.013
0.8-1.1	1.114	0.013
1.1-1.3	1.123	0.024
1.3-1.7	1.084	0.011
1.7-1.9	1.082	0.035
1.9-2.1	1.140	0.047
2.1-2.3	1.067	0.053
2.3-2.5	1.177	0.041

information by use of a multivariate technique. The secondary vertex is reconstructed from displaced tracks within a jet, as illustrated in Figure 4.6. The final state b quark is encapsulated in a B meson (e.g. B^\pm , B_0 , B_S) after the hadronisation. This B meson has relatively long lifetime and can travel a measurable distance from the primary vertex before decaying. After reconstruction, the secondary vertices are required to be in accordance with the B meson hypothesis based on the amount of shared tracks with the primary vertex, the invariant vertex mass to reject kaon decays, and the direction of the tracks compared to the jet axis.

**Figure 4.6:** Sketch showing the common principle of the identification of b-jets. Figure taken from [176].

1213 The b-tagging algorithm performances are evaluated taking into account two cases: discrim-
 1214 ination of b-tagged jets originating from charm quarks, and discrimination of b-tagged jets
 1215 against jets coming from gluons or light (u, d, s) quarks. In [Figure 4.7](#), the misidentification
 1216 probabilities for different b-tagging algorithms within CMS are shown. Based on the misidentifi-
 1217 cation probabilities for a certain threshold on the CSVv2 discriminator, different working points
 1218 are defined. These are shown in [Table 4.6](#). The analysis presented in this thesis uses the loose
 1219 working point which has an average efficiency of 81% and a misidentification rate of 10%.

NOTE: Find reason why I am not using cMVA, omdat CSVv2 op ttbar events is gemaan en cMVA op multijet?

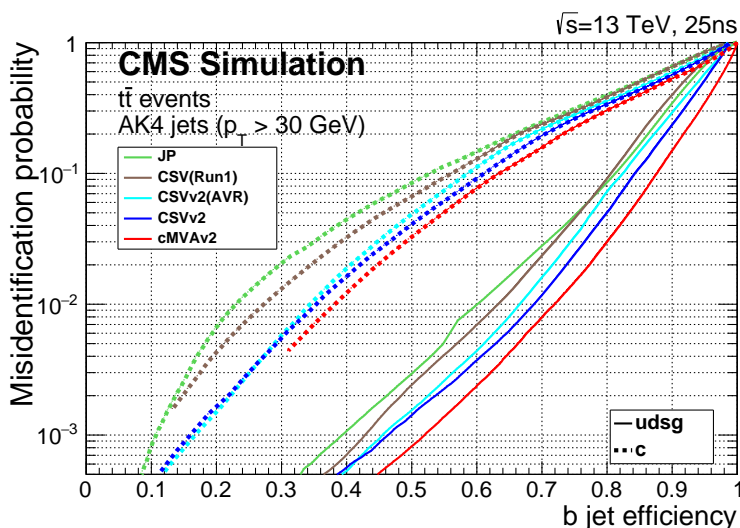


Figure 4.7: Misidentification probabilities of various b-tagging algorithms in simulation. Figure taken from [\[175\]](#).

Table 4.6: Working points used for tagging jets as coming from b quarks for the CSVv2 discriminant.

WP	CSVv2 discr cut	b-tag eff.	misid. prob.
Loose (L)	> 0.5426	≈ 81%	≈ 10%
Medium (M)	> 0.8484	≈ 66%	≈ 1%
Tight (T)	> 0.9535	≈ 46%	≈ 0.1%

1219

1220 The efficiency of tagging a jet as coming from a bottom quark in simulation typically deviates
 1221 somewhat from data. Efficiency scale factors $\epsilon_b^{\text{data}}/\epsilon_b^{\text{MC}}$ are derived from data to account for
 1222 those differences. These scale factors are η -, p_T -, and flavour dependent, where the flavour
 1223 of the jet is determined from matched generated hadrons. For cut based analyses these scale
 1224 factors are applied to the b-tagging efficiencies and mistag rates according to the chosen working
 1225 point [\[175\]](#). For shape based analysis however, such as the one presented in this thesis, the
 1226 scale factors are applied on the distribution of the b-tagging discriminator. This is the so-called
 1227 IterativeFit method [\[177\]](#).

1228 The uncertainties related to the IterativeFit method cover possible shape discrepancies between
 1229 data and simulation. The uncertainty coming from the purity of the sample is subdivided into
 1230 two uncorrelated uncertainties based on the purity of the light flavoured (lf) and heavy flavoured
 1231 (hf) jet contributions in the sample. Furthermore, the jet energy scale results in jets migrating
 1232 from one p_T bin to another, having an influence on bin dependent scale factors. The statistical
 1233 fluctuations of the limited amount of entries in each bin are also accounted for and have an
 1234 influence on the scale factor uncertainties. These have four uncorrelated sources: two for heavy
 1235 flavour and two for light flavour jets. Since the uncertainty on the scale factors for the jets
 1236 originating from a charm quark (cf) is determined from the uncertainty on the b scale factors
 1237 resulting in two independent uncertainties [177].

1238 4.4.5 Missing transverse energy

The missing transverse momentum \vec{p}_T and energy E_T^{miss} resulting from particles that do not interact with the detector material, are calculated by balancing the vectorial sum of the transverse momenta of all particles:

$$E_T = |\vec{p}_T|, \quad (4.5)$$

$$\vec{p}_T = - \sum_{i=1}^{N_{\text{particles}}} \vec{p}_{T,i}.$$

1239 The missing transverse energy is influenced by the minimum thresholds in calorimeters, the
 1240 inefficiencies in the tracker, and the non-linear response of the calorimeter to hadronic particles.
 1241 The bias is reduced by correcting the transverse momentum of the jets to particle jet p_T via the
 1242 JEC and propagating it to the missing transverse momentum. The performance of the missing
 1243 transverse energy reconstruction can be found in [178].

1244 4.5 Summary of corrections

1245 Throughout the chapter several corrections are introduced to improve the agreement between
 1246 data and simulation. These corrections are sources of systematic uncertainties for the anal-
 1247 ysis presented in this thesis. Therefore a summary of the corrections and their associated
 1248 uncertainties is provided.

1249 **Lepton scale factors** The systematic uncertainty on the lepton scale factors consists of three
 1250 sources: identification, isolation and tracking. The applied scale factors are varied
 1251 independently within one standard deviation of their measured uncertainties to account
 1252 for their systematic impact on the measurements.

1253 **Jet energy corrections** The momenta of the reconstructed jets are corrected to match the
 1254 expected true energy derived from the hadronisation products of partons in simulation.
 1255 Furthermore, residual corrections and smearing is applied to match the overall energy
 1256 scale and resolution for simulation and data. These corrections are also propagated to
 1257 the missing transverse energy. The systematic uncertainties due to these scale factors are
 1258 estimated by varying them within their uncertainties and repeating the measurements
 1259 with recalibrated jets and missing transverse energy.

1260 **CSVv2 discriminant shape reweighting** There are three sources of uncertainty contributing
1261 to the measurement of the scale factors: statistical uncertainties, jet energy scale and
1262 the purity of the sample. The jet energy scale uncertainty is 100% correlated to the jet
1263 energy uncertainties and is evaluated simultaneously. The uncertainty coming from the
1264 purity of the sample is subdivided into two uncorrelated uncertainties based on the purity
1265 of the light flavoured (lf) and heavy flavoured (hf) jet contributions in the sample. A
1266 one sigma shift in each of the two purity contributions corresponds to a higher/lower
1267 contribution in the purity of the considered flavours. The statistical uncertainties have
1268 four uncorrelated sources, two for heavy flavour and two for light flavour jets. One of
1269 the uncertainties correspond to the shift consistent with the statistical uncertainties of
1270 the sample, while the other is propagated in a way that the upper and lower ends of the
1271 distribution are affected with respect to the centre of the distribution. The uncertainty
1272 on the charm jet scale factors (cf) is obtained from the uncertainty on the heavy flavour
1273 scale factors, doubling it in size and constructing two nuisance parameters to control the
1274 charm flavour scale factors and treating them as independent uncertainties.

1275 **Pileup** Varying the minimum bias cross section, used to calculate the pileup distribution by
1276 $\pm 4.6\%$, results in a systematic shift in the pileup distribution. The uncertainty is estimated
1277 by recalculating the pileup weights to the distributions associated to the minimum bias
1278 cross sections.

1279 **Luminosity** The luminosity is measured with a global uncertainty of 2.5%, affecting the ex-
1280 pected number of events.

Event selection and categorisation

5

1281

1282 A basic event selection is made for selecting signal like events and is discussed in [Section 5.1](#).
1283 Also the effect corrections applied to simulation and data, summarised in [Section 4.5](#) is shown.
1284 The analysis strategy is presented in [Section 5.2](#), defining the signal and background regions
1285 to constrain the huge SM background compared to the expected signal. [Section 5.4](#) discusses
1286 each region that is entering the analysis. On top of the use of background estimation from
1287 control regions, backgrounds that have prompt leptons contaminated by real leptons either from
1288 decays of tau leptons or from hadronized mesons or baryons (collectively commonly referred as
1289 “non-prompt leptons”) as well as by hadrons or jets misidentified as leptons¹ are evaluated with
1290 a data-driven method discussed in [Section 5.3](#).

1291 5.1 Baseline event selection and filters

1292 In this analysis a search is performed in a final state made up of a Z boson and a top quark,
1293 associated or not with a jet, in the leptonic decay of the Z boson and the top quark. The leading
1294 order Feynman diagrams can be seen in [Figure 5.1](#) and [Figure 5.2](#). The signal considers both the
1295 single top quark FCNC (tZ in the final state) and the top quark pair FCNC (tZq with $q = c, u$ in
1296 the final state) events. Their final state signatures consist of three leptons, considering electrons
1297 or muons, and a jet originating from a b quark. For FCNC tZq , there is an additional up or charm
1298 jet. Leptons from tau decays are not vetoed and are entering the analysis via their leptonic
1299 decays. Four different lepton channels based on lepton flavour are considered: 3e, 2e1 μ , 1e2 μ ,
1300 and 3 μ .

1301 The CMS collaboration recorded in the course of 2016 proton collisions data at a centre-of-
1302 mass of 13 TeV with a total recorded integrated luminosity of 35.9 fb^{-1} . The baseline event
1303 selection has as goal to substantially reject SM background events, whilst maintaining a high
1304 signal efficiency. The CMS trigger system, described in [Section 2.2.3](#), filters out the main of
1305 the collision events from uninteresting processes, and dedicated trigger paths are defined to
1306 single out the events with our required detector signature. The trigger paths are chosen based
1307 on online triggering objects with at least one muon (M), at least one electron (E), at least two

¹These two classes of contamination will be referred to as not prompt-lepton (NPL) samples.

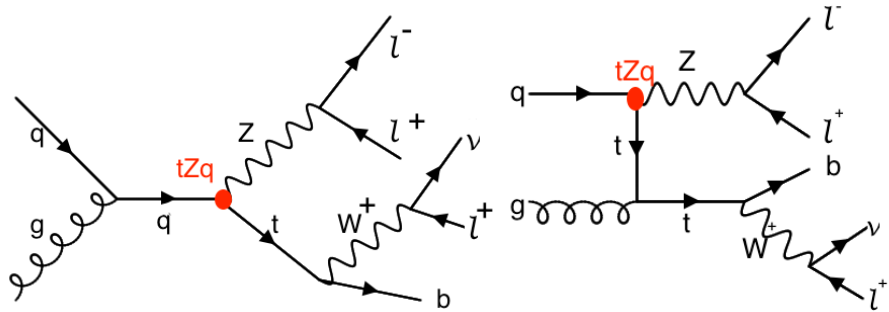


Figure 5.1: Single top quark Feynman diagrams at leading order. The vertex labelled tZq is the sought-for FCNC interaction.

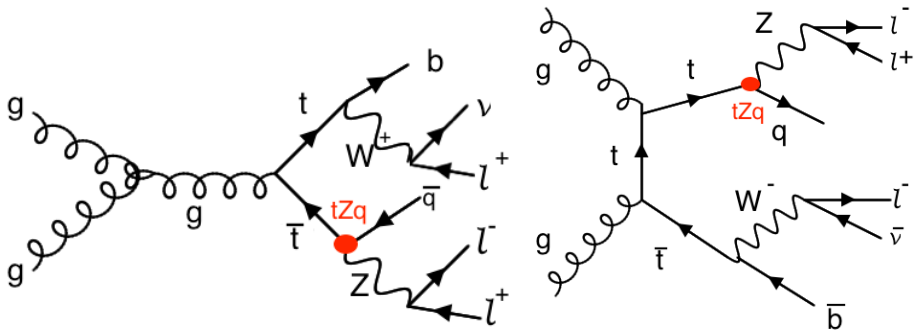


Figure 5.2: Top quark pair Feynman diagram at leading order. The vertex labelled tZq is the sought-for FCNC interaction.

1308 muons (MM), at least two electrons (EE), at least one muon and an electron (ME), at least three
 1309 muons (MMM), at least three electrons (EEE), at least two muons and one electron (MME), or
 1310 at least two electrons and one muon (EEM). For the MC simulation a simple *or* of all triggers is
 1311 taken and the event is considered when it passes one of the trigger paths. For data however,
 1312 double counting of the same event has to be taken into account and a procedure to avoid double
 1313 counting has been put into place. It consists of vetoing in a given dataset the events that are
 1314 already selected in another, as given in Table 5.1.

1315 For the single lepton triggers, at least one electron (muon) with a transverse momentum
 1316 p_T higher than 32 (24) GeV is required. The dilepton triggers require an electron (muon)
 1317 with $p_T > 23$ GeV and a muon (electron) with $p_T > 8$ GeV, or an electron (muon) with
 1318 $p_T > 23$ (17) GeV and an electron (muon) with $p_T > 12$ (8) GeV. Events collected by the
 1319 trilepton triggers require an electron (muon) with $p_T > 16$ (12) GeV, a second electron (muon)
 1320 of $p_T > 12$ (10) GeV, and a third electron (muon) with $p_T > 8$ (5) GeV. The mixed trilepton
 1321 trigger events require two electrons (muons) with $p_T > 12$ (9) GeV and a third muon (electron)
 1322 with $p_T > 8$ (9) GeV. The HLT trigger paths used in data and simulation are summarised in
 1323 Table 5.2.

1324 In order to ensure a full trigger efficiency, the off-line p_T thresholds are set higher than the

Table 5.1: Trigger logic used to select data events in order to avoid double counting.

Dataset	Trigger Logic
1e1μ	EM EEM MME
2μ	(MM MMM) && !(EM EEM MME)
2e	(EE EEE) && !(MM MMM) && !(EM EEM MME)
single μ	M && !(EE EEE) && !(MM MMM) && !(EM EEM MME)
single e	E && !M && !(EE EEE) && !(MM MMM) && !(EM EEM MME)

1325 online trigger thresholds. Selected electrons (muons) are required to have $p_T > 35$ (30) GeV and
 1326 $|\eta| < 2.1(2.4)$. The electrons and muons corresponding to a tight working point, as discussed
 1327 in [Section 4.4.1 \(Table 4.1\)](#) and [Section 4.4.2 \(Table 4.3\)](#), are used for analysis. Only events
 1328 with exactly three leptons are being considered. Events with extra leptons according to looser
 1329 working points are vetoed. The trigger efficiency estimation is described in [Section 5.1.2](#) and is
 1330 approximately 100%. To ensure that all reconstructed particles considered for the analysis are
 1331 corresponding to a proton interaction and remove signals from beam halo particles as well as
 1332 detector noise, several filters are used. These are described in [Section 5.1.1](#).

1333 In addition to three leptons, jets and missing transverse energy are expected from the signal
 1334 signature. The jets are reconstructed using the anti – k_T algorithm with a distance parameter of
 1335 0.4, using the particle flow particles that are not identified as isolated leptons as input. The jet
 1336 momentum is determined as the vectorial sum of the particles contained in the jet. Additional
 1337 selection criteria are applied to each event to remove spurious jet-like features originating
 1338 from isolated noise patterns in certain hadron calorimeter regions. The jet requirements are
 1339 discussed [Section 4.4.3](#). The jets are calibrated in simulation and in data separately, accounting
 1340 for deposits from pileup and the non-linear detector response. Calibrated jets with $p_T > 30$ GeV
 1341 and $|\eta| < 2.4$ are selected for the analysis. A selected jet may still overlap with the selected
 1342 leptons, leading to a double-counting of reconstructed objects. To prevent such cases, jets that
 1343 are found within a cone of $R = 0.3$ around any of the signal electrons (muons) are removed
 1344 from the collection of selected jets. The jets originating from b quarks are tagged using the
 1345 CSVv2 algorithm, which combines the information of displaced tracks with information of
 1346 secondary vertices associated with the jet using a multivariate technique. The jets are tagged as
 1347 a jet coming from a b quark (b-tagged) if the CSVv2 discriminator is above a certain threshold.
 1348 This analysis uses a threshold that results in an average b-tagging efficiency of 81% and a
 1349 misidentification rate of 10%. More information about b-tagging can be found in [Section 4.4.4](#).

1350 The missing transverse momentum vector \vec{p}_T is defined as the projection on the plane
 1351 perpendicular to the beams of the negative vector sum of the momenta of all reconstructed
 1352 particles in an event. Its magnitude is denoted by E_T^{miss} as shown in [Section 4.4.5](#). Its longitudinal
 1353 component is calculated by limiting the lepton + neutrino to the W boson mass. In case two
 1354 solutions arise, the mass closest to the known top quark mass is used.

Table 5.2: HLT trigger paths used to select data and simulation events.

Trigger path name	Trigger type
HLT_Mu23_TrkIsoVVL_Ele8_CaloIdL_TrackIdL_IsoVL_v	ME
HLT_Mu23_TrkIsoVVL_Ele8_CaloIdL_TrackIdL_IsoVL_DZ_v	ME
HLT_Mu8_TrkIsoVVL_Ele23_CaloIdL_TrackIdL_IsoVL_v	ME
HLT_Mu8_TrkIsoVVL_Ele23_CaloIdL_TrackIdL_IsoVL_DZ_v	ME
HLT_DiMu9_Ele9_CaloIdL_TrackIdL_v	MME
HLT_Mu8_DiEle12_CaloIdL_TrackIdL_v	EEM
HLT_IsoMu24_v	M
HLT_IsoTkMu24_v	M
HLT_Ele32_eta2p1_WPTight_Gsf_v	E
HLT_Mu17_TrkIsoVVL_Mu8_TrkIsoVVL_v	MM
HLT_Mu17_TrkIsoVVL_TkMu8_TrkIsoVVL_v	MM
HLT_Mu17_TrkIsoVVL_Mu8_TrkIsoVVL_DZ_v	MM
HLT_Mu17_TrkIsoVVL_TkMu8_TrkIsoVVL_DZ_v	MM
HLT_TripleMu_12_10_5_v	MMM
HLT_Ele23_Ele12_CaloIdL_TrackIdL_IsoVL_DZ_v	EE
HLT_Ele16_Ele12_Ele8_CaloIdL_TrackIdL_v	EEE

5.1.1 Event cleaning

Some events arising from instrumental noise and beam backgrounds might end up in the data [178, 179]. Spurious deposits may appear in the ECAL from non-collision origins such as beam halo particles, or from particles hitting the sensors in the ECAL photo-detectors. Conjointly, dead ECAL cells can cause artificial missing transverse energy. Also the HCAL can cause spurious energy from particle interactions with the light guides and the photomultiplier tubes of the HF, as well as noisy hybrid photo diodes. In CMS, different algorithms, so-called filters, are developed to identify and suppress these events.

The ECAL electronics noise and spurious signals from particle interactions with photo detectors are mostly removed via topological and timing-based selection using ECAL information only. The remaining effects such as anomalously high energy crystals and the lack of information for channels due to inefficiencies in the read-out are removed through dedicated events filters. Five ECAL endcap supercrystals have been identified for giving anomalously high energies due to high amplitude pulses in several channels at once, and are masked. Furthermore, the crystal read-out from a small amount of ECAL towers is not available. However, their trigger primitive

information is still available making it possible to estimate the magnitude of unmeasured energy and when the value is too large, the event is filtered out.

The machine induced particles via beam-gas / beam-pipe/... interactions, that are flying with the beam, affect the physics analysis. They leave a calorimeter deposit along a line at constant ϕ in the calorimeter, and interactions in the CSCs will often line up with this deposit. This can be seen in Figure 5.3. Therefore, events containing such beam halo particles are removed from the selection with the CSC Beam Halo Filter. This filter uses information related to the geometric quantities, energy deposits, and timing signatures. For 2016 proton collision data, the filter rejects 85% in a halo-enriched sample, whereas the mistag probability determined from simulation is found to be less than 0.01%.

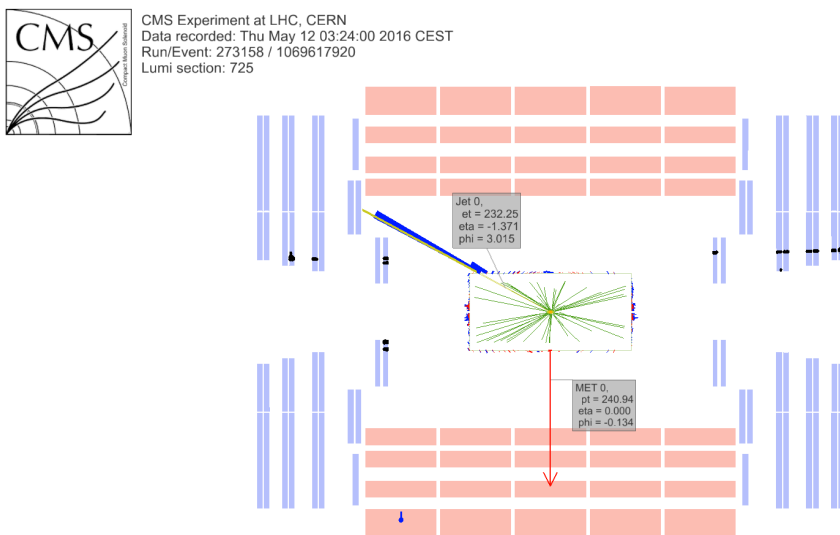


Figure 5.3: Event display of a beam halo event with collinear hits in the CSC (black), missing transverse energy of 250 GeV and a jet of 232 GeV. The hadronic deposit is spread in η , but narrow in ϕ . Figure taken from [178].

Furthermore, there is anomalous high missing transverse energy coming from low quality muons that lead to high- p_T tracks, but are considered not good by the particle flow algorithm. These low quality tracks will be mislabelled as charged hadrons and will therefore be used in the calculation of the missing transverse energy. By investigating the purity of the reconstructed tracks and the relative transverse momentum error of the muons, these events can be filtered out.

Supplementary to previous filters, only events where the first primary vertex is a well reconstructed primary vertex are selected. The reconstructed primary vertex should have at least five degrees of freedom, the longitudinal distance from the beam spot is maximally 24 cm ($d_z < 24$ cm), and the transversal distance from the beam spot is maximally 2 cm ($d_{xy} < 2$ cm).

1390 **5.1.2 Estimation of the trigger efficiency**

1391 The trigger efficiency in data is estimated using a data sample collected using unprescaled E_T^{miss}
 1392 triggers. These allow events with a missing transverse energy higher than 110 GeV(120 GeV)
 1393 and that the scalar sum of the transverse momenta of the reconstructed PF jets $H_T^{\text{trig.}}$ is at least
 1394 300 GeV (120 GeV), or a calorimeter (PF) E_T^{miss} higher than 200 GeV(300 GeV). For a HB-HE
 1395 cleaned event, the PF missing transverse energy threshold is lowered to 170 GeV. These trigger
 1396 paths are summarised in [Table 5.3](#) and chosen to be completely uncorrelated with the lepton
 triggers given in [Table 5.2](#).

Table 5.3: Unprescaled E_T^{miss} HLT trigger paths for estimating the trigger efficiency. An *or* of the triggers
 is used to select events.

Trigger path	Requirement
HLT_PFHT300_PFMET110_v*	PF $E_T^{\text{miss}} > 110$ GeV, PF $H_T^{\text{trig.}} > 300$ GeV
HLT_MET200_v*	calorimeter $E_T^{\text{miss}} > 200$ GeV
HLT_PFMET300_v*	PF $E_T^{\text{miss}} > 300$ GeV
HLT_PFMET120_PFHT120_IDTight_v*	PF $E_T^{\text{miss}} > 120$ GeV, PF $H_T^{\text{trig.,tightWP}} > 120$ GeV
HLT_PFMET170_HBHECleaned_v*	PF $E_T^{\text{miss}} > 170$ GeV, cleaned for HB/HE anomalous signals

1397

The trigger efficiency is studied on the main background, namely WZ+jets, with all corrections applied. For this study, the events passing a three lepton cut and at least one jet are being used. The corresponding efficiencies are then calculated as

$$\epsilon_{\text{data}} = \frac{\text{Nb. of events passing lepton and MET triggers}}{\text{Nb. of events passing MET triggers}} \quad (5.1)$$

$$\epsilon_{\text{MC}} = \frac{\text{Nb. of events passing lepton triggers}}{\text{Nb. of total events}} \quad (5.2)$$

The resulting efficiencies and scale factors can be found in [Table 5.4](#), where the scale factors are defined as

$$SF = \frac{\epsilon_{\text{data}}}{\epsilon_{\text{MC}}} \quad (5.3)$$

1398 More detailed scale factors and efficiencies can be found in [Appendix A](#).

1399 The trigger efficiencies are also measured in function of the p_T of the leptons for which the
 1400 distributions can be found in [Appendix A](#). The resulting scale factors can be found in Figure
 1401 [Figure 5.4](#). The trigger efficiencies are measured to be nearly 100% for both simulation and
 1402 data. The results are dominated by statistics and assigning a large uncertainty to the trigger
 1403 efficiency based on the dataset collected by E_T^{miss} triggers, would be over conservative. A one
 1404 percent uncertainty on the trigger selection for the 2e1 μ and 3 μ final states, and 5% for the
 1405 3e and 1e2 μ final states is assigned instead. No scale factors will be applied on simulation as
 1406 they are close to unity. Control plots are made in the dilepton region to validate all corrections
 applied to simulation and can be found in [Appendix B](#).

NOTE: 1407
 Make sure
 this is the
 case

Table 5.4: Trigger scale factors for each lepton channel, after three lepton plus jets selection, in the Z mass window, by counting the number of events.

	all	3 μ	3e	2e1 μ	1e2 μ
	1.0000	1.0000	0.9541	1.0006	1.0004%

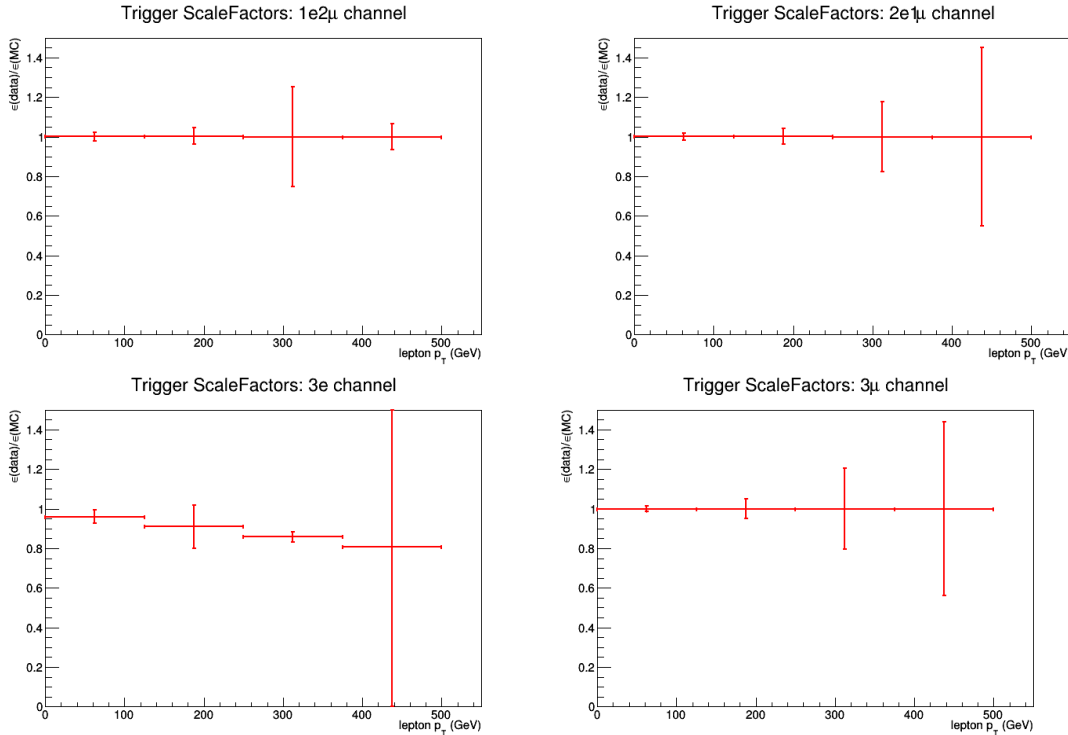


Figure 5.4: The trigger scale factors measured as a function of lepton p_T , using the dataset collected by E_T^{miss} triggers and WZ simulation, after a 3 lepton and jets selection, in the Z mass window. All corrections to simulation are applied. Left, upper: 1e2 μ channel. Right, upper: 2e1 μ channel. Left, lower: 3e channel. Right, lower: 3 μ channel.

5.1.3 Corrections

Mismatches between data and simulation are corrected via the use of scale factors. These are elaborately discussed in Section 4.4. In this section a short overview of the applied corrections is given, and their effect on a dilepton selection is shown.

Pileup reweighting

In data, the number of interactions per bunch crossing (pileup) is calculated with a minimum bias cross section of 69.2 mb. The number of simulated pileup events is then reweighted to match the expected number of pileup events in data. Pileup reweighting manifests itself as an altered shape of the number of reconstructed primary vertices as can be seen in Figure 5.5.

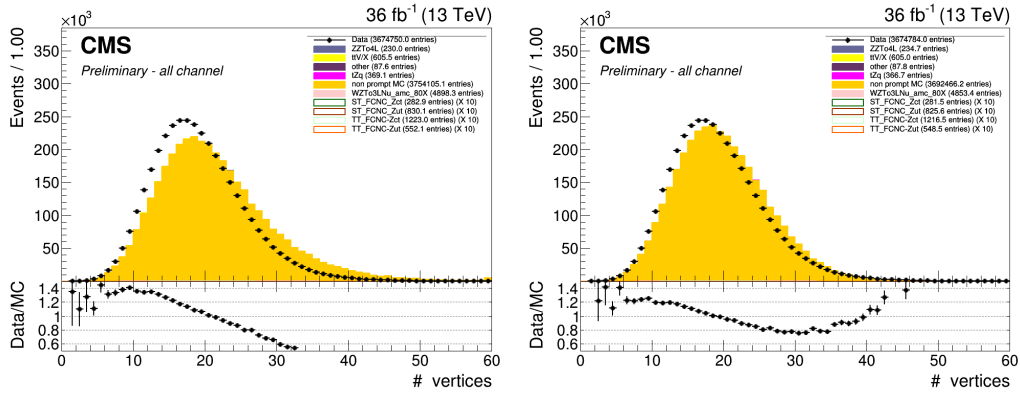


Figure 5.5: The number of primary vertices before (left) and after (right) pileup reweighting. After a dilepton plus jets selection, in the Z mass window.

1417 Note that Figure 5.5 indicates that even after pileup reweighting, the primary vertex multi-
 1418 plicity is not well described by simulation. This is a known effect, and using a minimum bias
 1419 cross section with a slightly lower value is found to better describe the data. However, the b
 1420 tagging scale factors are only provided for the nominal inelastic cross section, and thus this
 1421 value is used.

1422 Lepton scale factors

The efficiency to select leptons is different in simulation (ϵ_{MC}) compared to the data (ϵ_{data}). This is corrected by applying lepton scale factors (SF) to the simulation that are defined as

$$SF = \frac{\epsilon_{\text{data}}}{\epsilon_{\text{MC}}}. \quad (5.4)$$

These scale factors are measured for the identification, isolation, tracking and trigger efficiencies of the objects as a function of p_{T} and η (see Section 4.4.1 and Section 4.4.2). Multiplying these scale factors for each lepton provides an overall efficiency:

$$SF_{\text{global}}^{\mu} = \prod_{\text{i}}^{\#\mu} SF_{\text{ID}}^{\mu}(p_{\text{T}}, \eta) SF_{\text{Iso.}}^{\mu}(p_{\text{T}}, \eta) SF_{\text{Trig.}}^{\mu}(p_{\text{T}}, \eta) SF_{\text{track}}^{\mu}(p_{\text{T}}, \eta), \quad (5.5)$$

$$SF_{\text{global}}^e = \prod_{\text{i}}^{\#e} SF_{\text{ID}}^e(p_{\text{T}}, \eta) SF_{\text{Iso.}}^e(p_{\text{T}}, \eta) SF_{\text{Trig.}}^e(p_{\text{T}}, \eta) SF_{\text{track}}^e(p_{\text{T}}, \eta). \quad (5.6)$$

1423 The effect of the scale factors can be found in Figure 5.7 for the electron scaling and in Figure
 1424 5.6 for the muons. The trigger efficiencies are estimated in Section 5.1.2.

1425 Additionally, corrections are made for the energy resolution of the leptons. For the electrons,
 1426 energy smearing and regression is applied [180]. The energy regression uses the detector
 1427 information to correct the electron energy in order to have the best energy resolution by
 1428 correcting local energy containment, material effects, etc.. The energy scale and smearing

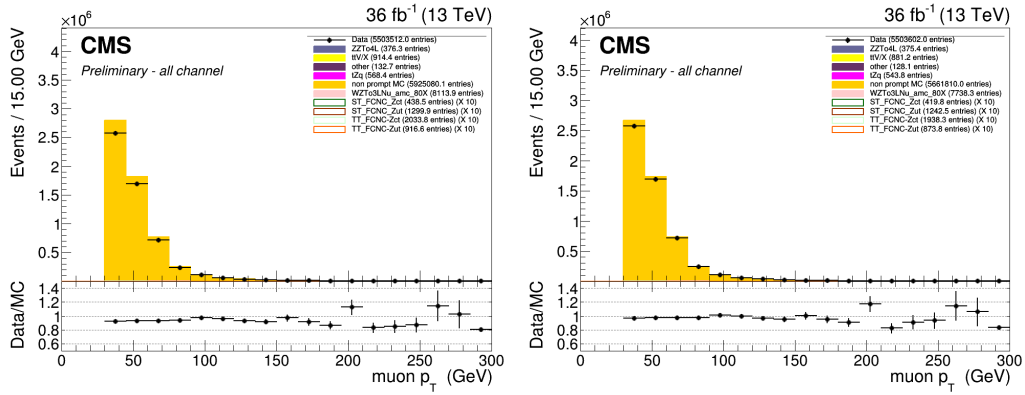


Figure 5.6: The p_T of the muons before (left) and after (right) muon scale factors. After a dilepton plus jets selection, in the Z mass window. Both after the Rochester correction.

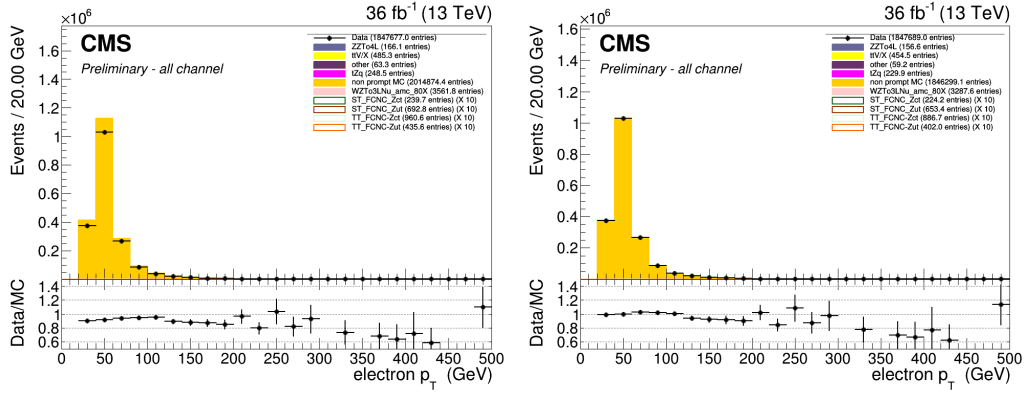


Figure 5.7: The p_T of the electrons before (left) and after (right) electron scale factors. After a dilepton plus jets selection, in the Z mass window. Both after energy scale corrections and smearing.

1429 is done in order to bring the data energy scale to simulation level. It smears the simulation
 1430 energies to have identical energy resolution in simulation and data. For the muons, the p_T is
 1431 corrected using the Rochester method [181, 182]. This correction removes the bias of the muon
 1432 p_T from any detector misalignment or any possible error of the magnetic field. The effect of
 1433 the Rochester correction can be found in Figure 5.8.

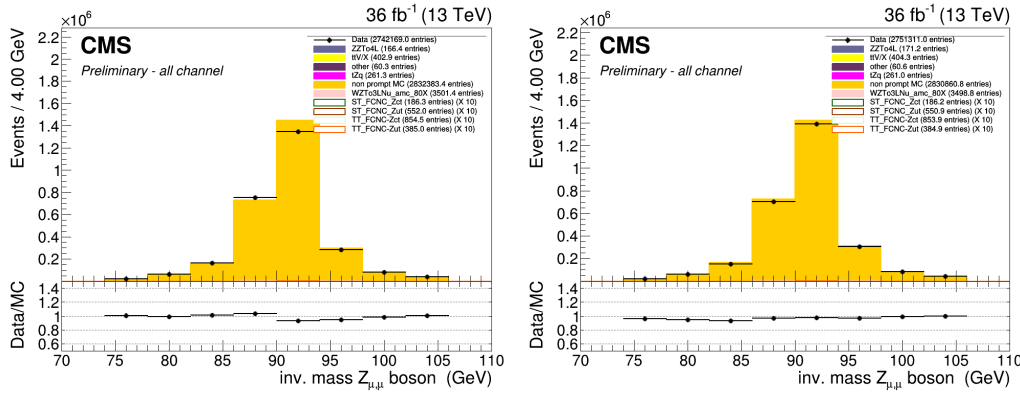


Figure 5.8: The mass of the Z boson consisting of the muons before (left) and after (right) the Rochester correction. After a dilepton plus jets selection, in the Z mass window.

1434 CSVv2 shape correction

1435 In order to make the shape of the CSVv2 b-tagging discriminant in simulation agree with data,
 1436 jet-by-jet based scale factors are applied. These scale factors are a function of the p_T , η and
 1437 CSVv2 value of the jet as discussed in Section 4.4.4. The effect of these scale factors can be
 1438 found in Figure 5.9.

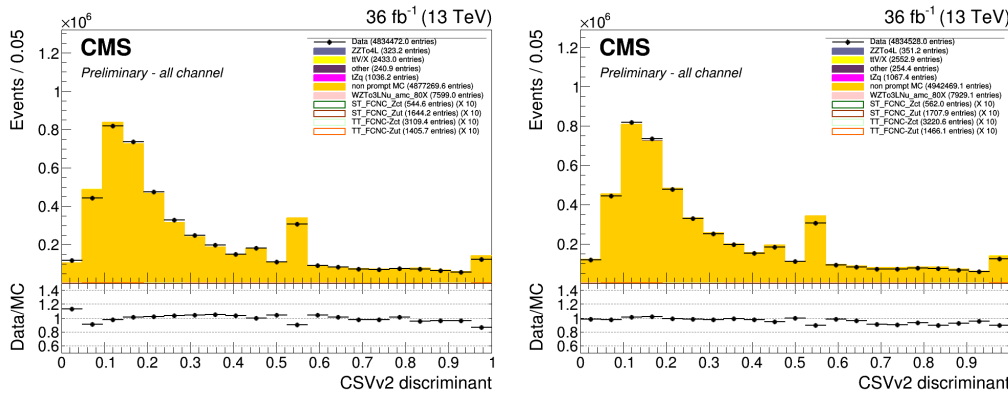


Figure 5.9: The CSVv2 discriminant of the jets before (left) and after (right) b-tag scale factors. After a dilepton plus jets selection, in the Z mass window.

1439 Jet energy

1440 The jet energy in data and simulation is corrected by the measured energy response of the
 1441 detector. This provides p_T - and η dependent scale factors and are directly taken from the
 1442 frontier condition database as discussed in Section 4.4.3. The effect of the jet energy corrections
 1443 can be found in Figure 5.10 and Figure 5.11.

NOTE: Figure 5.10 is a jet energy plot.

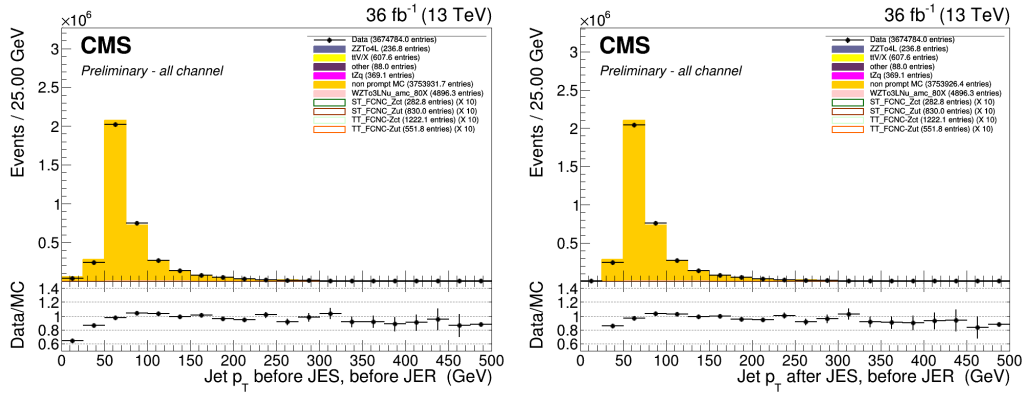


Figure 5.10: The p_T of the jets before (left) and after (right) jet energy scale corrections. After a dilepton plus jets selection, in the Z mass window.

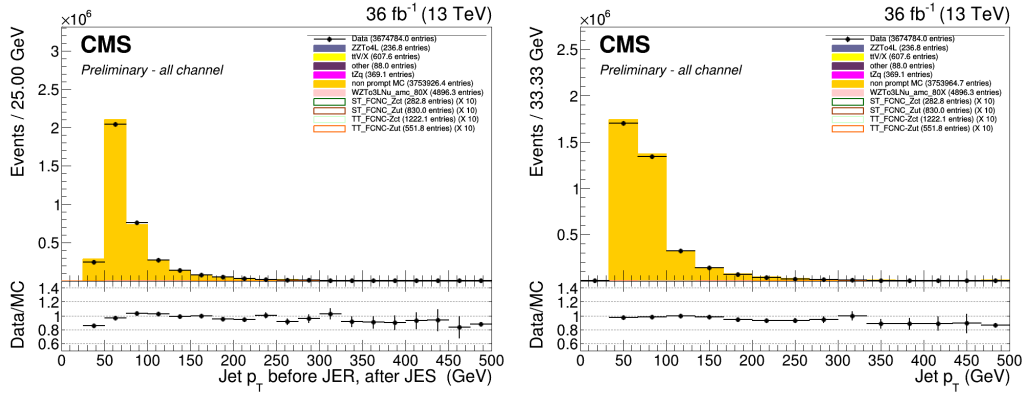


Figure 5.11: The p_T of the jets before (left) and after (right) jet energy resolution smearing. After a dilepton plus jets selection, in the Z mass window.

1444 Missing transverse energy

1445 The energy scale and resolution corrections applied to the jets are propagated back to the
 1446 missing transverse energy (smeared Type I correction) as discussed in [Section 4.4.5](#). This
 1447 rebalances the transverse net momentum of the event and improves the missing transverse
 1448 energy resolution itself.

1449 5.1.4 Reconstruction of kinematic variables

1450 The variables used for the training are related to the reconstructed leptons, jets, Z boson and
 1451 top quark candidates. The Z boson is reconstructed as the sum of the four vectors of the two
 1452 same flavour leptons of opposite sign giving the closest value to the Z mass. The third remaining
 1453 lepton is assigned as the lepton coming from the W boson decay. The reconstruction of the SM
 1454 top quark candidate is more difficult and done by summing the third lepton, the SM b-jet and
 1455 the neutrino (E_T^{miss}). The SM b jet is assigned to the jet with the highest CSVv2 discriminant.
 1456 The longitudinal momentum of the neutrino is calculated by putting a constraint on the lepton

1457 + neutrino system with the W mass. In case two solutions are found for the p_z^ν component, the
 1458 one that gives the reconstructed mass (lepton + neutrino + b jet) to the known top quark mass,
 1459 is used. The FCNC top quark is reconstructed by summing the reconstructed Z boson and the
 1460 jet giving the mass closest to the top mass, from the jet collection from which the SM b jet is
 1461 removed.

1462 The reconstructed objects are validated using simulation by matching the reconstructed
 1463 objects to their generated counterpart by minimizing ΔR . The efficiencies derived from the
 1464 simulated signal samples and the SM tZq background process can be found in [Table 5.5](#) and
 1465 [Table 5.6](#).

Table 5.5: Efficiencies of assigning the correct leptons in the analysis.

	FCNC tZq	FCNC tZ	SM tZq
W lepton	99%	98%	97%
leptons from the Z boson	99%	98%	97%
all leptons in the decay	99%	98%	97%

Table 5.6: Efficiencies of assigning the correct jets in the analysis.

	FCNC tZq	FCNC tZ	SM tZq
SM b jet	99%	98%	80%
c jet	71%	N/A	50%
u jet	83%	N/A	54%

1466 5.2 Analysis Strategy

1467 The analysis strategy uses five statistically independent regions to extract limits, using a like-
 1468 lihood fit of various observables. Two signal regions, the tZ (STSR) and tZq (TTSR) signal
 1469 regions, are constructed using the jet multiplicity, focussed on each signal signature (see Tab.
 1470 [5.9](#)). In order to constrain the rate of WZ+jet events as well as that of NPL backgrounds, three
 1471 control regions are defined. The WZ control region (WZCR) focusses on NPLs originating from
 1472 Z/ γ^* + jets and simultaneously constrains the WZ+jets background rate. The NPL backgrounds
 1473 coming from a $t\bar{t}$ process are constrained by two control regions, TTCR and STCR, one for each
 1474 signal region (TTSR and STSR). In the STSR and TTSR, multivariate discriminants based on
 1475 Boosted Decision Trees (BDT) (see [Section 3.3](#)) are used to respectively discriminate FCNC
 1476 tZ and FCNC tZq from backgrounds. In the WZCR, a discriminating variable between the two
 1477 backgrounds, WZ+jets and NPLs, is used. In TTCR and STCR, the dominating process is the $t\bar{t}$
 1478 process, and its rate is estimated by subtracting all other background predictions from data.
 1479 A simultaneous global fit using the Higgs Combined Tool ([Section 3.4](#)) is performed taking

1480 into account each region (STS_R, TTS_R, WZCR, TTCR and STCR) for the four different leptonic
 1481 channels.

1482 **5.3 Data driven NPL background simulation**

1483 One of the most important backgrounds consists of events with not prompt leptons. These are
 1484 mostly instrumental backgrounds and are therefore very difficult to model. The NPL background
 1485 is estimated from data for both its shape and its normalisation.

1486 The NPL background originates from hadronic objects wrongly reconstructed as leptons, real
 1487 leptons coming from the semi-leptonic decay of a b or c hadron, or real leptons coming from
 1488 the conversion of photons that pass the identification and isolation requirements. The dominant
 1489 source of these NPLs depends on the flavour of the leptons and therefore the events with a
 1490 not prompt muon (NP μ) are treated differently than those with a not prompt electron (NPe).
 1491 For muons, the dominant source is the semi-leptonic decay of heavy flavour hadrons, while for
 1492 electrons, the dominant sources are hadrons and photon conversions.

1493 The backgrounds causing NPL contributions are mostly $Z/\gamma^* + \text{jets}$ (Drell–Yan) and $t\bar{t} + \text{jets}$
 1494 dilepton processes, and in a smaller amount WW processes. All of these backgrounds contain
 1495 two real leptons and one NPL. Due to the fact that the probability for a lepton to be a NPL is
 1496 small, backgrounds containing two or more NPL are neglected in this search. The assumption is
 1497 made that for $Z/\gamma^* + \text{jets}$ the two leptons compatible with a Z boson decay are the real leptons,
 1498 and the additional lepton is coming from a NPL source, while for $t\bar{t} + \text{jets}$ the NPL is associated
 1499 to the Z boson. This has been validated using a Monte Carlo simulation.

1500 The NPL sample is constructed from data by requiring exactly three leptons, from which two
 1501 are considered real isolated leptons and the third lepton is identified as a NPL. This NPL is
 1502 created by loosening its identification and inverting its isolation criteria. The full requirements
 1503 on the not prompt leptons are given in [Table 5.7](#) and [Table 5.8](#). For NPes, a large fraction
 1504 is coming from misidentified photons. These are removed by applying a tighter cut on the
 1505 $1/E - 1/p$ variable, and by limiting the isolation values to be smaller than one.

Table 5.7: Non prompt electron requirements used in this analysis. The requirements are set in the barrel ($|\eta_{supercluster}| \leq 1.479$) and the end caps ($|\eta_{supercluster}| > 1.479$).

Properties	$ \eta_{supercluster} \leq 1.479$	$ \eta_{supercluster} > 1.479$
$\sigma_{\eta\eta}$	< 0.011	< 0.0314
$ \Delta\eta_{in} $	< 0.00477	< 0.00868
$ \Delta\phi_{in} $	< 0.222	< 0.212
H/E	< 0.298	< 0.101
relative isolation	$\geq 0.0588 \ \&\& < 1$	$\geq 0.0571 \ \&\& < 1$
$ 1/E - 1/p $	$< 0.0129 \text{ GeV}^{-1}$	$< 0.0129 \text{ GeV}^{-1}$
expected missing inner hits	≤ 1	≤ 1
pass conversion veto	Y	Y
p_T	$> 35 \text{ GeV}$	$> 35 \text{ GeV}$

Table 5.8: Non prompt muon requirements used in the analysis.

Properties	modified Loose Muon WP
Global muon or Tracker Muon	Both
Particle Flow muon	Y
χ^2/ndof of global muon track fit	N/A
Nb. of hit muon chambers	N/A
Nb. of muon stations contained in the segment	N/A
Size of the transverse impact parameter of the track wrt. PV	N/A
Longitudinal distance wrt. PV	N/A
Nb. of pixel hits	N/A
Nb. of tracker layers with hits	N/A
Relative Isolation	≥ 0.15
p_T	$> 30 \text{ GeV}$

1506 **5.4 Statistical independent regions**

The regions are defined as in Table 5.9 after a common selection of exactly three leptons containing one opposite sign same flavour pair that is assigned to the Z boson, at least one jet and at the most three jets, and the transverse mass of the W boson to be maximal 300 GeV. The transverse mass $m_T(W)$ is reconstructed using

$$m_T(W) = \sqrt{(p_T(l_W) + p_T(v_W))^2 - (p_x(l_W) + p_x(v_W))^2 - (p_y(l_W) + p_y(v_W))^2}. \quad (5.7)$$

Table 5.9: The statistically independent regions used in the analysis.

	WZCR	STS R	TTSR	STCR	TTCR
Number of jets	≥ 1	1	≥ 2	1	≥ 2
Number of b jets	0	1	≥ 1	1	≥ 1
$ m_Z^{\text{reco}} - m_Z < 7.5 \text{ GeV}$	Yes	Yes	Yes	No	No
$ m_Z^{\text{reco}} - m_Z < 30 \text{ GeV}$	Yes	Yes	Yes	Yes	Yes
Number of leptons	3	3	3	3	3

1507 Additional leptons with a looser identification are vetoed in order to reduce the contamination
 1508 of backgrounds with four or more leptons in the final state, e.g. ZZ, t̄Z, and t̄H. The most
 1509 important backgrounds are the ones that contain three prompt leptons in the final state. These
 1510 are mainly WZ+jets, t̄Z and SM tZq. For these backgrounds, the three lepton topology is
 1511 identical to the FCNC signal: two opposite sign leptons of the same flavour decaying from the Z
 1512 boson, and a third additional, high p_T lepton coming from the W boson decay.

1513 For the FCNC tZ final state, one b jet coming from the SM top decay is expected. For the
 1514 FCNC tZq, an additional light jet is expected. In the t̄Z final state, two b jets are present in the
 1515 final state. However, due to inefficiencies of the b-tagging algorithm, one of the two b jets may
 1516 be identified as a light quark jet, giving the same final state as the FCNC tZq final state. For
 1517 the WZ+jets final states, one of the b jets produced by gluon splitting, can be b-tagged or light
 1518 flavour jets coming from the WZ+jets production can be mis-tagged as b jets. The SM tZq final
 1519 state expects the same signal as FCNC tZq.

1520 The NPL events give a significant background contribution. This background is mainly coming
 1521 from $Z/\gamma^* + \text{jets}$ and $t\bar{t} + \text{jets}$ processes (in a less significant way, also WW and tWZ contributes),
 1522 which have very high cross sections and cause a large number of NPL background events
 1523 compared to the signal.

1524 In order to reduce the large uncertainties in backgrounds, five independent regions are used
 1525 as defined in Table 5.9. In Figure 5.12, the strategy and usage of each region is illustrated.

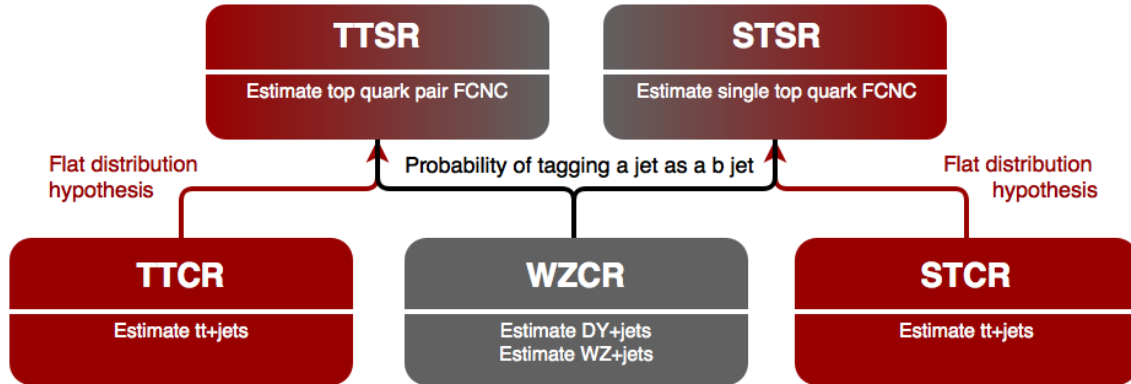


Figure 5.12: The strategy used for this search. The WZCR region is used to estimate the WZ+jets background process as well as the NPL background coming from the $Z/\gamma^* + \text{jets}$ process. The TTCR and STCR regions are used to estimate the contributions of the NPL background coming from the $t\bar{t} + \text{jets}$ process.

1526 5.4.1 WZCR

1527 The WZCR is constructed by vetoing events with jets tagged as being a b-jet, making it statistically
 1528 independent from the signal regions where at least one b-tagged jet is required. In this region,
 1529 a fit is performed on the transverse mass of the W boson, in order to estimate the NPL yield
 1530 coming from $Z/\gamma^* + \text{jets}$ and the WZ+jets backgrounds.

A transfer factor is used to account for going from a region without b-tagged jets to a region with exactly, or at least, one b-tagged jet. For this, the probability of tagging at least one jet with the CSVv2 algorithm at the loose working point is used to calculate the expected number of events, N_b , after b-tagging:

$$N_b = \frac{\sum_{\text{events}} \mathcal{P}_b}{\text{total nb of events}}, \quad (5.8)$$

where \mathcal{P}_b is the probability that an event survives the b-tagging requirement,

$$\begin{aligned} \mathcal{P}_b &= 1 - P(\text{event doesn't survive b tag}), \\ &= 1 - \left(\prod_b P(\text{b not tagged}) \prod_c P(\text{c not tagged}) \prod_{\text{udsq}} P(\text{light not tagged}) \right), \end{aligned} \quad (5.9)$$

1531 with the products going over all b-, c-, and light jets. The jet flavour is determined by means of
 1532 matching the reconstructed jet to the generated quarks, based on the distance in the $\eta\phi$ plane.
 1533 In order to estimate the probability for exactly one b-tagged jet, the expected number of events
 1534 is corrected by the fraction of events with exactly one jet in the WZCR. The resulting transfer
 1535 factors are given in [Appendix C](#). The yield of WZ+jets events in the signal region estimated
 1536 using the above described transfer factor, and the yield calculated with simulated events, are in
 1537 agreement.

1538 **5.4.2 TTCR and STCR**

The TTCR and STCR are constructed with the same selection criteria as TTSR and STSR, but are outside the Z mass window (sidebands):

$$7.5 \text{ GeV} < |m_Z^{\text{reco}} - m_Z| < 30 \text{ GeV}, \quad (5.10)$$

where m_Z^{reco} is the reconstructed mass of the Z boson in the event, and m_Z the mass of the Z boson. These regions are dominated by $t\bar{t}$ +jets (see Appendix C) and are used to estimate the NPL coming from $t\bar{t}$ +jets in the STSR and TTSR. Since there aren't enough events entering these regions, no shapes are used in the fit. The distribution of the mass of the Z boson is flat for $t\bar{t}$ +jets events, as shown in Fig. Figure 5.13, and thus the number of expected events, N_s , in the signal regions estimated from the number of expected events, N_c , in the control region is obtained as

$$N_s = \frac{15}{60 - 15} N_c. \quad (5.11)$$

1539 The resulting transfer factors are given in Appendix C. The expected yield in the signal region
 1540 estimated from the TTCR (STCR) is in agreement with the yield calculated from simulated events.

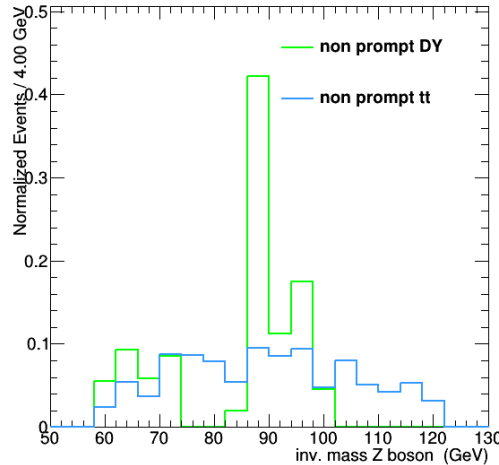


Figure 5.13: The normalized distribution for $Z/\gamma^* + \text{jets}$ and $t\bar{t} + \text{jets}$ events before dividing the events in to regions, after $|m_Z^{\text{reco}} - m_Z| < 30 \text{ GeV}$. All leptonic channels combined.

1541

1542 **5.4.3 TTSR and STSR**

1543 The TTSR is defined to target top quark pair FCNC (tZq), while the STSR focusses on single top
 1544 quark FCNC (tZ). They have NPL contributions coming from $Z/\gamma^* + \text{jets}$ and $t\bar{t} + \text{jets}$ events. In
 1545 this region, the data driven NPL template is split into two templates, based on the presence
 1546 of the NPL in the Z boson. The NPL associated with W boson is assigned to $Z/\gamma^* + \text{jets}$ and
 1547 estimated in the WZCR, while the NPL associated with Z boson is assigned to $t\bar{t} + \text{jets}$ and
 1548 estimated in the TTCR and STCR.

The search for FCNC involving a top quark and a Z boson

6

1549

1550 6.1 Construction of template distributions

1551 There were no selection criteria found to make a clear rejection of the background events without
1552 sacrificing a significant amount of signal. For this reason, a multivariate approach using Boosted
1553 Decision Trees that combines several discriminating variables in the TMVA framework is used.
1554 For the training, the BDTs are trained against all backgrounds, where the NPL background is not
1555 taken into account. The BDT settings avoid over-training and maintain a good discriminating
1556 power against all backgrounds. The background and signal yields follow the relative fractions
1557 predicted by the simulation.

1558 The pre fit distributions of the variables used for creating the multivariate discriminator are
1559 given in [Section 6.1.1](#). The resulting multivariate discriminator are shown in [Section 6.1.2](#). The
1560 technical details of the BDTs can be found in [Appendix D](#).

1561 6.1.1 Distributions of the BDT variables

1562 The variables used to construct the BDTs include the angles, distances, masses and transverse
1563 momenta:

- 1564 1. pseudo rapidity of the SM top: TT+ST tZ_u, ST tZ_c
- 1565 2. invariant mass of the W lepton and the SM b jet: TT+ST tZ_u, TT+ST tZ_c
- 1566 3. $\Delta\Phi$ between the W lepton and the SM b jet: TT+ST tZ_u, ST tZ_c
- 1567 4. minimal ΔR between the W lepton and jets: TT tZ_u
- 1568 5. invariant mass of the Z boson: TT tZ_u, TT tZ_c
- 1569 6. $\Delta\Phi$ between the W lepton and the Z boson: TT+ST tZ_u, TT tZ_c
- 1570 7. ΔR between the W lepton and the SM b jet: TT+ST tZ_u, TT tZ_c

- 1571 8. number of CSVv2 medium WP b jets: TT tZu, TT tZc
- 1572 9. invariant mass of the FCNC top: TT tZu, TT tZc
- 1573 10. ΔR between the Z boson and the FCNC light jet: TT tZu, TT tZc
- 1574 11. ΔR between the FCNC light jet and the SM b jet: TT tZu, TT tZc
- 1575 12. charge of the W lepton times the absolute pseudo rapidity of the W lepton: ST tZu
- 1576 13. b discriminant of the highest p_T jet: ST tZu, ST tZc
- 1577 14. total Ht of the leptons: ST tZu
- 1578 15. the p_T of the W lepton times its charge: ST tZu
- 1579 16. total invariant mass of the leptons: ST tZc
- 1580 17. ΔR between the W lepton and Z boson: TT+ST tZc
- 1581 18. total invariant mass of the event: TT tZc
- 1582 19. b discriminant of the FCNC light jet: TT tZc
- 1583 20. ΔR between the SM b jet and Z boson: TT tZc

1584 The normalised distributions of the BDT input variables for the tZu vertex in the TTSR and
1585 STSR are shown. Their prefit distributions can be found in [Appendix E.3](#).

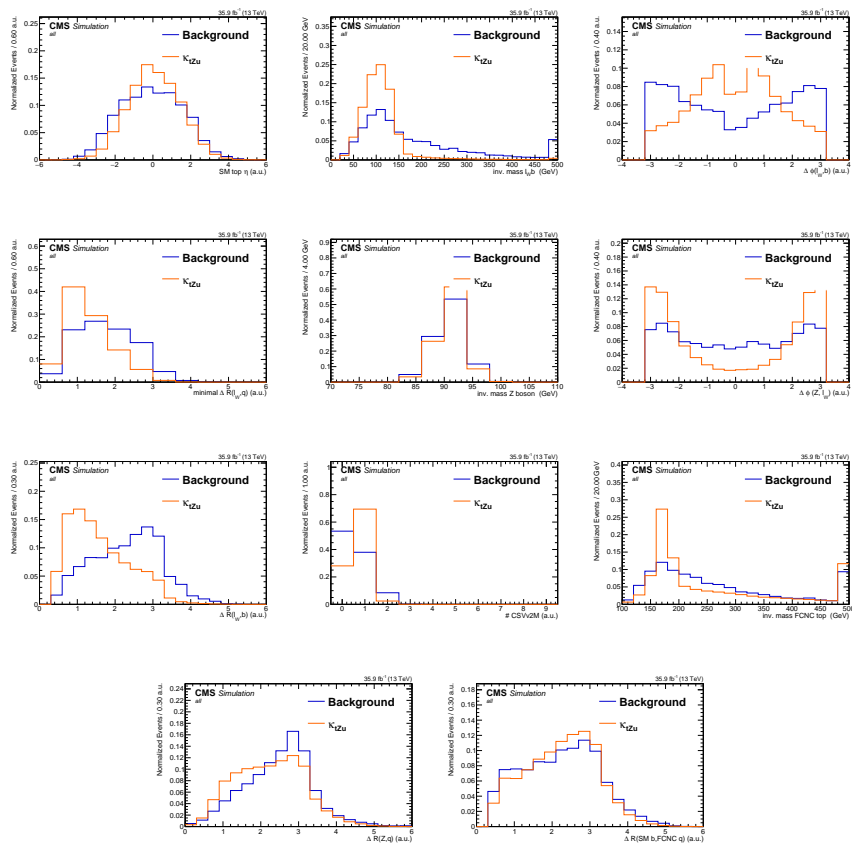


Figure 6.1: The normalised input variables for reconstructing the multivariate discriminator in the TTSR for the tZu vertex.

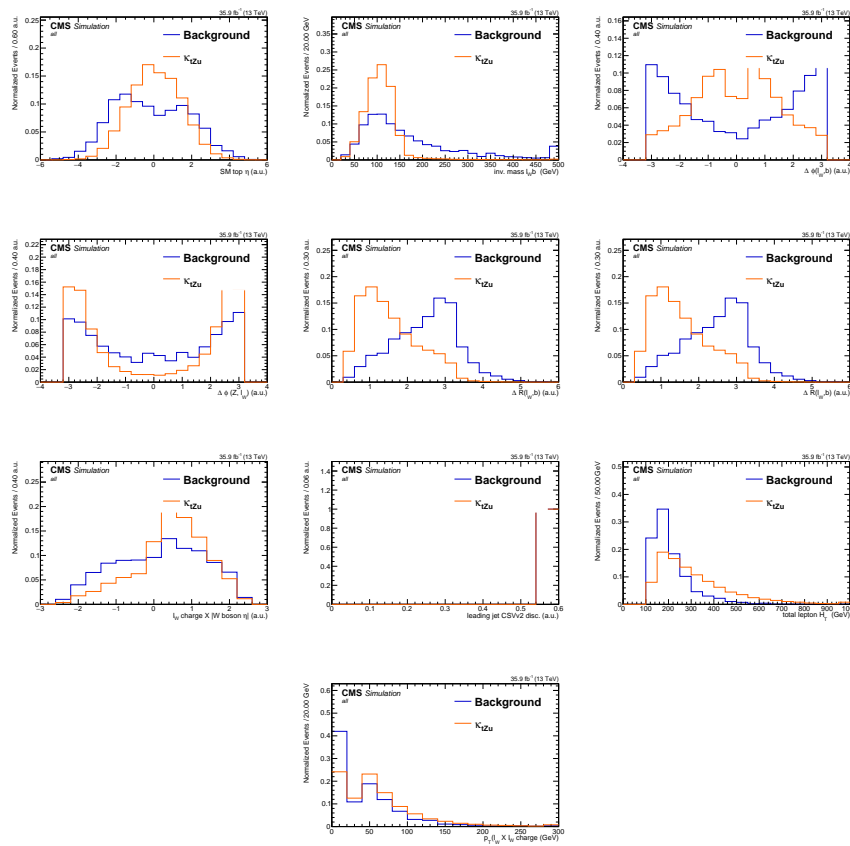


Figure 6.2: The normalised input variables for reconstructing the multivariate discriminator in the STSR for the tZu vertex.

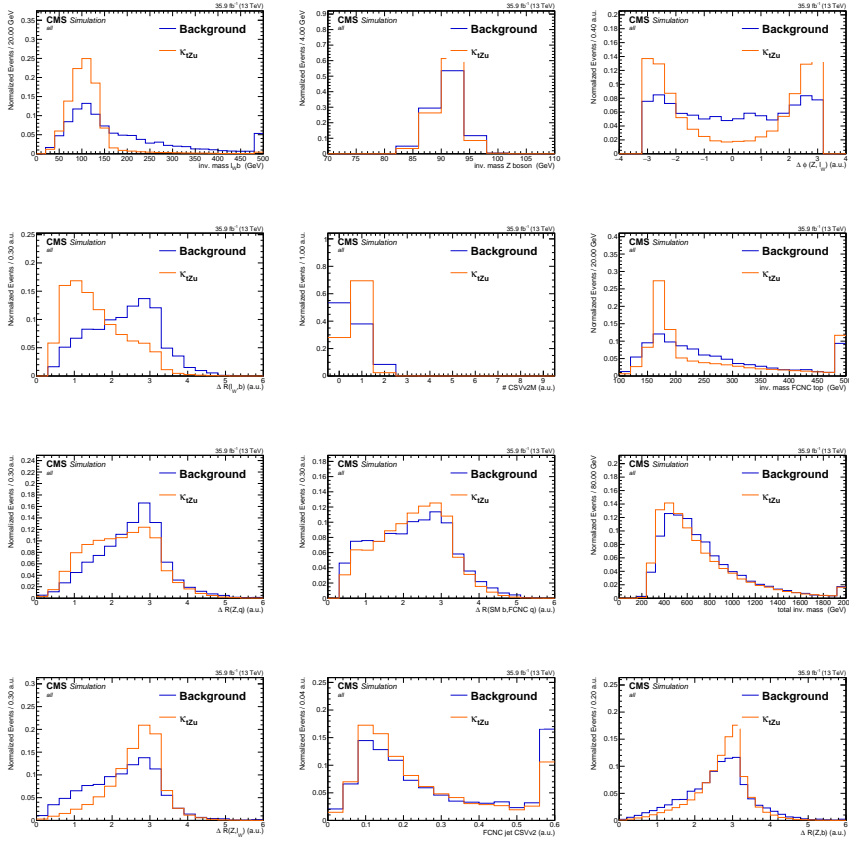


Figure 6.3: The normalised input variables for reconstructing the multivariate discriminator in the TTSR for the tZc vertex.

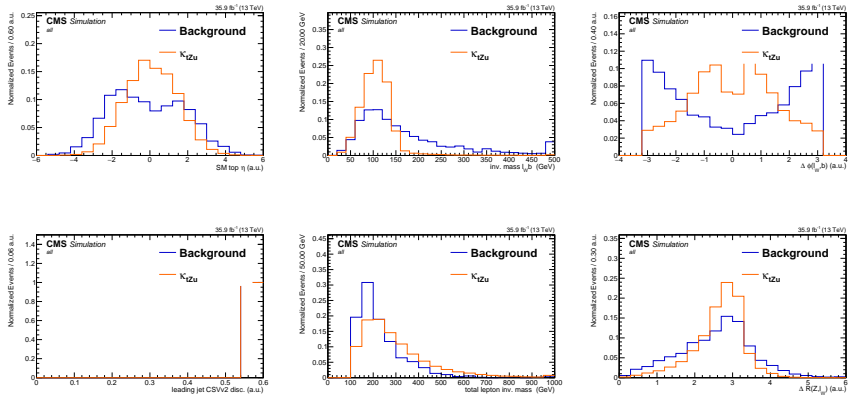


Figure 6.4: The normalised input variables for reconstructing the multivariate discriminator in the STSR for the tZc vertex.

1586 **6.1.2 BDTs**

1587 In Appendix E.1, one can find the prefit BDT distributions with data, while the normalised
 1588 distributions are shown in Figure 6.5 and Figure 6.6.

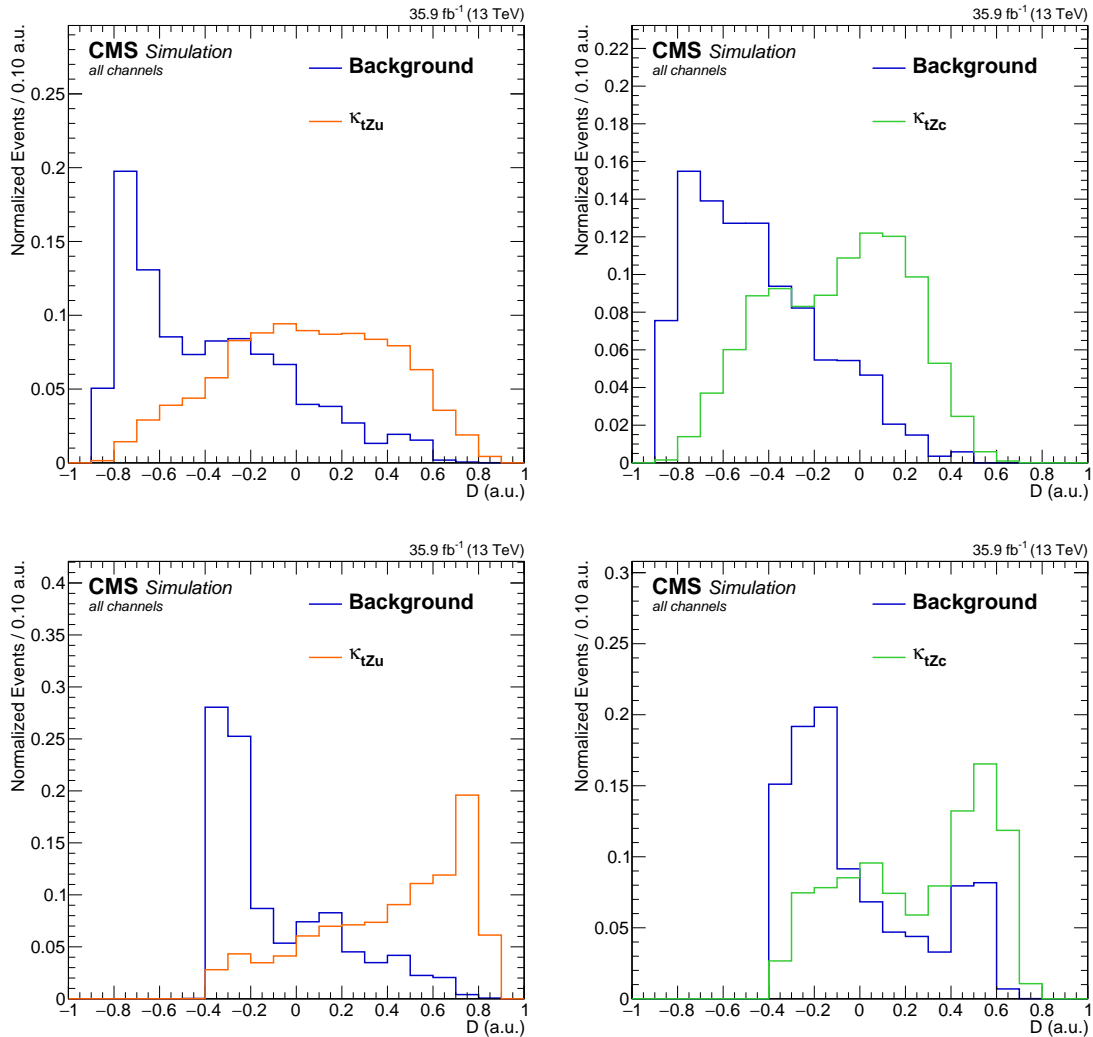


Figure 6.5: Normalised distributions of the discriminating variable before the fit, all different leptonic channels together. Upper left: TTSR tZu , upper right: TTSR tZc ; lower left: STSR tZu , lower right: STSR tZc .

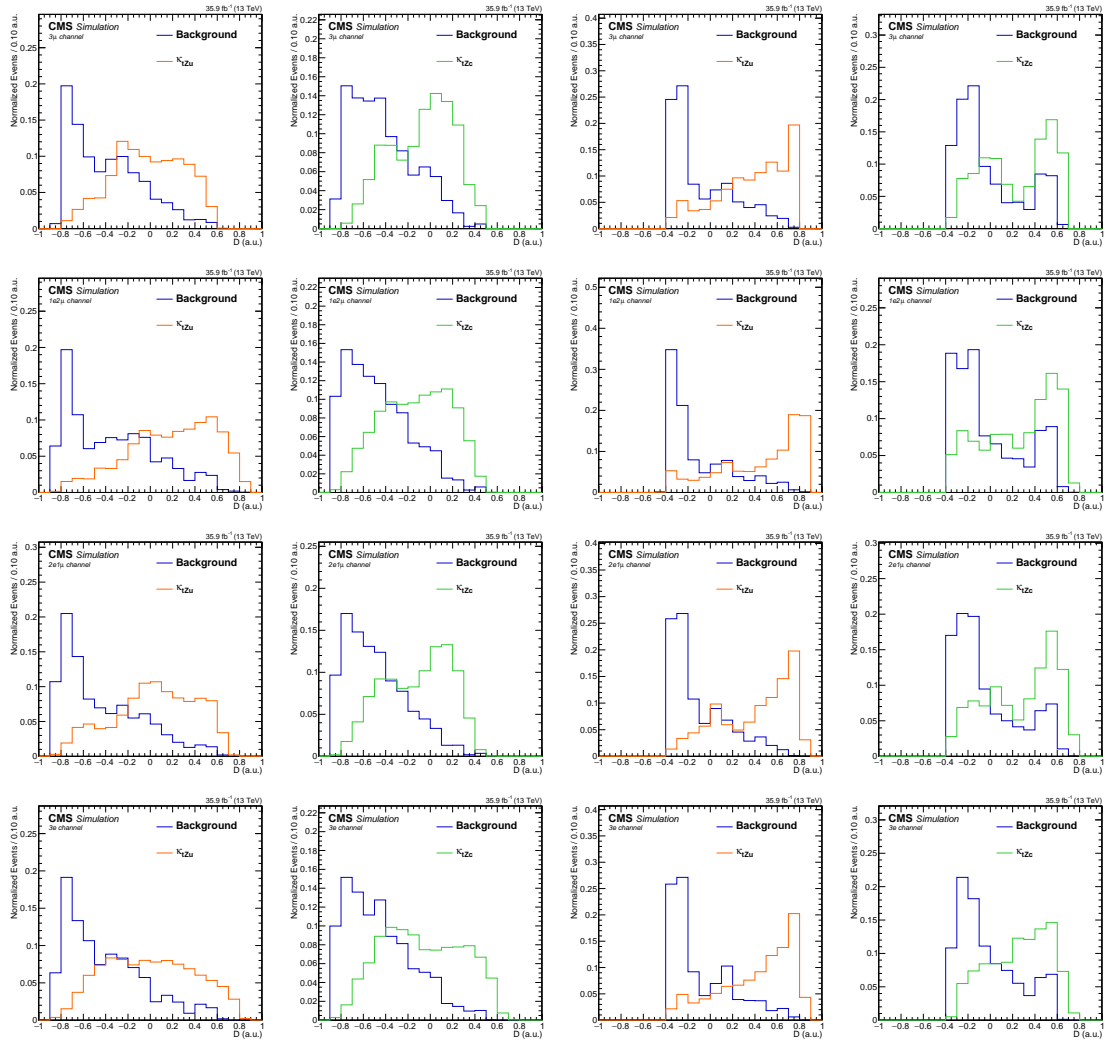


Figure 6.6: Normalised distributions of the discriminating variable before the fit. Each row contains: left: TTSR tZu , left-middle: TTSR tZc ; right-middle: STSR tZu , right: STSR tZc . First row: 3μ leptonic channel, second row: $1e2\mu$, third row: $2e1\mu$, and last row: $3e$ leptonic channel.

1589 **6.1.3 Transverse mass in WZCR**

1590 The WZCR is used to estimate the contribution from WZ+jets and NPL background. In this
 1591 region, a fit is performed on the transverse mass distribution of the W boson. The pre-fit
 1592 normalised templates are given in [Figure 6.7](#) and [Figure 6.8](#), while the the templates with data
 1593 are shown in Appendix ??.

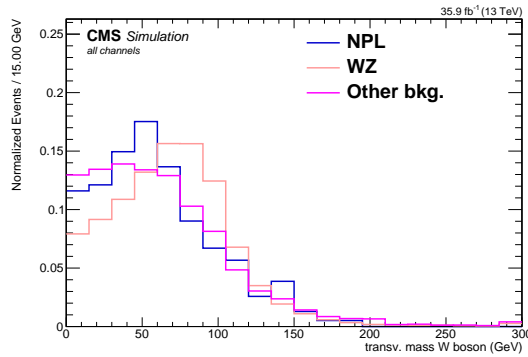


Figure 6.7: The normalised distribution of the transverse mass of the W boson in the WZCR, before the fit. All different leptonic channels together.

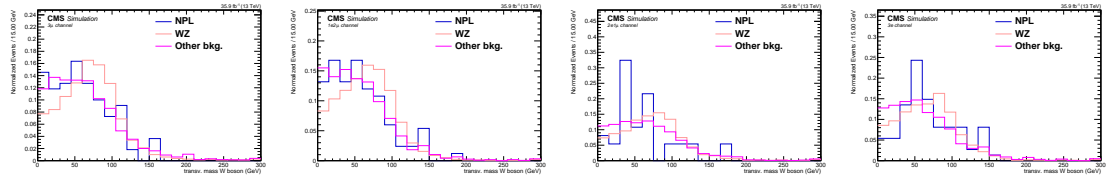


Figure 6.8: The normalised distribution of the transverse mass of the W boson in the WZCR, before the fit. Left: 3 μ , left-middle: 1e2 μ , right-middle: 2e1 μ , and right: 3e leptonic channel.

1594 **6.2 Systematic uncertainties**

1595 The systematic uncertainties entering the analysis are coming from different sources. The
 1596 experimental uncertainties arise from the reconstruction of the objects and are discussed in
 1597 [Section 4.4](#). These influence the number of events passing the selection, so-called normalisation
 1598 uncertainties, or the relative occupancies of the distributions, so-called shape uncertainties. The
 1599 normalisation uncertainties coming from reconstruction include the uncertainty of 2.5% on
 1600 the measured integrated luminosity and the efficiency of the trigger logic used for the analysis
 1601 which has a 1% (5%) uncertainty on the 3 μ and 1e2 μ (2e1 μ and 3e) channels. The pileup
 1602 distribution is calculated via the minimum bias cross section which has a 4.6% uncertainty. This
 1603 uncertainty results in a systematic shift in the pileup distribution and its shape effect is estimated
 1604 by recalculating the pileup distribution for each variation of the minimum bias cross section.
 1605 The shape uncertainties also include the uncertainties coming from the applied lepton scale
 1606 factors. Their systematic uncertainty originates from three sources: identification, isolation and
 1607 tracking. The uncertainties arising from jet energy corrections require a recalculation of all jet
 1608 related kinematic observables and its effect is propagated to the missing transverse energy. The

1609 reweighting of the CSVv2 discriminant is also a source of uncertainty. There are three sources
 1610 of uncertainty contributing to the measurement of the b-tag related scale factors: statistical
 1611 uncertainties, jet energy scale and the purity of the sample. These result in eight uncorrelated
 1612 contributions.

1613 Since the NPL sample is artificially made from data by inverting the isolation of the third
 1614 lepton. Its effect has to be estimated. The shape uncertainty one the NPL processes is obtained
 1615 by varying the isolation inversion with respect to tight working point to the loose working point
 1616 for electrons and muons at the same time. This found to have negligible effect. The uncertainty
 1617 on the normalisation of the overall NPL yield is taken as 50% in accordance the the SM tZq
 1618 search [183].

1619 The uncertainty on the expected yield of the simulated backgrounds is taken to be 30%
 1620 of the yield such that it covers all uncertainties at next to leading order accuracy. Theory
 1621 uncertainties originating from the modelling of the main backgrounds are estimated to account
 1622 for the effect on the shape of the distributions from the choice of parton density funnctions, and
 1623 renormalization (μ_R) and factorization (μ_F) scales. The effect of the renormalization (μ_R) and
 1624 factorization (μ_F) scales is estimated by varying each independently and correlated up and
 1625 down by a factor of two, where the anti-correlated variations are dropped. The envelope of
 1626 these variations is used as an uncertainty. The uncertainties coming from the parton density
 1627 functions used for simulation are estimated using the PDF4LHC recipe [184], which combines
 1628 the MMHT14, CT14, and NNPDF3.0 PDF sets [184]. The theory uncertainties are considered
 1629 for the main backgrounds coming from simulation: WZ+jets, ZZ+jets, t̄tZ, and tZq. This is
 1630 found to have a negligible effect.

1631 The way the uncertainties are treated as nuisance parameters is summarized in Table 6.1.
 1632 The effect of systematic uncertainties that are treated as shape uncertainties is shown in Section
 1633 6.2.1 and Section 6.2.2 .

NOTE: IN-
CLUDE EF-
FECT PDF
AND FAC-
T/RENO

Table 6.1: Uncertainties used in this analysis. The column labelled type represents how the uncertainty is treated for the fit.

Source	Systematic input	Type
nonprompt muon norm.	50%	normalisation
nonprompt electron norm.	50%	normalisation
background $t\bar{t}Z$ norm.	30%	normalisation
background WZ norm.	30%	normalisation
background tZq norm.	30%	normalisation
background ZZ norm.	30%	normalisation
background other MC norm.	30%	normalisation
trigger	1% (5%)	normalisation
lepton identification	$\pm\sigma(p_T, \eta)$	shape
JES	$\pm\sigma(p_T, \eta)$	shape
JER	$\pm\sigma(p_T, \eta)$	shape
b-tagging	$\pm\sigma(p_T, \eta)$	shape
pileup	$\pm\sigma$ of min. bias cross section	shape
PDF	PDF4LHC recipe	shape (WZ, tZq, ttZ, ZZ)
luminosity	2.5%	normalisation
renorm. and fact. scales	varying indep. and corr.	shape

1634 6.2.1 Effect of systematic uncertainties on the transverse mass distribution

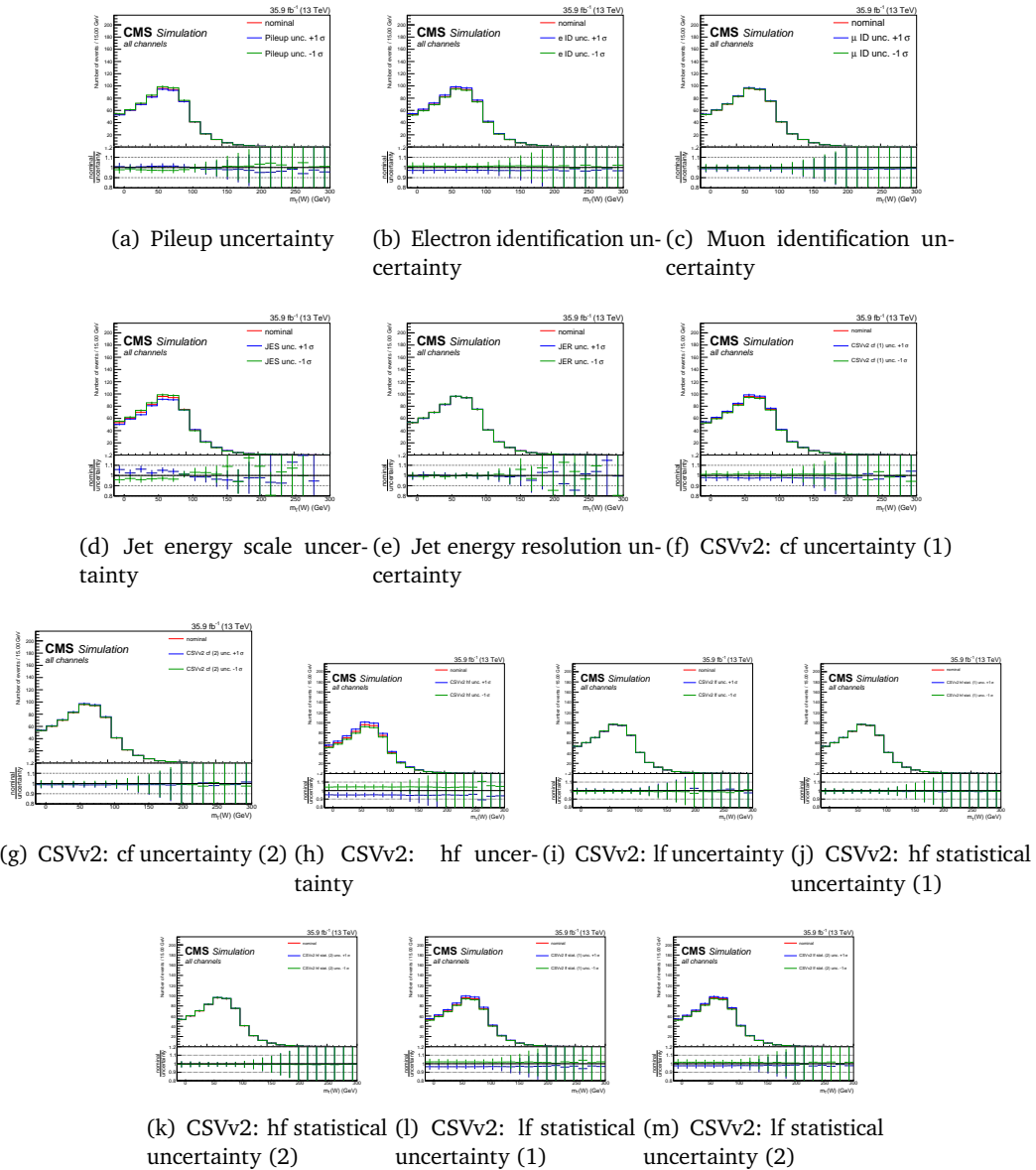


Figure 6.9: Distribution of the nominal values and shift due to systematic uncertainties for the transverse mass of the W boson in the WZCR for the WZ process. All leptonic channels summed.

1635 6.2.2 Effect of the systematic uncertainties on the multivariate discriminator distributions
1636

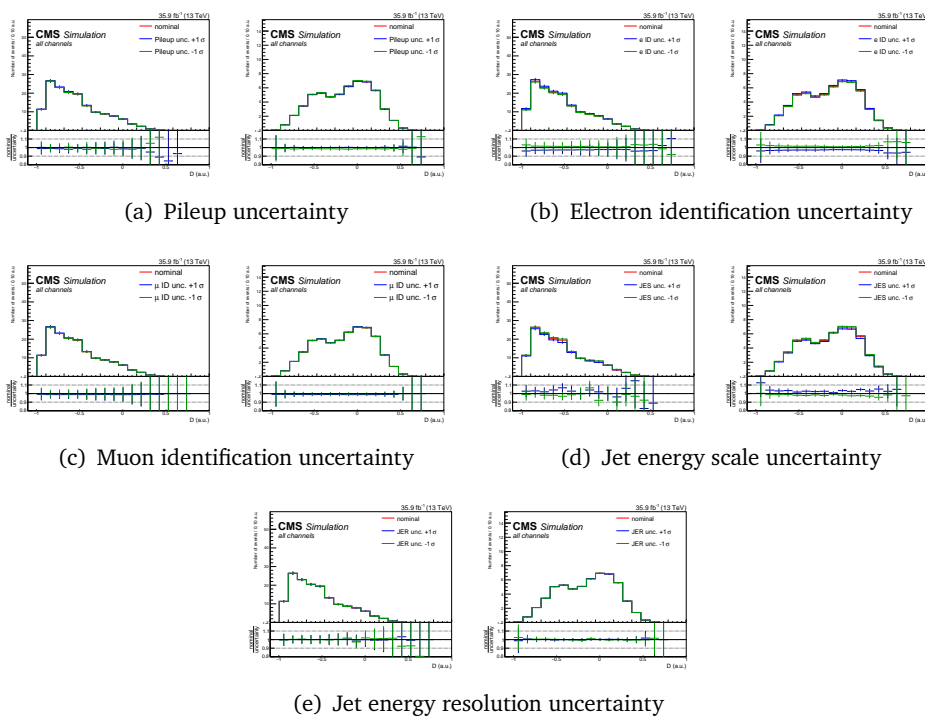


Figure 6.10: Distribution of the nominal values and shift due to systematic uncertainties for the transverse mass of the W boson in the TTSR for the WZ process and FCNC signal involving a tZc vertex. All leptonic channels summed. Part one.

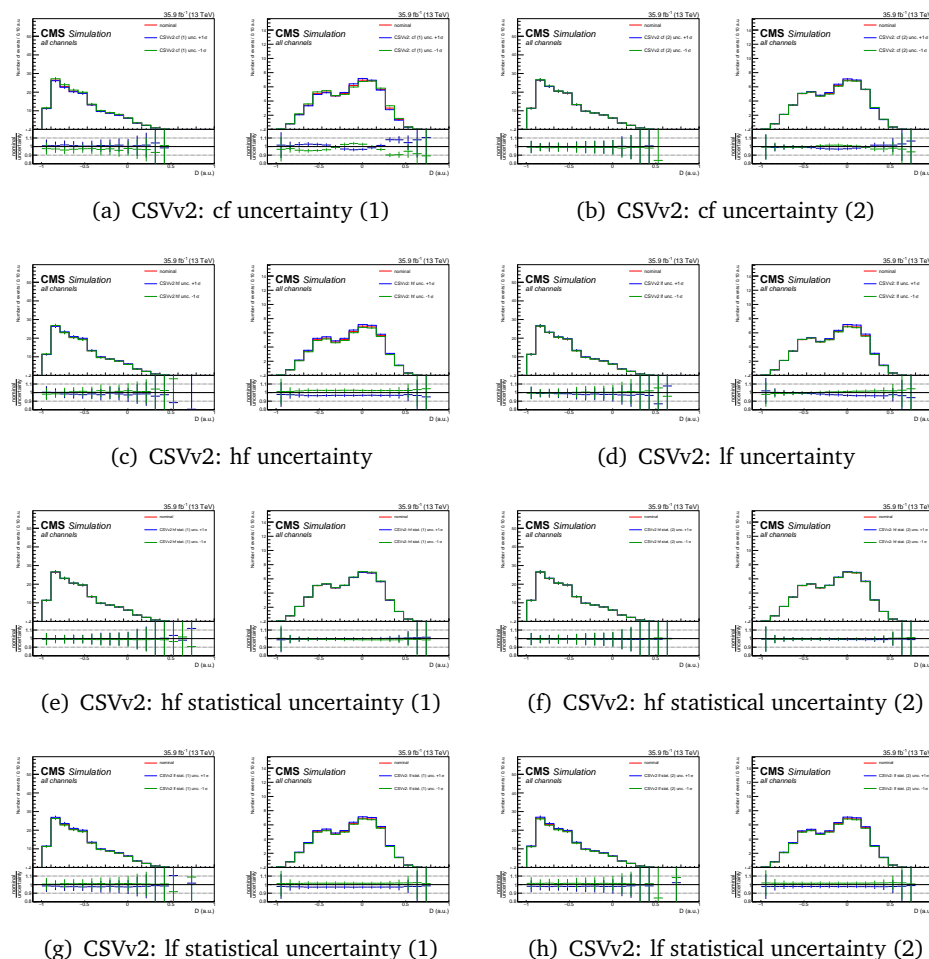


Figure 6.11: Distribution of the nominal values and shift due to systematic uncertainties for the transverse mass of the W boson in the TTSR for the WZ process and FCNC signal involving a tZc vertex. All leptonic channels summed. Part two.

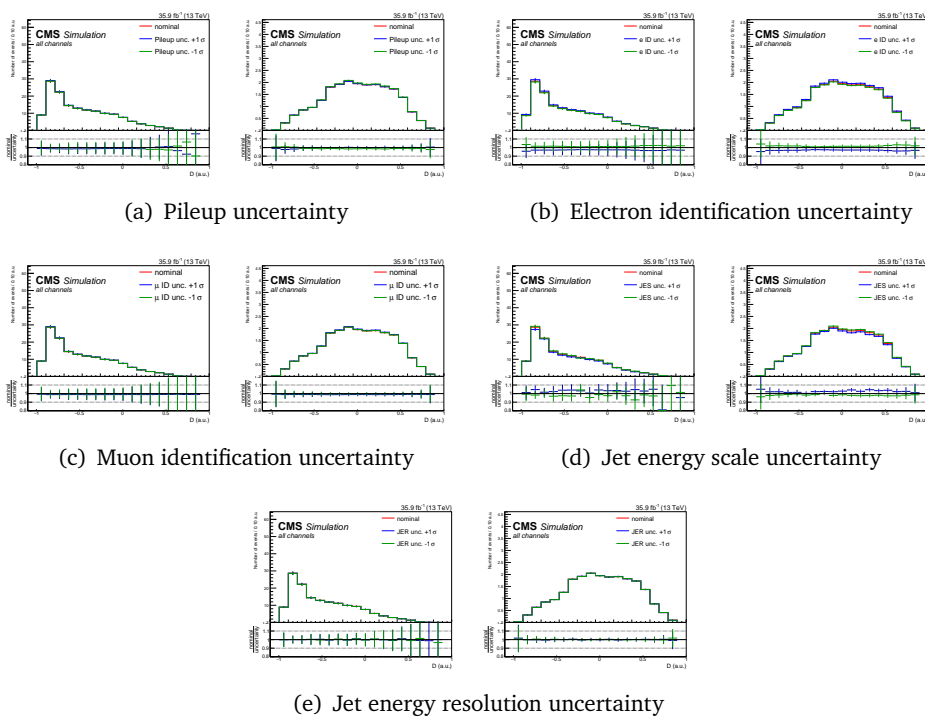


Figure 6.12: Distribution of the nominal values and shift due to systematic uncertainties for the transverse mass of the W boson in the TTSR for the WZ process and FCNC signal involving a tZu vertex. All leptonic channels summed. Part one.

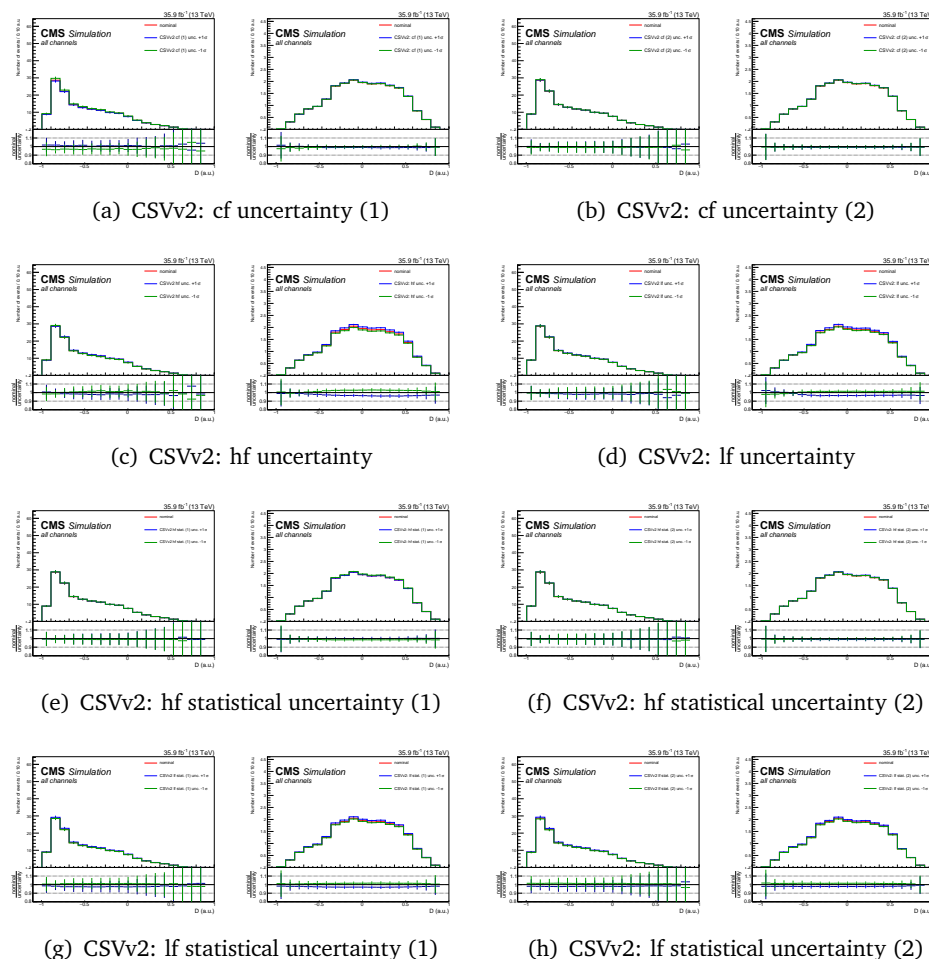


Figure 6.13: Distribution of the nominal values and shift due to systematic uncertainties for the transverse mass of the W boson in the TTSR for the WZ process and FCNC signal involving a tZu vertex. All leptonic channels summed. Part two.

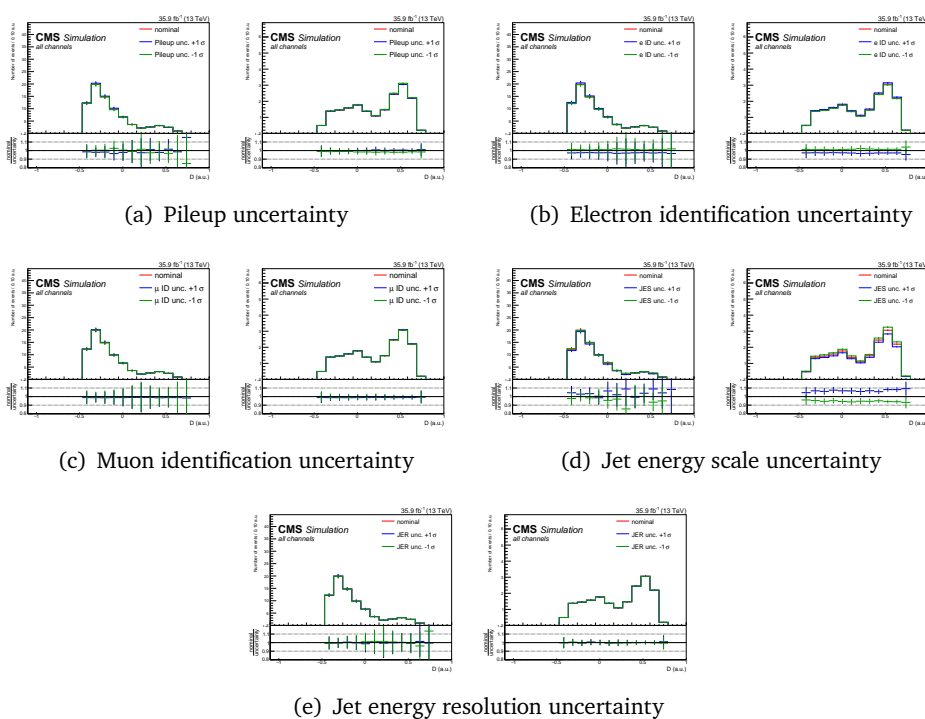


Figure 6.14: Distribution of the nominal values and shift due to systematic uncertainties for the transverse mass of the W boson in the STSR for the WZ process and FCNC signal involving a tZc vertex. All leptonic channels summed. Part one.

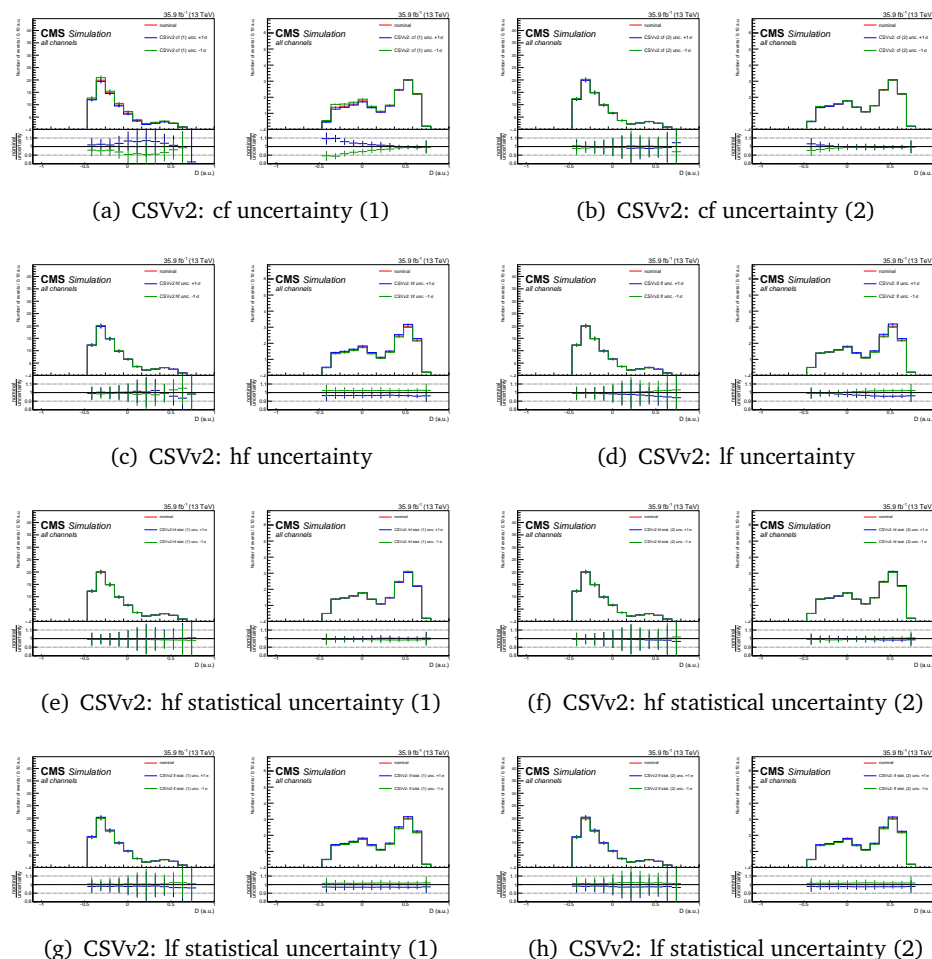


Figure 6.15: Distribution of the nominal values and shift due to systematic uncertainties for the transverse mass of the W boson in the STSR for the WZ process and FCNC signal involving a tZc vertex. All leptonic channels summed. Part two.

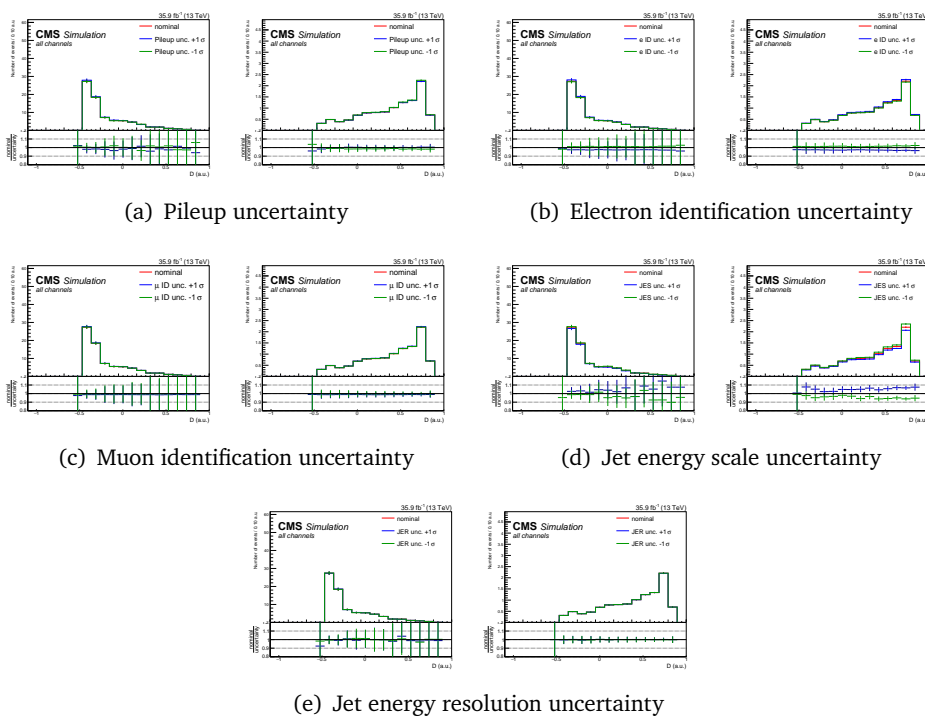


Figure 6.16: Distribution of the nominal values and shift due to systematic uncertainties for the transverse mass of the W boson in the STSR for the WZ process and FCNC signal involving a tZu vertex. All leptonic channels summed. Part one.

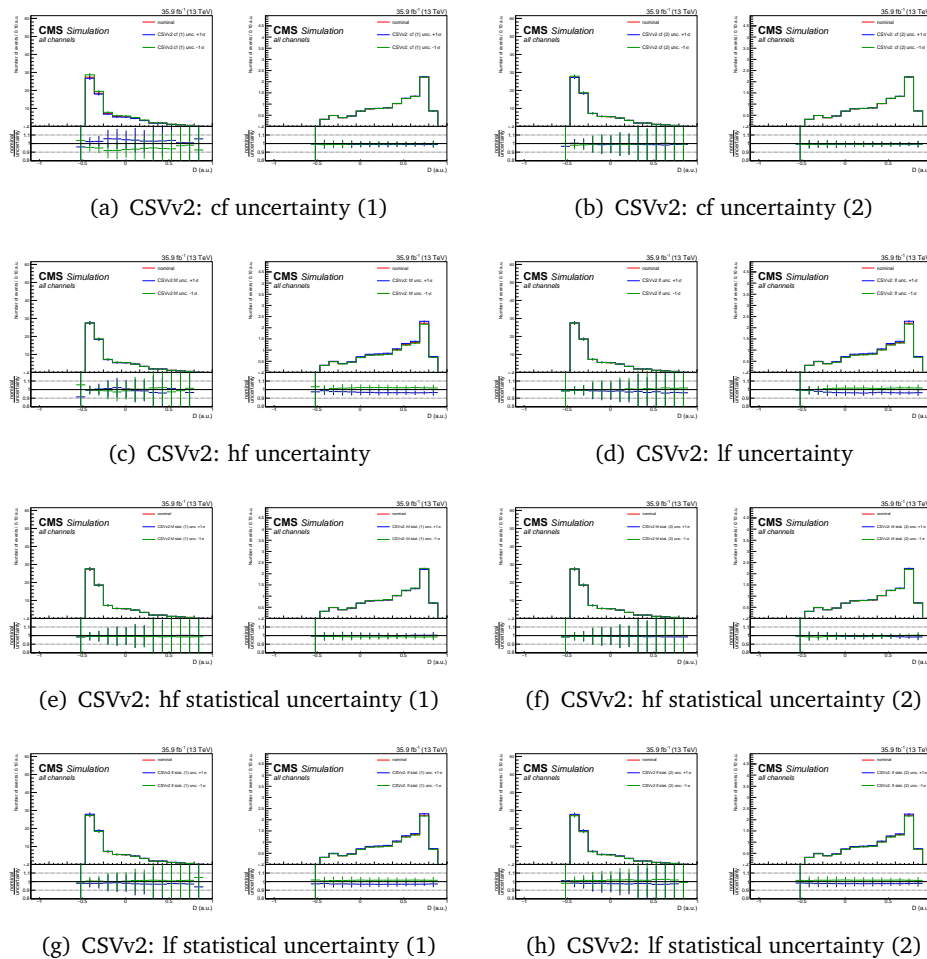


Figure 6.17: Distribution of the nominal values and shift due to systematic uncertainties for the transverse mass of the W boson in the STSR for the WZ process and FCNC signal involving a tZu vertex. All leptonic channels summed. Part two.

1637 **6.3 Limit setting procedure validation**

1638 The analysis strategy has been established using a blinded strategy. Through the use of a pseudo
 1639 dataset, the limit setting procedure has been validated. Signal injection tests for which the
 1640 signal strength from a pseudo dataset with a pre-set signal strength is estimated are performed
 and shown in [Figure 6.18](#).

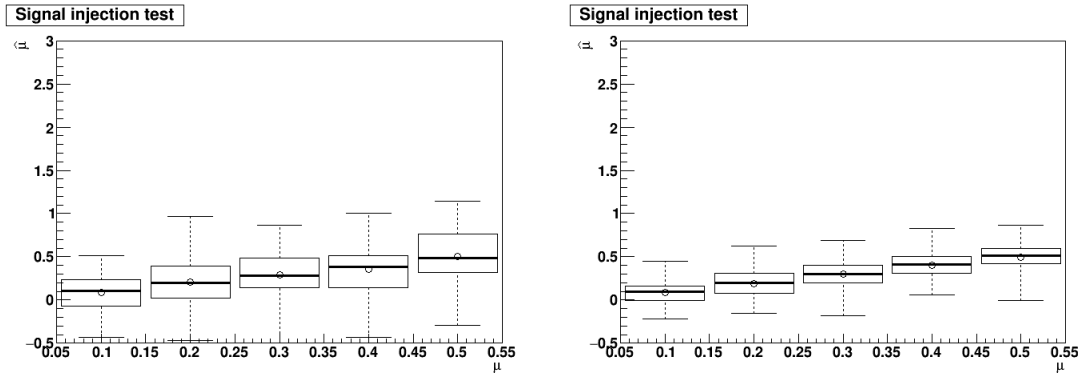


Figure 6.18: The obtained signal strength with the Maximum Likelihood method is in agreement with the signal strength used to generate the Asimov data set for the tZu (left) and tZc (right) couplings.

1641

1642 Another validation has been done by performing a Maximum Likelihood fit in the WZCR only,
 1643 considering all lepton channels. A simultaneous fit of the signal strength of the NPe, NP μ and
 1644 the WZ+jets backgrounds is done by using the multi-dimensional fit in Higgs Combine Tool.
 1645 The resulting signal strengths can then be applied on the distribution of the transverse mass
 1646 of the W boson to verify data/MC agreement, as can be seen in Fig. [6.20](#). Furthermore, a
 1647 goodness of fit test is performed, resulting in a p-value of 0.3 (see Fig. [6.19](#)).

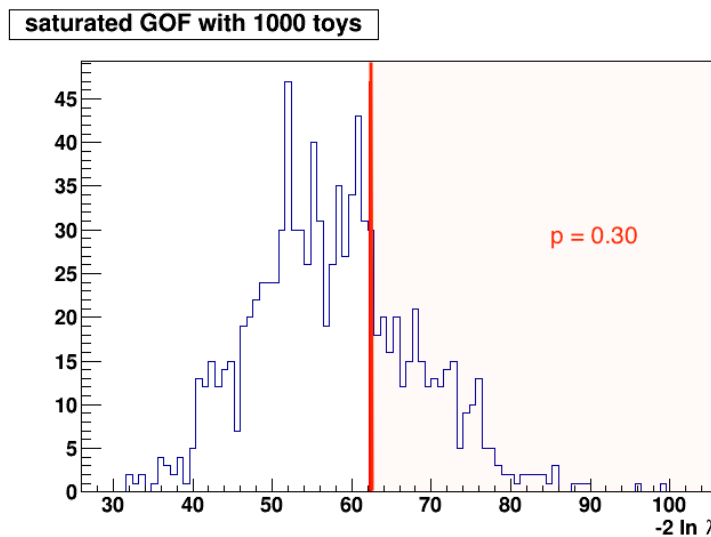


Figure 6.19: Goodness of fit testing in the WZCR with 1000 toys. The likelihood ratio is denoted as λ .

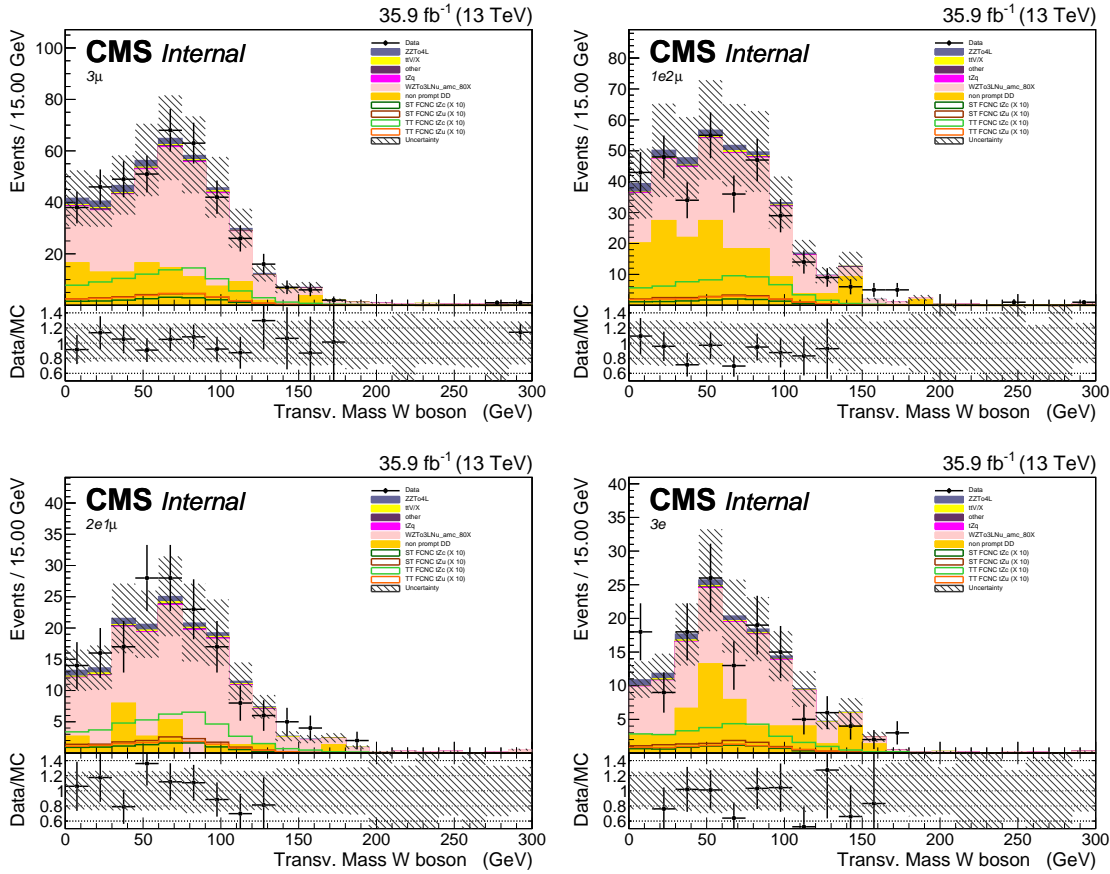


Figure 6.20: The transverse mass of the W boson in the WZCR for the 3μ channel (left, upper), $1e2\mu$ channel (right, upper), $2e1\mu$ channel (left, lower), and $3e$ channel (right, lower). The uncertainty band does not include theoretical uncertainties.

1648 6.4 Results and discussion

1649 The limit setting procedure explained in [Section 3.4](#) is applied and results are obtained for each
 1650 lepton channel separately as well as the combination. For both the tZu and tZc coupling, the
 1651 maximum likelihood estimator of their signal strengths $\hat{\mu}$ is compatible with zero. This is shown
 1652 in [Figure 6.21](#). One can see that the $3e$ leptonic channel has the largest uncertainty. This is due
 1653 to the fact that this channel is the most influenced by the lack of statistics for this search.

The maximum likelihood estimators for the nuisance parameters $\hat{\theta}$ are shown in [Figure 6.23](#) and [Figure 6.24](#). Their values obtained from the signal plus background or background only fits are in agreement. The transfer factors have an initial value different than one and have small uncertainties. The normalisation uncertainties on the yields of the simulated backgrounds get constrained by the fit. A well known verification of the error coverage for the fit is the pull distribution. For a random variable x following a Gaussian distribution of mean m and width w , the pull g is defined as

$$g = \frac{x - m}{w}, \quad (6.1)$$

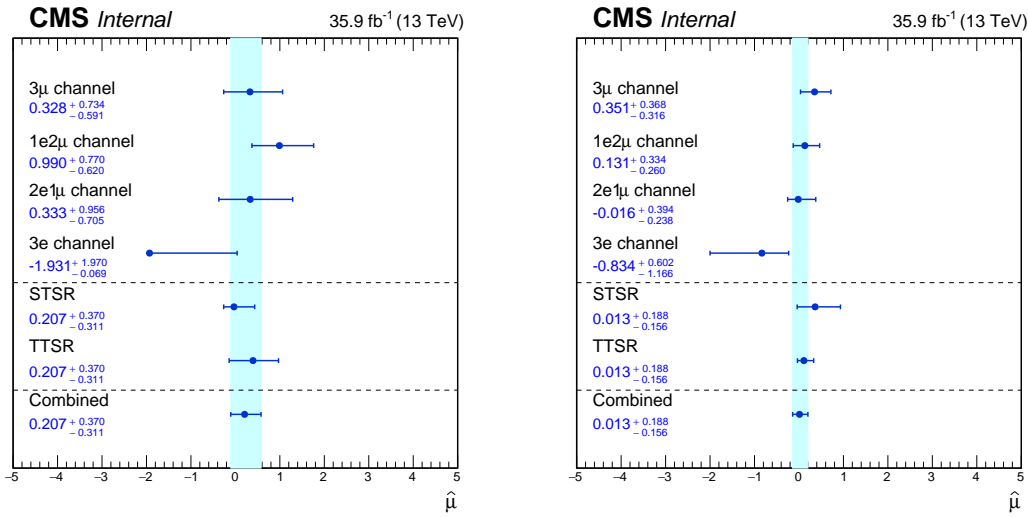


Figure 6.21: The maximum likelihood estimators for the signal strengths for the tZu vertex (right) and tZc vertex (left) per lepton channel as well as the combination in the STSR, TTSR, and all regions combined.

1654 and follows a standard Gaussian with mean zero and unit width. This property can be applied to
 1655 our case of parameter estimation due to the central limit theorem [185]. The pull distributions
 are shown in Figure 6.22. These are peaking at zero with tails going to ± 2.5 .

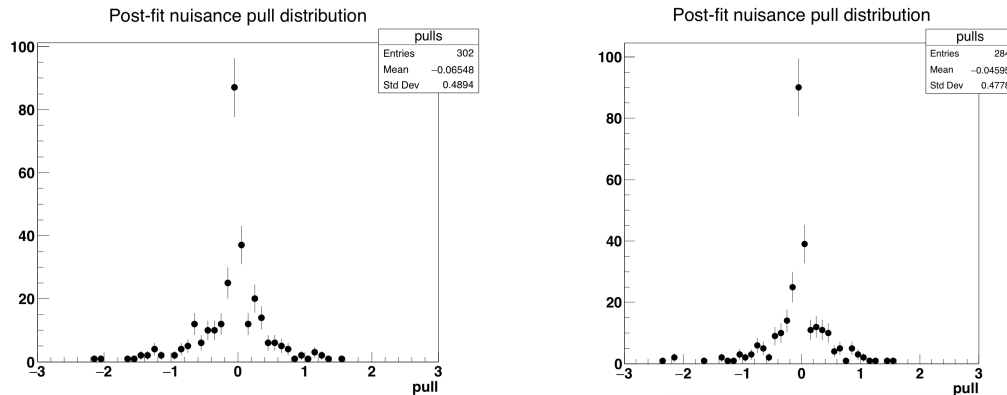


Figure 6.22: Post-fit distribution of the pulls for the tZu (left) and tZc (right) vertex.

1657 The nuisance parameters causing the tails in the pull distributions are the ones related to the
1658 NPL background as can be seen in [Figure 6.25](#), [Figure 6.26](#), [Figure 6.27](#), and [Figure 6.28](#). Here
1659 one can see that the nuisance parameters related to the NPL normalisations are shifted with
1660 respect to their initial values. This is to be expected since their initial normalisation is arbitrary.
1661 Furthermore, the effect of the uncertainties on the maximum likelihood estimate of the signal
1662 strength is shown. The search is limited by lack of data, as can be seen from [Figure 6.35](#) and
1663 [Figure 6.36](#). After the limited data statistics, the most important systematic uncertainty are the
1664 ttZ normalisation, JES uncertainty and the NPL normalisation uncertainty.

1665 The distributions of multivariate discriminating variables as well as the distribution of the
1666 transverse mass of the W boson are recreated with the maximum likelihood estimations of the
1667 nuisance parameters. The resulting distributions are shown in [Figure 6.29](#), [Figure 6.30](#), [Figure](#)
1668 [6.31](#), [Figure 6.32](#), and [Figure 6.33](#). The pre fit distributions are given in [Appendix E](#). The postfit
1669 distributions of the inputvariables for the BDTs are given in [Appendix F.2](#).

NOTE:
MAKE
THESE

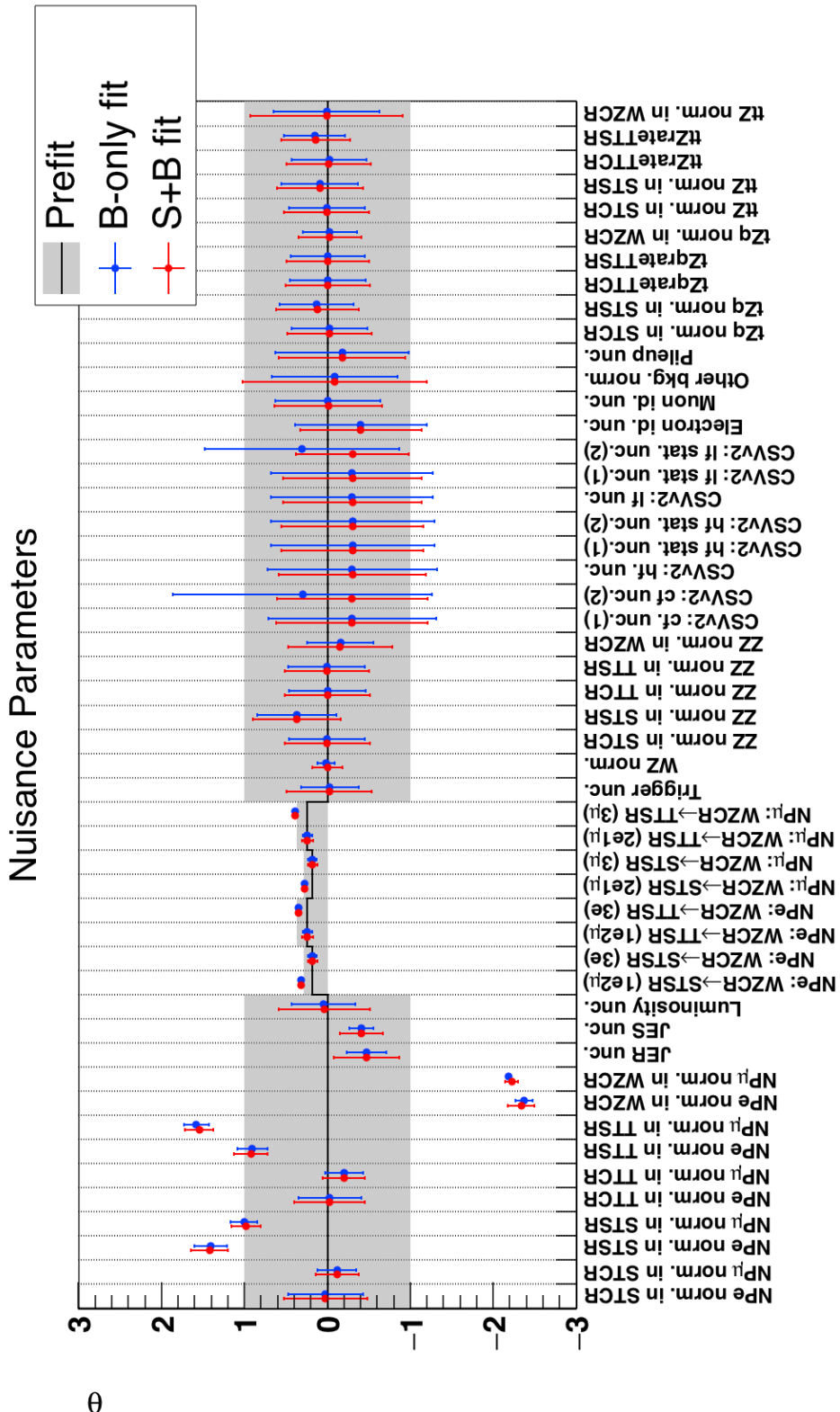


Figure 6.23: Maximum likelihood estimators for the tZ_c vertex.

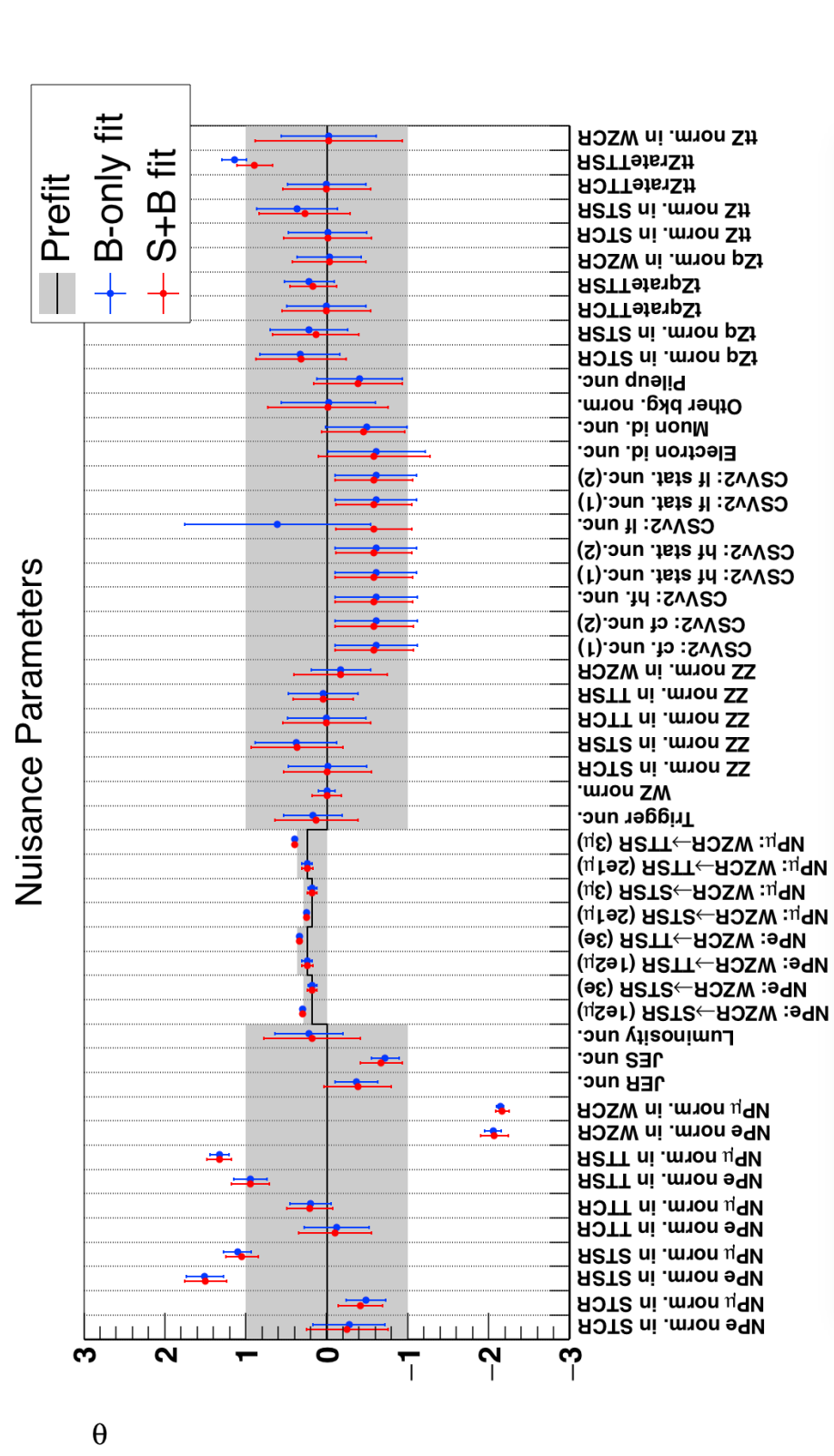


Figure 6.24: Maximum likelihood estimators for the tZu vertex.

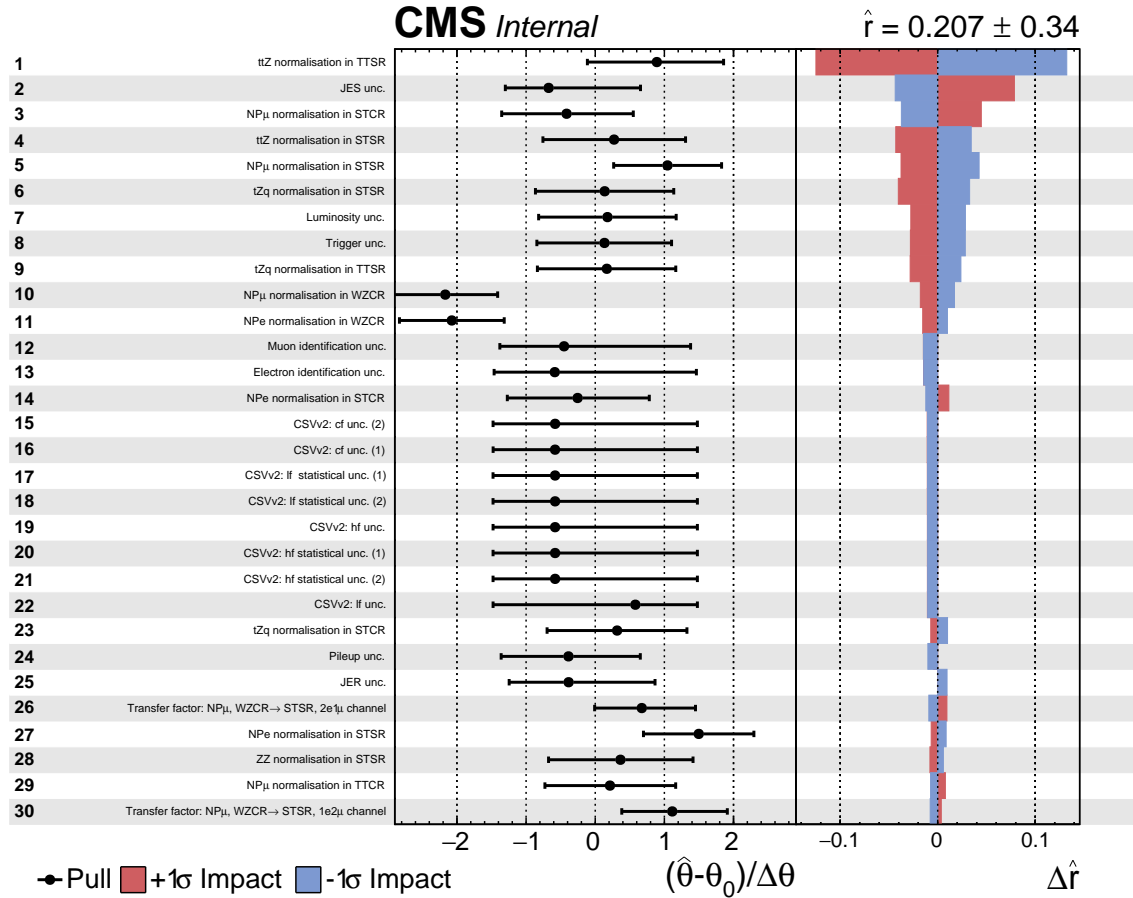


Figure 6.25: The pulls of each nuisance parameter and the influence of their uncertainty on the maximum likelihood estimation of the signal strength \hat{r} for the tZu vertex, part one.

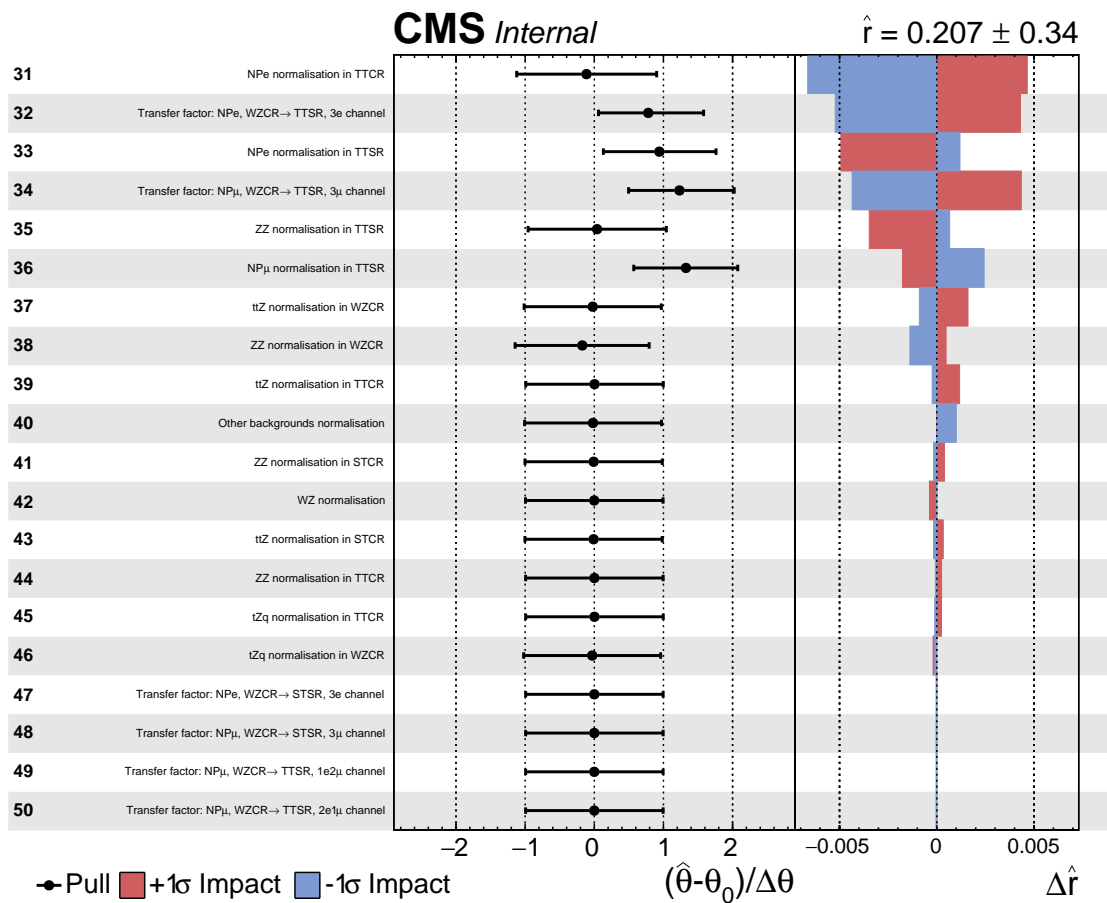


Figure 6.26: The pulls of each nuisance parameter and the influence of their uncertainty on the maximum likelihood estimation of the signal strength \hat{r} for the tZu vertex, part two.

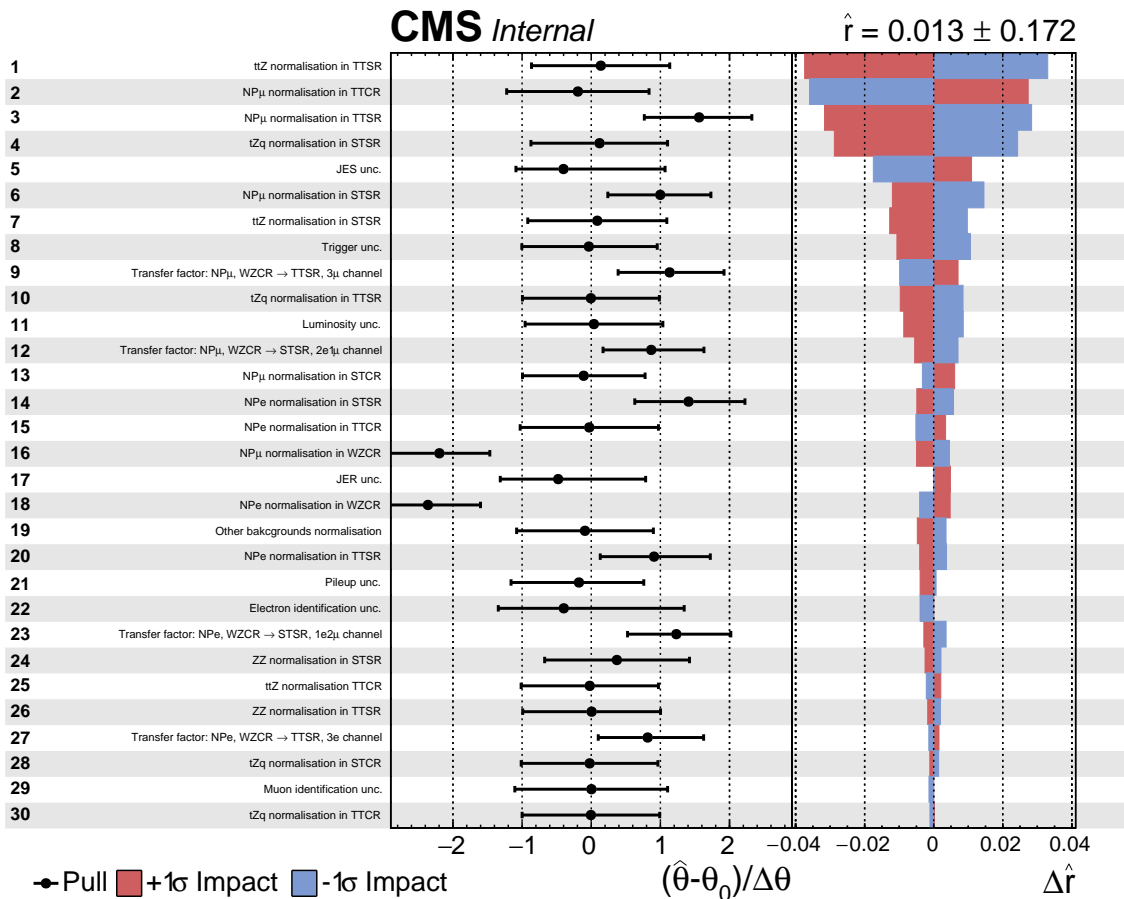


Figure 6.27: The pulls of each nuisance parameter and the influence of their uncertainty on the maximum likelihood estimation of the signal strength \hat{r} for the tZc vertex, part one.

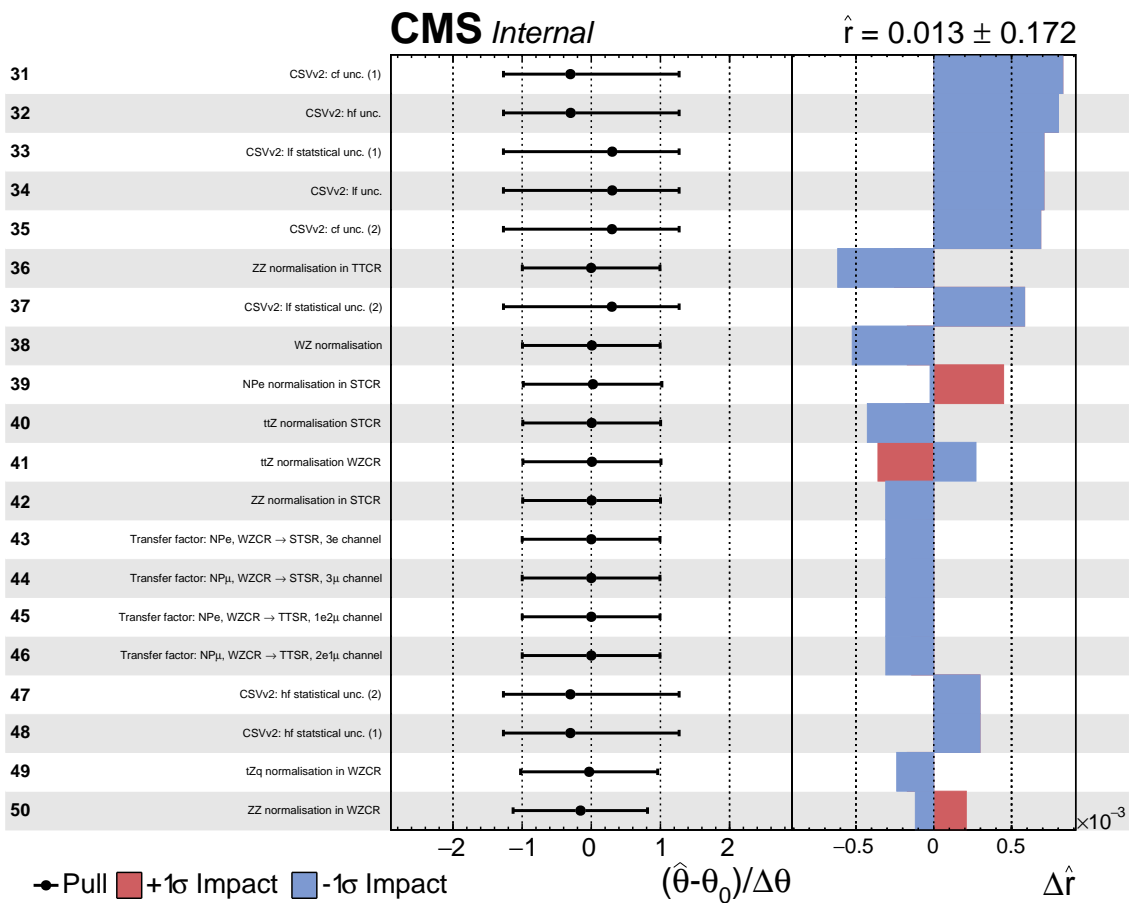


Figure 6.28: The pulls of each nuisance parameter and the influence of their uncertainty on the maximum likelihood estimation of the signal strength \hat{r} for the tZc vertexg, part two.

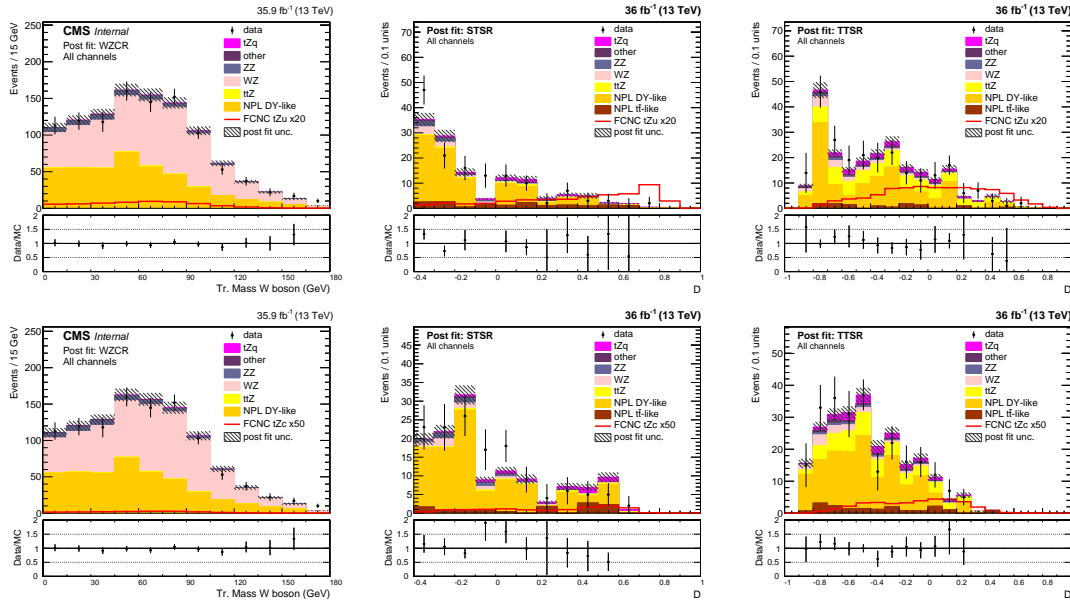


Figure 6.29: Post fit distributions for the all leptonic channels of the transverse mass of the W boson in the WZCR (left), the multivariate discriminating variable in the STSR (middle), and the multivariate discriminating variable in the TTSR (right) for the tZu (top) and tZc (bottom) couplings.

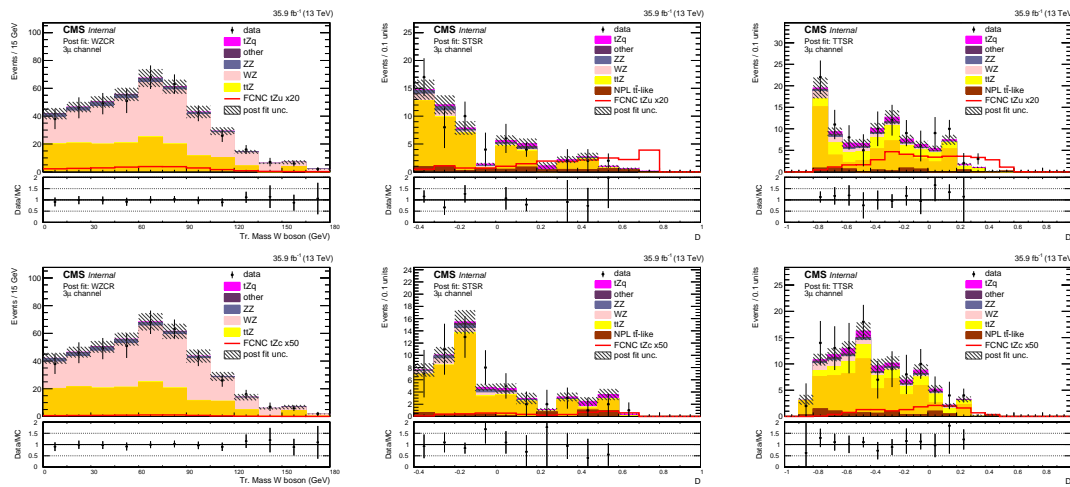


Figure 6.30: Post fit distributions for the 3μ leptonic channel of the transverse mass of the W boson in the WZCR (left), the multivariate discriminating variable in the STSR (middle), and the multivariate discriminating variable in the TTSR (right) for the tZu (top) and tZc (bottom) couplings.

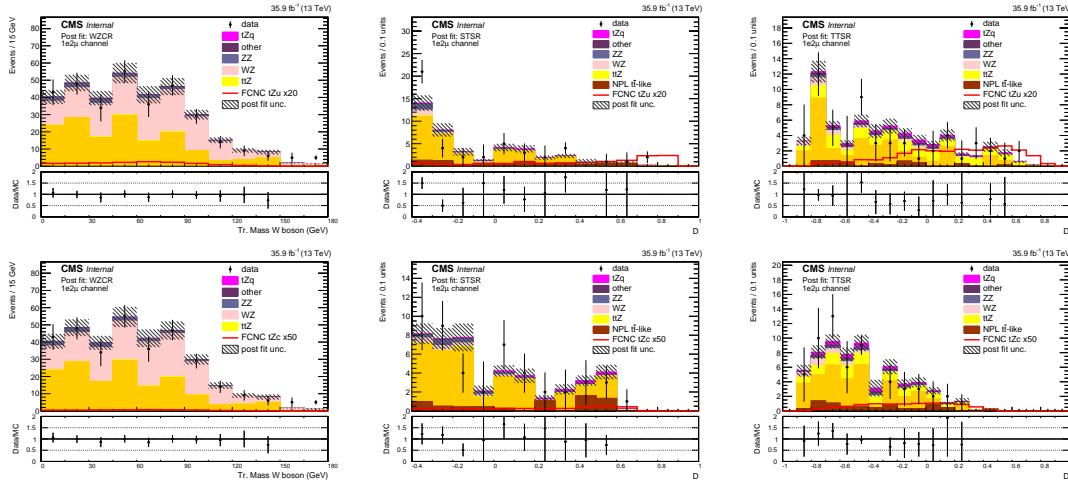


Figure 6.31: Post fit distributions for the $1e2\mu$ leptonic channel of the transverse mass of the W boson in the WZCR (left), the multivariate discriminating variable in the STSR (middle), and the multivariate discriminating variable in the TTSR (right) for the tZu (top) and tZc (bottom) couplings.

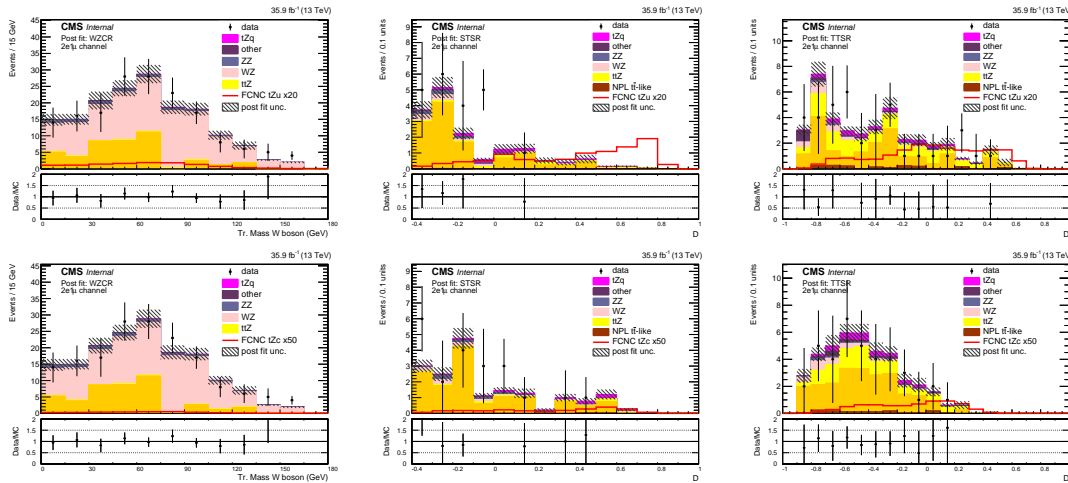


Figure 6.32: Post fit distributions for the $2e1\mu$ leptonic channel of the transverse mass of the W boson in the WZCR (left), the multivariate discriminating variable in the STSR (middle), and the multivariate discriminating variable in the TTSR (right) for the tZu (top) and tZc (bottom) couplings.

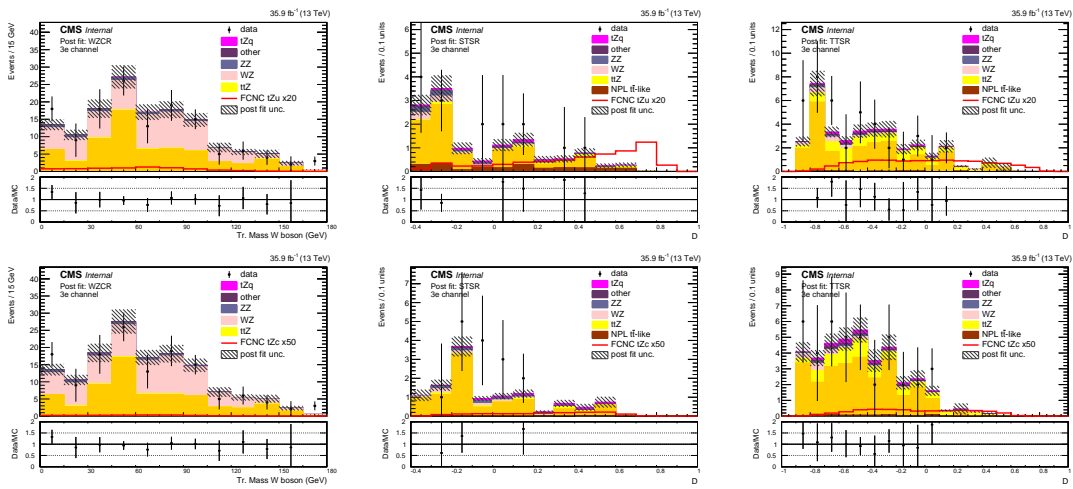


Figure 6.33: Post fit distributions for the 3e leptonic channel of the transverse mass of the W boson in the WZCR (left), the multivariate discriminating variable in the STSR (middle), and the multivariate discriminating variable in the TTSR (right) for the tZu (top) and tZc (bottom) couplings.

1670 **6.4.1 One dimensional limits**

1671 The limit setting procedure used in this search returns limits on the signal strength modifier
 1672 which can be translated to signal cross sections. These limits are translated to a limit on the
 1673 branching fraction using Equation 1.39. Additionally, the limit on the couplings are extracted
 1674 using the fact that the cross sections are quadratically dependent on the couplings. In Figure
 1675 6.34, the resulting limits at 95% CL on the branching fraction and couplings related to the
 1676 tZu vertex is shown. This observed (expected) limit amounts to $\mathcal{B} < 0.024\%$ (0.015%) when
 1677 $\kappa_{tZu}/\Lambda \neq 0$ and $\kappa_{tZc}/\Lambda = 0$. The expected limit surpasses the CMS search at a centre-of-mass of
 1678 8 TeV expected limits of 0.027% [41]. The observed limit of 0.024% for the tZu interaction
 1679 doesn't surpass the CMS 8 TeV observed limit of 0.022% [41]. The ATLAS collaboration has set
 1680 limits 95% CL at a centre-of-mass of 13 TeV [40] with observed (expected) limits of 0.017%
 1681 (0.024%) for the tZu coupling. The expected limit presented in this analysis surpasses the
 1682 expected limit for tZu.

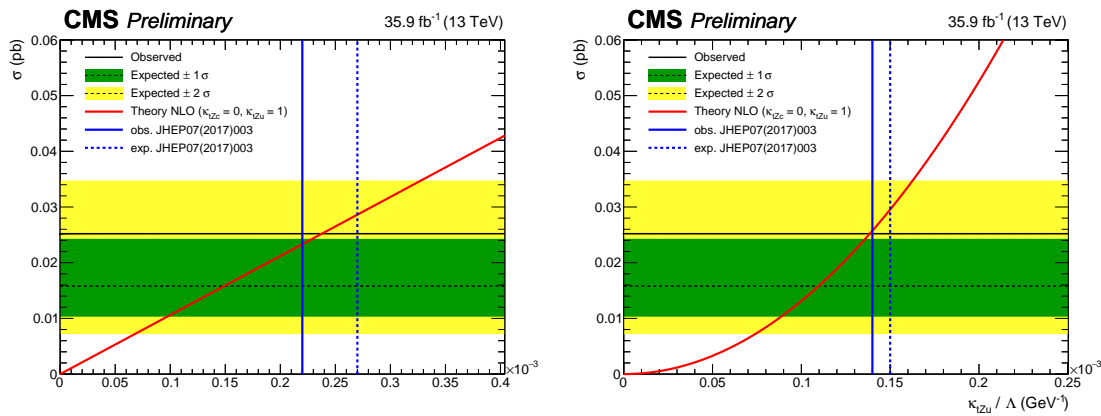


Figure 6.34: Exclusion limits at 95% CL on the FCNC branching fractions (left) and couplings (right) as a function of the cross section of the FCNC process, considering only the tZu vertex. The CMS observed (expected) limit at 95% CL at a centre-of-mass of 8 TeV [41] is given with a blue line (dashed line).

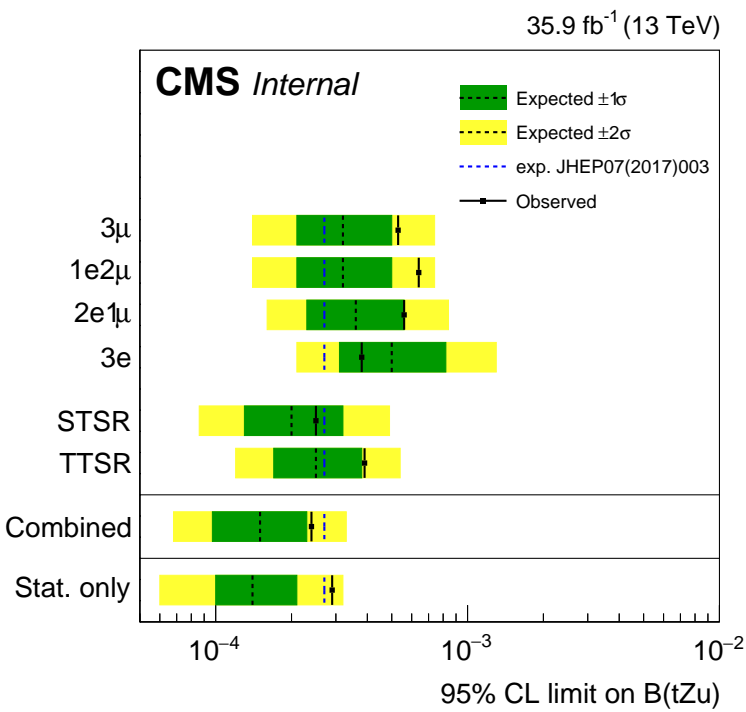
1682

1683 In Figure 6.35 and Table 6.2, the limits for each leptonic channel separate as well as their
 1684 combined limits are shown for the tZu vertex. The leptonic channels are in agreement with
 1685 each other, where the presence of a muon helps pushing the limit further. The STSR is the
 1686 most sensitive region because of the higher presence of the targeted single top quark signal.
 1687 Further, one can see that by combining signle top quark and top quark pair signals, one gains
 1688 in sensitivity.

1689 In Figure 6.36, the resulting limits at 95% CL on the branching fraction and couplings
 1690 related to the tZc vertex is shown. or this coupling, the observed (expected) limit at 95%
 1691 CL is $\mathcal{B} < 0.045\%$ (0.037%) when $\kappa_{tZc}/\Lambda \neq 0$ and $\kappa_{tZu}/\Lambda = 0$. The expected limit surpasses
 1692 the CMS search at a centre-of-mass of 8 TeV expected limits of 0.118% [41]. This also the
 1693 case for the observed limit of 0.045% for the tZc interaction, which surpasses the CMS 8 TeV
 1694 observed limit of 0.049% [41]. The observed (expected) limits set by the ATLAS collaboration
 1695 at a centre-of-mass of 13 TeV [40] are 0.023% (0.032%) for the tZc coupling. The expected
 1696 limit presented in this analysis is in accordance with this limit.

Table 6.2: Expected limits on the branching fractions at 95% CL for the tZu coupling [40, 41].

	expected	+2 σ	+1 σ	-1 σ	-2 σ	observed
3 μ	0.032%	0.074%	0.050%	0.021%	0.014%	0.053%
1e2 μ	0.032%	0.074%	0.050%	0.021%	0.014%	0.064%
2e1 μ	0.036%	0.084%	0.056%	0.023%	0.016%	0.056%
3e	0.050%	0.13%	0.082%	0.031%	0.021%	0.038%
STSR only	0.020%	0.049%	0.032%	0.013%	0.0086%	0.025%
TTSR only	0.025%	0.054%	0.038%	0.025%	0.017%	0.039%
combined	0.015%	0.033%	0.023%	0.0097%	0.0068%	0.024%
8 TeV CMS (19.7 fb^{-1})	0.027%	-%	0.42%	0.018%	-%	0.022%
13 TeV ATLAS (36 fb^{-1})	0.024%	-%	0.35%	0.017%	-%	0.017%

**Figure 6.35:** Exclusion limits at 95% CL for each leptonic channel and signal region on the FCNC tZu branching fractions considering one non-vanishing coupling at a time. The CMS observed (expected) limit at 95% CL at a centre-of-mass of 8 TeV [41] is given with a blue line (dashed line).

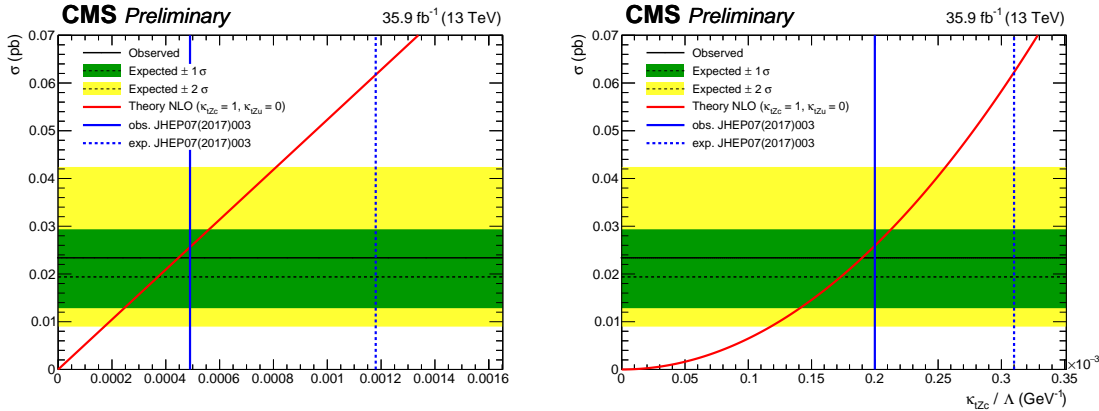


Figure 6.36: Exclusion limits at 95% CL on the FCNC branching fractions (left) and couplings (right) as a function of the cross section of the FCNC process, considering only the tZc vertex. The CMS observed (expected) limit at 95% CL at a centre-of-mass of 8 TeV [41] is given with a blue line (dashed line).

1697 The limits for each leptonic channel separate as well as their combined limits are shown for
 1698 the tZc vertex in [Figure 6.37](#) and [Table 6.3](#). Also here, the leptonic channels are in agreement
 1699 with each other, and the presence of a muon helps the sensitivity. For the tZu vertex, the TTSR
 1700 is the most sensitive region and by combining single top quark and top quark pair signals, one
 1701 also gains in sensitivity.

Table 6.3: Expected limits on the branching fractions at 95% CL for the tZc coupling [40, 41].

	expected	+2σ	+1σ	-1σ	-2σ	observed
3μ	0.070%	0.15%	0.10%	0.046%	0.032%	0.12%
1e2μ	0.079%	0.18%	0.12%	0.052%	0.036%	0.096%
2e1μ	0.089%	0.20%	0.14%	0.058%	0.040%	0.099%
3e	0.12%	0.29%	0.19%	0.075%	0.050%	0.095%
STSR only	0.10%	0.2%	0.16%	0.066%	0.045%	0.17%
TTSR only	0.044%	0.094%	0.066%	0.029%	0.020%	0.043%
combined	0.037%	0.081%	0.056%	0.025%	0.017%	0.045%
8 TeV CMS (19.7 fb^{-1})	0.118%	-%	0.222%	0.071%	-%	0.049%
13 TeV ATLAS (36 fb^{-1})	0.032%	-%	0.046%	0.022%	-%	0.023%

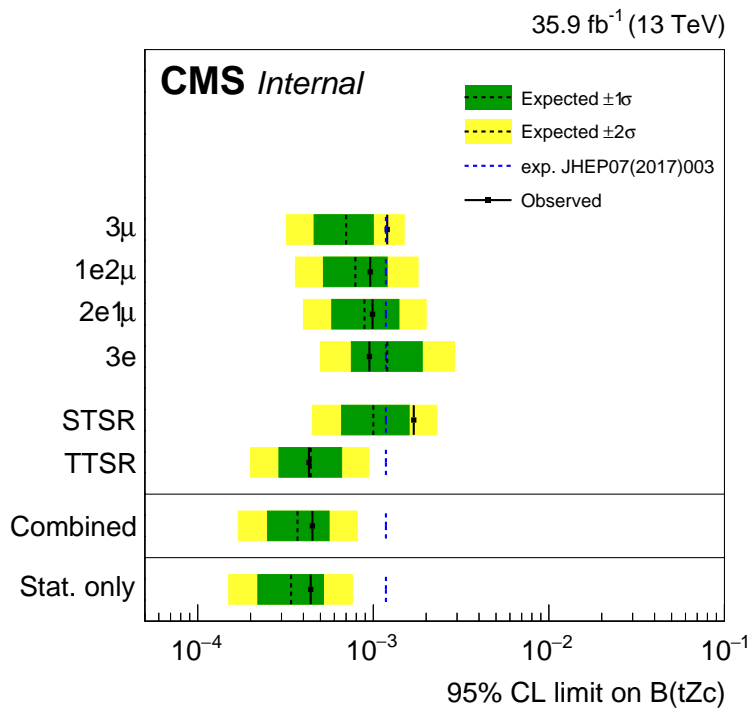


Figure 6.37: Exclusion limits at 95% CL for each leptonic channel and signal region on the FCNC tZc branching fractions considering one non-vanishing coupling at a time. The CMS observed (expected) limit at 95% CL at a centre-of-mass of 8 TeV [41] is given with a blue line (dashed line).

1702 6.4.2 Two-dimensional limits

One can interpolate the one dimensional limits λ_{tZq}^{1D} to a scenario where both couplings are on-vanishing. The interpolation is taken from Ref. [45], where an experimental extrapolation formulae

$$\kappa_{tZc}/\Lambda = \lambda_{tZc}^{1D} \sqrt{1 - \frac{\kappa_{tZu}/\Lambda}{\lambda_{tZu}^{1D}}}, \quad (6.2)$$

is found from 100 benchmark scenarios. These scenarios are constructed from existing signal samples as

$$\text{Signal yield} = (\kappa_{tZu}/\Lambda)^2 (\text{ST Zut yield} + \text{TT Zut yield}) + (\kappa_{tZc}/\Lambda)^2 (\text{ST Zct yield} + \text{TT Zct yield}). \quad (6.3)$$

1703 For each scenario a dedicated BDT training is performed and the expected limit at 95% CL are
1704 calculated. The resulting two-dimensional limits are shown in Figure 6.38.

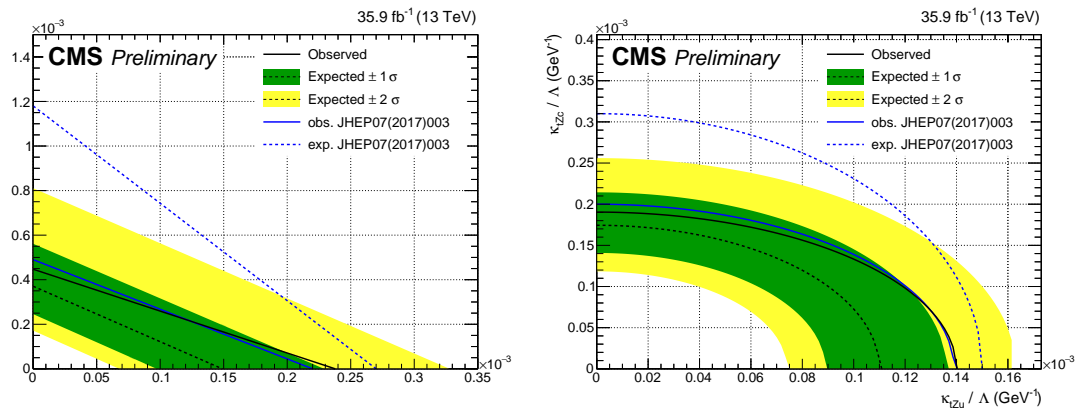


Figure 6.38: Two-dimensional limits on the branching fractions (left) and couplings (right) for FCNC interactions involving a tZq vertex. The CMS observed (expected) limit at 95% CL at a centre-of-mass of 8 TeV [41] is given with a blue line (dashed line).

Denouement of the top-Z FCNC hunt at 13 TeV

1705

7

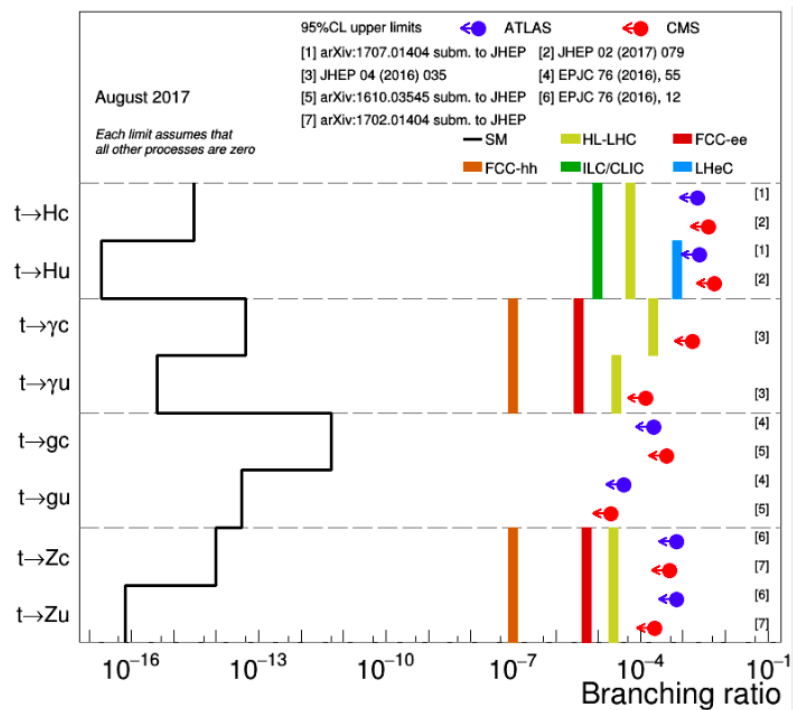


Figure 7.1:

Trigger scale factors



1707 The trigger scale factors measured as a function of lepton p_T , using the dataset collected by
 1708 E_T^{miss} triggers and WZ simulation, after a 3 lepton and jets selection, in the Z mass window. All
 1709 corrections to simulation are applied.

Table A.1: Trigger efficiencies on data events selected with E_T^{miss} triggers and WZ simulation for all leptonic channels together. The unweighed number of events is quoted. When there are no events passing the cuts, it is indicated with N/A. The uncertainties are statistical uncertainties.

ALL CHANNEL	data		WZ simulations	
	Efficiency	unc.	Efficiency	unc.
3 lep, at least one jet	117/118 = 99.15 %	12.94%	18047/18055 = 99.96%	1.05%
STSR	6/6 = 100.00%	57.74%	1541/1541 = 100.00%	3.60%
TTSR	26/27 = 96.30%	26.46%	1791/1792 = 99.94%	3.34%
WZCR	69/69 = 100.00 %	17.03%	14405/14412=99.95%	1.18%

Table A.2: Trigger efficiencies on data events selected with E_T^{miss} triggers and WZ simulation for 3 μ leptonic channel together. The unweighed number of events is quoted. When there are no events passing the cuts, it is indicated with N/A. The uncertainties are statistical uncertainties.

3 μ CHANNEL	data		WZ simulations	
	Efficiency	unc.	Efficiency	unc.
3 lep, at least one jet	40/40 = 100.00 %	22.36 %	7814/7814 = 100.00%	1.60%
STSR	N/A	N/A	687/687 = 100%	5.40%
TTSR	13/13 = 100.00%	39.22%	763/763 = 100.00%	5.12%
WZCR	22/22 = 100.00 %	30.15%	6238/6238=100.00%	1.79%

Table A.3: Trigger efficiencies on data events selected with E_T^{miss} triggers and WZ simulation for 3e leptonic channel together. The unweighted number of events is quoted. When there are no events passing the cuts, it is indicated with N/A. The uncertainties are statistical uncertainties.

3e CHANNEL	data		WZ simulations	
	Efficiency	unc.	Efficiency	unc.
3 lep, at least one jet	20/21 = 95.24%	29.76%	2211/2215 = 99.82 %	3.00%
STS R	4/4 = 100.00%	70.71%	176/176 = 100.00%	10.66%
TTS R	2/3 = 66.67%	60.86%	242/242 = 100.00%	9.09%
WZCR	14/14 = 100.00 %	37.80%	1744/1748=99.77%	3.38%

Table A.4: Trigger efficiencies on data events selected with E_T^{miss} triggers and WZ simulation for 2e1 μ leptonic channel together. The unweighted number of events is quoted. When there are no events passing the cuts, it is indicated with N/A. The uncertainties are statistical uncertainties.

2e1 μ CHANNEL	data		WZ simulations	
	Efficiency	unc.	Efficiency	unc.
3 lep, at least one jet	32/32 = 100.00 %	25.00 %	3116/3118 = 99.94%	2.53%
STS R	1/1 = 100.00%	141.42%	255/255 = 100%	8.86%
TTS R	9/9 = 100.00%	47.14%	291/291 = 100.00%	8.29%
WZCR	14/14 = 100.00 %	37.80%	2529/2531=99.92%	2.81%

Table A.5: Trigger efficiencies on data events selected with E_T^{miss} triggers and WZ simulation for 1e2 μ leptonic channel together. The unweighted number of events is quoted. When there are no events passing the cuts, it is indicated with N/A. The uncertainties are statistical uncertainties.

1e2 μ CHANNEL	data		WZ simulations	
	Efficiency	unc.	Efficiency	unc.
3 lep, at least one jet	25/25 = 100.00%	28.28%	4906/4908 = 99.96 %	2.02%
STS R	1/1 = 100.00%	141.42%	423/423 = 100.00%	6.88%
TTS R	2/2 = 100.00%	100.00%	495/496 = 99.80%	6.34%
WZCR	19/19 = 100.00 %	32.44%	3894/3895 =99.97%	2.27%

Dilepton controlplots

B

Statistical independent regions

1711

C

	STSR	TTSR	WZCR	TTCR	STCR	$Tr_{WZCR \rightarrow STSR}$	$Tr_{WZCR \rightarrow TTSR}$	$Tr_{TTCR \rightarrow TTSR}$	$Tr_{STCR \rightarrow STSR}$
FCNC tZu	3.9 ± 0.0	11.2 ± 0.0	7.3 ± 0.0	0.6 ± 0.0	0.3 ± 0.0	0.22 ± 0.00	0.46 ± 0.00	—	—
FCNC tZc	14.1 ± 0.1	30.9 ± 0.1	15.5 ± 0.1	1.7 ± 0.0	1.2 ± 0.0	0.39 ± 0.01	0.76 ± 0.01	—	—
DY	-4.6 ± 21.7	22.3 ± 14.3	136.9 ± 48.5	-14.0 ± 22.2	-15.9 ± 11.3	0.08 ± 0.09	0.10 ± 0.10	—	—
ttbar	13.1 ± 2.5	9.7 ± 2.1	8.5 ± 1.9	22.3 ± 3.1	33.7 ± 3.8	0.54 ± 0.31	0.70 ± 0.31	0.33 ± 0.00	0.33 ± 0.00
DD fake	62.0 ± 7.9	63.0 ± 7.9	204.0 ± 14.3	41.0 ± 6.4	56.0 ± 7.5	—	—	—	—
WZ+jets	60.9 ± 1.6	83.0 ± 1.7	552.7 ± 4.6	11.9 ± 0.6	8.5 ± 0.6	0.10 ± 0.00	0.15 ± 0.00	—	—
tZq	8.0 ± 0.2	16.9 ± 0.2	7.3 ± 0.2	2.2 ± 0.1	1.0 ± 0.1	0.36 ± 0.02	0.67 ± 0.03	—	—
ttZ	3.5 ± 0.3	42.5 ± 0.9	9.6 ± 0.5	6.8 ± 0.4	0.5 ± 0.1	0.14 ± 0.02	0.61 ± 0.05	—	—
ZZ	4.6 ± 0.1	4.8 ± 0.1	46.2 ± 0.3	0.8 ± 0.0	0.6 ± 0.0	0.10 ± 0.00	0.13 ± 0.00	—	—
other	1.2 ± 0.3	5.6 ± 0.3	6.8 ± 0.5	7.5 ± 0.7	2.4 ± 0.5	0.16 ± 0.03	0.30 ± 0.03	—	—

Table C.1: Event yields: All channel. The last three columns represent the transfer factors that have to be applied.

1712

Details about the BDTs



1713 The boosted decision are trained without the NPL background.

1714 **Boosted Decision Tree Factory in STSR**

1715 In the TMVA factory,

```
1716 TMVA::Factory(bdt_type.Data(), output_file,  
1717   "!V:!Silent:Color:!DrawProgressBar:Transformations=I:AnalysisType=Classification"),
```

1718 the trees are trained and tested by

```
1719 factory→PrepareTrainingAndTestTree( mycuts, mycutb,  
1720   "nTrain_Signal=0:nTrain_Background=0:SplitMode=Random:NormMode=NumEvents:!V")■
```

1721 and the BDT is constructed as:

```
1722 factory→BookMethod( TMVA::Types::kBDT,method_title.Data(),  
1723   "!H:!V:NTrees=25:MinNodeSize=15%:BoostType=Grad:Shrinkage=0.3:  
1724   SeparationType=GiniIndex:nCuts=15:MaxDepth=3:NegWeightTreatment=Pray:  
1725   PruneMethod=NoPruning:UseBaggedBoost:BaggedSampleFraction=0.5" ).
```

1726 **Boosted Decision Tree Factory in TTSR**

1727 In the TMVA factory,

```
1728 TMVA::Factory(bdt_type.Data(), output_file,  
1729   "!V:!Silent:Color:!DrawProgressBar:Transformations=I;D;P;G,D:AnalysisType=Classification")■
```

1730 the trees are trained and tested by

```
1731 factory→PrepareTrainingAndTestTree( mycuts, mycutb,  
1732 "nTrain_Signal=0:nTrain_Background=0:SplitMode=Random:NormMode=NumEvents:!V")■
```

1733 and the BDT is constructed as:

```
1734 factory→BookMethod( TMVA::Types::kBDT,method_title.Data(),  
1735 "!H:!V:NTrees=225:MinNodeSize=5%:BoostType=Grad:Shrinkage=0.2:  
1736 UseBaggedBoost:BaggedSampleFraction=0.8:SeparationType=GiniIndex:nCuts=15:  
1737 MaxDepth=3:NegWeightTreatment=Pray" ).
```

1738 **BDT control distributions**

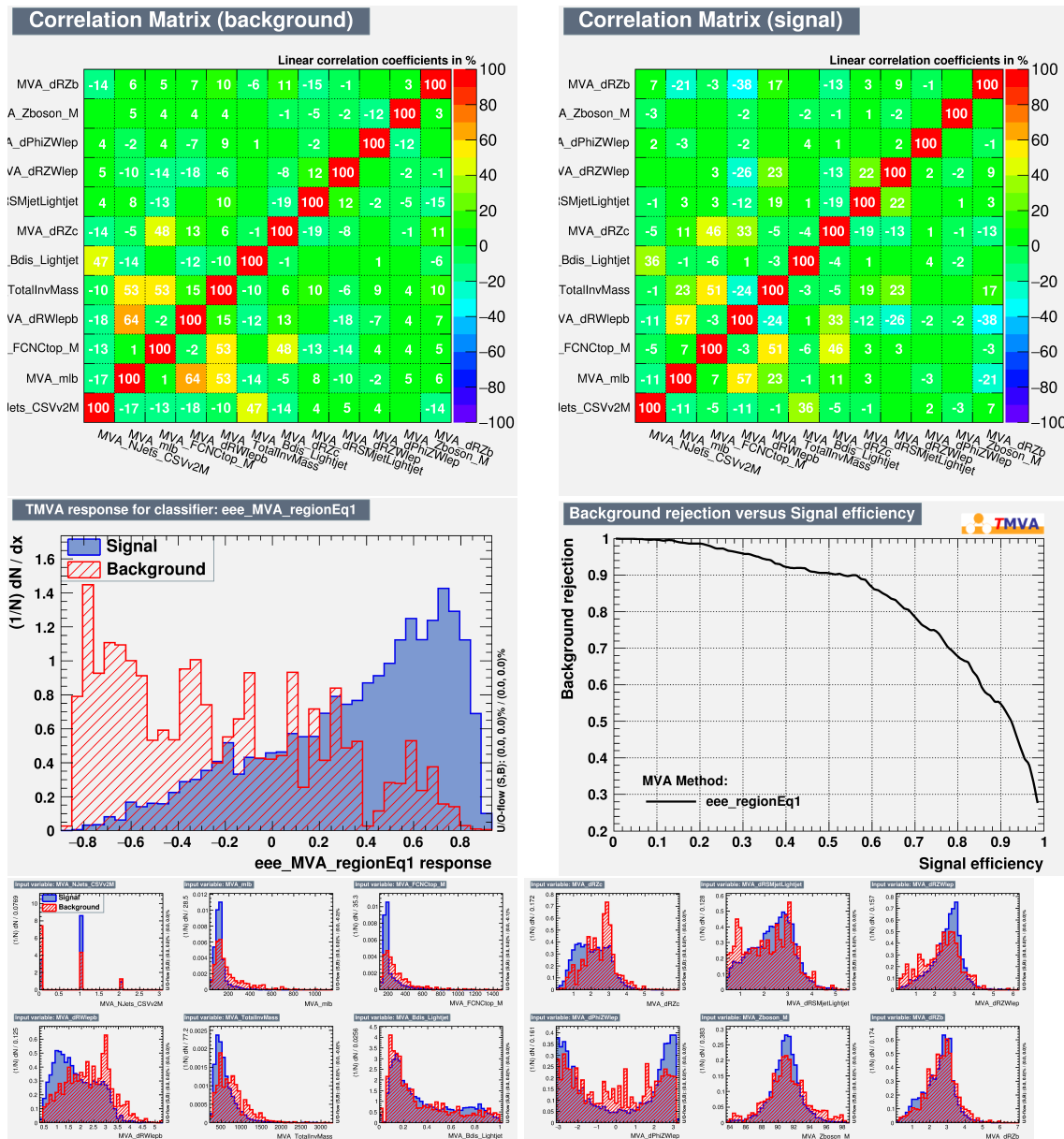


Figure D.1: 3e channel. TTSR: TZc vertex

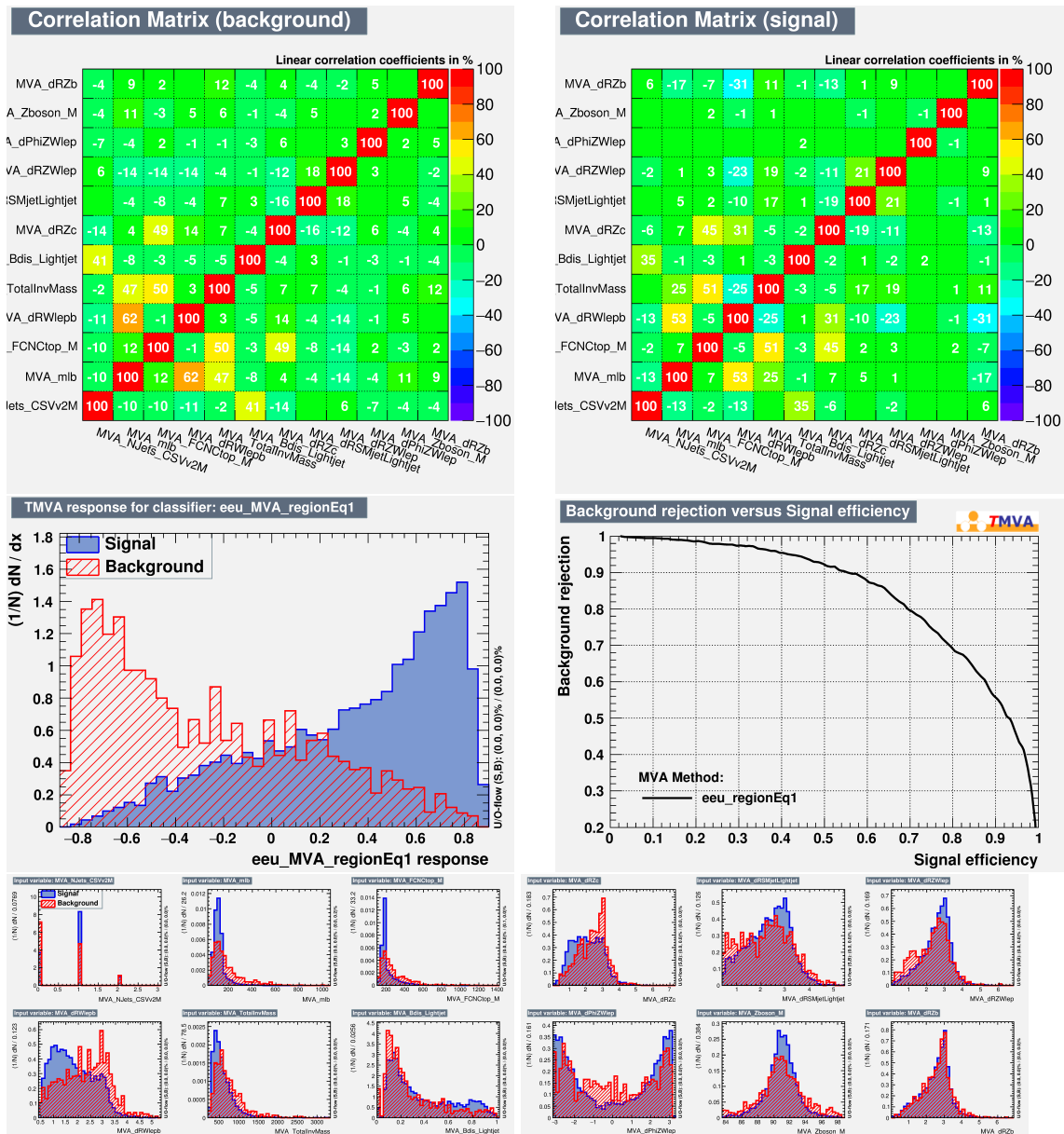
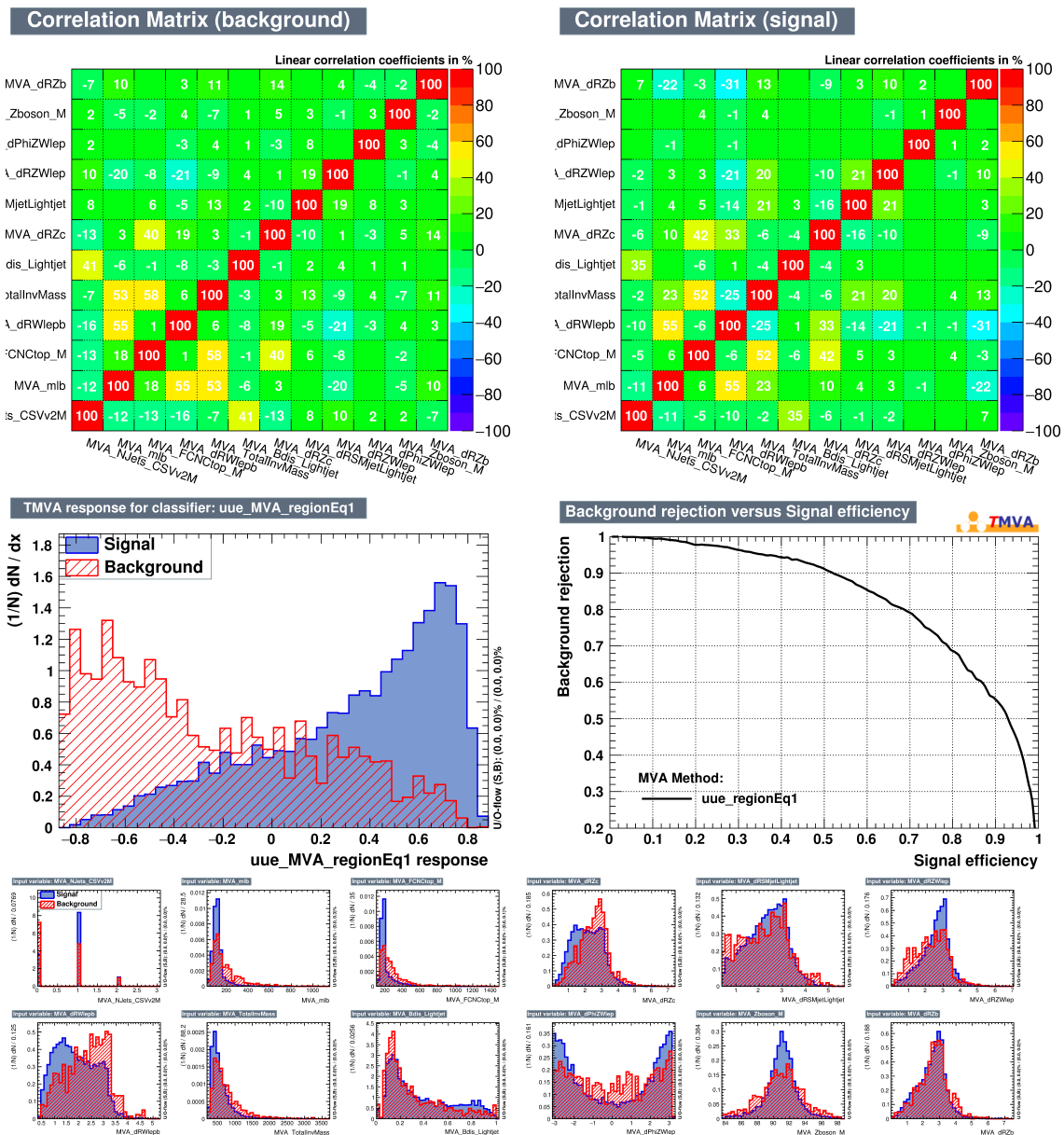
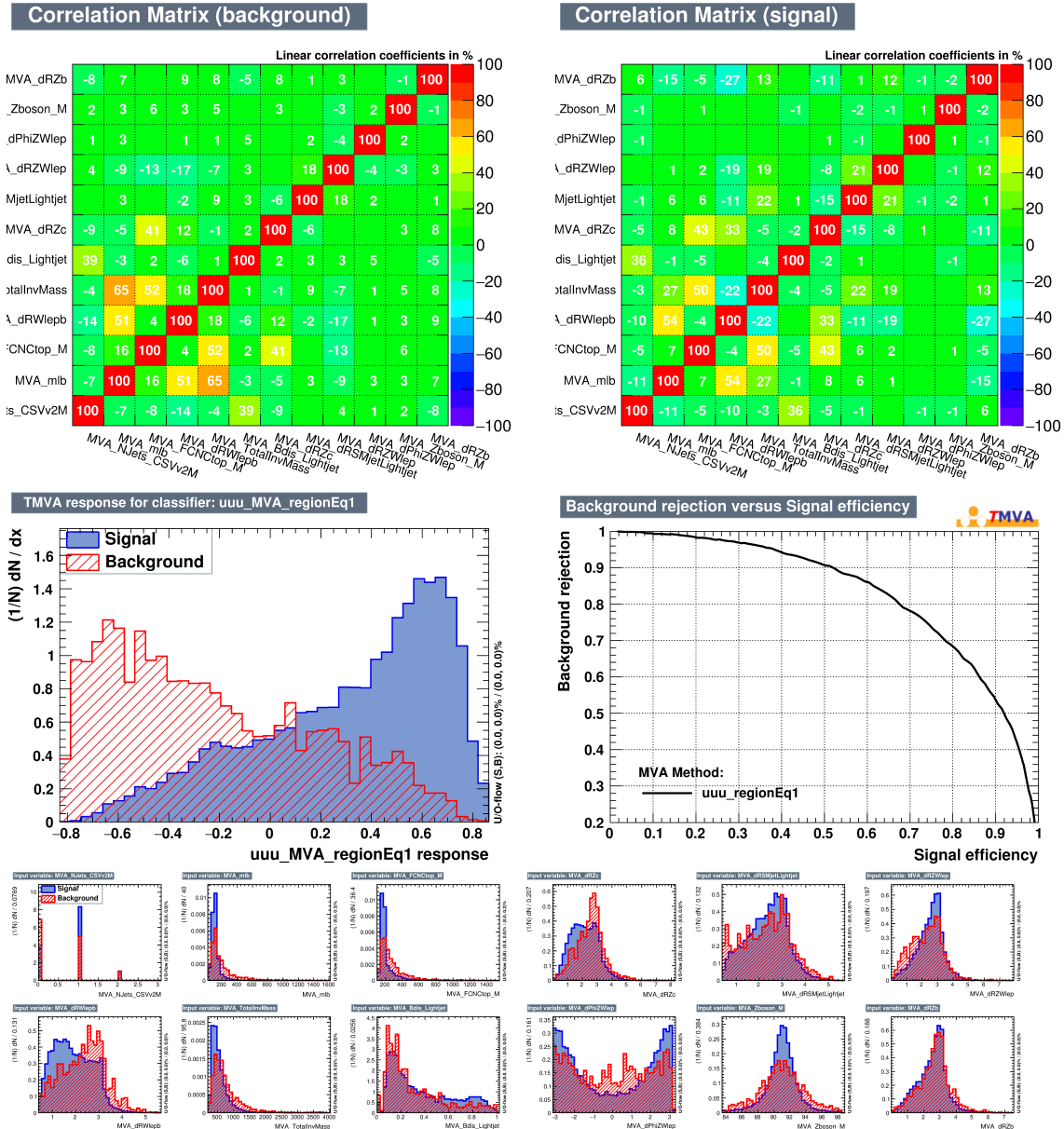


Figure D.2: 2e1μ channel. TTSR: tZc vertex

Figure D.3: 1e2 μ channel. TTSR: tZc vertex

Figure D.4: 3 μ channel. TTSR: tZc vertex

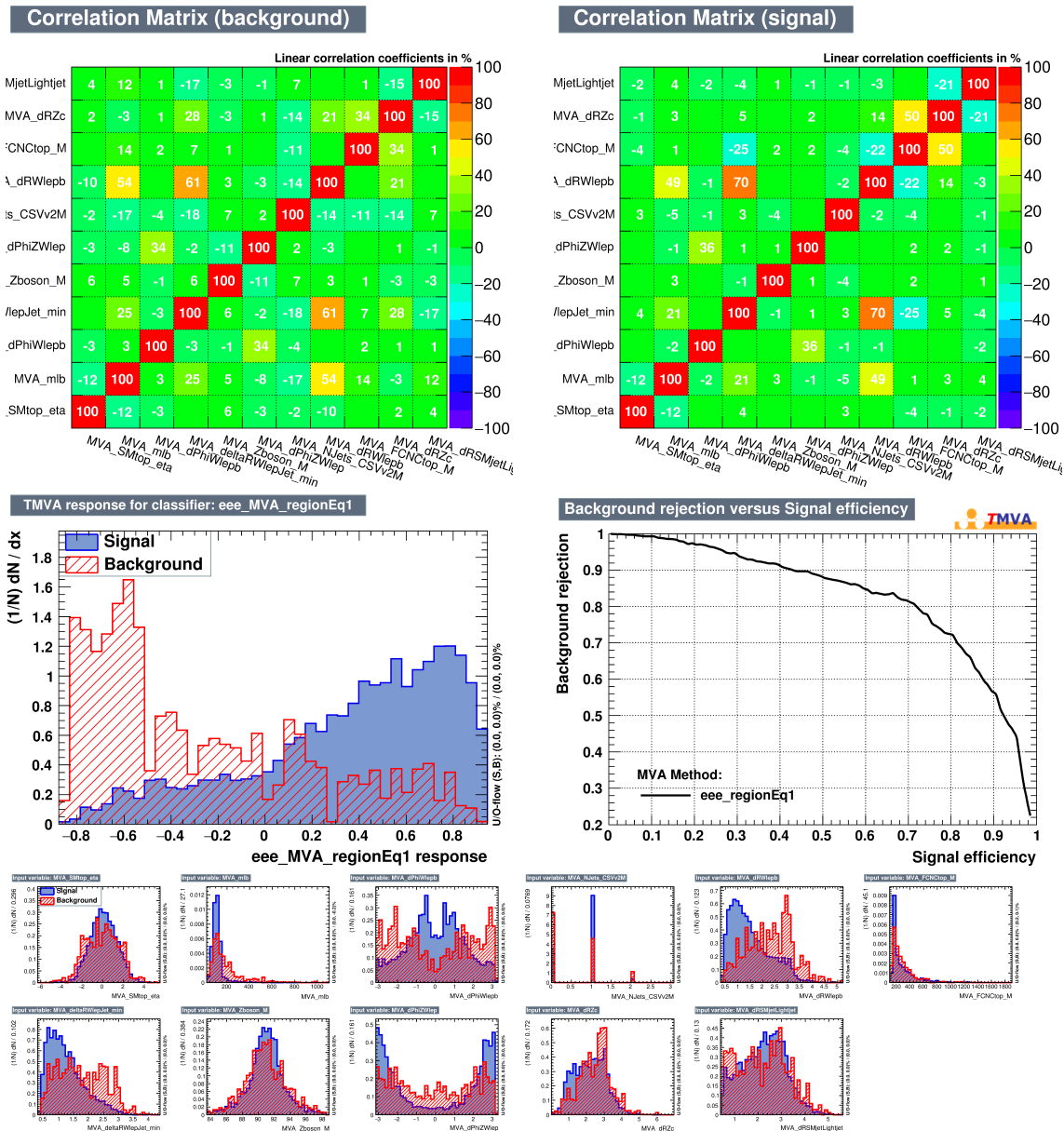


Figure D.5: 3e channel. TTSR: Tzu vertex

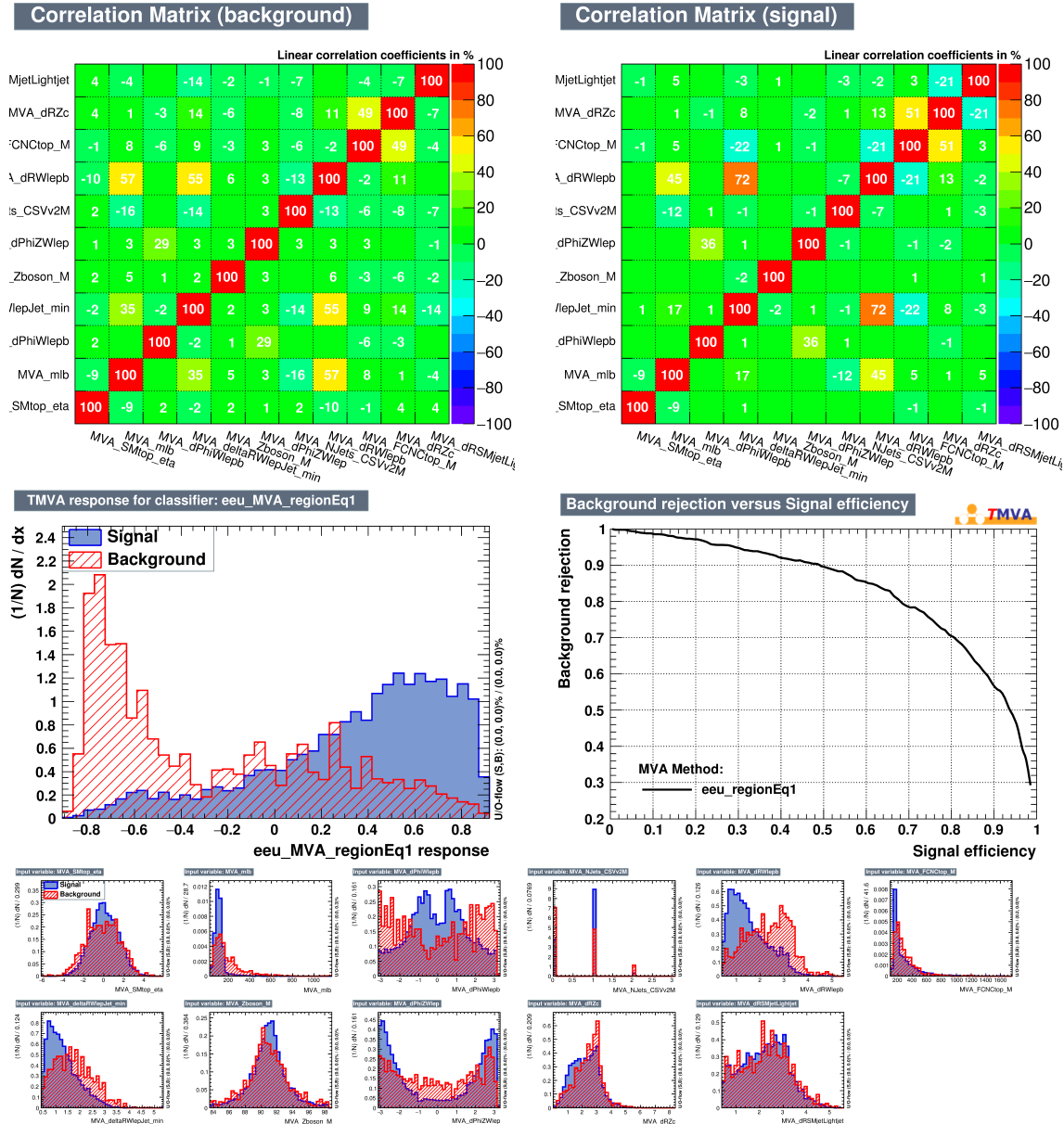
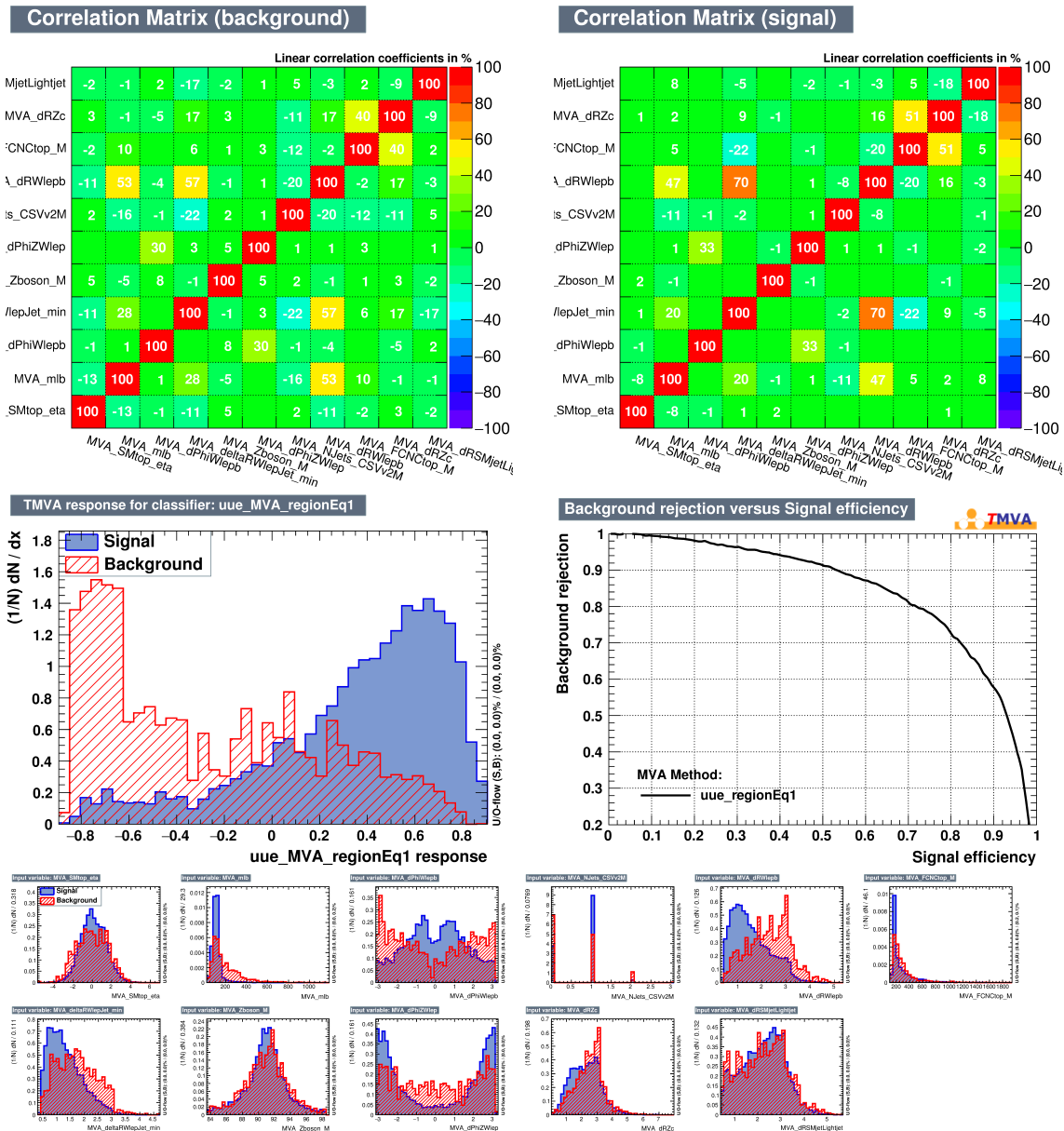


Figure D.6: 2e1 μ channel. TTSR: tZu vertex

Figure D.7: 1e2 μ channel. TTSR: tZu vertex

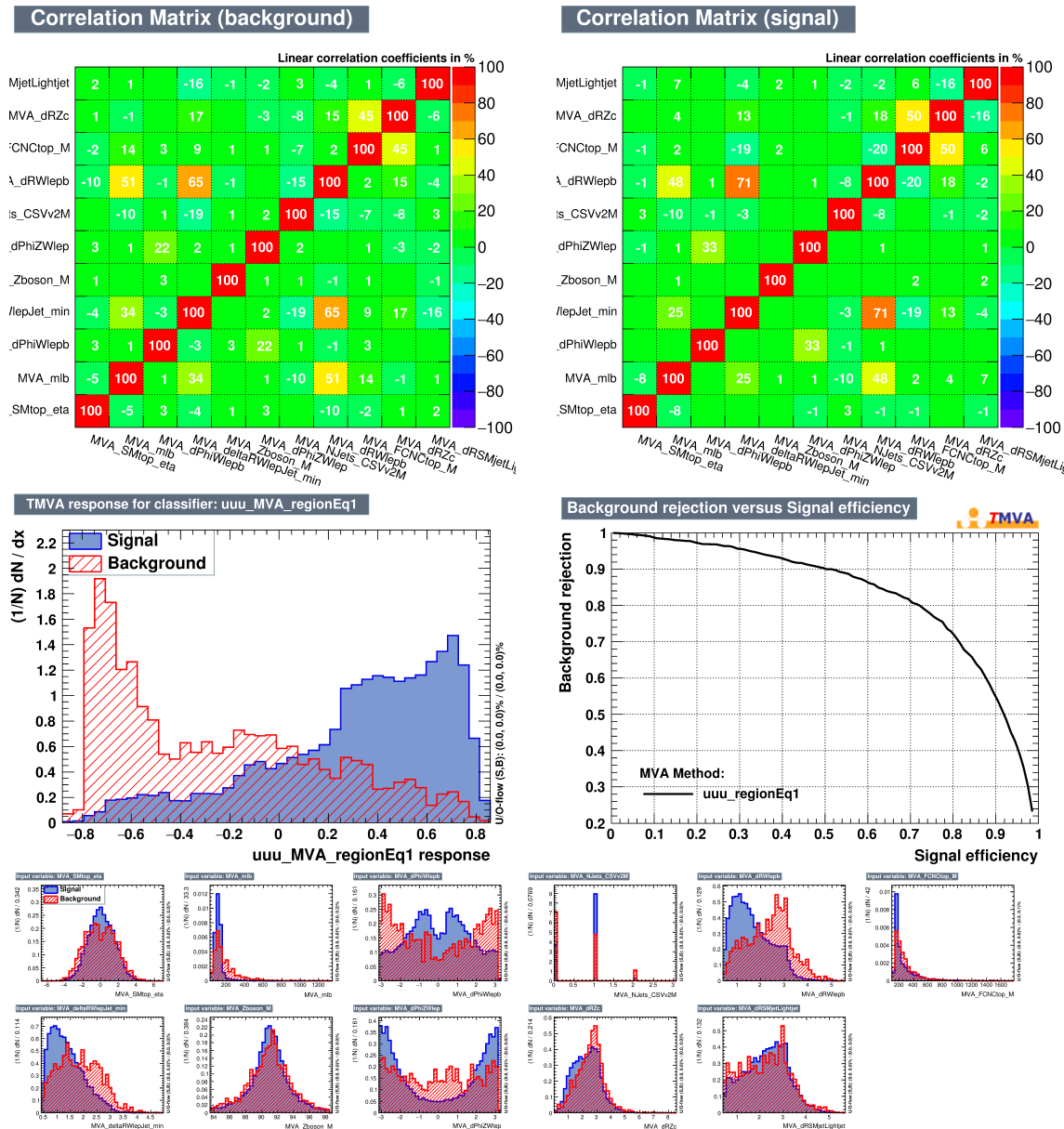


Figure D.8: 3μ channel. TTSR: tZu vertex

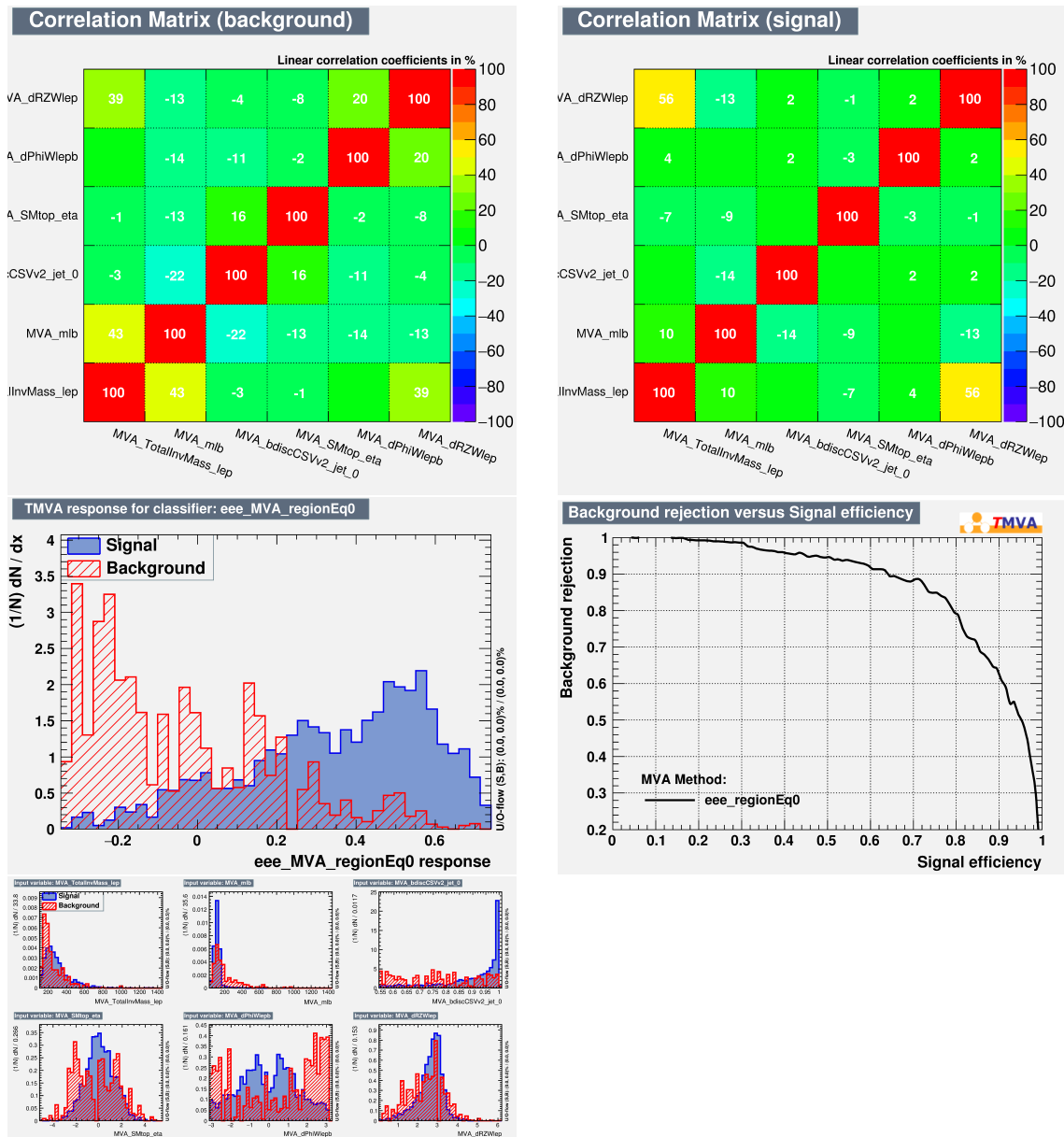


Figure D.9: 3e channel. STSR: tZc vertex

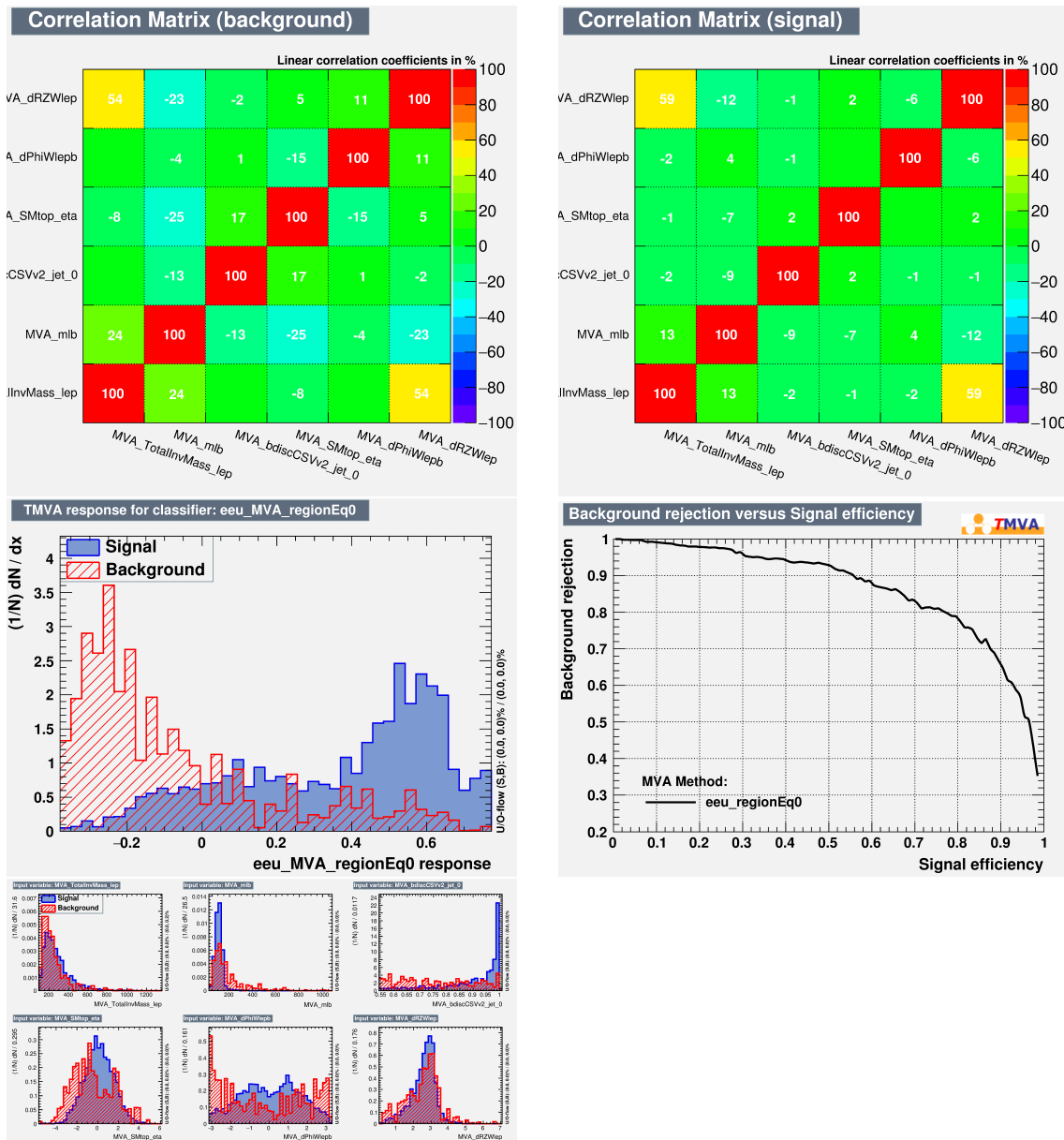
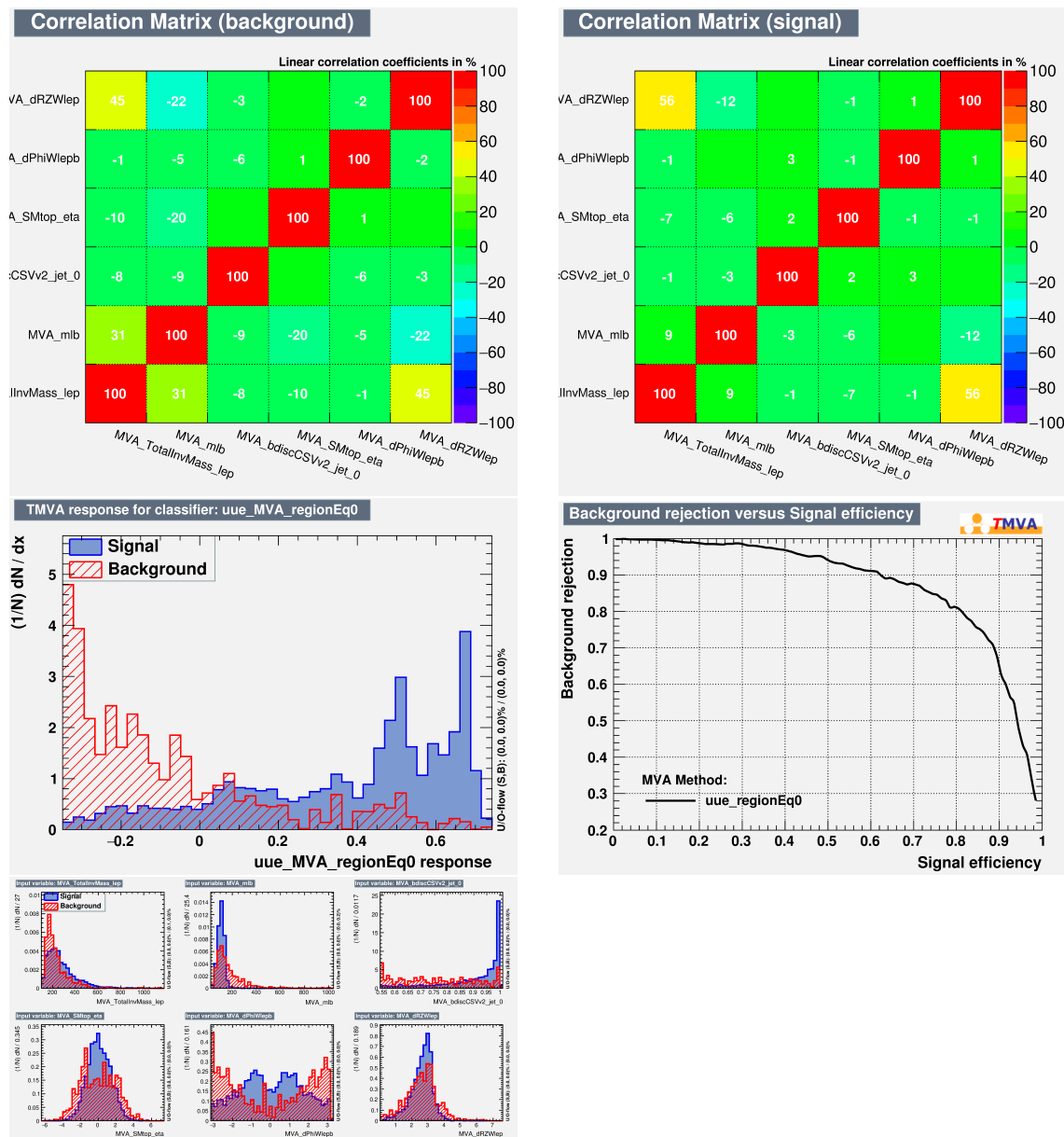
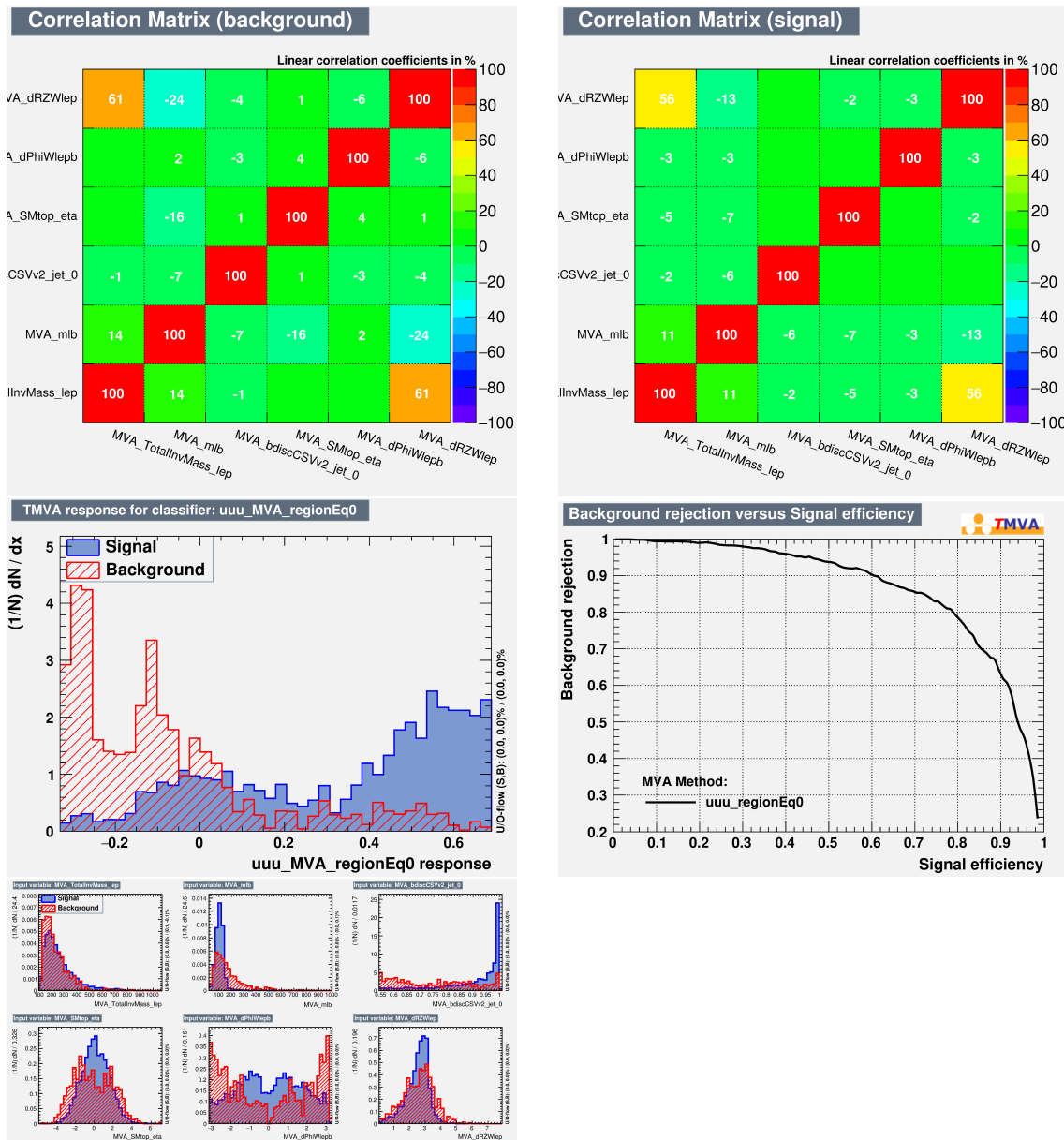


Figure D.10: 2e1μ channel. STSR: tZc vertex

Figure D.11: 1e2 μ channel. STSR: tZc vertex

Figure D.12: 3μ channel. STSR: tZc vertex

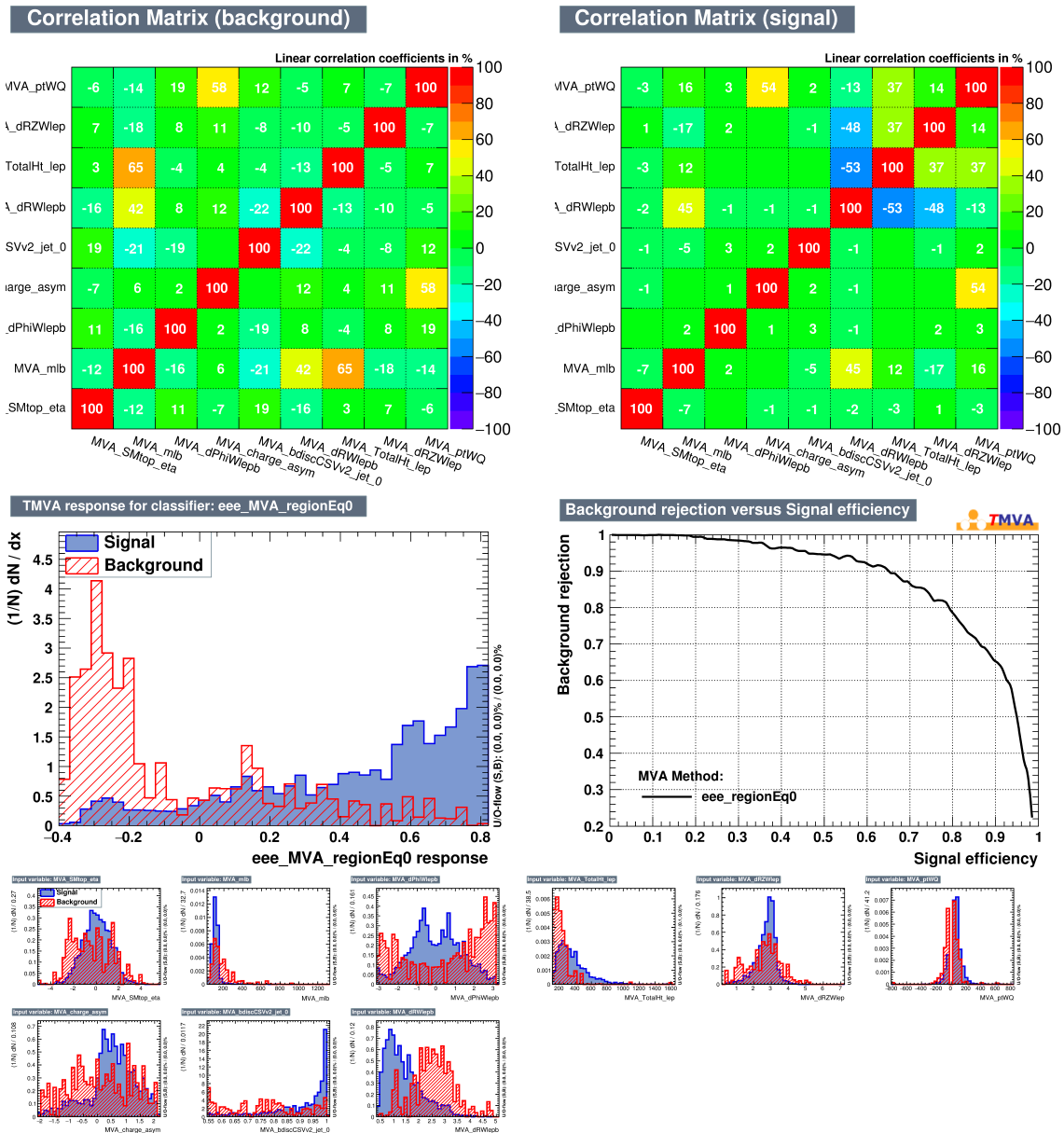
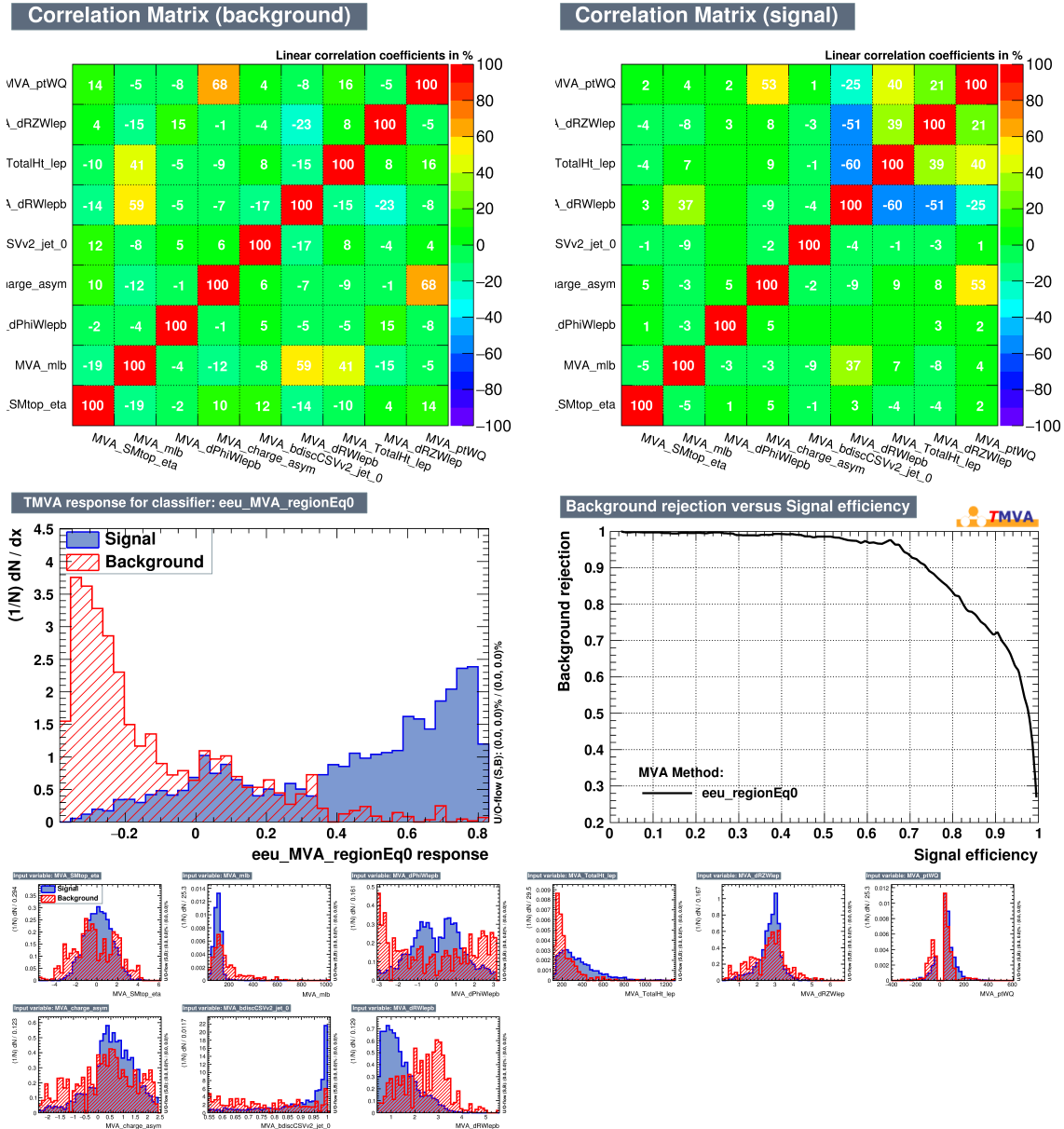
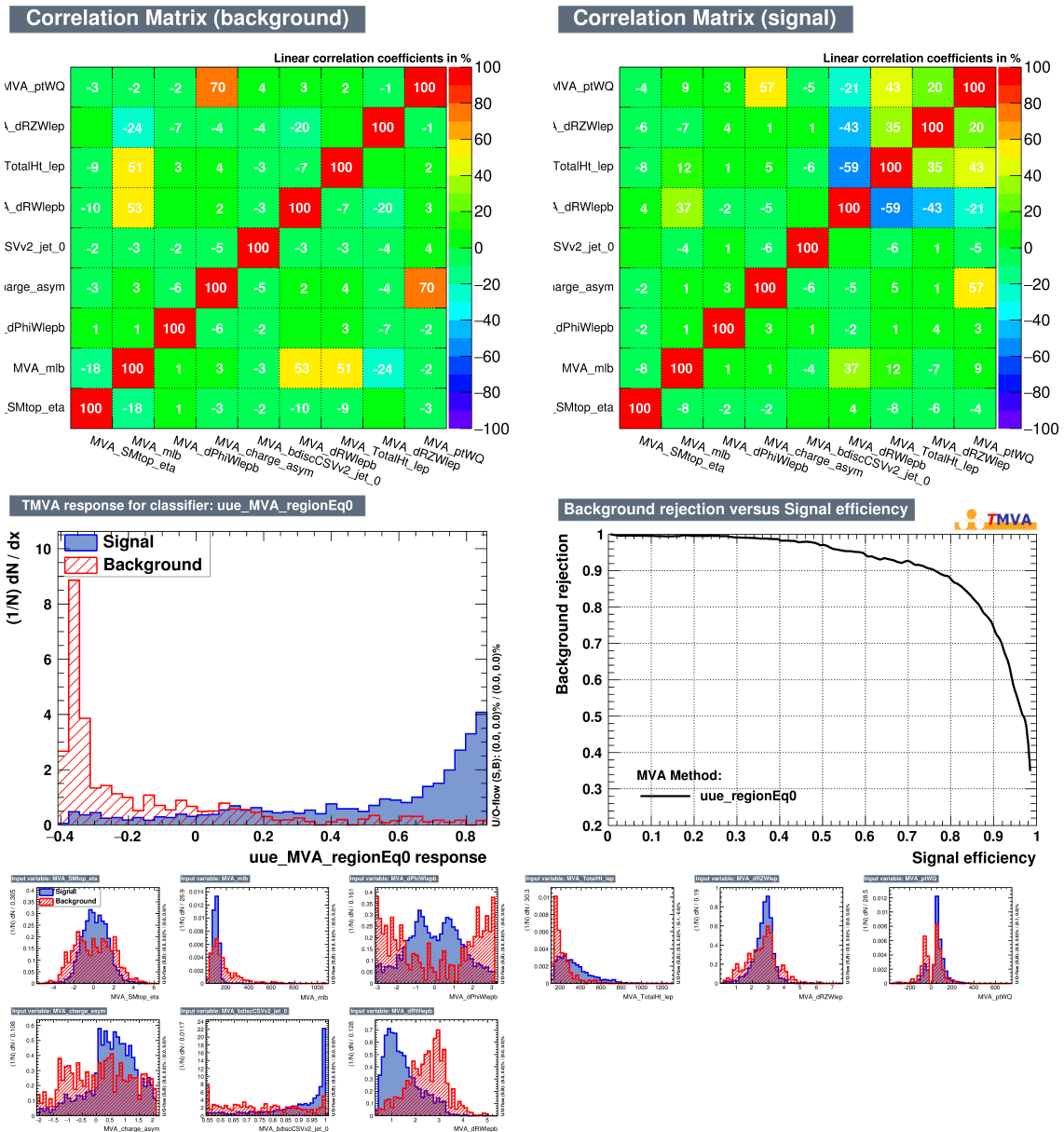
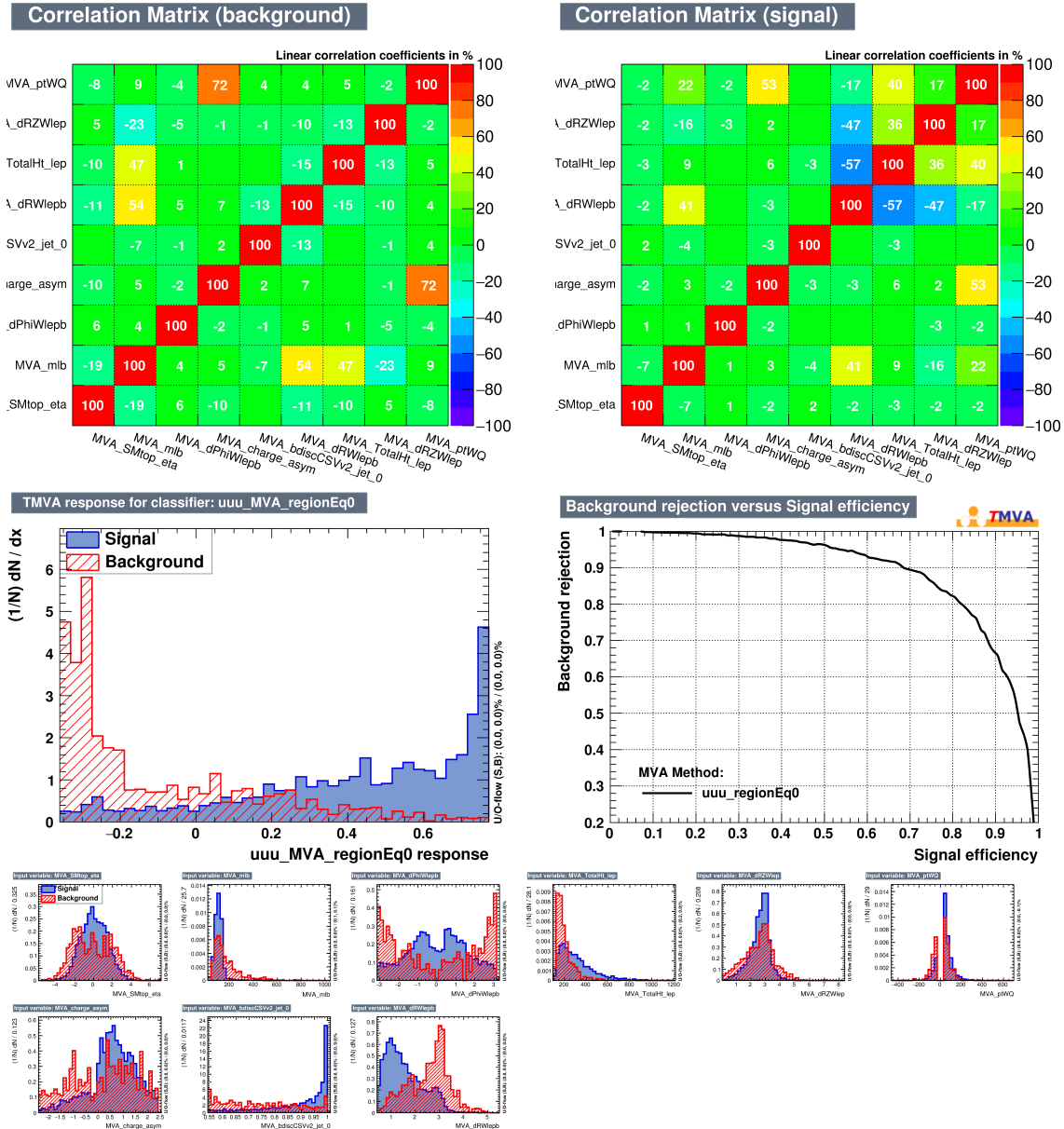


Figure D.13: 3e channel. STSR: tZu vertex

Figure D.14: 2e1 μ channel. STSR: tZu vertex

Figure D.15: 1e2 μ channel. STSR: tZu vertex

Figure D.16: 3μ channel. STSR: tZu vertex

Prefit distributions

E

1740 E.1 BDT distributions

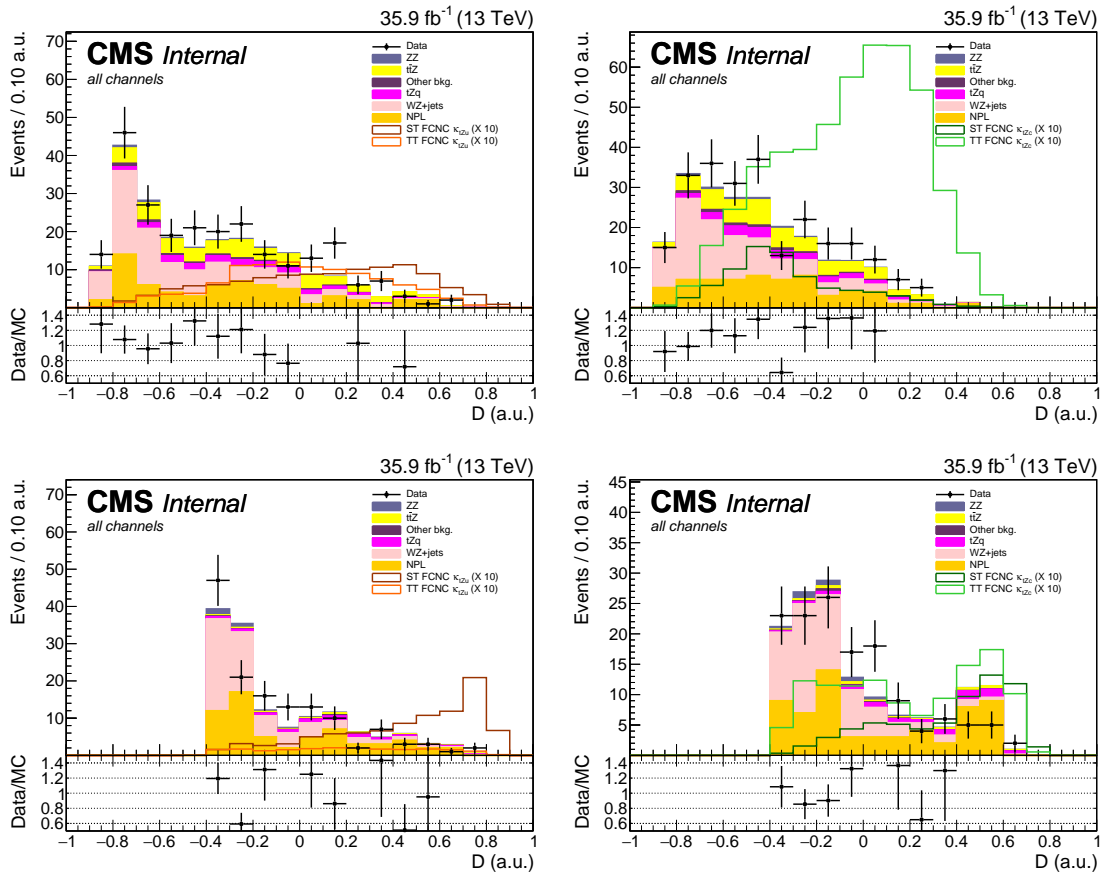


Figure E.1: Distributions of the discriminating variable before the fit, all different leptonic channels together. Upper left: TTSR: tZu vertex , upper right: TTSR: tZc vertex ; lower left: STSR: tZu vertex , lower right: STSR: tZc vertex .

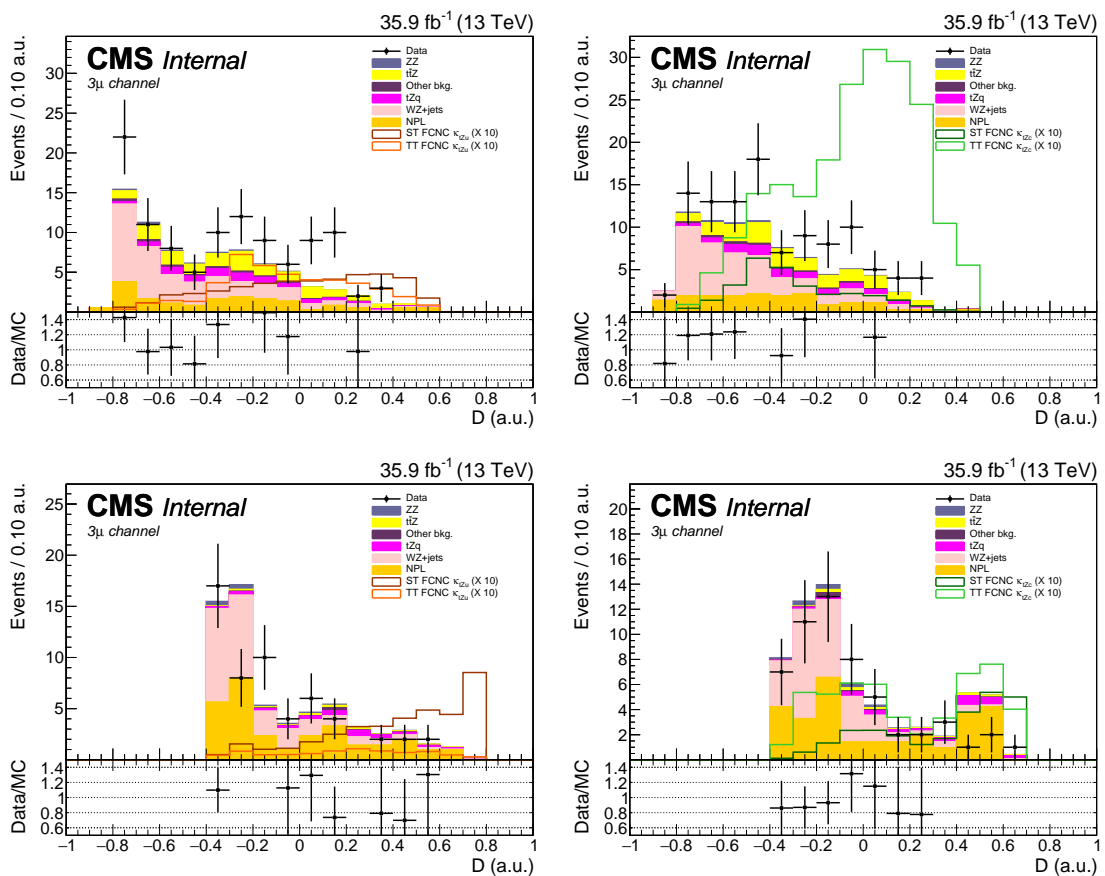


Figure E.2: Distributions of the discriminating variable before the fit, 3 μ channel. Upper left: TTSR: tZu vertex , upper right: TTSR: tZc vertex ; lower left: STSR: tZu vertex , lower right: STSR: tZc vertex .

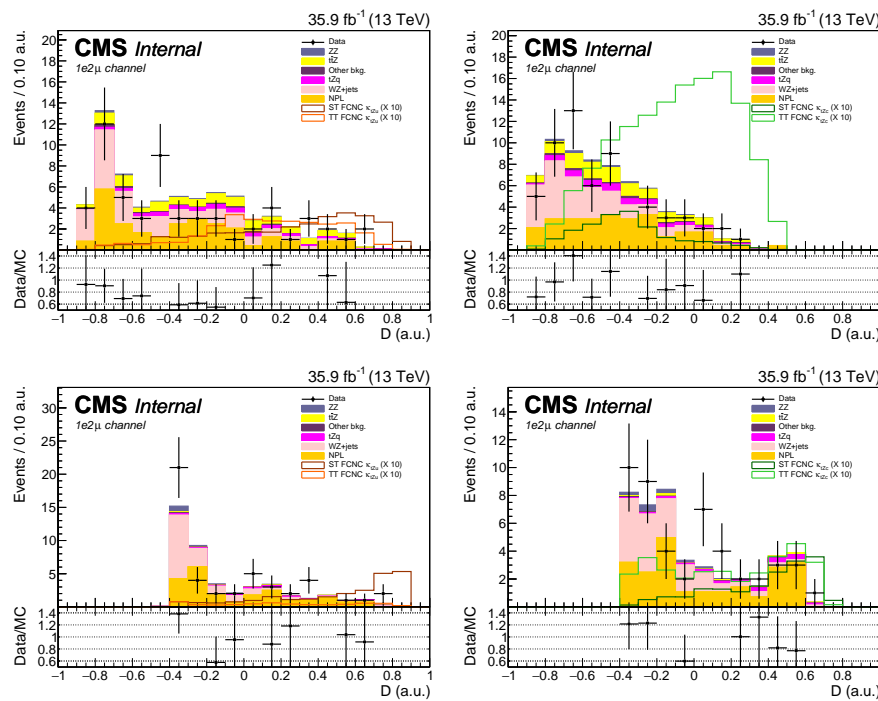


Figure E.3: Distributions of the discriminating variable before the fit, $1e2\mu$ channel. Upper left: TTSR: tZ_u vertex , upper right: TTSR: tZ_c vertex ; lower left: STSR: tZ_u vertex , lower right: STSR: tZ_c vertex .

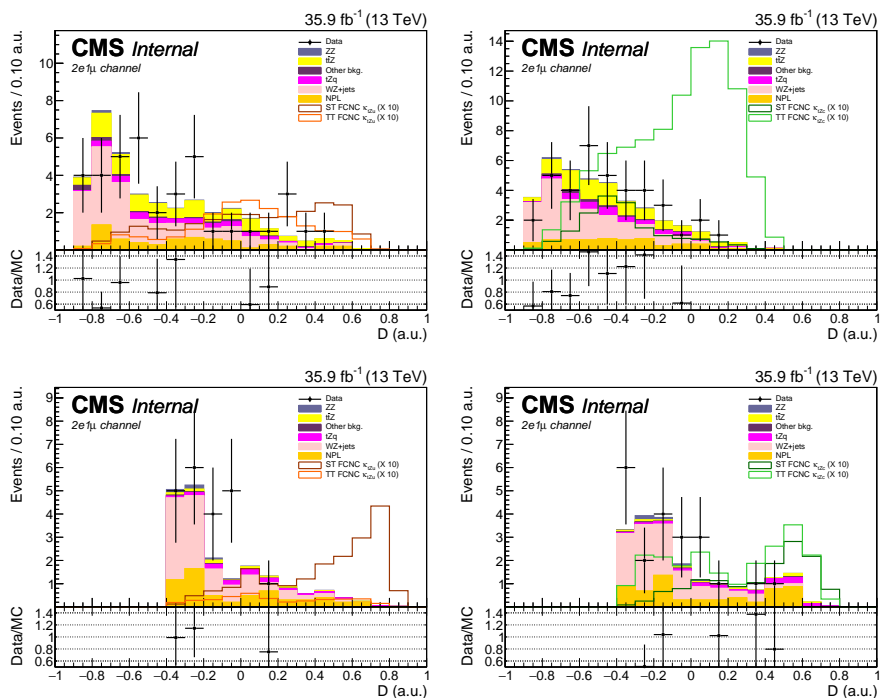


Figure E.4: Distributions of the discriminating variable before the fit, 2e1 μ channel. Upper left: TTSR: tZu vertex , upper right: TTSR: tZc vertex ; lower left: STSR: tZu vertex , lower right: STSR: tZc vertex .

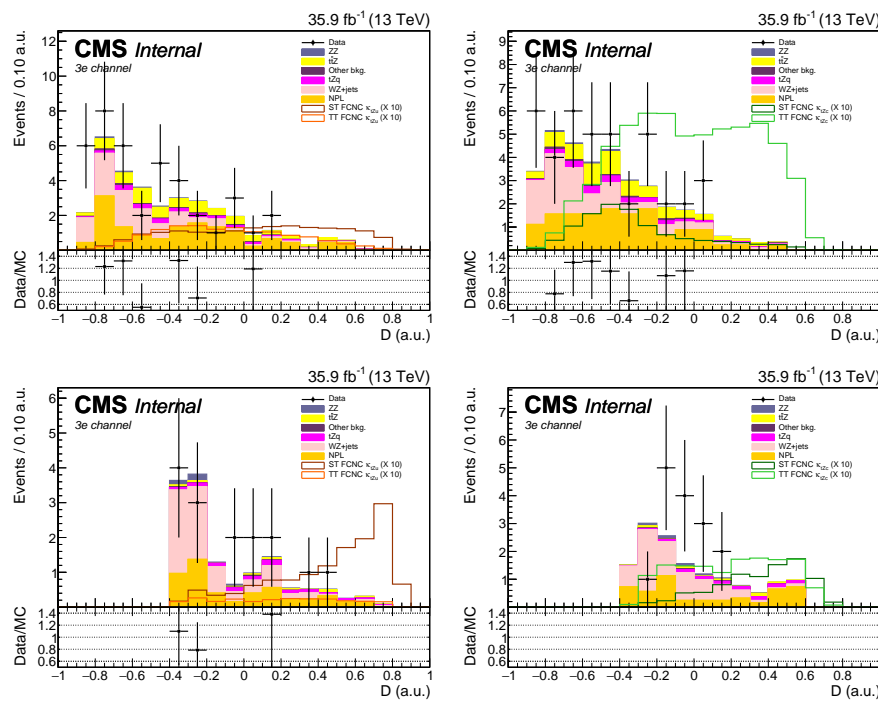


Figure E.5: Distributions of the discriminating variable before the fit, 3e channel. Upper left: TTSR: tZu vertex , upper right: TTSR: tZc vertex ; lower left: STSR: tZu vertex , lower right: STSR: tZc vertex .

1741 **E.2 Transverse W boson mass distributions**

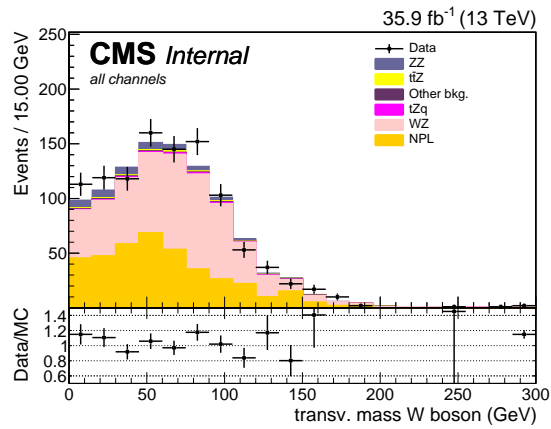


Figure E.6: Distributions of the transverse mass of the W boson before the fit, all different leptonic channels together. Upper left: TTSR: tZu vertex , upper right: TTSR: tZc vertex ; lower left: STSR: tZu vertex , lower right: STSR: tZc vertex .

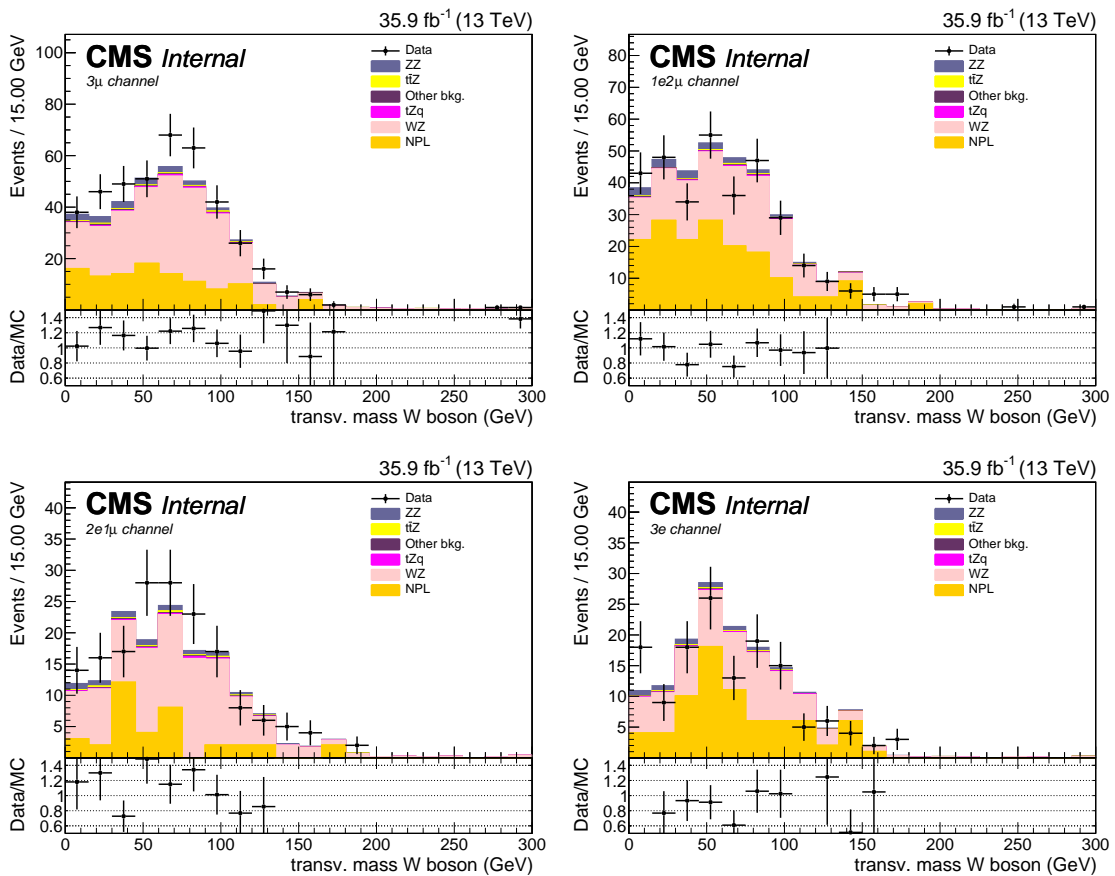


Figure E.7: Distributions of the transverse mass of the W boson before the fit, all different leptonic channels together. Upper left: TTSR: tZu vertex , upper right: TTSR: tZc vertex ; lower left: STSR: tZu vertex , lower right: STSR: tZc vertex .

1742 E.3 Input variables of the BDT

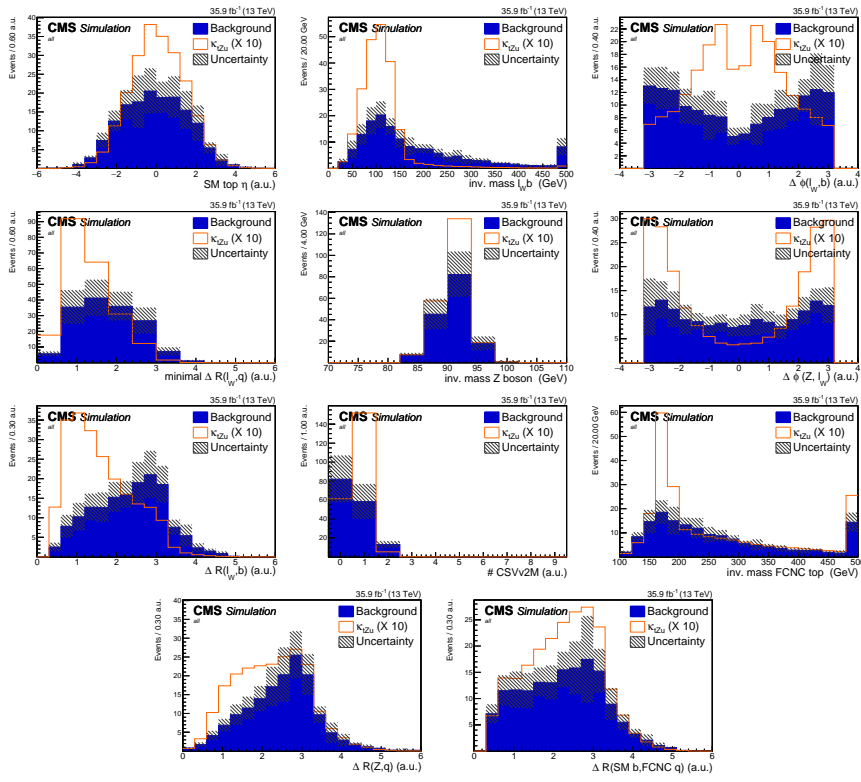


Figure E.8: The normalised input variables for reconstructing the multivariate discriminator in the TTSR for the tZu vertex.

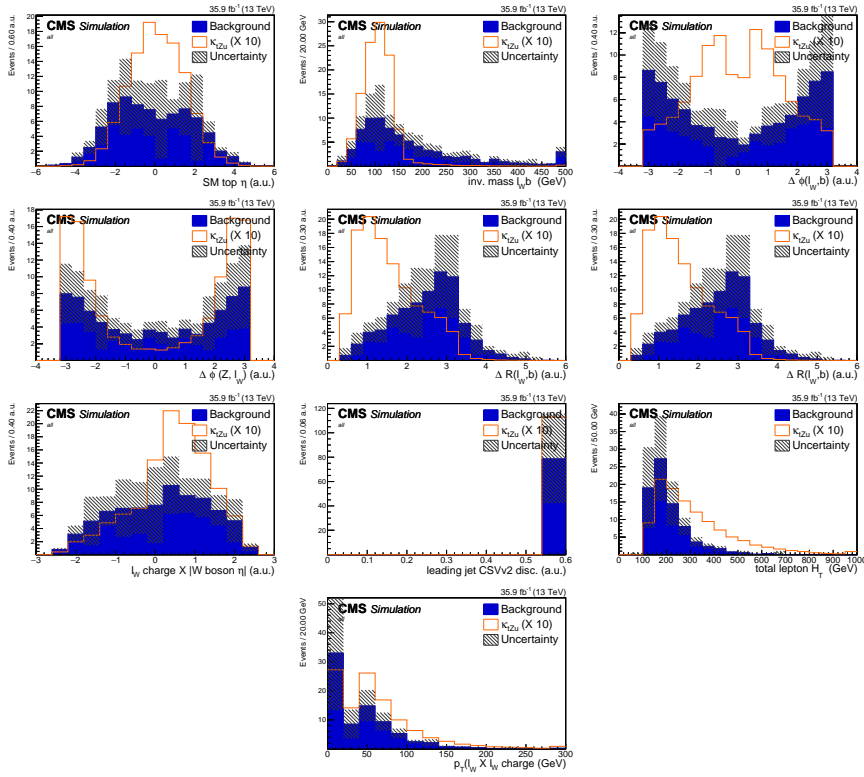


Figure E.9: The normalised input variables for reconstructing the multivariate discriminator in the STSR for the tZu vertex.

Figure E.10: The normalised input variables for reconstructing the multivariate discriminator in the TTSR for the tZc vertex.

Figure E.11: The normalised input variables for reconstructing the multivariate discriminator in the STSR for the tZc vertex.

1743

Limit setting validations

F

1744 F.1 Blinded initial fit, postfit distributions

1745 **F.2 Post fit distributions of the BDT input vars**

Bibliography

- 1747 [1] MICHAEL E PESKIN and DANIEL V SCHROEDER: **An introduction to quantum field**
 1748 **theory; 1995 ed.** Includes exercises. Boulder, CO: Westview, 1995. URL: <https://cds.cern.ch/record/257493> (see pp. 1, 6, 11, 16).
- 1750 [2] C. P. BURGESS: **Introduction to Effective Field Theory**. In: *Ann. Rev. Nucl. Part.*
 1751 *Sci.*, **57**: (2007), pp. 329–362. DOI: [10.1146/annurev.nucl.56.080805.140508](https://doi.org/10.1146/annurev.nucl.56.080805.140508). arXiv:
 1752 [hep-th/0701053 \[hep-th\]](https://arxiv.org/abs/hep-th/0701053) (see p. 1).
- 1753 [3] NADIA ROBOTTI: **The discovery of the electron: I**. In: *European Journal of Physics*,
 1754 **18**:3 (1997), p. 133. URL: <http://stacks.iop.org/0143-0807/18/i=3/a=002> (see p. 2).
- 1755 [4] Y. FUKUDA et al.: **Evidence for oscillation of atmospheric neutrinos**. In: *Phys. Rev.*
 1756 *Lett.*, **81**: (1998), pp. 1562–1567. DOI: [10.1103/PhysRevLett.81.1562](https://doi.org/10.1103/PhysRevLett.81.1562). arXiv: [hep-ex/9807003 \[hep-ex\]](https://arxiv.org/abs/hep-ex/9807003) (see pp. 2, 14).
- 1758 [5] Y. ABE et al.: **Indication of Reactor $\bar{\nu}_e$ Disappearance in the Double Chooz Experiment**. In: *Phys. Rev. Lett.*, **108**: (13 Mar. 2012), p. 131801. DOI: [10.1103/PhysRevLett.108.131801](https://doi.org/10.1103/PhysRevLett.108.131801) (see pp. 2, 14).
- 1761 [6] C. PATRIGNANI et al.: **Review of Particle Physics**. In: *Chin. Phys.*, **C40**:10 (2016),
 1762 p. 100001. DOI: [10.1088/1674-1137/40/10/100001](https://doi.org/10.1088/1674-1137/40/10/100001) (see pp. 2–3, 6–8, 10, 42–43).
- 1763 [7] S. ABACHI et al.: **Observation of the top quark**. In: *Phys. Rev. Lett.*, **74**: (1995),
 1764 pp. 2632–2637. DOI: [10.1103/PhysRevLett.74.2632](https://doi.org/10.1103/PhysRevLett.74.2632). arXiv: [hep-ex/9503003 \[hep-ex\]](https://arxiv.org/abs/hep-ex/9503003)
 1765 (see p. 2).
- 1766 [8] F. ABE et al.: **Observation of top quark production in $\bar{p}p$ collisions**. In: *Phys. Rev.*
 1767 *Lett.*, **74**: (1995), pp. 2626–2631. DOI: [10.1103/PhysRevLett.74.2626](https://doi.org/10.1103/PhysRevLett.74.2626). arXiv: [hep-ex/9503002 \[hep-ex\]](https://arxiv.org/abs/hep-ex/9503002) (see p. 2).
- 1769 [9] **First combination of Tevatron and LHC measurements of the top-quark mass**. In:
 1770 (2014). arXiv: [1403.4427 \[hep-ex\]](https://arxiv.org/abs/1403.4427) (see p. 2).
- 1771 [10] SERGUEI CHATRCHYAN et al.: **Observation of a new boson at a mass of 125 GeV**
 1772 **with the CMS experiment at the LHC**. In: *Phys. Lett.*, **B716**: (2012), pp. 30–61. DOI:
 1773 [10.1016/j.physletb.2012.08.021](https://doi.org/10.1016/j.physletb.2012.08.021). arXiv: [1207.7235 \[hep-ex\]](https://arxiv.org/abs/1207.7235) (see pp. 2, 23).
- 1774 [11] GEORGES AAD et al.: **Observation of a new particle in the search for the Standard**
 1775 **Model Higgs boson with the ATLAS detector at the LHC**. In: *Phys. Lett.*, **B716**:
 1776 (2012), pp. 1–29. DOI: [10.1016/j.physletb.2012.08.020](https://doi.org/10.1016/j.physletb.2012.08.020). arXiv: [1207.7214 \[hep-ex\]](https://arxiv.org/abs/1207.7214)
 1777 (see pp. 2, 23).

- [12] NICOLA CABIBBO: **Unitary Symmetry and Leptonic Decays**. In: *Phys. Rev. Lett.*, **10**: (12 June 1963), pp. 531–533. doi: [10.1103/PhysRevLett.10.531](https://doi.org/10.1103/PhysRevLett.10.531) (see p. 5).
- [13] S. L. GLASHOW, J. ILIOPoulos, and L. MAIANI: **Weak Interactions with Lepton-Hadron Symmetry**. In: *Phys. Rev. D*, **2**: (7 Oct. 1970), pp. 1285–1292. doi: [10.1103/PhysRevD.2.1285](https://doi.org/10.1103/PhysRevD.2.1285) (see p. 5).
- [14] B.J. BJØRKEN and S.L. GLASHOW: **Elementary particles and SU(4)**. In: *Physics Letters*, **11**:3 (1964), pp. 255–257. doi: [https://doi.org/10.1016/0031-9163\(64\)90433-0](https://doi.org/10.1016/0031-9163(64)90433-0) (see p. 5).
- [15] LUCIANO MAIANI: **The GIM Mechanism: origin, predictions and recent uses**. In: *Proceedings, 48th Rencontres de Moriond on Electroweak Interactions and Unified Theories: La Thuile, Italy, March 2-9, 2013*. 2013, pp. 3–16. arXiv: [1303.6154 \[hep-ph\]](https://arxiv.org/abs/1303.6154). URL: <https://inspirehep.net/record/1225307/files/arXiv:1303.6154.pdf> (see p. 5).
- [16] PATRICK KOPPENBURG and SEBASTIEN DESCOTES-GENON: **The CKM Parameters**. In: (2017). arXiv: [1702.08834 \[hep-ex\]](https://arxiv.org/abs/1702.08834) (see p. 6).
- [17] J. A. AGUILAR-SAAVEDRA: **Top flavor-changing neutral interactions: Theoretical expectations and experimental detection**. In: *Acta Phys. Polon.*, **B35**: (2004), pp. 2695–2710. arXiv: [hep-ph/0409342 \[hep-ph\]](https://arxiv.org/abs/hep-ph/0409342) (see pp. 6, 15–17).
- [18] S. ABACHI et al.: **Observation of the top quark**. In: *Phys. Rev. Lett.*, **74**: (1995), pp. 2632–2637. doi: [10.1103/PhysRevLett.74.2632](https://doi.org/10.1103/PhysRevLett.74.2632). arXiv: [hep-ex/9503003 \[hep-ex\]](https://arxiv.org/abs/hep-ex/9503003) (see p. 6).
- [19] F. ABE et al.: **Observation of top quark production in $\bar{p}p$ collisions**. In: *Phys. Rev. Lett.*, **74**: (1995), pp. 2626–2631. doi: [10.1103/PhysRevLett.74.2626](https://doi.org/10.1103/PhysRevLett.74.2626). arXiv: [hep-ex/9503002 \[hep-ex\]](https://arxiv.org/abs/hep-ex/9503002) (see p. 6).
- [20] LHCTOP WORKING GROUP: **LHCTopWG Summary plots**. Sept. 2017. URL: <https://twiki.cern.ch/twiki/bin/view/LHCPhysics/LHCTopWGSummaryPlots> (see pp. 9, 21).
- [21] ANDREA GIAMMANCO and JEANNINE WAGNER-KUHR: **Measurement of the t-channel single Top-quark production rates in pp collisions at 7 TeV**. Sept. 2011. URL: <http://cms.web.cern.ch/news/measurement-t-channel-single-top-quark-production-rates-pp-collisions-7-tev> (see p. 9).
- [22] LHCTOP WORKING GROUP: **ATLAS-CMS recommended predictions for single top cross sections using the Hathor v2.1 program**. Sept. 2017. URL: https://twiki.cern.ch/twiki/bin/view/LHCPhysics/SingleTopRefXsec#Predictions_at_7_8_13_and_14_TeV (see p. 10).
- [23] CMS COLLABORATION: **Summaries of CMS cross section measurements**. Oct. 2017. URL: <https://twiki.cern.ch/twiki/bin/view/CMSPublic/PhysicsResultsCombined> (see pp. 10, 20, 22, 50).
- [24] CÉLINE DEGRANDE: **Effective field theories in the Standard Model and beyond**. Thesis. Université Catholique de Louvain, Sept. 2011. URL: <https://cp3.irmp.ucl.ac.be/upload/theses/phd/degrande.pdf> (see p. 11).
- [25] ENRICO FERMI: **Tentativo di una Teoria Dei Raggi β** . In: *Il Nuovo Cimento (1924-1942)*, **11**:1 (Sept. 20, 2008), p. 1. doi: [10.1007/BF02959820](https://doi.org/10.1007/BF02959820) (see p. 11).

- 1819 [26] B. GRZADKOWSKI, M. ISKRZYNSKI, M. MISIAK, and J. ROSIEK: **Dimension-Six Terms**
 1820 **in the Standard Model Lagrangian.** In: *JHEP*, **1010**: (2010), p. 085. doi: [10.1007/JHEP10\(2010\)085](https://doi.org/10.1007/JHEP10(2010)085). arXiv: [1008.4884 \[hep-ph\]](https://arxiv.org/abs/1008.4884) (see pp. 12–13, 16).
- 1822 [27] J.A. AGUILAR SAVVEDRA, C. DEGRANDE, G. DURIEUX, et al.: **Constraining the MSMEFT**
 1823 **in the top sector at the LHC.** Working document for the TOP LHC WG. June 2017.
 1824 URL: http://www.desy.de/~durieux/topbasis/basis_note.pdf (see p. 12).
- 1825 [28] ANDY BUCKLEY, CHRISTOPH ENGLERT, JAMES FERRANDO, et al.: **Constraining top**
 1826 **quark effective theory in the LHC Run II era.** In: *JHEP*, **04**: (2016), p. 015. doi:
 1827 [10.1007/JHEP04\(2016\)015](https://doi.org/10.1007/JHEP04(2016)015). arXiv: [1512.03360 \[hep-ph\]](https://arxiv.org/abs/1512.03360) (see p. 13).
- 1828 [29] YORIKIYO NAGASHIMA: **Beyond the standard model of elementary particle physics.**
 1829 Weinheim, Germany: Wiley-VCH Verlag, 2014. URL: <http://www-spires.fnal.gov/spires/find/books/www?cl=QC793.2.N34::2014> (see p. 14).
- 1831 [30] P. A. R. ADE et al.: **Planck 2015 results. XIII. Cosmological parameters.** In: *Astron.*
 1832 *Astrophys.*, **594**: (2016), A13. doi: [10.1051/0004-6361/201525830](https://doi.org/10.1051/0004-6361/201525830). arXiv: [1502.01589 \[astro-ph.CO\]](https://arxiv.org/abs/1502.01589) (see p. 14).
- 1834 [31] P. J. E. PEEBLES and BHARAT RATRA: **The Cosmological constant and dark energy.**
 1835 In: *Rev. Mod. Phys.*, **75**: (2003), pp. 559–606. doi: [10.1103/RevModPhys.75.559](https://doi.org/10.1103/RevModPhys.75.559). arXiv: [astro-ph/0207347 \[astro-ph\]](https://arxiv.org/abs/astro-ph/0207347) (see p. 14).
- 1837 [32] A. D. SAKHAROV: **Violation of CP Invariance, c Asymmetry, and Baryon Asymmetry of the Universe.** In: *Pisma Zh. Eksp. Teor. Fiz.*, **5**: (1967). [*Usp. Fiz. Nauk* **161**, 61 (1991)], pp. 32–35. doi: [10.1070/PU1991v034n05ABEH002497](https://doi.org/10.1070/PU1991v034n05ABEH002497) (see p. 14).
- 1840 [33] GUSTAVO BURDMAN: **New solutions to the hierarchy problem.** In: *Braz. J. Phys.*, **37**:
 1841 (2007), pp. 506–513. doi: [10.1590/S0103-97332007000400006](https://doi.org/10.1590/S0103-97332007000400006). arXiv: [hep-ph/0703194 \[hep-ph\]](https://arxiv.org/abs/hep-ph/0703194) (see p. 14).
- 1843 [34] T. ET AL. AALTONEN: **Search for the Flavor-Changing Neutral-Current Decay $t \rightarrow Zq$ in $p\bar{p}$ Collisions at $\sqrt{s} = 1.96$ TeV.** In: *Phys. Rev. Lett.*, **101**: (19 Nov. 2008),
 1844 p. 192002. doi: [10.1103/PhysRevLett.101.192002](https://doi.org/10.1103/PhysRevLett.101.192002) (see p. 15).
- 1846 [35] VICTOR MUKHAMEDOVICH ABAZOV et al.: **Search for flavour changing neutral currents via quark-gluon couplings in single top quark production using 2.3 fb^{-1} of $p\bar{p}$ collisions.** In: *Phys. Lett.*, **B693**: (2010), pp. 81–87. doi: [10.1016/j.physletb.2010.08.011](https://doi.org/10.1016/j.physletb.2010.08.011). arXiv: [1006.3575 \[hep-ex\]](https://arxiv.org/abs/1006.3575) (see p. 15).
- 1850 [36] GEORGES AAD et al.: **Search for flavour-changing neutral current top-quark decays to qZ in pp collision data collected with the ATLAS detector at $\sqrt{s} = 8$ TeV.** In: *Eur. Phys. J.*, **C76**:1 (2016), p. 12. doi: [10.1140/epjc/s10052-015-3851-5](https://doi.org/10.1140/epjc/s10052-015-3851-5). arXiv: [1508.05796 \[hep-ex\]](https://arxiv.org/abs/1508.05796) (see p. 15).
- 1854 [37] GEORGES AAD et al.: **Search for single top-quark production via flavour-changing neutral currents at 8 TeV with the ATLAS detector.** In: *Eur. Phys. J.*, **C76**:2 (2016),
 1855 p. 55. doi: [10.1140/epjc/s10052-016-3876-4](https://doi.org/10.1140/epjc/s10052-016-3876-4). arXiv: [1509.00294 \[hep-ex\]](https://arxiv.org/abs/1509.00294) (see pp. 15, 19).
- 1858 [38] GEORGES AAD et al.: **Search for flavour-changing neutral current top quark decays $t \rightarrow Hq$ in pp collisions at $\sqrt{s} = 8$ TeV with the ATLAS detector.** In: *JHEP*, **12**:
 1859 (2015), p. 061. doi: [10.1007/JHEP12\(2015\)061](https://doi.org/10.1007/JHEP12(2015)061). arXiv: [1509.06047 \[hep-ex\]](https://arxiv.org/abs/1509.06047) (see
 1860 p. 15).
- 1861

- 1862 [39] MORAD AABOUD et al.: **Search for top quark decays $t \rightarrow qH$, with $H \rightarrow \gamma\gamma$, in**
- 1863 $\sqrt{s} = 13$ TeV pp collisions using the ATLAS detector. In: (2017). arXiv: [1707.01404](https://arxiv.org/abs/1707.01404) [hep-ex] (see pp. 15, 19).
- 1864
- 1865 [40] **Search for flavour-changing neutral current top quark decays $t \rightarrow qZ$ in proton-**
- 1866 **proton collisions at $\sqrt{s} = 13$ TeV with the ATLAS Detector.** Tech. rep. ATLAS-CONF-
- 1867 2017-070. Geneva: CERN, Sept. 2017. URL: <https://cds.cern.ch/record/2285808>
- 1868 (see pp. 15, 19, 121–123).
- 1869 [41] ALBERT M SIRUNYAN et al.: **Search for associated production of a Z boson with a**
- 1870 **single top quark and for tZ flavour-changing interactions in pp collisions at \sqrt{s}**
- 1871 **= 8 TeV.** In: (2017). arXiv: [1702.01404](https://arxiv.org/abs/1702.01404) [hep-ex] (see pp. 15, 19, 121–125).
- 1872 [42] SERGUEI CHATRCHYAN et al.: **Search for Flavor-Changing Neutral Currents in Top-**
- 1873 **Quark Decays $t \rightarrow Zq$ in pp Collisions at $\sqrt{s} = 8$ TeV.** In: *Phys. Rev. Lett.*, **112**:17
- 1874 (2014), p. 171802. doi: [10.1103/PhysRevLett.112.171802](https://doi.org/10.1103/PhysRevLett.112.171802). arXiv: [1312.4194](https://arxiv.org/abs/1312.4194) [hep-ex]
- 1875 (see p. 15).
- 1876 [43] VARDAN KHACHATRYAN et al.: **Search for anomalous single top quark production in**
- 1877 **association with a photon in pp collisions at $\sqrt{s} = 8$ TeV.** In: *JHEP*, **04**: (2016),
- 1878 p. 035. doi: [10.1007/JHEP04\(2016\)035](https://doi.org/10.1007/JHEP04(2016)035). arXiv: [1511.03951](https://arxiv.org/abs/1511.03951) [hep-ex] (see pp. 15, 19).
- 1879 [44] VARDAN KHACHATRYAN et al.: **Search for top quark decays via Higgs-boson-mediated**
- 1880 **flavor-changing neutral currents in pp collisions at $\sqrt{s} = 8$ TeV.** In: *JHEP*, **02**:
- 1881 (2017), p. 079. doi: [10.1007/JHEP02\(2017\)079](https://doi.org/10.1007/JHEP02(2017)079). arXiv: [1610.04857](https://arxiv.org/abs/1610.04857) [hep-ex] (see
- 1882 p. 15).
- 1883 [45] **Search for the flavor-changing interactions of the top quark with the Higgs boson**
- 1884 **in $H \rightarrow b\bar{b}$ channel at $\sqrt{s} = 13$ TeV.** Tech. rep. CMS-PAS-TOP-17-003. Geneva:
- 1885 CERN, 2017. URL: <https://cds.cern.ch/record/2284743> (see pp. 15, 124).
- 1886 [46] M. BENEKE et al.: **Top quark physics.** In: *1999 CERN Workshop on standard model*
- 1887 *physics (and more) at the LHC, CERN, Geneva, Switzerland, 25-26 May: Proceedings.*
- 1888 2000, pp. 419–529. arXiv: [hep-ph/0003033](https://arxiv.org/abs/hep-ph/0003033) [hep-ph]. URL: <http://weblib.cern.ch/abstract?CERN-TH-2000-100> (see p. 17).
- 1889
- 1890 [47] JUN GAO, CHONG SHENG LI, and HUA XING ZHU: **Top Quark Decay at Next-to-Next-**
- 1891 **to Leading Order in QCD.** In: *Phys. Rev. Lett.*, **110**:4 (2013), p. 042001. doi:
- 1892 [10.1103/PhysRevLett.110.042001](https://doi.org/10.1103/PhysRevLett.110.042001). arXiv: [1210.2808](https://arxiv.org/abs/1210.2808) [hep-ph] (see pp. 18, 47).
- 1893 [48] STEPHEN MYERS: **The LEP Collider, from design to approval and commissioning.**
- 1894 John Adams' Lecture. Delivered at CERN, 26 Nov 1990. Geneva: CERN, 1991. URL:
- 1895 [http://cds.cern.ch/record/226776](https://cds.cern.ch/record/226776) (see p. 23).
- 1896 [49] STEPHEN HOLMES, RONALD S MOORE, and VLADIMIR SHILTSEV: **Overview of the**
- 1897 **Tevatron collider complex: goals, operations and performance.** In: *Journal of In-*
- 1898 *strumentation*, **6**:08 (2011), T08001. URL: <http://stacks.iop.org/1748-0221/6/i=08/a=T08001> (see p. 23).
- 1899
- 1900 [50] R. BARATE et al.: **Search for the standard model Higgs boson at LEP.** In: *Phys.*
- 1901 *Lett.*, **B565**: (2003), pp. 61–75. doi: [10.1016/S0370-2693\(03\)00614-2](https://doi.org/10.1016/S0370-2693(03)00614-2). arXiv: [hep-ex/0306033](https://arxiv.org/abs/hep-ex/0306033) [hep-ex] (see p. 23).
- 1902

- 1903 [51] KENNETH HERNER: **Higgs Boson Studies at the Tevatron**. In: *Nucl. Part. Phys. Proc.*,
1904 273-275: (2016), pp. 852–856. doi: [10.1016/j.nuclphysbps.2015.09.131](https://doi.org/10.1016/j.nuclphysbps.2015.09.131) (see p. 23).
- 1905 [52] ABDELHAK DJOUADI: **The Anatomy of electro-weak symmetry breaking. I: The
1906 Higgs boson in the standard model**. In: *Phys. Rept.*, 457: (2008), pp. 1–216. doi:
1907 [10.1016/j.physrep.2007.10.004](https://doi.org/10.1016/j.physrep.2007.10.004). arXiv: [hep-ph/0503172 \[hep-ph\]](https://arxiv.org/abs/hep-ph/0503172) (see p. 23).
- 1908 [53] LYNDON EVANS and PHILIP BRYANT: **LHC Machine**. In: *Journal of Instrumentation*,
1909 3:08 (2008), S08001. url: <http://stacks.iop.org/1748-0221/3/i=08/a=S08001> (see
1910 p. 23).
- 1911 [54] THOMAS SVEN PETTERSSON and P LEFÈVRE: **The Large Hadron Collider: conceptual
1912 design**. Tech. rep. CERN-AC-95-05-LHC. Oct. 1995, p. 20 and 22. url: <https://cds.cern.ch/record/291782> (see p. 23).
- 1914 [55] JORG WENNINGER and EZIO TODESCO: **Large Hadron Collider momentum calibration
1915 and accuracy**. Tech. rep. CERN-ACC-2017-0007. Geneva: CERN, Feb. 2017. url:
1916 <https://cds.cern.ch/record/2254678> (see p. 24).
- 1917 [56] CINZIA DE MELIS: **The CERN accelerator complex. Complexe des accélérateurs du
1918 CERN**. In: (July 2016). General Photo. url: <https://cds.cern.ch/record/2197559>
1919 (see p. 24).
- 1920 [57] J. A. MURILLO QUIJADA: **Recent upgrades and results from the CMS experiment**. In:
1921 *J. Phys. Conf. Ser.*, 912:1 (2017), p. 012005. doi: [10.1088/1742-6596/912/1/012005](https://doi.org/10.1088/1742-6596/912/1/012005)
1922 (see p. 24).
- 1923 [58] ANTONELLA DEL ROSSO: **HL-LHC updates in Japan. Projet HL-LHC : une réunion
1924 fait le point au Japon**. In: BUL-NA-2014-272. 51/2014 (Dec. 2014), p. 4. url:
1925 <https://cds.cern.ch/record/1975962> (see p. 25).
- 1926 [59] OLIVER SIM BRÜNING, PAUL COLLIER, P LEBRUN, et al.: **LHC Design Report**. CERN
1927 Yellow Reports: Monographs. Geneva: CERN, 2004. url: <https://cds.cern.ch/record/782076> (see p. 25).
- 1929 [60] G. AAD et al.: **The ATLAS Experiment at the CERN Large Hadron Collider**. In: *JINST*,
1930 3: (2008), S08003. doi: [10.1088/1748-0221/3/08/S08003](https://doi.org/10.1088/1748-0221/3/08/S08003) (see p. 25).
- 1931 [61] S. CHATRCHYAN et al.: **The CMS Experiment at the CERN LHC**. In: *JINST*, 3: (2008),
1932 S08004. doi: [10.1088/1748-0221/3/08/S08004](https://doi.org/10.1088/1748-0221/3/08/S08004) (see pp. 25, 33–35).
- 1933 [62] K. AAMODT et al.: **The ALICE experiment at the CERN LHC**. In: *JINST*, 3: (2008),
1934 S08002. doi: [10.1088/1748-0221/3/08/S08002](https://doi.org/10.1088/1748-0221/3/08/S08002) (see p. 25).
- 1935 [63] A. AUGUSTO ALVES JR. et al.: **The LHCb Detector at the LHC**. In: *JINST*, 3: (2008),
1936 S08005. doi: [10.1088/1748-0221/3/08/S08005](https://doi.org/10.1088/1748-0221/3/08/S08005) (see p. 25).
- 1937 [64] M. BONGI et al.: **Astroparticle physics at LHC: The LHCf experiment ready for data
1938 taking**. In: *Nucl. Instrum. Meth.*, A612: (2010), pp. 451–454. doi: [10.1016/j.nima.2009.08.039](https://doi.org/10.1016/j.nima.2009.08.039) (see p. 26).
- 1940 [65] G. ANELLI et al.: **The TOTEM experiment at the CERN Large Hadron Collider**. In:
1941 *JINST*, 3: (2008), S08007. doi: [10.1088/1748-0221/3/08/S08007](https://doi.org/10.1088/1748-0221/3/08/S08007) (see p. 26).
- 1942 [66] B. ACHARYA et al.: **The Physics Programme Of The MoEDAL Experiment At The LHC**.
1943 In: *Int. J. Mod. Phys.*, A29: (2014), p. 1430050. doi: [10.1142/S0217751X14300506](https://doi.org/10.1142/S0217751X14300506).
1944 arXiv: [1405.7662 \[hep-ph\]](https://arxiv.org/abs/1405.7662) (see p. 26).

- 1945 [67] BY JAMES GILLIES: **Luminosity? Why don't we just say collision rate?** In: (Mar.
1946 2011). URL: <http://cds.cern.ch/record/1997001> (see p. 26).
- 1947 [68] BY HARRIET JARLETT and HARRIET KIM JARLETT: **LHC pushes limits of performance.**
1948 In: (Aug. 2016). URL: <http://cds.cern.ch/record/2212301> (see p. 26).
- 1949 [69] CMS COLLABORATION. Okt 2017. URL: https://twiki.cern.ch/twiki/bin/view/CMSPublic/LumiPublicResults#Online_Luminosity_AN2 (see p. 27).
- 1950
1951 [70] **Technical proposal.** LHC Tech. Proposal. Cover title : CMS, the Compact Muon
1952 Solenoid : technical proposal. Geneva: CERN, 1994. URL: <https://cds.cern.ch/record/290969> (see p. 27).
- 1953
1954 [71] G. L. BAYATIAN et al.: **CMS physics: Technical design report.** In: (2006) (see p. 27).
- 1955 [72] G L BAYATIAN, S CHATRCHYAN, G HMAYAKYAN, et al.: **CMS Physics: Technical Design**
1956 **Report Volume 1: Detector Performance and Software.** Technical Design Report
1957 CMS. There is an error on cover due to a technical problem for some items. Geneva:
1958 CERN, 2006. URL: <https://cds.cern.ch/record/922757> (see pp. 27, 32, 57).
- 1959 [73] CMS COLLABORATION: **Detector Drawings.** CMS Collection. Mar. 2012. URL: <https://cds.cern.ch/record/1433717> (see p. 28).
- 1960
1961 [74] S CHATRCHYAN, V KHACHATRYAN, A M SIRUNYAN, et al.: **Performance of the CMS**
1962 **Drift Tube Chambers with Cosmic Rays.** In: *J. Instrum.*, 5:arXiv:0911.4855. CMS-
1963 CFT-09-012 (Nov. 2009), T03015. URL: <http://cds.cern.ch/record/1223944> (see
1964 pp. 30–31).
- 1965 [75] TOM DODINGTON: **News from the CMS experimental site: 22 November 2013.** Nov.
1966 2013. URL: <http://cms.web.cern.ch/news/news-point-5-22-november-2013> (see
1967 p. 31).
- 1968 [76] INSTITUTE OF RESEARCH INTO THE FUNDAMENTAL LAWS THE UNIVERSE: **The CMS**
1969 **detector superconducting solenoid.** Jan. 2006. URL: http://irfu.cea.fr/en/Phocea/Vie_des_labos/Ast/ast_visu.php?id_ast=839 (see p. 33).
- 1970
1971 [77] FERGUS WILSON: **Experimental Particle Physics.** Apr. 2012. URL: <http://slideplayer.com/slide/794631/> (see p. 33).
- 1972
1973 [78] EMRAH TIRAS, BURAK BILKI, and YASAR ONEL: **Commissioning of CMS Forward**
1974 **Hadron Calorimeters with Upgraded Multi-anode PMTs and μTCA Readout.** In:
1975 (2016). arXiv: [1611.05232 \[physics.ins-det\]](1611.05232) (see p. 34).
- 1976 [79] LUCAS TAYLOR: **Experimental Particle Physics.** Nov. 2011. URL: <http://cms.web.cern.ch/news/electromagnetic-calorimeter> (see p. 34).
- 1977
1978 [80] **Proceedings, 34th International Conference on High Energy Physics (ICHEP 2008)** URL: <http://www.slac.stanford.edu/econf/C080730> (see p. 34).
- 1979
1980 [81] L. BRIANZA: **Precision crystal calorimetry in LHC Run II with the CMS ECAL.** In:
1981 *Journal of Instrumentation*, 12:01 (2017), p. C01069. URL: <http://stacks.iop.org/1748-0221/12/i=01/a=C01069> (see pp. 35, 38).
- 1982

- 1983 [82] SERGUEI CHATRCHYAN, KHACHATRYAN, et al.: **Description and performance of track**
1984 **and primary-vertex reconstruction with the CMS tracker.** In: *J. Instrum.*, **9**:arXiv:1405.6569
1985 CERN-PH-EP-2014-070. CMS-TRK-11-001 (May 2014). Comments: Replaced with
1986 published version. Added journal reference and DOI, P10009. 80 p. URL: <http://cds.cern.ch/record/1704291> (see pp. 35, 58).
- 1988 [83] BY CHRISTINE SUTTON: **Chronicles of CMS: the saga of LS1.** In: (May 2015). URL:
1989 <http://cds.cern.ch/record/2024986> (see p. 36).
- 1990 [84] **A beautiful barrel for CMS.** In: (Mar. 2014). URL: <http://cds.cern.ch/record/1998635> (see p. 36).
- 1992 [85] VARDAN KHACHATRYAN et al.: **The CMS trigger system.** In: *JINST*, **12**:01 (2017),
1993 P01020. doi: [10.1088/1748-0221/12/01/P01020](https://doi.org/10.1088/1748-0221/12/01/P01020). arXiv: [1609.02366 \[physics.ins-det\]](https://arxiv.org/abs/1609.02366)
1994 (see p. 37).
- 1995 [86] BY CORINNE PRALAVORIO and CORINNE PRALAVORIO: **Major work to ready the LHC**
1996 **experiments for Run 2.** In: (May 2015). URL: <http://cds.cern.ch/record/2024977>
1997 (see p. 37).
- 1998 [87] LUIGI GUIDUCCI: **CMS muon system towards LHC Run 2 and beyond.** Tech. rep.
1999 CMS-CR-2014-333. Geneva: CERN, Oct. 2014. URL: <https://cds.cern.ch/record/1966038> (see p. 38).
- 2001 [88] CARLO BATTILANA: **The CMS muon system status and upgrades for LHC run-2 and**
2002 **performance of muon reconstruction with 13 TeV data.** Tech. rep. CMS-CR-2016-
2003 437. Geneva: CERN, Dec. 2016. URL: <http://cds.cern.ch/record/2239185> (see
2004 p. 38).
- 2005 [89] SERGUEI CHATRCHYAN et al.: **Energy Calibration and Resolution of the CMS Elec-**
2006 **tromagnetic Calorimeter in pp Collisions at $\sqrt{s} = 7$ TeV.** In: *JINST*, **8**: (2013).
2007 [*JINST*8,9009(2013)], P09009. doi: [10.1088/1748-0221/8/09/P09009](https://doi.org/10.1088/1748-0221/8/09/P09009). arXiv: [1306.2016 \[hep-ex\]](https://arxiv.org/abs/1306.2016) (see p. 38).
- 2009 [90] **Cool running for CMS tracker.** In: (Mar. 2014). URL: <http://cds.cern.ch/record/1998606> (see p. 38).
- 2011 [91] L. CADAMURO: **The CMS Level-1 trigger system for LHC Run II.** In: *Journal of*
2012 *Instrumentation*, **12**:03 (2017), p. C03021. URL: <http://stacks.iop.org/1748-0221/12/i=03/a=C03021> (see p. 38).
- 2014 [92] DAVID AARON MATZNER DOMINGUEZ, D. ABBANE, K. ARNDT, et al.: **CMS Technical**
2015 **Design Report for the Pixel Detector Upgrade.** In: (2012) (see p. 39).
- 2016 [93] HANNO CHRISTOPHER PERREY: **Plans and Status of the Phase I Upgrade of the**
2017 **CMS Pixel Tracker.** Tech. rep. CMS-CR-2014-005. Geneva: CERN, Jan. 2014. URL:
2018 <http://cds.cern.ch/record/1644757> (see p. 39).
- 2019 [94] CLAUDIO GRANDI, DAVID STICKLAND, LUCAS TAYLOR, ACHILLE PETRILLI, and ALAIN
2020 HERVÉ: **CMS Computing Model: The "CMS Computing Model RTAG".** Tech. rep.
2021 CMS-NOTE-2004-031. CERN-LHCC-2004-035. LHCC-G-083. Geneva: CERN, Dec.
2022 2004. URL: <http://cds.cern.ch/record/814248> (see p. 39).

- 2023 [95] CHRISTOPH ECK, J KNOBLOCH, LESLIE ROBERTSON, et al.: **LHC computing Grid: Technical Design Report. Version 1.06** (20 Jun 2005). Technical Design Report LCG. Geneva: CERN, 2005. URL: <https://cds.cern.ch/record/840543> (see p. 39).
- 2024 [96] WORLDWIDE LHC COMPUTING GRID: **WorldWide LHC Computing Gird - 2017**. Oct. 2017. URL: <http://wlcg-public.web.cern.ch> (see p. 40).
- 2025 [97] JOHN C. COLLINS, DAVISON E. SOPER, and GEORGE F. STERMAN: **Factorization of Hard Processes in QCD**. In: *Adv. Ser. Direct. High Energy Phys.*, **5**: (1989), pp. 1–91. doi: [10.1142/9789814503266_0001](https://doi.org/10.1142/9789814503266_0001). arXiv: [hep-ph/0409313 \[hep-ph\]](https://arxiv.org/abs/hep-ph/0409313) (see p. 41).
- 2026 [98] RINGAILE PLACAKYTE: **Parton Distribution Functions**. In: *Proceedings, 31st International Conference on Physics in collisions (PIC 2011): Vancouver, Canada, August 28-September 1, 2011*. 2011. arXiv: [1111.5452 \[hep-ph\]](https://arxiv.org/abs/1111.5452). URL: <https://inspirehep.net/record/954990/files/arXiv:1111.5452.pdf> (see p. 41).
- 2027 [99] RICHARD D. BALL, VALERIO BERTONE, STEFANO CARRAZZA, et al.: **Parton distributions for the LHC run II**. In: *Journal of High Energy Physics*, **2015**:4 (2015), p. 40. doi: [10.1007/JHEP04\(2015\)040](https://doi.org/10.1007/JHEP04(2015)040) (see p. 41).
- 2028 [100] JON BUTTERWORTH et al.: **PDF4LHC recommendations for LHC Run II**. In: *J. Phys.*, **G43**: (2016), p. 023001. doi: [10.1088/0954-3899/43/2/023001](https://doi.org/10.1088/0954-3899/43/2/023001). arXiv: [1510.03865 \[hep-ph\]](https://arxiv.org/abs/1510.03865) (see pp. 41–42).
- 2029 [101] H. ABRAMOWICZ and A. CALDWELL: **HERA collider physics**. In: *Rev. Mod. Phys.*, **71**: (1999), pp. 1275–1410. doi: [10.1103/RevModPhys.71.1275](https://doi.org/10.1103/RevModPhys.71.1275). arXiv: [hep-ex/9903037 \[hep-ex\]](https://arxiv.org/abs/hep-ex/9903037) (see p. 42).
- 2030 [102] STEPHEN HOLMES, RONALD S. MOORE, and VLADIMIR SHILTSEV: **Overview of the Tevatron Collider Complex: Goals, Operations and Performance**. In: *JINST*, **6**: (2011), T08001. doi: [10.1088/1748-0221/6/08/T08001](https://doi.org/10.1088/1748-0221/6/08/T08001). arXiv: [1106.0909 \[physics.acc-ph\]](https://arxiv.org/abs/1106.0909) (see p. 42).
- 2031 [103] JUAN ROJO et al.: **The PDF4LHC report on PDFs and LHC data: Results from Run I and preparation for Run II**. In: *J. Phys.*, **G42**: (2015), p. 103103. doi: [10.1088/0954-3899/42/10/103103](https://doi.org/10.1088/0954-3899/42/10/103103). arXiv: [1507.00556 \[hep-ph\]](https://arxiv.org/abs/1507.00556) (see p. 42).
- 2032 [104] ALAN D. MARTIN: **Proton structure, Partons, QCD, DGLAP and beyond**. In: *Acta Phys. Polon.*, **B39**: (2008), pp. 2025–2062. arXiv: [0802.0161 \[hep-ph\]](https://arxiv.org/abs/0802.0161) (see p. 42).
- 2033 [105] J. PUMPLIN, D. STUMP, R. BROCK, et al.: **Uncertainties of predictions from parton distribution functions. 2. The Hessian method**. In: *Phys. Rev.*, **D65**: (2001), p. 014013. doi: [10.1103/PhysRevD.65.014013](https://doi.org/10.1103/PhysRevD.65.014013). arXiv: [hep-ph/0101032 \[hep-ph\]](https://arxiv.org/abs/hep-ph/0101032) (see p. 42).
- 2034 [106] FRANZ MANDL and GRAHAM G SHAW: **Quantum field theory; 2nd ed.** New York, NY: Wiley, 2010. URL: <https://cds.cern.ch/record/1236742> (see p. 44).
- 2035 [107] S BANERJEE: **CMS Simulation Software**. In: *Journal of Physics: Conference Series*, **396**:2 (2012), p. 022003. URL: <http://stacks.iop.org/1742-6596/396/i=2/a=022003> (see p. 44).
- 2036 [108] M HILDRETH, V N IVANCHENKO, D J LANGE, and M J KORTELAINEN: **CMS Full Simulation for Run-2**. In: *Journal of Physics: Conference Series*, **664**:7 (2015), p. 072022. URL: <http://stacks.iop.org/1742-6596/664/i=7/a=072022> (see p. 44).

- 2064 [109] S. AGOSTINELLI, J. ALLISON, K. AMAKO, et al.: **Geant4-a simulation toolkit**. In: *Nuclear Instruments and Methods in Physics Research Section A: Accelerators, Spectrometers, Detectors and Associated Equipment*, **506**:3 (2003), pp. 250–303. doi: [https://doi.org/10.1016/S0168-9002\(03\)01368-8](https://doi.org/10.1016/S0168-9002(03)01368-8) (see pp. 44, 46).
- 2065 [110] MICHAEL H. SEYMOUR and MARILYN MARX: **Monte Carlo Event Generators**. In: *Proceedings, 69th Scottish Universities Summer School in Physics : LHC Phenomenology (SUSSP69): St.Andrews, Scotland, August 19-September 1, 2012.* 2013, pp. 287–319.
- 2066 DOI: [10.1007/978-3-319-05362-2_8](https://doi.org/10.1007/978-3-319-05362-2_8). arXiv: [1304.6677 \[hep-ph\]](https://arxiv.org/abs/1304.6677) (see p. 44).
- 2067 [111] TORBJORN SJÖSTRAND: **Monte Carlo Tools**. In: *Proceedings, 65th Scottish Universities Summer School in Physics: LHC Physics (SUSSP65): St. Andrews, UK, August 16-29, 2009.* 2009, pp. 309–339. doi: [10.1201/b11865-14](https://doi.org/10.1201/b11865-14). arXiv: [0911.5286 \[hep-ph\]](https://arxiv.org/abs/0911.5286) (see p. 44).
- 2068 [112] STEFAN HÖCHE: **Introduction to parton-shower event generators**. In: *Proceedings, Theoretical Advanced Study Institute in Elementary Particle Physics: Journeys Through the Precision Frontier: Amplitudes for Colliders (TASI 2014): Boulder, Colorado, June 2-27, 2014.* 2015, pp. 235–295. doi: [10.1142/9789814678766_0005](https://doi.org/10.1142/9789814678766_0005). arXiv: [1411.4085 \[hep-ph\]](https://arxiv.org/abs/1411.4085) (see pp. 44–45).
- 2069 [113] ADAM ALLOUL, NEIL D. CHRISTENSEN, CÉLINE DEGRANDE, CLAUDE DUHR, and BENJAMIN FUKS: **FeynRules 2.0 - A complete toolbox for tree-level phenomenology**. In: *Comput. Phys. Commun.*, **185**: (2014), pp. 2250–2300. doi: [10.1016/j.cpc.2014.04.012](https://doi.org/10.1016/j.cpc.2014.04.012). arXiv: [1310.1921 \[hep-ph\]](https://arxiv.org/abs/1310.1921) (see p. 44).
- 2070 [114] CELINE DEGRANDE, CLAUDE DUHR, BENJAMIN FUKS, et al.: **UFO - The Universal FeynRules Output**. In: *Comput. Phys. Commun.*, **183**: (2012), pp. 1201–1214. doi: [10.1016/j.cpc.2012.01.022](https://doi.org/10.1016/j.cpc.2012.01.022). arXiv: [1108.2040 \[hep-ph\]](https://arxiv.org/abs/1108.2040) (see p. 44).
- 2071 [115] JOHAN ALWALL, MICHEL HERQUET, FABIO MALTONI, OLIVIER MATTELAER, and TIM STELZER: **MadGraph 5 : Going Beyond**. In: *JHEP*, **06**: (2011), p. 128. doi: [10.1007/JHEP06\(2011\)128](https://doi.org/10.1007/JHEP06(2011)128). arXiv: [1106.0522 \[hep-ph\]](https://arxiv.org/abs/1106.0522) (see pp. 45, 48).
- 2072 [116] MICHELANGELO L. MANGANO, MAURO MORETTI, FULVIO PICCININI, and MICHELE TREC-CANI: **Matching matrix elements and shower evolution for top-quark production in hadronic collisions**. In: *JHEP*, **01**: (2007), p. 013. doi: [10.1088/1126-6708/2007/01/013](https://doi.org/10.1088/1126-6708/2007/01/013). arXiv: [hep-ph/0611129 \[hep-ph\]](https://arxiv.org/abs/hep-ph/0611129) (see p. 45).
- 2073 [117] TORBJORN SJOSTRAND, STEFAN ASK, JESPER R. CHRISTIANSEN, et al.: **An introduction to {PYTHIA} 8.2**. In: *Computer Physics Communications*, **191**: (2015), pp. 159–177. doi: <http://dx.doi.org/10.1016/j.cpc.2015.01.024> (see pp. 45–46).
- 2074 [118] TORBJORN SJOSTRAND, STEPHEN MRENNA, and PETER Z. SKANDS: **PYTHIA 6.4 Physics and Manual**. In: *JHEP*, **0605**: (2006), p. 026. doi: [10.1088/1126-6708/2006/05/026](https://doi.org/10.1088/1126-6708/2006/05/026). arXiv: [hep-ph/0603175 \[hep-ph\]](https://arxiv.org/abs/hep-ph/0603175) (see pp. 45–46).
- 2075 [119] TORBJORN SJOSTRAND, STEFAN ASK, JESPER R. CHRISTIANSEN, et al.: **An Introduction to PYTHIA 8.2**. In: *Comput. Phys. Commun.*, **191**: (2015), pp. 159–177. doi: [10.1016/j.cpc.2015.01.024](https://doi.org/10.1016/j.cpc.2015.01.024). arXiv: [1410.3012 \[hep-ph\]](https://arxiv.org/abs/1410.3012) (see pp. 45–46, 48–49).

- 2104 [120] JOHAN ALWALL et al.: **Comparative study of various algorithms for the merging**
 2105 **of parton showers and matrix elements in hadronic collisions.** In: *Eur. Phys. J.*,
 2106 **C53:** (2008), pp. 473–500. doi: [10.1140/epjc/s10052-007-0490-5](https://doi.org/10.1140/epjc/s10052-007-0490-5). arXiv: [0706.2569](https://arxiv.org/abs/0706.2569)
 2107 [[hep-ph](#)] (see p. 45).
- 2108 [121] J. ALWALL, R. FREDERIX, S. FRIXIONE, et al.: **The automated computation of tree-level**
 2109 **and next-to-leading order differential cross sections, and their matching to parton**
 2110 **shower simulations.** In: *JHEP*, **07:** (2014), p. 079. doi: [10.1007/JHEP07\(2014\)079](https://doi.org/10.1007/JHEP07(2014)079).
 2111 arXiv: [1405.0301](https://arxiv.org/abs/1405.0301) [[hep-ph](#)] (see p. 45).
- 2112 [122] STEFANO FRIXIONE and BRYAN R. WEBBER: **Matching NLO QCD computations and**
 2113 **parton shower simulations.** In: *JHEP*, **06:** (2002), p. 029. doi: [10.1088/1126-6708/2002/06/029](https://doi.org/10.1088/1126-6708/2002/06/029). arXiv: [hep-ph/0204244](https://arxiv.org/abs/hep-ph/0204244) [[hep-ph](#)] (see pp. 45, 48).
- 2115 [123] RIKKERT FREDERIX and STEFANO FRIXIONE: **Merging meets matching in MC@NLO.**
 2116 In: *JHEP*, **12:** (2012), p. 061. doi: [10.1007/JHEP12\(2012\)061](https://doi.org/10.1007/JHEP12(2012)061). arXiv: [1209.6215](https://arxiv.org/abs/1209.6215)
 2117 [[hep-ph](#)] (see p. 45).
- 2118 [124] SIMONE ALIOLI, PAOLO NASON, CARLO OLEARI, and EMANUELE RE: **A general frame-**
 2119 **work for implementing NLO calculations in shower Monte Carlo programs: the**
 2120 **POWHEG BOX.** In: *Journal of High Energy Physics*, **2010**:6 (2010), p. 43. doi: [10.1007/JHEP06\(2010\)043](https://doi.org/10.1007/JHEP06(2010)043) (see pp. 45, 48).
- 2122 [125] SIMONE ALIOLI, PAOLO NASON, CARLO OLEARI, and EMANUELE RE: **NLO single-top**
 2123 **production matched with shower in POWHEG: s - and t -channel contributions.**
 2124 In: *Journal of High Energy Physics*, **2009**:09 (2009), p. 111. URL: <http://stacks.iop.org/1126-6708/2009/i=09/a=111> (see pp. 45, 48).
- 2126 [126] STEFANO FRIXIONE, PAOLO NASON, and CARLO OLEARI: **Matching NLO QCD com-**
 2127 **putations with parton shower simulations: the POWHEG method.** In: *Journal of*
 2128 *High Energy Physics*, **2007**:11 (2007), p. 070. URL: <http://stacks.iop.org/1126-6708/2007/i=11/a=070> (see pp. 45, 48).
- 2130 [127] SIMONE ALIOLI, PAOLO NASON, CARLO OLEARI, and EMANUELE RE: **A general frame-**
 2131 **work for implementing NLO calculations in shower Monte Carlo programs: the**
 2132 **POWHEG BOX.** In: *JHEP*, **06:** (2010), p. 043. doi: [10.1007/JHEP06\(2010\)043](https://doi.org/10.1007/JHEP06(2010)043). arXiv:
 2133 [1002.2581](https://arxiv.org/abs/1002.2581) [[hep-ph](#)] (see pp. 45, 48).
- 2134 [128] STEFANO FRIXIONE, PAOLO NASON, and CARLO OLEARI: **Matching NLO QCD com-**
 2135 **putations with Parton Shower simulations: the POWHEG method.** In: *JHEP*, **11:**
 2136 (2007), p. 070. doi: [10.1088/1126-6708/2007/11/070](https://doi.org/10.1088/1126-6708/2007/11/070). arXiv: [0709.2092](https://arxiv.org/abs/0709.2092) [[hep-ph](#)] (see
 2137 pp. 45, 48).
- 2138 [129] PAOLO NASON: **A New method for combining NLO QCD with shower Monte Carlo**
 2139 **algorithms.** In: *JHEP*, **11:** (2004), p. 040. doi: [10.1088/1126-6708/2004/11/040](https://doi.org/10.1088/1126-6708/2004/11/040).
 2140 arXiv: [hep-ph/0409146](https://arxiv.org/abs/hep-ph/0409146) [[hep-ph](#)] (see pp. 45, 48).
- 2141 [130] ANDREI V. GRITSAN, RAOUL RÖNTSCH, MARKUS SCHULZE, and MENG XIAO: **Constrain-**
 2142 **ing anomalous Higgs boson couplings to the heavy flavor fermions using matrix**
 2143 **element techniques.** In: *Phys. Rev.*, **D94**:5 (2016), p. 055023. doi: [10.1103/PhysRevD.94.055023](https://doi.org/10.1103/PhysRevD.94.055023). arXiv: [1606.03107](https://arxiv.org/abs/1606.03107) [[hep-ph](#)] (see pp. 45, 48).

- 2145 [131] IAN ANDERSON et al.: **Constraining anomalous HVV interactions at proton and**
 2146 **lepton colliders.** In: *Phys. Rev.*, **D89**:3 (2014), p. 035007. doi: [10.1103/PhysRevD.89.035007](https://doi.org/10.1103/PhysRevD.89.035007). arXiv: [1309.4819 \[hep-ph\]](https://arxiv.org/abs/1309.4819) (see pp. 45, 48).
- 2148 [132] SARA BOLOGNESI, YANYAN GAO, ANDREI V. GRITSAN, et al.: **On the spin and parity of**
 2149 **a single-produced resonance at the LHC.** In: *Phys. Rev.*, **D86**: (2012), p. 095031.
 2150 doi: [10.1103/PhysRevD.86.095031](https://doi.org/10.1103/PhysRevD.86.095031). arXiv: [1208.4018 \[hep-ph\]](https://arxiv.org/abs/1208.4018) (see pp. 45, 48).
- 2151 [133] YANYAN GAO, ANDREI V. GRITSAN, ZIJIN GUO, et al.: **Spin determination of single-**
 2152 **produced resonances at hadron colliders.** In: *Phys. Rev.*, **D81**: (2010), p. 075022.
 2153 doi: [10.1103/PhysRevD.81.075022](https://doi.org/10.1103/PhysRevD.81.075022). arXiv: [1001.3396 \[hep-ph\]](https://arxiv.org/abs/1001.3396) (see pp. 45, 48).
- 2154 [134] PIERRE ARTOISENET, RIKKERT FREDERIX, OLIVIER MATTELAER, and ROBBERT RIETKERK:
 2155 **Automatic spin-entangled decays of heavy resonances in Monte Carlo simulations.** In: *JHEP*, **03**: (2013), p. 015. doi: [10.1007/JHEP03\(2013\)015](https://doi.org/10.1007/JHEP03(2013)015). arXiv: [1212.3460 \[hep-ph\]](https://arxiv.org/abs/1212.3460) (see p. 46).
- 2158 [135] V. KHACHATRYAN and ETAL: **Event generator tunes obtained from underlying event**
 2159 **and multiparton scattering measurements.** In: *The European Physical Journal C*,
 2160 **76**:3 (Mar. 17, 2016), p. 155. doi: [10.1140/epjc/s10052-016-3988-x](https://doi.org/10.1140/epjc/s10052-016-3988-x) (see p. 46).
- 2161 [136] RICHARD D. BALL et al.: **Parton distributions with LHC data.** In: *Nucl. Phys.*, **B867**:
 2162 (2013), pp. 244–289. doi: [10.1016/j.nuclphysb.2012.10.003](https://doi.org/10.1016/j.nuclphysb.2012.10.003). arXiv: [1207.1303 \[hep-ph\]](https://arxiv.org/abs/1207.1303) (see p. 46).
- 2164 [137] YUE ZHANG, BO HUA LI, CHONG SHENG LI, JUN GAO, and HUA XING ZHU: **Next-to-**
 2165 **leading order QCD corrections to the top quark associated with γ production via**
 2166 **model-independent flavor-changing neutral-current couplings at hadron colliders.** In: *Phys. Rev.*, **D83**: (2011), p. 094003. doi: [10.1103/PhysRevD.83.094003](https://doi.org/10.1103/PhysRevD.83.094003). arXiv: [1101.5346 \[hep-ph\]](https://arxiv.org/abs/1101.5346) (see p. 47).
- 2169 [138] J ALWALL, R FREDERIX, S FRIXIONE, et al.: **The automated computation of tree-**
 2170 **level and next-to-leading order differential cross sections, and their matching to**
 2171 **parton shower simulations.** In: *JHEP*, **07**:arXiv:1405.0301. CERN-PH-TH-2014-064.
 2172 CP3-14-18. LPN14-066. MCNET-14-09. ZU-TH 14-14 (May 2014), 079. 158 p. URL:
<http://cds.cern.ch/record/1699128> (see p. 48).
- 2174 [139] RIKKERT FREDERIX and STEFANO FRIXIONE: **Merging meets matching in MC@NLO.**
 2175 In: *JHEP*, **12**:arXiv:1209.6215. CERN-PH-TH-2012-247. ZU-TH 21-12 (Sept. 2012).
 2176 Comments: 40 pages, 14 figures, 061. 40 p. URL: <http://cds.cern.ch/record/1481985>
 2177 (see p. 48).
- 2178 [140] **CMS Monte Carlo Generator Group** (see pp. 48–49).
- 2179 [141] T. GEHRMANN, M. GRAZZINI, S. KALLWEIT, et al.: **W^+W^- Production at Hadron**
 2180 **Colliders in Next to Next to Leading Order QCD.** In: *Phys. Rev. Lett.*, **113**:21 (2014),
 2181 p. 212001. doi: [10.1103/PhysRevLett.113.212001](https://doi.org/10.1103/PhysRevLett.113.212001). arXiv: [1408.5243 \[hep-ph\]](https://arxiv.org/abs/1408.5243) (see
 2182 p. 49).
- 2183 [142] A. HOECKER, P. SPECKMAYER, J. STELZER, et al.: **TMVA - Toolkit for Multivariate Data**
 2184 **Analysis.** In: *ArXiv Physics e-prints*, (Mar. 2007). eprint: [physics/0703039](https://arxiv.org/abs/physics/0703039) (see p. 50).
- 2185 [143] R. BRUN and F. RADEMAKERS: **ROOT: An object oriented data analysis framework.**
 2186 In: *Nucl. Instrum. Meth.*, **A389**: (1997), pp. 81–86. doi: [10.1016/S0168-9002\(97\)00048-X](https://doi.org/10.1016/S0168-9002(97)00048-X) (see p. 50).

- 2188 [144] A. MAYR, H. BINDER, O. GEFELLER, and M. SCHMID: **The Evolution of Boosting**
 2189 **Algorithms - From Machine Learning to Statistical Modelling.** In: *ArXiv e-prints*,
 2190 (Mar. 2014). arXiv: [1403.1452 \[stat.ME\]](https://arxiv.org/abs/1403.1452) (see p. 51).
- 2191 [145] OLAF BEHNKE, KEVIN KRONINGER, GREGORY SCHOTT, and THOMAS SCHORNER-SADENIUS: **Data Analysis in High Energy Physics: A Practical Guide to Statistical Methods.** 1st.
 2192 Wiley-VCH, 2013 (see p. 51).
- 2193 [146] CHRISTIAN BÖSER, SIMON FINK, and STEFFEN RÖCKER: **Introduction to Boosted**
 2194 **Decision Trees: A multivariate approach to classification problems.** Presented at
 2195 the 'KSETA Doktoranden' workshop, Lauterbad. July 2014. URL: <https://indico.scc.kit.edu/indico/event/48/session/4/contribution/35/material/slides/0.pdf> (see
 2196 p. 51).
- 2197 [147] SERGUEI CHATRHYAN et al.: **Combined results of searches for the standard model**
 2198 **Higgs boson in pp collisions at $\sqrt{s} = 7$ TeV.** In: *Phys. Lett.*, **B710**: (2012), pp. 26–
 2199 48. DOI: [10.1016/j.physletb.2012.02.064](https://doi.org/10.1016/j.physletb.2012.02.064). arXiv: [1202.1488 \[hep-ex\]](https://arxiv.org/abs/1202.1488) (see p. 52).
- 2200 [148] GLEN COWAN, KYLE CRANMER, EILAM GROSS, and OFER VITELLS: **Asymptotic formulae**
 2201 **for likelihood-based tests of new physics.** In: *Eur. Phys. J.*, **C71**: (2011). [Erratum:
 2202 Eur. Phys. J.C73,2501(2013)], p. 1554. DOI: [10.1140/epjc/s10052-011-1554-0](https://doi.org/10.1140/epjc/s10052-011-1554-0), [10.1140/epjc/s10052-013-2501-z](https://doi.org/10.1140/epjc/s10052-013-2501-z). arXiv: [1007.1727 \[physics.data-an\]](https://arxiv.org/abs/1007.1727) (see
 2203 pp. 52–53).
- 2204 [149] **Observation of a new boson with a mass near 125 GeV.** Tech. rep. CMS-PAS-HIG-
 2205 12-020. Geneva: *CERN*, 2012. URL: <https://cds.cern.ch/record/1460438> (see
 2206 p. 52).
- 2207 [150] **Procedure for the LHC Higgs boson search combination in Summer 2011.** Tech.
 2208 rep. CMS-NOTE-2011-005. ATL-PHYS-PUB-2011-11. Geneva: *CERN*, Aug. 2011. URL:
 2209 [http://cds.cern.ch/record/1379837](https://cds.cern.ch/record/1379837) (see p. 52).
- 2210 [151] HIGGS WORKING GROUP: **Documentation of the RooStats based statistics tools for**
 2211 **Higgs PAG.** Aug. 2017. URL: <https://twiki.cern.ch/twiki/bin/viewauth/CMS/SWGuideHiggsAnalysisCombinedLimit> (see p. 52).
- 2212 [152] LORENZO MONETA, KEVIN BELASCO, KYLE S. CRANMER, et al.: **The RooStats Project.**
 2213 In: *PoS, ACAT2010*: (2010), p. 057. arXiv: [1009.1003 \[physics.data-an\]](https://arxiv.org/abs/1009.1003) (see p. 52).
- 2214 [153] GLEN COWAN, KYLE CRANMER, EILAM GROSS, and OFER VITELLS: **Asymptotic formulae**
 2215 **for likelihood-based tests of new physics.** In: *The European Physical Journal C*, **71**:2
 2216 (Feb. 2011). DOI: [10.1140/epjc/s10052-011-1554-0](https://doi.org/10.1140/epjc/s10052-011-1554-0). arXiv: [1007.1727 \[hep-ph\]](https://arxiv.org/abs/1007.1727) (see
 2217 p. 52).
- 2218 [154] THOMAS JUNK: **Confidence level computation for combining searches with small**
 2219 **statistics.** In: *Nuclear Instruments and Methods in Physics Research Section A: Accelerators,*
 2220 *Spectrometers, Detectors and Associated Equipment*, **434**:2 (1999), pp. 435–443.
 2221 DOI: [https://doi.org/10.1016/S0168-9002\(99\)00498-2](https://doi.org/10.1016/S0168-9002(99)00498-2) (see p. 52).
- 2222 [155] AL READ: **Presentation of search results: the CL s technique.** In: *Journal of Physics G: Nuclear and Particle Physics*, **28**:10 (2002), p. 2693. URL: <http://stacks.iop.org/0954-3899/28/i=10/a=313> (see p. 52).

- 2229 [156] A. M. SIRUNYAN et al.: **Particle-flow reconstruction and global event description**
 2230 **with the CMS detector.** In: *JINST*, **12**: (2017), P10003. DOI: [10.1088/1748-0221/12/10/P10003](https://doi.org/10.1088/1748-0221/12/10/P10003). arXiv: [1706.04965 \[physics.ins-det\]](https://arxiv.org/abs/1706.04965) (see pp. 56–60, 62).
- 2232 [157] R. FRÜHWIRTH: **Application of Kalman filtering to track and vertex fitting.** In: *Nuclear Instruments and Methods in Physics Research Section A: Accelerators, Spectrometers, Detectors and Associated Equipment*, **262**:2 (1987), pp. 444–450. DOI: [http://dx.doi.org/10.1016/0168-9002\(87\)90887-4](http://dx.doi.org/10.1016/0168-9002(87)90887-4) (see p. 57).
- 2236 [158] PIERRE BILLOIR: **Progressive track recognition with a Kalman like fitting procedure.** In: *Comput. Phys. Commun.*, **57**: (1989), pp. 390–394. DOI: [10.1016/0010-4655\(89\)90249-X](https://doi.org/10.1016/0010-4655(89)90249-X) (see p. 57).
- 2239 [159] SERGUEI CHATRCHYAN et al.: **Performance of CMS muon reconstruction in $p p$ collision events at $\sqrt{s} = 7$ TeV.** In: *JINST*, **7**: (2012), P10002. DOI: [10.1088/1748-0221/7/10/P10002](https://doi.org/10.1088/1748-0221/7/10/P10002). arXiv: [1206.4071 \[physics.ins-det\]](https://arxiv.org/abs/1206.4071) (see p. 57).
- 2242 [160] W ADAM, R FRÜHWIRTH, A STRANDLIE, and T TODOROV: **Reconstruction of electrons with the Gaussian-sum filter in the CMS tracker at the LHC.** In: *Journal of Physics G: Nuclear and Particle Physics*, **31**:9 (2005), N9. URL: <http://stacks.iop.org/0954-3899/31/i=9/a=N01> (see p. 57).
- 2246 [161] **Performance of electron reconstruction and selection with the CMS detector in proton-proton collisions at $\sqrt{s} = 8$ TeV.** In: *Journal of Instrumentation*, **10**:06 (2015), P06005. URL: <http://stacks.iop.org/1748-0221/10/i=06/a=P06005> (see p. 58).
- 2249 [162] **Electron and photon performance in CMS with the full 2016 data sample.** In: (Mar. 2017). URL: <http://cds.cern.ch/record/2255497> (see pp. 58, 62, 64).
- 2251 [163] K. ROSE: **Deterministic annealing for clustering, compression, classification, regression, and related optimization problems.** In: *Proceedings of the IEEE*, **86**:11 (Nov. 1998), pp. 2210–2239. DOI: [10.1109/5.726788](https://doi.org/10.1109/5.726788) (see p. 58).
- 2254 [164] WOLFGANG WALTENBERGER: **Adaptive Vertex Reconstruction.** Tech. rep. CMS-NOTE-2008-033. Geneva: CERN, July 2008. URL: <https://cds.cern.ch/record/1166320> (see p. 58).
- 2257 [165] ANDREAS KORNMAYER: **The CMS Pixel Luminosity Telescope.** Tech. rep. CMS-CR-2015-121. Geneva: CERN, June 2015. URL: <https://cds.cern.ch/record/2039978> (see p. 59).
- 2260 [166] **CMS Luminosity Measurements for the 2016 Data Taking Period.** Tech. rep. CMS-PAS-LUM-17-001. Geneva: CERN, 2017. URL: <http://cds.cern.ch/record/2257069> (see p. 59).
- 2263 [167] **Measurement of the inelastic proton-proton cross section at $\sqrt{s} = 13$ TeV.** Tech. rep. CMS-PAS-FSQ-15-005. Geneva: CERN, 2016. URL: <https://cds.cern.ch/record/2145896> (see p. 60).
- 2266 [168] **Muon Identification and Isolation efficiency on full 2016 dataset.** In: (Mar. 2017). URL: <http://cds.cern.ch/record/2257968> (see pp. 60–61).
- 2268 [169] **Effective areas used for Summer16 samples.** May 2017. URL: https://indico.cern.ch/event/482673/contributions/2187022/%20attachments/1282446/1905912/talk_electron_ID_spring16.pdf (see p. 63).

- 2271 [170] MATTEO CACCIARI, GAVIN P. SALAM, and GREGORY SOYEZ: **The Anti-k(t) jet clustering**
 2272 **algorithm**. In: *JHEP*, **04**: (2008), p. 063. doi: [10.1088/1126-6708/2008/04/063](https://doi.org/10.1088/1126-6708/2008/04/063). arXiv:
 2273 [0802.1189 \[hep-ph\]](https://arxiv.org/abs/0802.1189) (see p. 63).
- 2274 [171] **Jet algorithms performance in 13 TeV data**. Tech. rep. CMS-PAS-JME-16-003.
 2275 Geneva: CERN, 2017. URL: <http://cds.cern.ch/record/2256875> (see p. 63).
- 2276 [172] V. KHACHATRYAN et al.: **Jet energy scale and resolution in the CMS experiment in**
 2277 **pp collisions at 8 TeV**. In: *Journal of Instrumentation*, **12**:02 (2017), P02014. URL:
 2278 <http://stacks.iop.org/1748-0221/12/i=02/a=P02014> (see pp. 65–66).
- 2279 [173] **Jet energy scale and resolution performances with 13TeV data**. In: (June 2016).
 2280 URL: <http://cds.cern.ch/record/2160347> (see pp. 65–66).
- 2281 [174] THE CMS COLLABORATION: **Identification of b-quark jets with the CMS experiment**.
 2282 In: *Journal of Instrumentation*, **8**:04 (2013), P04013. URL: <http://stacks.iop.org/1748-0221/8/i=04/a=P04013> (see p. 66).
- 2284 [175] **Identification of b quark jets at the CMS Experiment in the LHC Run 2**. Tech. rep.
 2285 CMS-PAS-BTV-15-001. Geneva: CERN, 2016. URL: <http://cds.cern.ch/record/2138504> (see pp. 66, 68).
- 2287 [176] NAZAR BARTOSIK: **Diagram showing the common principle of identification of jets**
 2288 **initiated by b-hadron decays**. May 2016. URL: http://bartosik.pp.ua/hep_sketches/btagging (see p. 67).
- 2290 [177] **Identification of b quark jets at the CMS Experiment in the LHC Run 2**. Tech. rep.
 2291 CMS-PAS-BTV-16-001. unpublished. Geneva: CERN, 2017 (see pp. 68–69).
- 2292 [178] **Performance of missing energy reconstruction in 13 TeV pp collision data using**
 2293 **the CMS detector**. Tech. rep. CMS-PAS-JME-16-004. Geneva: CERN, 2016. URL:
 2294 <http://cds.cern.ch/record/2205284> (see pp. 69, 74–75).
- 2295 [179] JORDAN DAMGOV: **Missing Et Optional Filters Run 2**. Oct. 2017. URL: <https://twiki.cern.ch/twiki/bin/viewauth/CMS/MissingETOptionalFiltersRun2> (see p. 74).
- 2297 [180] **EGM corrections for Moriond17**. URL: https://indico.cern.ch/event/613162/contributions/2472046/attachments/1410308/2156822/EGMSmearerAndRegression_PPD_022017.pdf (see p. 78).
- 2300 [181] **Misalignment and Muon Scale corrections**. URL: https://www-cdf.fnal.gov/~jyhan/cms_momscl/rochcor_cmsnote.pdf (see p. 79).
- 2302 [182] **Rochestor Correction**. Accessed: 2017-05-20. URL: <https://twiki.cern.ch/twiki/bin/viewauth/CMS/RochcorMuon> (see p. 79).
- 2304 [183] **Evidence for the standard model production of a Z boson with a single top quark**
 2305 **in pp collisions at $\sqrt{s} = 13$ TeV**. Tech. rep. CMS-PAS-TOP-16-020. Geneva: CERN,
 2306 2017. URL: <http://cds.cern.ch/record/2284830> (see p. 97).
- 2307 [184] RICHARD D. BALL et al.: **Parton distributions from high-precision collider data**. In:
 2308 *Eur. Phys. J. C*, **77**: (2017), p. 663. doi: [10.1140/epjc/s10052-017-5199-5](https://doi.org/10.1140/epjc/s10052-017-5199-5). arXiv:
 2309 [1706.00428 \[hep-ph\]](https://arxiv.org/abs/1706.00428) (see p. 97).
- 2310 [185] L DEMORTIER and L LYONS: **Everything you always wanted to know about pulls**.
 2311 Tech. rep. CDF/ANAL/PUBLIC/5776. CDF, Feb. 2002 (see p. 110).